Magnetic multilayer for magnetic memories

Thomas Hauet

▶ **To cite this version:**

Thomas Hauet. Magnetic multilayer for magnetic memories. Materials Science [cond-mat.mtrl-sci]. Université de Lorraine, 2016. tel-01569111

HAL Id: tel-01569111
https://hal.science/tel-01569111

Submitted on 26 Jul 2017

HAL is a multi-disciplinary open access archive for the deposit and dissemination of scientific research documents, whether they are published or not. The documents may come from teaching and research institutions in France or abroad, or from public or private research centers.

L'archive ouverte pluridisciplinaire **HAL**, est destinée au dépôt et à la diffusion de documents scientifiques de niveau recherche, publiés ou non, émanant des établissements d'enseignement et de recherche français ou étrangers, des laboratoires publics ou privés.

Distributed under a Creative Commons Attribution - NonCommercial - ShareAlike 4.0 International License

Habilitation à Diriger des Recherches

En Physique

Par :

Thomas Hauet

Maître de conférences à l'Université de Lorraine

Magnetic multilayer for magnetic memories

Soutenance publique le 28 novembre 2016 devant le jury :

Rapporteurs : Vincent Cros, Directeur de recherche CNRS
Kristiaan Temst, Professeur des Universités
Dominique Givord, Directeur de recherche CNRS

Examinateurs : Véronique Dupuis, Directeur de recherche CNRS (présidente)
Stéphane Andrieu, Professeur des Universités
Marc Respaud, Professeur des Universités
Philippe Lecoeur, Professeur des Universités

Institut Jean Lamour
Faculté des Sciences et Techniques - BP 329 - 54506 Vandoeuvre lès Nancy

Outline :

Part I.
Introduction

I.1) Magnetic memories and spintronic

Information or data can be recorded using virtually any form of energy, from manual muscle power in handwriting, to acoustic vibrations in phonographic recording, to electromagnetic energy modulating magnetic tape and optical discs. The capacity of stored information is usually measured in bits, where one bit corresponds to the smallest division of the information, i.e. a "1" or a "0" in the binary language. Magnetic storage and magnetic recording refer to systems that store data on a magnetic medium, providing non-volatility and unlimited rewriting capability. As described in the following, one can mainly distinguished two types of magnetic memories: the so-called Magnetic random access memory MRAM (Fig.1(a)) and head/media based devices (Fig.1(b)).

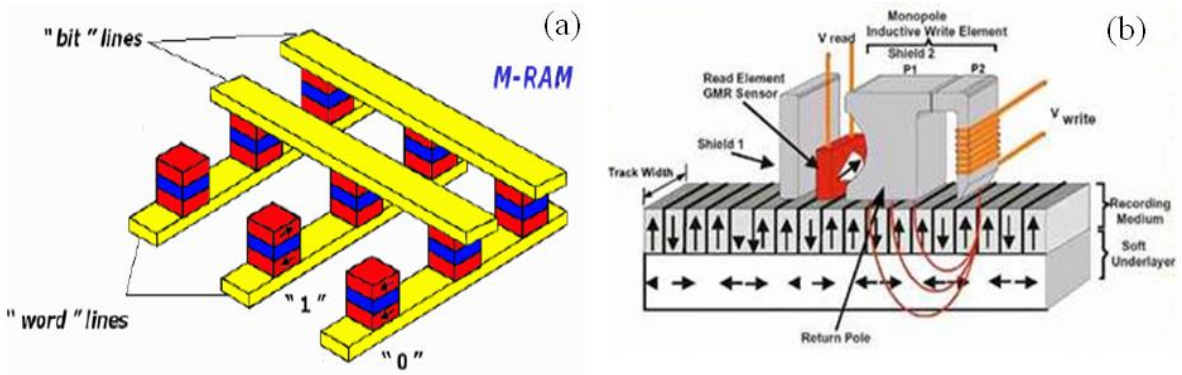

Fig.1. Typical architecture of a Spin transfer torque MRAM (a) and a hard disk drive (b).

The first head/media type memory was tape recorder, demonstrated in 1935 by BASF in Germany. In 1956 IBM introduced the 305 RAMAC computer system. It included the first magnetic disk drive, the IBM 350, which had a storage capacity of 4 Mbytes, was the size of two large refrigerators, and weighed two tons. Tape and disk drive both rely on a magnetic media made of nanometric grain whose magnetization points either up or down to mark a "0" or a "1" of the binary language. The head is composed of the writing head that is in charge of sending a magnetic field on the media to orient the magnetization of the media and of a reading head, i.e. a sensor that senses the magnetic field coming from the grains magnetization to deduce if they hold a "0" or a "1" information. Today, laptop computers commonly have disk drives that can store in excess of 1 Terabytes and are the size of a pack of cards. This represents an increase in the areal density (number of bits per square inch of disk surface) of more than nine orders of magnitude from 2 kbits/in^2 in 1956 to 1.5 terabits/in^2 in today's state-of-the-art drives. Through the first 5 years IBM sold a total of about 1000 magnetic disk drives, with a total storage capacity of about 4 Gbytes (or $32 \cdot 10^9$ bits) some of which are still operational to this day in museums. For 2010, it has been estimated that 1000 Exabytes (10^{22} bits) of data were created and replicated worldwide [1]. As of now, magnetic storage media, primarily hard disk drive (HDD) or tape, are widely used to store computer data as well as audio and video signals. Magnetic tape is used when storing large amounts of data mostly for backups and archives (e.g. for Banks or archival data centers like Oracle) where accessing time is not an issue and where infinite life time and extremely low cost are

required. Part II.1 will be devoted head/media memory, more precisely to new schemes for HDD media.

The Head/media memory technologies described above (similarly to today's MRAM technologies) have always been tightly connected to scientific breakthroughs and especially the new discoveries regarding interplays between electronic spin and magnetic moments, that have led to the so-called spintronic (see Fig. 2). For instance, current HDD is the consequence of half-century of development. Over the years the read head sensor has evolved from inductive heads, i.e., sensing coils wound around magnetic poles, to inductive thin film heads, where the poles and coils were deposited by thin film processing, and then starting in the early 1990s a rapid succession of magnetoresistance (MR) effects to probe the field emerging from the medium. The most commonly known of these effects is probably giant magnetoresistance (GMR) which was independently discovered in the late 1980's by Albert Fert in France and Peter Gruenberg in Germany. Fert and Gruenberg shared the 2007 Nobel Prize in Physics for their discovery. Subsequently, scientists at IBM rapidly turned this scientific discovery into a mature technology, and in 1996 IBM shipped the first products with GMR spin-valve read heads. Starting in 2005 the newest generations of heads have been using a related technology based on magnetic tunnel junction (MTJ). In both these cases, the sensor is based on a trilayer stack in which a non-magnetic spacer layer allows decoupling magnetically a free layer from a reference layer. The fields originating from successive bits orient the magnetization of the probe layer relatively to the other magnetic layer whose magnetization is kept fixed. During the reading process an electrical current is sent in the sensor stack whose resistance varies with the relative orientation of the magnetizations. If the exchange-decoupling layer is metallic, the device is called spin-valve and the MR effect is the GMR whereas if it is an insulator, the device is called MTJ and the MR effect is called tunneling magnetoresistance (TMR). These two devices have led to dramatic improvements in sensitivity and signal-to-noise ratio of the read sensors and allowed to continuously decrease the area allocated to one bit.

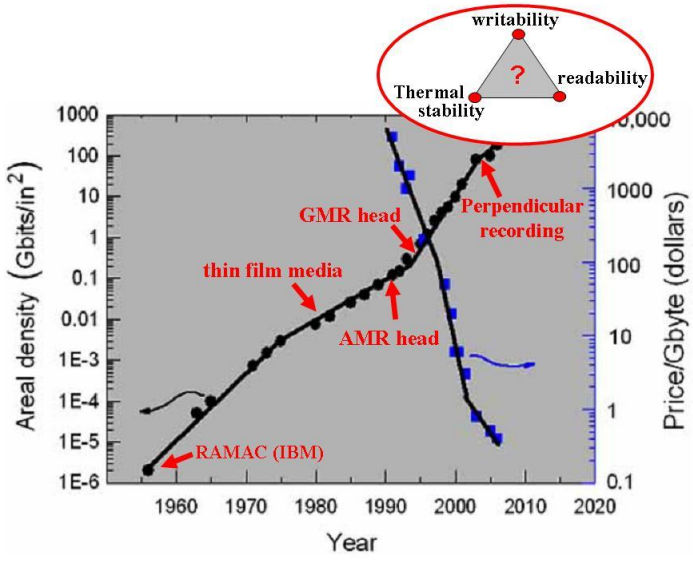

Fig. 2. Evolution of areal density and price per Gigabyte (1 byte = 8 bits) of magnetic HDD with time since 1956 (RAMAC). After 2010, the recording trilemma, i.e. the requested equilibrium between writability, readability and thermal stability, leads to uncertainties on the areal density growth trend. [Sbiaa2007]

All these advances in head technology have been accompanied by similar improvements in media technology enabled by many years of intense research on material sciences. The first media were based on grains with randomly orientated anisotropy from iron oxide embedded in epoxy binder materials. Ultra-high vacuum techniques allowed to develop in-plane magnetized thin film media media. Today the industry has transitioned to a technology called perpendicular magnetic recording (PMR) thanks to the understanding of the magnetic anisotropy features in CoPtCr alloys that are quite close to the Co/Pt or Co/Ni multilayer discussed in details in my manuscript. As we can see on Fig. 2, each of this new scientific development, translated into technology has affected positively the areal density progess rate vs time curve as well as has helped decreasing HDD cost. Although current MRAM is much younger than HDDs, its renewal, as well as its future are directly linked to the scientific achievements around magnetic tunnel junctions and spintronics.

Why do I talk about renewal? Because one has to remember that the Danish engineer Valdemar Poulsen is indeed considered as the first developer of a functioning magnetic storage apparatus. It was in 1898 and he used a magnetic wire as a recording medium and a nail with an electrical wire wound around it for inductive recording and read-back. When the superposition of fields provided by a simultaneous set of current pulses along each line was sufficient to switch the magnetization direction of the element, it was written into a new state. A destructive read was enabled through monitoring the inductive signal on a separate read line. In order to read the bit, an attempt to write it into a known state was made. The lack of an induced voltage pulse revealed that the bit was in that known state, while an inductive pulse revealed the other state. Such magnetic cross point architecture has persisted through the 20th century [2] and contemporary magnetic random access memories (MRAM) harkens back to it. Today's conventional MRAM are based on MTJs for read and write process. Each memory cell or bit is composed of one MTJ. The high and low resistance state, for anti-parallel (AP) and parallel (P) state respectively, correspond to the "0" and "1" of the binary language. The reading process is therefore a resistance measurement of a selected cell through the random access architecture. The writing process can be performed either by a field induced by an Oersted line or by the application of a large current in the MTJ. In the latest case, the free layer magnetization is switched by spin-transfer torque. This effect will be discussed in details in Part I.2. The first commercial MRAM product of this kind appeared approximately in 2006 and had 4 Mbyte capacity (Freescale Semiconductor now Everspin Technologies). Currently there is great hope in MRAM replacing Flash memory and DRAM. Many of the largest worldwide companies (Toshiba, Samsung, IBM, etc.) invest to develop this technology. Although the market growth may be dramatic within few years, the current market is mainly restricted to extreme condition uses (Aerospace, airplane, automotive) and data areal density remains low 64Mbytes. MRAM differentiates itself from the other magnetic data storage through fast read and write times, good thermal stability and directly pairing with a microprocessor, rather than a system for storing extensive volumes of information as for tape memory and Hard disk drives. Note that three dimensional (3D) recording systems, for instance based on RAM principle, is heavily investigated as it would ally all the nice features of 2D MRAM with huge increase of recording areal density. I will propose and demonstrate, in Part II.2, one architecture for 3D memory device.

As the third dimension is still far from being tamed, one has to continue to improve the 2D areal storage density. Nevertheless, among many other technical issues, it requires a perpetual work on developing new materials and on implementing new scientific discoveries in order to go over the common challenge to all magnetic memory, the so-called recording trilemma (see Fig. 2). The first key aspect of the trilemma consists in maintaining magnetic information in volumes so small that the total magnetic energy related to preserving the direction of the magnetization, commonly expressed as the product of the magnetic anisotropy, K_U, and the magnetic grain volume, V, becomes comparable to the energy of thermal fluctuations at room temperature, commonly expressed as the product of Boltzmann's constant, k_B, and the temperature, T. This phenomenon is generally referred to as superparamagnetism and can result in a loss of the stored information. A good thermal stability is usually reached when $K_uV \geq 40\text{-}60\ k_BT$. As the areal density growth decreases, the grain volume V has to be reduced. It is then obvious to conclude that the solution to maintain the magnetic stability of the media while decreasing the grain size is to increase the magnetic anisotropy of the grain. But stability is not the only important parameter for a memory bit to perform. Equally important are writability and readability. In terms of writability, the ability to switch bit magnetization (e.g. with the head field in HDD and with spin transfer torque in MRAM) is in first approximation proportional to K_U. Since, the field currently produced by the HDD head is close to its maximum and since write-current in MRAM needs to remain low for energy consumption quality, writability places an upper limit in the value of K_U for the medium. Besides bit-to-bit switching field distribution explode has the bit size decreases and average Ku increases which leads to a large raise of data error-rate. Third, as of readability, large Ku material are not the best materials to provide high voltage variation output in MRAM and, in HDD, the reduction of the bit size leads to strong constrains on the read-head position and width.

Because of the recording trilemma issue, the past twenty years has known a large effort of numerous scientifics in the field to create new heterostructures controlled at the atomic level, to develop new measurement tools capable of sensing at the nanoscale and at the nanosecond scale, to understand new phenomena originating from the film thickness and lateral size reduction, and to use them all towards improving magnetic media and sensors. I have been involved in that adventure.

I.2. Perpendicular anisotropy in magnetic multilayers

Co/Pt, Co/Pd and Co/Ni interfaces, discussed in the present manuscript, as well as Co/Au, Fe/V, Fe/Ag, Ni/Cu, Ni/Au, etc., have been studied since the very end of the 1980's when complex thin films get more easy to be grown, when new techniques were developed to measure properties of small amount of materials or at the nanoscale, and because of the discovery of major effects linked to interfaces to like RKKY coupling or giant magnetoresistance. Light has been especially shed on Co/Pt, Co/Pd and Co/Ni multilayers (MLs) with Co thicknesses of few angstroms as they hold perpendicular magnetic anisotropy (PMA) of high interest for magnetic recording, especially so-called magneto-optical recording

[3,4]. Since the first observations, PMA MLs have been heavily used as model system to test in details the models describing magnetic anisotropy as well as to help developing magnetic recording media both for HDD and MRAM. My manuscript (and the references therein) as well as recent and today's large number of publications based on MLs show that the interest remain high for these systems and that they are still source of new discoveries (e.g. see DMI interactions and transport phenomena related to spin-orbit interactions). In the following I briefly sum up the main experimental results of the literature, the main origins of PMA in MLs and the theoretical models used to describe them.

The most studied systems are Co/Pt and Co/Pd that have very similar behaviors and the advantage to have only one ferromagnetic atom to study whereas Co/Ni holds two. The magnetic anisotropy energy is defined as the difference of energy between the out-of-plane magnetized configuration and the in-plane magnetized configuration. It can be measured in following the MLs overall magnetization reorientation under a field that points either in-plane or out-of-plane with vibrating sample magnetometry, torque magnetometry, ferromagnetic resonance, Brillouin scattering. The most usefull plot to understand PMA in MLs is shown in Fig. 3 in the case of a $[Co/Pd]_N$ from [5]. The effective magnetic anisotropy energy K_{eff} ($J.m^{-3}$), the weighted average of the volumic magnetic anisotropy energy (MAE) of Co atoms in Co/Pd MLs, is phenomenologically separated in a Co volume contribution Kv ($J.m^{-3}$) and a contribution from the Co/Pd interfaces Ks ($J.m^{-2}$) and approximately obeyed the relation:

$$K_{eff} t_{Co} = K_V t_{Co} + K_S$$

where t_{Co} is the Co thickness within one Co/Pd bilayer, so that the number of repeat N should not affect Kv and Ks. A positive K_{eff} describes the case of a preferred direction of the magnetization perpendicular to the layer plane. The negative slope indicates a negative volume anisotropy Kv, favouring in-plane magnetization, while the intercept at zero Co thickness indicates positive interface anisotropy Ks, favoring perpendicular magnetization. Below a certain thickness (here 1.3 nm), the interface anisotropy contribution outweighs the volume contribution, resulting in a perpendicularly magnetized system.

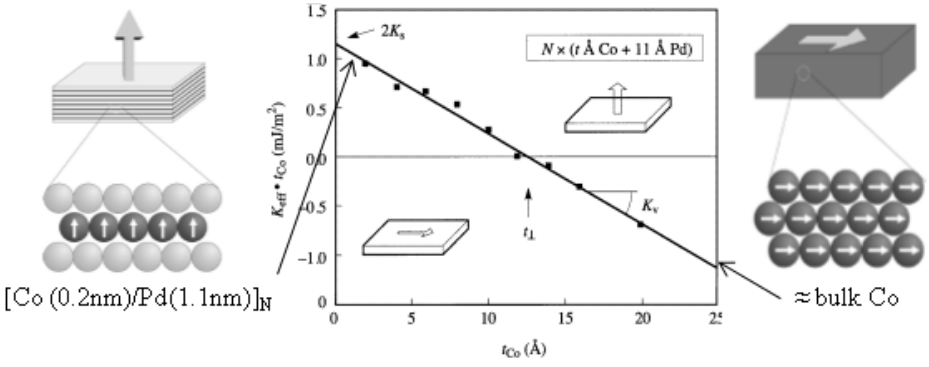

Fig.3. Total anisotropy times the individual Co layer thickness (t_{Co}) versus the individual Co layer thickness of Co/Pd multilayers. The vertical axis intercept equals twice the interface anisotropy, whereas the slope gives the volume contribution [5]. On the left and right are schemes of the Co atom moment orientation when Co atoms are placed in a Co/Pt multilayer or alone as a pure Co thin film.

Although it is very usefull to disentangle the role of the interface in inducing PMA, the phenomenological equation hides the nature of the phenomena behind Kv and Ks. In Co/Pd MLs, the volumic anisotropy holds at least three different origin of anisotropy. The first one is the long range magnetic dipolar interaction, also called shape anisotropy or demagnetization field, as it depends on the outer boundaries of the sample. For a thin film, its contribution favours an in-plane preferential orientation for the magnetization and, under the assumption of a magnetization continuum instead of considering individual dipoles [6], its amplitude depends on the square of the magnetization amplitude (Ms). Demagnetization field amplitude is usually of the order of -10^6 J.m^{-3} for 3d metals like Fe and Co having large Ms. One can wonder in the case of few atomic layers if the continuum assumption is still valid. But in the literature, most of the calculations show that, in fcc (111) crystal, the overall gap with the continuum dipolar calculations is negligible.

The second volumic contribution is the so-called magneto-crystalline anisotropy which originates from the spin-orbit coupling. In 3d metals, although magnetism is mostly due to spin moment because the orbital moment is quenched and small, the electron spin is weakly coupled to the orbital moment via spin-orbit coupling, and as a consequence the total energy of the system depends on the relative orientation between magnetization (all spins) and crystal axes. The high symmetry of regular bulk 3d metals, as Co fcc lattice, leads to small magnetic anisotropies of the order of 10^4 J.m^{-3}. In fcc Co, the magneto-crystalline anisotropy is positive along the (111) direction, i.e. magnetization tends to align along (111) direction [7,8]. This has been evidenced in comparing the slope of $K_{eff}*t_{Co}$ vs t_{Co} line for different epitaxial growth directions [9,10]. As a consequence, in (111) Co/Pd and Co/Pt MLs, the magneto-crystalline anisotropy energy favors PMA.

The third volumic term is the magneto-elastic energy which is a correction to the ideal magnetocristalline anisotropy due to distortion of the ideal lattice. Such distortion is most of the time induced by a difference of lattice parameter between the two constituents of the ML or between the ML and the substrate on which it has been deposited [4]. The amplitude of magneto-elastic anisotropy energy is usually much larger than the magneto-crystalline contribution itself [8], up to the order of 10^5 to 10^6 J.m^{-3} [11,12]. Although it originates from interfacial mismatch, the lattice distortion is spread over many atomic layer so that the effect is mostly calculated as a volumic contribution. In Co/Pd and Co/Pt, 10% lattice mismatch may generate significant PMA due to the tensile strain of Pd of Co [13-15]. The role of a small CoPd alloying at the interface coupled to strain has been also heavily investigated. Note that the role of strain as primary contribution to the interfacial anisotropy has also been widely discussed [5,16,17] and recent works on FeCo/Pt systems [12,18].

Of course, when considering this latest Ref. [18] where very large PMA is induced by tuning FeCo atomic layer lattice parameter through strain on one or two atomic layer, the notion of volume does no longer make sense. Nevertheless, when looking at Fig. 3, it is clear that even for thick Co thickness, a contribution from the interface adds to the PMA. It was first pointed out by Neel that a enhanced anisotropy energy may occur at a surface due to reduced symmetry [19]. Nevertheless, in this model, a Co/X multilayer, X being a non-

magnetic atom, the interface anisotropy would not depend on X only through its influence on the Co structure. But in (111) Co/Pt, Co/Au, Co/Pd or Co/Cu, the (111) Co structure is kept more or less constant whereas anisotropy varies a lot. One has to consider the influence of the chemical bonding between Co and Pd (or Pt) to understand interfacial PMA. The effect of this bonding coupled to Co electrons spin-orbit coupling has been theoretically studied either by ab-initio calculations of the total energy and band structure of ML system [12,18,20-22] or by calculating more explicitly the terms of spin-orbit interaction Hamiltonian in first and second order perturbation theory, the anisotropy energy (due to the spin-orbit coupling) being much smaller than the total energy [23,24]. Both methods should be equivalent and provide the good order of magnetitude for Ks, i.e. 0.5 to 1 $mJ.m^{-2}$. Although the first one is supposed to be exact, the "error bars" are large since magnetic anisotropy energy is very small. Moreover the second one has the advantage of highlighting the link between orbital moment anisotropy and magnetic anisotropy energy [24,25]. In the case of Co/Pd [21], the most accepted theory (it is not the only one [26]) associates interface PMA to the hybridization of Co atoms with Pd atoms that brings electronic states of mostly Co d_{x2-y2} and d_{xy} orbitals at the Fermi energy. These states are degenerated in the absence of spin-orbit coupling. Co spin-orbit (at first order) splits this degeneracy as the magnetization is forced to be out-of-plane but not when the magnetization is forced in-plane. Therefore a difference of energy may exist between the magnetization laying in-plane or out-of-plane. This difference of energy, due to the fact that d_{x2-y2} and d_{xy} orbitals are splitted below and above the Fermi energy in the out-of-plane direction, is enhanced because these states are hybridized with Pd orbitals which hold a strong spin-orbit coupling. Taking into account the spin-orbit constant of Pd, the anisotropy energy doubles. This is the reason usually invoked to explain why Co/Pd has double PMA amplitude as compared with Co/Ni or Co/Ag [27]. This theory is experimentally very difficult to verify and to my knowledge it has not been directly verified. Nevertheless, the efficiency of magnetic anisotropy energy calculation by second order perturbation theory, as well as the link with orbital moment anisotropy [23,24], have been beautifully demonstrated in several reports [3,12,28-30]. We will discuss in more details these concepts in part II.1 when studying Co/Ni Perpendicular magnetic anisotropy with XMCD measurements.

Overall Co/Pd and Co/Pt MLs have very interesting features for magnetic recording. They hold naturally uniaxial magnetic anisotropy perpendicular to the layering whose amplitude can be tuned at will by changing the thickness of Co. For Co thickness close to 1 monolayer, large anisotropy of the order of 10 $MJ.m^{-3}$ can be achieve which will provide high thermal stability for recording media. Magnetization at saturation can also be tuned similarly by tuning Co thickness. I will present in Part III examples of implementation of Co/Pd as media for bit pattern (BPM) recording system and 3D Page Memory. The above description of the various anisotropy sources will be very usefull to understand the switching field distribution properties. Before, in part II, I will focus on a similar type of multilayer, the so-called Co/Ni MLs. Despite the fact that Co and Ni are both magnetic transition metals and differ by only one valence electron, PMA was predicted and experimentally demonstrated for [Co(1ML)/Ni(2 ML)] fcc (111) superlattices in 1991 by Daalderop et al. [31]. The initial calculations [31], as well as further calculations by Kyuno et al. [32], suggest that the PMA may arise from interface electronic structure close to the Fermi energy consisting in bands

with $d_{x^2-y^2}$ and d_{xy} character that favors perpendicular. On the experimental side, few authors [33-36]studied PMA as a function of the Co layer thickness and report a maximum of PMA for Co thicknesses between 1 and 2 monolayers (MLs), which is consistent with an interface anisotropy model. Co/Ni perpendicular interface anisotropy was not only shown for (111), but also for (100) and (110) oriented superlattices [33,34]. The strongest interface anisotropy can be found in the case of (111) oriented samples where the magneto-crystalline contribution for the (111) structures also contributes to PMA. Tuning of growth conditions, substrates, and seed layers was reported to be essential in order to increase the (111) texture and hence the PMA of Co/Ni multilayers [35, 37-39]. Unless Co/Pd and Co/Pt that have been extensively studied over the last 20 years for their PMA, interest about [Co/Ni] MLs PMA has been lower because of its lower amplitude. As a consequence there are still no conclusion about the main origins of anisotropy in this system. In particular, the relative influence of interfacial hybridization and magnetoelastic effect is still to be quantified [4,33]. Besides Co/Ni MLs have been studied for their unusual transport properties. First, unusual high anisotropic magnetoresistance (AMR) values could be obtained [40-45] and attributed to the Co/Ni interfaces [46]. Second Gallego et al. [47-49] reported an oscillatory behavior of the electrical resistance of [Co/Ni] superlattices as a function of the layer periodicity. Those oscillations were explained by electron localization in the superlattice structure and motivated band structure calculations that predicted high spin polarization [50-52]. Nevertheless, no spectroscopy experiment has been performed yet to confirm either electron localization or high spin-polarization. Part II.1 will be devoted to carefully characterize structural, magnetic (especially PMA) and spin-dependant electronic transport features of Co/Ni MLs. In part II.2, we will focus on the effect of spin transfer torque that has motivated the renewal interest for Co/Ni since 2006 [53].

Part II.

[Co/Ni] multilayer features and spintronic devices

II.1. Understanding magnetic feature of epitaxial [Co/Ni] Multilayer films

II.1.1 Molecular beam epitaxy growth process for epitaxial [Co/Ni] MLs

As discussed in the brief description of the literature in Part I.2, interfaces seem to play a crucial role in all the features of Co/Pt, Co/Pd and Co/Ni (111) multilayers. Therefore to highlight the intrinsic electronic and magnetic features of these systems one has to insure good control of the chemical ordering down to the atomic scale. This can be achieved by using molecular beam epitaxy under ultra-high vaccum and in-situ (RHEED) as well as ex-situ (TEM, X-ray diffraction) structural characterization tools. In literature, epitaxial growth of [Co/Ni](111) superlattices has been obtained on [11-20] sapphire Al2O3 substrates covered with a 5 to 8 nm of Co buffer [47]. However the large magnetic coupling between the Co buffer and Co/Ni would bring Co/Ni magnetization in-plane because of the overall demagnetization field. Co/Ni has also been grown epitaxially on single crystal Cu substrate [34]. However such substrate cannot be used for further device fabrication. From 2008 to 2009, S. Girod and M. Gottwald, under the supervision of S. Andrieu, have developed and optimized the process of epitaxial growth at IJL, before I joined in sept. 2009. Details on epitaxial growth of [Co/Ni](111) multilayers can also be found in Ref. [47].

The structure of a α-Al2O3 (11-20) plane, which we used as substrate, is shown in fig.4. The lattice parameters that can be defined for this plane are $a\sqrt{3} = 0.8249$nm (with a = 0.476nm a lattice parameter of the hexagonal description of the α -Al2O3 crystal). In order to clean the surface of the substrate the sapphire is always annealed in the analysis chamber of the MBE system at 950°C during 10 to 15 minutes. Non-magnetic V[110]/Au[111] bilayer was chosen as buffer layer. The growth of V(110) on Al2O3 (11-20) is well known in literature [54,55]. The bcc-V(110) lattice is rectangular. When grown on sapphire, the diagonal of this rectangle is oriented parallel to the short edge of the rectangle formed by the O atoms of Al2O3 (11-20) (direct space). We have two equivalent epitaxial growth: V [-111] // α-Al2O3[0001] and V [-11-2] // α-Al2O3 [1-100] or V [-11-1] // α-Al2O3[0001] and V [-112] // α-Al2O3 [1-100] as shown in Fig.4. High substrate temperatures during deposition (T > 800°C) favor a single domain. However if the temperature is too high, the V does no longer adhere to the substrate. The chosen substrate temperature during deposition between 800°C and 850°C is a compromise. Vanadium was evaporated using an electron gun. The deposition rate is controlled using quartz micro balances. The typical deposition rate is of the order of 0.1 to 0.2 nm/s. At the beginning of the deposition process the RHEED pattern is spotty but for thicknesses of more than 3 to 5 nm the RHEED pattern changes to lines indicating a well ordered V(110) surface (Fig. 4(e) and (f)).

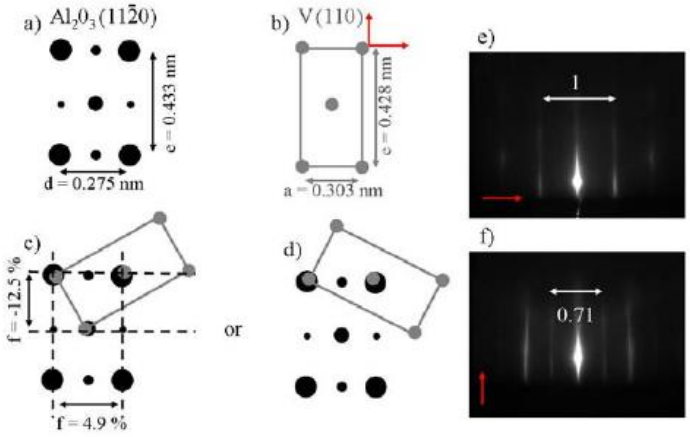

Fig.4. Growth of V(110) on sapphire. a) sapphire lattice. b) bcc-V(110) lattice. c) and d) are two possible epitaxial relations. e) and f) results from RHEED for two direction perpendicular to each other for V.

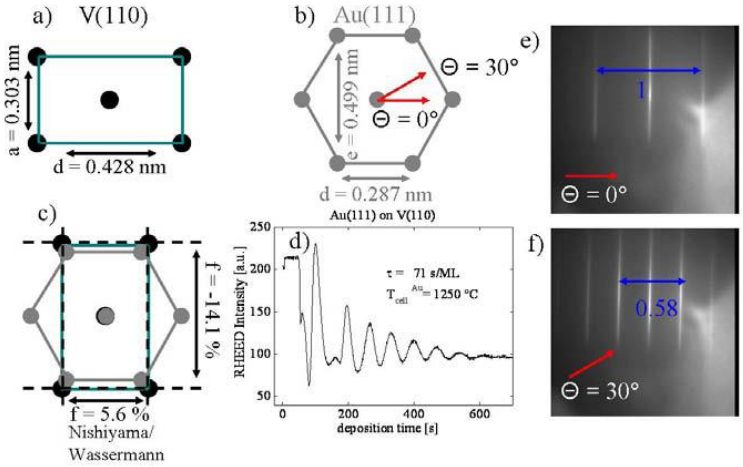

Fig.5. Growth of Au(111) on V(110). a) bcc V(110) lattice. b) fcc Au(111) lattice. c) Nishiyama/Wassermann epitaxial relation for Au on V. d) RHEED oscillations observed for growth of Au(111) on V(110). e) and f) RHEED diffraction patterns of Au(111) after annealing at 300°C during 15 minutes.

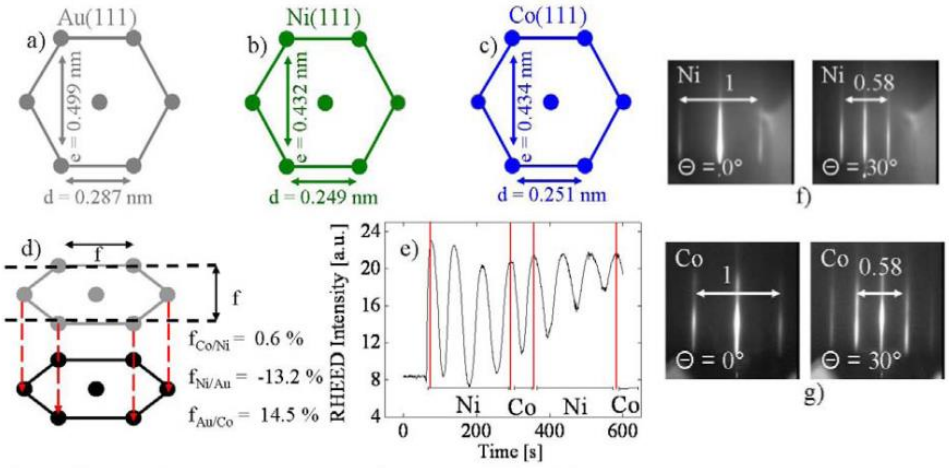

Fig.6. Growth of [Co/Ni](111) multilayer on Au(111). a) Au(111) -lattice. b) Ni(111)-lattice. c) Co(111)-lattice. d) lattice mismatches f. e) RHEED oscillations during growth of a [Co/Ni](111) superlattice. f) RHEED diffraction pattern of Ni (111). g) RHEED diffraction pattern of Co(111).

The second layer of the buffer is a fcc Au(111) layer deposited on V(110). Gold is evaporated in Knudsen cells at 1250°C after the substrate has cooled down to room temperature. The observed epitaxial relation of the hexagonal Au(111) on the rectangular V(110) is of Nishiyama/Wassermann type (see fig.5]. The 2D atomic layer by atomic layer growth mode for Au on V is confirmed by the RHEED oscillations (Fig. 5(d)) [56]. The RHEED oscillations also allow the determination of the growth velocity (of the order of 100 s per atomic layer). After deposition of the Au buffer the substrate is annealed at approximately 300°C during 15 minutes. This leads to a very flat Au surface, what can be seen from the very thin lines of the diffraction image.

Finally, the [Co/Ni] multilayer (ML) is grown on the Au(111) buffer once it has cooled down to room temperature after the Au annealing process. Co and Ni are deposited with Knudsen cells. Co, Ni and Au are fcc crystals. Consequently the (111) planes correspond to hexagons with atoms on all edges of the hexagon and one in the center of the hexagon (Fig.6). The misfit between Co and Ni lattice is smaller than 1%. However the missfit between Ni and Au is of the order of 13% (Fig.6.). We start the deposition of the superlattice with Ni since Co does not show layer by layer growth when deposited on Au. When starting the growth with Ni the layer by layer growth of the [Co/Ni] MLs is confirmed by RHEED oscillations, which also allow to control the deposition rate (see fig.6). We will show below that, when deposited on Au, the Ni actually relaxes immediately to its own lattice parameter. The good crystalline structure of the deposited Co and Ni layers is confirmed by their RHEED pattern (see Fig.6). Lattice spacing for bulk fcc (111) Ni and Co is respectively equal to 0.2034 nm and 0.2046 nm. In the following, we will always refer to 0.2 nm for the thickness of one monolayer of Co or Ni. Finally few atomic layers to few nanometers of Au are usually deposited on the sample as capping layer in order to prevent it from oxidation once exposed to air.

II.1.2. Ex-situ structural characterization of epitaxial [Co/Ni] MLs

To get better knowledge about the atomic order of our epitaxial Co/Ni MLs, scanning transmission electron microsopy (STEM) were carried out by E. Snoeck (CEMES Toulouse) and C. Magen (LMA Zaragoza) on a FEI Titan 60-300 kV microscope fitted with a probe aberration corrector (CEOS) allowing forming a probe size below 0.1 nm. As the Z difference between Co (Z_{Co} = 27) and Ni (Z_{Ni} = 28) is small, Co and Ni layers cannot be distinguished using normal TEM viewing. Chemical analyses were carried on cross sectional samples by high-angle-annular-dark-field (HAADF) imaging. In this mode, an annular detector collects the electrons which are incoherently scattered at high angles, whose intensity increases with the average atomic number (Z) of the atomic columns. Thus, aberration corrected STEM-HAADF allows obtaining atomic resolution Z-contrast images, which is not achievable in conventional HRTEM mode due to lack of strong chemical contrast [Nellist2008]. In addition, quantitative measurements of the strain state of the stacking were performed using the geometrical phase analyze (GPA) method [Hytch1998]. Fig. 7 shows a large field of view HAADF STEM image of V(5)/Au(2)/$[Co(0.2)/Ni(0.6)]_{20}$/Au(5)/$[Co(0.6)/Ni(0.6)]_{20}$/Au(2)

stack (with the thicknesses in nanometer). The gold layers which have the highest atomic number ($Z_{(Au)}$ = 79) appear the brightest, whereas darker areas correspond to the Co/Ni stacks. Optimizing the contrasts within the Co/Ni stacking regions, a weak contrast modulation is observed that can be attributed to the small Z difference (Z_{Co} = 27, Z_{Ni} = 28) between the alternating Co and Ni layers (Insets of Fig. 7(a)). These results confirm the layer by layer 2D-growth of the bilayers and the absence of any clear Co and Ni intermixing. Fig. 7(b) displays the crystal structure of the Co/Ni stack of the spin valve sample observed along the <110> zone axis. The fcc structure of the Co/Ni layer is evidenced over the entire multilayer. The (111) cobalt (resp. nickel) atomic planes continue the stacking layer of nickel (resp. cobalt) on which they are deposited. Finally, GPA is used to analyze the deformation state of the Co/Ni stacking [Hytch1998]. The measurement of the deformation of the (111) stacking of the Co/Ni in the growth direction relative to the (111) planes of the Au layer is reported in Fig.7(c). The (111) Au interplanar distance is found to be about 15% larger than the Co/Ni one. The lattice mismatch between fcc Ni/Co and Au is of that magnitude, thus confirming the totally relaxed growth of Au on Ni/Co and vice versa. It should be noted that this Au incommensurate growth process on Co/Ni is also observed by RHEED (sensitive only to the top surface for grazing incidence electron beam). Indeed, an incommensurate growth between Au and Co/Ni should lead to two different lattices on RHEED patterns during the growth of the first Au atomic plane. Since the misfit is large, we actually observed double streaks corresponding to both Au and Co/Ni surface lattices. Meanwhile, no variation is observed within the Co/Ni stacking (within the spatial resolution of the GPA method used here). The (111) spacing observed in HAADF images of ~0.20 nm consistent with the (111) lattice spacing of bulk fcc Ni and Co lattice spacing(resp. 0.2034 nm and 0.2046 nm).

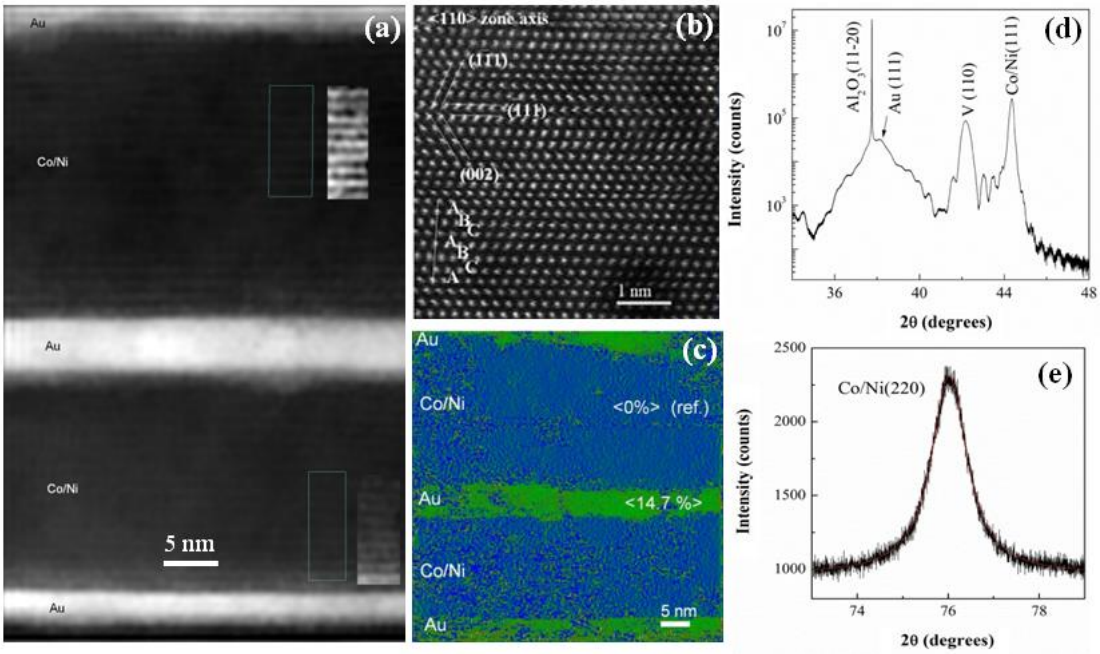

FIG. 7. STEM analysis of a $[Co(0.2)Ni(0.6)]_{20}$/Au/$[Co(0.6)Ni(0.6)]_{20}$ spin valve : (a) Low-magnification HAADF image showing the Au and Co/Ni stacking and, adjusting the contrast, the Co/Ni bilayers inset; (b) Atomic-resolution HAADF image of the Co/Ni layer evidencing the fcc structure of the stacking; (c) GPA measurement of the relative out-of plane deformation of the Co/Ni and Au(111) planes showing the full relaxation of the two stackings. Structure analysis of an Al_2O_3/V/Au/ $[Co(0.6)Ni(0.6)]_{75}$ / Au superlattice : (d) X-Ray diffraction θ-2θ spectrum which gives d(111)= 0.2040nm. (e) in-plane X-Ray diffraction spectrum which gives d(110)= 0.2501nm.

The STEM analysis indicates that Co and Ni layers are pseudomorphic and constrain coherently with each other, but are not constrained by Au. This conclusion matters since magneto-elastic effect [57] has be invoked to explain Co/Ni or Co/Pt interface magnetic anisotropy. The strain in the Co/Ni film can be further quantified in calculating using this mutual Co and Ni pseudomorphic growth by minimizing the total elastic energy [58]. First, the in-plane lattice (resulting from mutual stress between Co and Ni at equilibrium) and the out-of-plane lattice spacing (using the elastic relationship between stress and strain) will be calculated. The calculated values will be compared with experimental in-plane and out-of-plane lattice spacing obtained by X-Ray Diffraction (XRD). Finally, by using the bulk magnetoelastic coefficient of Co and Ni, the bulk part of the total magnetoelastic energy will be evaluated.

In such an elastic approach, the in-plane lattice spacing $a_{//}$ is constant throughout the structure and is fixed by the minimization of the total elastic energy density stored in the superlattice (e_{elast} energy per unit volume). If we assume first that both Ni and Co structures are isotropic on the elastic point of view (that is if we consider that C_{11}-C_{12}=C_{44}), the total elastic energy can be expressed as [Landau1986]:

$$e_{elast} = \frac{1}{2}\Sigma_{i\neq j}\sigma_{ij}\varepsilon_{ij} = \left\{\left(A\epsilon_{//}^2\right)_{Co} + \left(A\epsilon_{//}^2\right)_{Ni}\right\} \text{ with } A = \left(\frac{1-\nu}{E}\right)n \quad \text{and} \quad \varepsilon_{//} = \frac{a_{//}-a_0}{a_0}$$

where E is the Young's modulus, ν the Poisson's ratio, n the thicknesses of the Co and Ni layers and a_0 the lattice parameter of the relaxed structures. The minimization of this energy density leads to the value of the in-plane lattice distance as:

$$a_{//} = a_{Ni}(1-\alpha) + a_{Co}\alpha \qquad \text{with} \qquad \alpha = \frac{A_{Co}}{A_{Ni}+A_{Co}}.$$

Knowing the in-plane lattice distance, we can calculate the out-of-plane distance in each Co and Ni layers, and finally the out-of-plane lattice spacing for the superlattice <d>, defined as the average of lattice distances in each Ni and Co layer weighted by the respective number of atomic planes, as [58]:

$$< d >= \frac{n_{Co}d_{Co}+n_{Ni}d_{Ni}}{n_{Co}+n_{Ni}}$$

where n_{Co} and n_{Ni} are the number of monolayers that are accurately known with the help of RHEED oscillations, and d_{Co} and d_{NI} the (111) lattice spacing in each layers. Such a model may be tested by XRD measurements.

	$a_{//}$(100) (nm)	$\varepsilon_{//}^{Ni}$ (%)	$\varepsilon_{\perp}^{Ni}$ (%)	$\varepsilon_{//}^{Co}$ (%)	$\varepsilon_{\perp}^{Co}$ (%)	$d_{\perp}^{Ni}$(111) (nm)	$d_{\perp}^{Co}$(111) (nm)	<d>(111) (nm)
Measured	0.3537							0.2040
Calculated (isotropic)	0.35363	+0.36	-0.41	-0.24	+0.33	0.35090	0.35567	0.20397

TABLE 1 : lattice distances measured by XRD on a ($Co_{3ML}Ni_{3ML}$)x75 superlattice (fig.7(d) and (e)) compared to calculation using elastic theory. The calculation were performed assuming a perfect isotropic crystal (i.e. C_{11}-C_{12}=C_{44}).

In Fig. 7(d,e) the XRD spectra obtained on a V/Au/$[(Co(0.6)/Ni(0.6)]_{75}$/Au superlattice is reported. A first measurement was performed with the scattering wave vector perpendicular to the stacking in order to get the (111) peak of the superlattice, and consequently <d> in the previous equation (Fig.7(d)). A second experiment was performed with the diffusion vector in the plane of the stacking, allowing us to determine the in-plane lattice (220) distance, noted $a_{//}$ below (Fig.7(e)). Finally, in Table1, the experimental and calculated values are reported, using the bulk fcc Ni and Co lattice spacing (0.35236 nm and 0.35447nm respectively). The agreement between experiment and calculation is excellent. It confirms that the mutual constraint layers of Co and Ni apart from Au and strain values agree with the results deduced from nuclear magnetic resonance reported in Ref. [59]. The mutual strain between Co and Ni is very small since the misfit is only 0.6%. Information about the strain will be used to calculate the bulk magneto-elastic anisotropy in the following part.

II.1.3. Magnetic features of epitaxial [Co/Ni] MLs

Using vibrating sample magnetometer (VSM) and superconducting quantum interference device (SQUID) magnetometer, one can extract magnetization and anisotropy constant of Co/Ni MLs. Generally, in this system (both for sputtered or MBE-grown films), magnetic anisotropy does not strongly depend on Ni thickness for thickness larger than 2 atomic layers (i.e. 0.4 nm). In the following part, we will focus on the influence of Co thickness. Several V/Au/$[Ni(0.6nm)/Co(x)]_{10}$/Ni(0.6nm)/Au samples were grown by MBE to this purpose. Values of average magnetization at saturation Ms are shown in Fig. 8(a) and compared with the theoretical averaging considering bulk magnetization for Co (1400 kA/m) and Ni (490 kA/m), balanced by the thickness ratio. Both show a similar increase of Ms while increasing Co thickness. From these experimental data, we may notice a magnetization peak around 1 monolayer of Co. Although it would have to be confirmed on a new sample series, this result could be coherent with the larger value of Co spin moment measured by XMCD for Ni/Co(0.2nm)/Ni as compared to similar sample with ticker Co thickness (see Fig. 11).

From in-plane field magnetometry measurements, we also extracted the effective anisotropy field (H_{keff}) from which the effective anisotropy constant K_{keff} = ½ Ms.H_{keff} is calculated. K_{keff} is plotted as a function of Co thickness in Fig.8(b). Although K_{keff} is positive (i.e. anisotropy is perpendicular) for the whole range of tested Co thicknesses, two regimes exist. For Co thickness lower than 1 atomic layer, a linear increase of K_{keff} is indicative of the increase of Co/Ni interface area. For larger thickness, K_{keff} decreases linearly since the amount of Co/Ni interface area is constant and only Co/Co interface and therefore bulk anisotropy and demagnetization field are added. As in the previous Kerr experiments, the main role of Co/Ni interface is highlighted here.

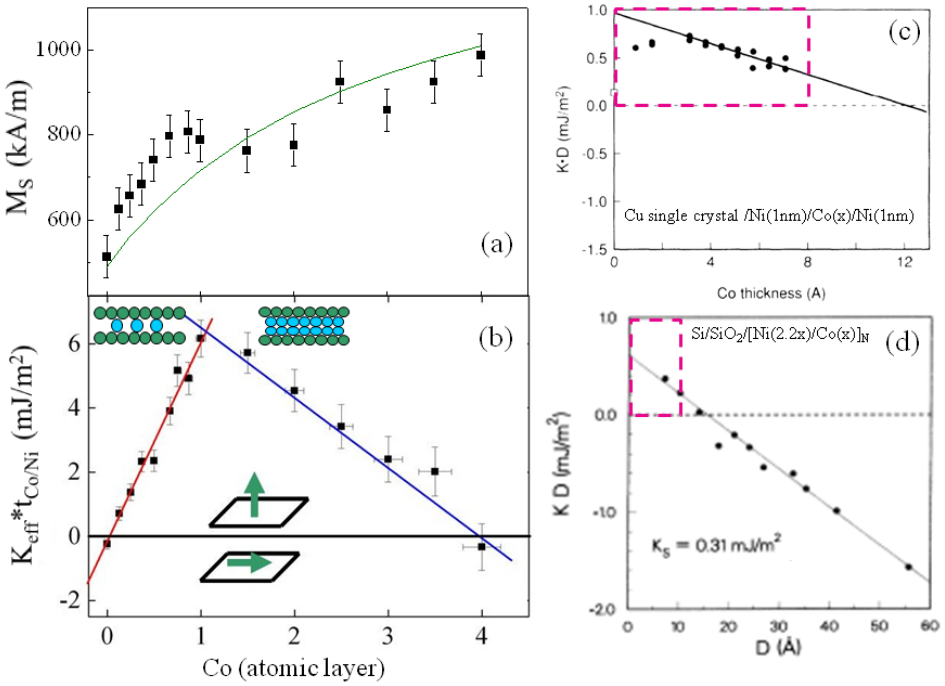

Fig.8. (a) Magnetization at saturation for sapphire/V/Au/[Ni(0.6nm)/Co(x)]$_{10}$/Au as a function of Co thickness x. The solid line is the theoretical average value obtained in taking into account the bulk values for Co magnetization and Ni magnetization. (b) to (d) show product of total anisotropy K and total magnetic layer thickness ($t_{Co/Ni}$ or D) plotted as a function of Co thickness or total thickness for (b) MBE grown sapphire/V/Au/[Ni(0.6nm)/Co(x)]$_{10}$/Ni(0.6nm)/Au, (c) MBE grown Ni(1nm)/Co(x)/Ni(1nm) on a single crystal (111) Cu substrate [33], and (d) MBE grown samples [Co(x)/Ni(2.2x)]$_N$ grown on Si/SiO$_2$ and glass substrate [31]. The pink square in (c) and (d) indicates the work space of (b).

The various origins of effective anisotropy K_{eff} (hybridization and strain interface anisotropy, bulk magnetocrystalline anisotropy, shape anisotropy) are usually disentangled using the following equation, [4] :

$$K_{eff} \cdot t_{Co/Ni} = t_{Ni} \cdot (K^{Ni}{}_v - 2\pi M_{Ni}{}^2) + t_{Co} \cdot (K^{Co}{}_v - 2\pi M_{Co}{}^2) + 20\, K_S{}^{Co/Ni} + 2\, K_S{}^{Ni/Au}$$

$t_{Co/Ni}$ is the total thickness of the Co/Ni stack, $K^{Ni}{}_v$ and $K^{Co}{}_v$ are the volume magnetocristalline anisotropies, $K_S{}^{Co/Ni}$ and $K_S{}^{Ni/Au}$ are Co/Ni (considered as equivalent to Ni/Co) and Ni/Au interface anisotropy (i.e. the anisotropy energy value per interface) respectively. The $2\pi Ms^2$ term comes from the shape anisotropy for a thin film. Dissociating Ni and Co shape anisotropy brings an error due to the cross product that we neglect here. By fitting the two linear variations in Fig. 8(b), one can extract the values for all these constants. First, the total anisotropy linked to the Ni layer is small as compared to the maximum of PMA value reached for one monolayer of Co. $t_{Ni} \cdot (K^{Ni}{}_v - 2\pi M_{Ni}{}^2) + 2\, K_S{}^{Ni/Au} = -0.08 \pm 0.20 mJ/m^2$. Secondly, $K^{Co}{}_v - 2\pi M_{Co}{}^2 = -1.10 \pm 0.15\ MJ/m^3$ is close to the magnitude of $-0.8 MJ/m^3$ found in Fig. 8(c) for MBE grown Ni(1nm)/Co(x)/Ni(1nm) on a single crystal (111) Cu substrate [33] and to a large range of other stacks [4]. We deduce a Co magneto-crystalline "bulk-like" anisotropy of $K^{Co}{}_v = +0.13 \pm 0.15 MJ/m^3$. Positive $K^{Co}{}_v$ value may originate from the (111) fcc structure which favors PMA as hcp (0001). Another origin of bulk anisotropy can be the magneto-elastic. In the case of our cubic structures where the magnetization is along (111),

the volumic magnetostriction energy (in J/m^3) is estimated for a single Co/Ni bilayer by using the bulk magnetoelastic coefficient of Co and Ni as [57]:

$$E_{magel}(bulk) = \{B_2(\varepsilon_{//} - \varepsilon_{\perp})\}_{Ni} + \{B_2(\varepsilon_{//} - \varepsilon_{\perp})\}_{Co}$$

where $B_2^{Co} = -29\ MJ/m^3$ and $B_2^{Ni} = +10\ MJ/m^3$. The different stress values are given for the sample measured by XRD in Table 1. We thus obtained a density magnetostrictive energy of +0.2 MJ/m^3 that favors PMA and is of the same order of magnitude as the experimental value of K^{Co}_v.

The most important parameter for our study is finally $K_S^{Co/Ni}$ which we find to be equl to +0.44 ± 0.04 mJ/m^2. The positive sign confirm that it favor perpendicular anisotropy. Fig. 8(c) presents the same experiment for Cu single crystal/Ni(1nm)/Co(x)/Ni(1nm) having $K_S^{Co/Ni}$ = +0.42mJ/m^2 [33]. This value is about 2 times larger than the value found for sputtered [Co/Ni] multilayers (+0.23 mJ/m^2) as reported in Ref [35] and for MBE grown Co/Ni MLs deposited on Si/SiO2 or glass (+0.31mJ/m^2) as shown in Fig. 8(d) [31]. The same difference between epitaxial and textured samples is observed for Co/Pd and Co/Pt MLs, where the interface anisotropy for MBE-grown ultrathin (111) Pd/Co/Pd and Pt/Co/Pt trilayers deposited on single-crystal substrates (0.92 and 1.15 mJ/m^2, respectively [60]) always exceed corresponding values for thicker MBE-grown (111)-oriented Co/Pd and Co/Pt multilayers grown on coated GaAs or glass as well as for sputtered Co/Pd and Co/Pt films [4]. The interface quality (no roughness and no intermixing) is critical to get large interface anisotropy.

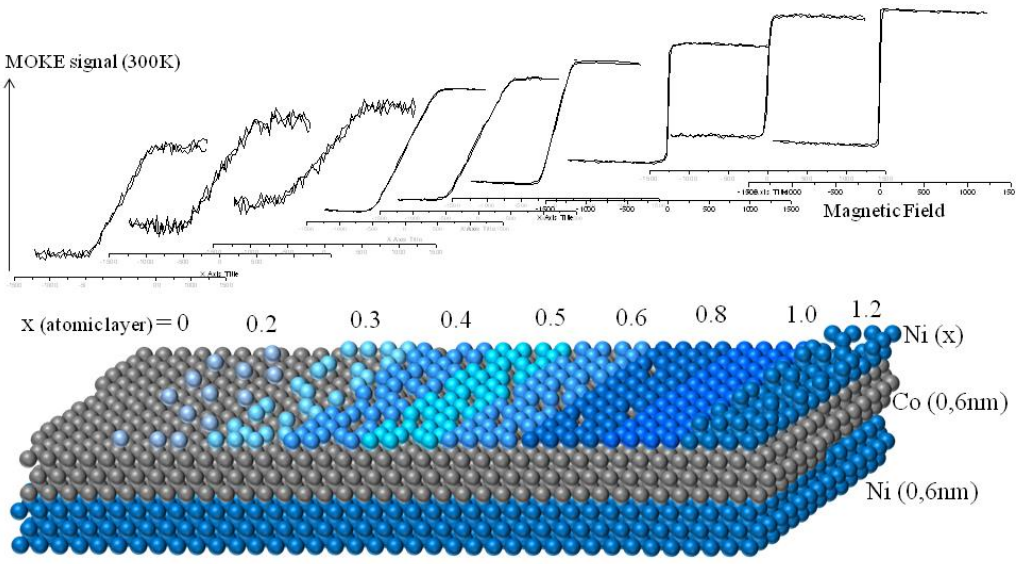

Fig.9. Scheme of a Ni(0.6nm)/Co(0.6nm)/Ni(x) with the corresponding magneto-optical Kerr signal corresponding to the various values for x. Measurements ahave been performed at room temperature and magnetic field was applied perpendicular to the interfaces. A transition from in-plane anisotropy to out-of-plane anisotropy is observed between x = 0.6 and 0.8 atomic layers.

After having quantified the contribution of the various sources of magnetic anisotropy in Co/Ni MLs, let us highligth in a simple experiment the role of the Ni/Co interface. Magneto-optical Kerr (MOKE) measurement (with external field applied perpendicularly to

the sample) has been performed on a V(50nm)/Au(2nm)/Ni(0.6nm)/Co(0.6nm)/Ni(x)/MgO(2.5nm) where Ni thickness is changed every 5 millimeter along one direction of the sample to form a so-called wedge (Fig.9). Ni thickness is varied from 0 to 1.2 atomic layers. In the present geometry, the MOKE signal is proportional to the projection of the magnetization along the direction perpendicular to the film. For any Ni thickness lower than 0.6 atomic layer, the trilayer magnetization lays preferentially in-plane at remanence and then reversibly reorientates along the field direction as it its amplitude is increased. Such so-called "hard axis loop" behavior is typical of an overall in-plane anisotropy. As the Ni thickness increases from the zero to 0.6 atomic layer, the saturation field, so-called anisotropy field, decreases revealing the decrease of the in-plane anisotropy amplitude. For Ni thickness equal or larger than 0.8 atomic layer, MOKE loop is square with full magnetization at remanence. It implies that the anisotropy has now switched to out-of-plane direction. As Co/MgO interface provides a small PMA [61] and Ni/MgO no significant interface anisotropy [62], the reorientation transition occurring over 0.2 monolayers is a beautiful proof of the strong influence of electronic hybridization at Co/Ni interface on magnetic anisotropy (as compared to strain).

As a conclusion of this part, we confirm that good quality (111) Co/Ni MLs with large PMA can be grown by MBE on α-Al2O3/V/Au. The strong PMA mainly originates from the Co/Ni interface hybridization. Magneto-elastic effect and "bulk-type" magnetocristalline anistopropy are secondary contributions (about a quarter of the total anisotropy) in contrast with the Ni/Cu(001) system for instance [63]. Any type of chemical disorder (interface inter-diffusion, layer granularity, etc.) that breaks Co/Ni layering strongly affects anisotropy in this system, similarly to Co/Pt and Co/Pd MLs. The effects of volumic anisotropy and chemical disorder on switching field distribution of assembly of dots will be further described in part III.1. In the next part, we are getting deeper into understanding the origin of interface anisotropy from both sides of Co and Ni by means of angle-dependant X-ray magnetic circular dichroism measurements.

II.1.4. Orbital moment, spin moment and their anisotropies measured by XMCD

X-ray magnetic circular dichroism (XMCD) effect in transition metals film corresponds to the X-ray absorption by the film due to transition of electrons from two p states to empty states (mostly d type) above the Fermi level (see Ref. [28] for a review). Therefore, for one transition metal, when recording X-ray absorption as a function of photon energy, two main absorption peaks are observed, so-called L_2 and L_3 whose intensity and integrals can be used to get information about the features of the atoms. As the transition depends on the atomic band structure, this technique is chemically sensitive and can be used to disentangle features from two different transition metal atoms in a unique alloy or multilayer film. Moreover, in magnetized films, using circular polarized light (left or right) allows to separately excite transitions for electrons with minority and majority spins. Therefore XMCD can be used to independently probe the density of state for minority spins

and majority spins bands. It finally allows the element specific determination of spin and orbital moments through the sum rules [63-65].

A first set of XMCD measurements were performed by S. Andrieu at the Advanced Light Source on beamline B04 and performed on two Au/Ni(0.6nm)/Co(x nm)/Ni(0.4nm)/MgO wedges as depicted in Fig. 10(a). All the measurement have been obtained at room temperature. In Fig. 10(b) the X-ray absorption spectrum (XAS) at the Co *L*3 edge is shown. The variation of the Co and Ni edges as a function of the thickness of Co is shown in Figs. 10(c) and 10(d). It should be noted that the magnitude of the Ni edge slightly decreases for increasing Co thickness, which results from the increased absorption of the upper Co layer with increased thickness. Moreover, we notice a discrepancy between the Ni edge intensity variations with the Co thickness for one wedge compared to the other. This discrepancy comes from the thickness of the MgO capping layer slightly different for the two wedges (about half an atomic plane) and is easy to correct. The Ni and Co edges intensity variations may be modeled by considering that the total yield *I* can be expressed as a sum of the contribution of the nth atomic plane exponentially attenuated by the n-1 planes on top of it. We can, thus, plot the edge variation as a function of Co thickness and determine the electrons escaping depth, using the equation :

$$I_{Co} = K_{MgO+Ni}\, I_{Co}^{\infty}(1 - K_{Co}^{n})$$

where K_{Co}= *exp(-1/* λ) is the attenuation factor by one Co atomic plane, which is linked to the escape depth λ. I^{∞}_{Co} is the total yield of thick Co film. *n* is the number of Co atomic planes, K_{MgO+Ni} is the attenuation factor through the MgO capping layer and Ni layer on top of Co, and K_{Co} the attenuation factor of a Co atomic plane. We obtain λ = 12 ± 0.5 ML (Fig. 10), in agreement with published values [66,67]. Finally, it is also possible to plot the Co to Ni edge intensity ratio, which is of great interest since it is independent of the thickness of the capping. The Ni intensity is calculated using the same method. For our wedges stacking this ratio is finally equal to :

$$\frac{I_{Co}}{I_{Ni}} = \frac{I_{Co}^{\infty}}{I_{Ni}^{\infty}}\left\{\frac{K_{Ni}^{2}(1 - K_{Co}^{n})}{(1 - K_{Ni}^{2}) + K_{Ni}^{2}K_{Co}^{n}(1 - K_{Ni}^{3})}\right\}$$

where K_{Ni}= *exp(-1/* λ) is the attenuation factor by one Co atomic plane. As the Co and Ni edges are close in energy, the mean-free paths are theoretically very close, which has been shown experimentally by Nakajima *et* [66]. I^{∞}_{Co} and I^{∞}_{Ni} are the total yield corresponding to thick Co and Ni layers. The only parameter that is not known here is $I^{\infty}_{Co}/ I^{\infty}_{Ni}$ ratio which is equal to the ratio of number of holes (i.e. unoccupied states in the spd band above the fermi level) in Co and Ni [68]. To get them, we performed XMCD measurements on thick epitaxial hcp Co(0001) and fcc Ni(111) films, applied the sum rules to obtain the spin and orbital moments per holes, and compared them to their magnetization measured using macroscopic magnetic measurements (superconducting quantum interference device and vibrating sample magnetometer). We have *n*Co = 2.55 ± 0.1 and *n*Ni = 1.1 ± 0.1, giving $I^{\infty}_{Co}/ I^{\infty}_{Ni}$ = 2.3 ± 0.3.

The edge intensity ratio I_{Co}/I_{Ni} can thus be calculated without adjustable parameters and compared to measurements. The agreement between experiment and calculation is excellent as shown in Fig.10(c). All these results confirm the sample quality and give an experimental determination of the Co to Ni number of holes ratio. Note that it is not obvious that the number of holes is identical for each atomic plane in the stacking (especially close and far from Co/Ni interfaces). However, the change in the number of holes with Co and Ni thicknesses in Co/Ni multilayer were calculated by Lionel Calmels using ab initio calculations and were found to be negligible.

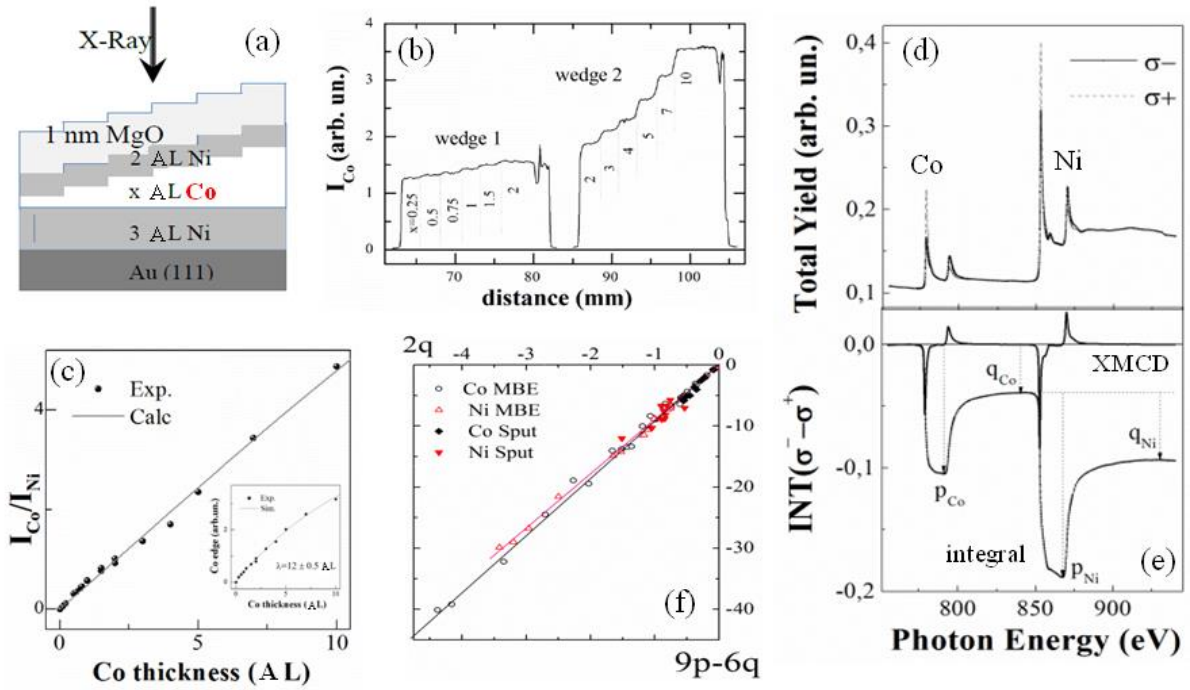

Fig. 10. (a) Scheme of the wedge samples with a Co thickness variation in the range x = 0.25 to 10 atomic layers (AL). Each region of constant Co thickness is about 3mm long. (b) Isotropic absorption intensity of the Co *L*3 edge in the two wedges. The Co edges are more attenuated by the capping for wedge 1 due to a slightly thicker capping. (c) Using the equation in the text, the Co-to-Ni intensity ratio is reproduced. In inset, the Co edge intensity follows an exponential increase, which allows us to precisely determine the escape depth *λ*. (d) Co and Ni absorption edges measured by applying both right and left light polarization and ±0.5-T applied magnetic field (see text) and (e) corresponding XMCD signal and XMCD signal integration. All of the curves are obtained without any absorption baseline correction, which allows a precise determination of Co and Ni orbitals to the effective spin magnetic moments ratio calculated using *p* and *q* values. (f) Variation of the effective spin magnetic moment (proportional to 2q) with the orbital magnetic moment (proportional to 9p-6q) for various MBE and sputtered samples and at both Co and Ni edges. (d) to (f) data have been obtained on a third wedge sample consisting in a multilayer Au/Ni(0.6nm)[Co(x)/Ni(0.6nm)]$_5$/MgO.

The XMCD measurements were performed at room temperature on a third wedge composed of a 5 repeats multilayer, Au/Ni(0.6nm)[Co(x)/Ni(0.6nm)]$_5$/MgO, in order to enhance the XMCD signals. Both Co and Ni $L_{2,3}$ edges were investigated using nearly 100% circularly polarized light. The orbital and magnetic moments were determined by applying the sum rules proposed by Thole *et al.* and Carra *et al.* [63,64] and using the procedure proposed in [65]. The measurements were performed in total yield for both left and right circular polarization and magnetic field in both directions along the normal of the surface, leading to

four absorption curves σij (i = +,− light polarization, and j =+,− magnetic field direction). Such measurements allow us to eliminate the asymmetry by calculating the absorption curves using $\sigma+ = \sigma++ + \sigma--$ and $\sigma- = \sigma+- + \sigma-+$. The XMCD spectrum is, thus, given by $\sigma+ - \sigma-$, and the isotropic edge used to obtain the integral r is here defined as $(\sigma+ + \sigma-)/2$.

The spin sum rule gives the *effective* spin angular momentum, which depends on the actual spin angular momentum, on n_h the number of holes in the *d* bands for the atom under consideration, and is given by :

$$m_{spin}^{eff} = n_h \left(\frac{3p - 2q}{r}\right) \mu_B$$

where p and q correspond to the dichroic spectrum integrated over the $L3$ and over the $L3$ + L2 edges, respectively. r is the area of the isotropic $L2,3$ edge that has to be measured in order to determine the absolute value of the effective spin and orbital magnetic moments. nh is not known and is very difficult to obtain with a sufficiently good accuracy in experiments. In addition, the orbital momentum sum rule is given by :

$$m_{orb} = n_h \left(\frac{2q}{3r}\right) \mu_B$$

An example is reported in Fig. 10(d) and 10(e), showing the determination of p and q without any adjustment of the spectra. It should be noted that the asymmetries are eliminated since the difference between the absorption curves is zero between the edges. This means that the XMCD signal is obtained using raw absorption data and is afterward integrated without any data correction. The ratio of Co and Ni orbital moments, which only depends on the p and q area needed to calculate the magnetic moments, is thus not data treatment dependent. The variation of ($9p$-$6q$) vs $2q$ is also plotted in Fig. 10(f) for Co and Ni edges and for the MBE-grown Co/Ni multilayer wedge and similar sputtered Co/Ni samples (comparison and discussion about the influence of the two growth technique will be done later here). Within the measurement error, Co and Ni have similar slope. This slope corresponds to the orbital moment per spin moment ratio which can be related to the spectroscopic splitting factor g by:

$$\frac{m_{orb}}{m_{spin}} = \frac{g - 2}{2}$$

Applying this formula, we find g = 2.19±0.04. It is in very good agreement with previous report such as Ref. [69] for bulk and Ref. [70] for Co/Ni multilayer and alloys. Such good agreemnt gives a lot of credit to our XMCD measurements. It is especially important since the spin and orbital moment values that I am presenting in the following paragraph are quite surprising.

The dependence of the orbital and effective spin magnetic moments are plotted vs Co thickness Fig. 11(a) and 11(c) for Co and Ni respectively. Let us first focus on the Co behavior. We found Co bulk orbital moment of 0.16 ± 0.02 μB/atom and Co bulk spin moment of 1.5 ± 0.1 μB/atom. These values are in good agreement with the values from the literature. Interestingly, for small Co thicknesses, both the orbital moment and the spin

moments increase significantly. The orbital moment reaches up to 0.21 ± 0.02 μB/atom, i.e. an increase of approximately 25% as compared to the bulk value. In parallel, we also observe a similar increase of the effective spin moment up to 2.0 ± 0.1 μB/atom. At this stage it is instructive to plot the magnetic moments according to the inverse of the thickness (Fig. 11(b)). Two regimes are then clearly observed. In a first regime between 0 and 2 ML, both Co spin and orbital moments are constant, and a linear decrease occurs beyond 2 ML. Our experimental results can then be nicely fitted using a linear combination of m_{spin} = 2 μB/at (resp. m_{orb} = 0.21 μB/at) for atoms in contact with Ni and m_{spin} =1.5 μB/atom (resp. m_{orb} = 0.16 μB/at) for the other Co atoms. At this stage, due to the measurement errors, it is unclear if the Co surrounded by one Ni atom has the same moment as the Co atom surrounded by two Ni atoms. Regarding the Ni edge data, only very weak variations are observed in Fig. 11(c). Especially the spin moment seems to decrease for less than one atomic layer of Co. The increase of Co spin moment and possible decrease of Ni spin moment at the interface must be a sign of charge transfer at the interface. Similar variations have been reported in Co/Pt multilayers (see for instance [71]).

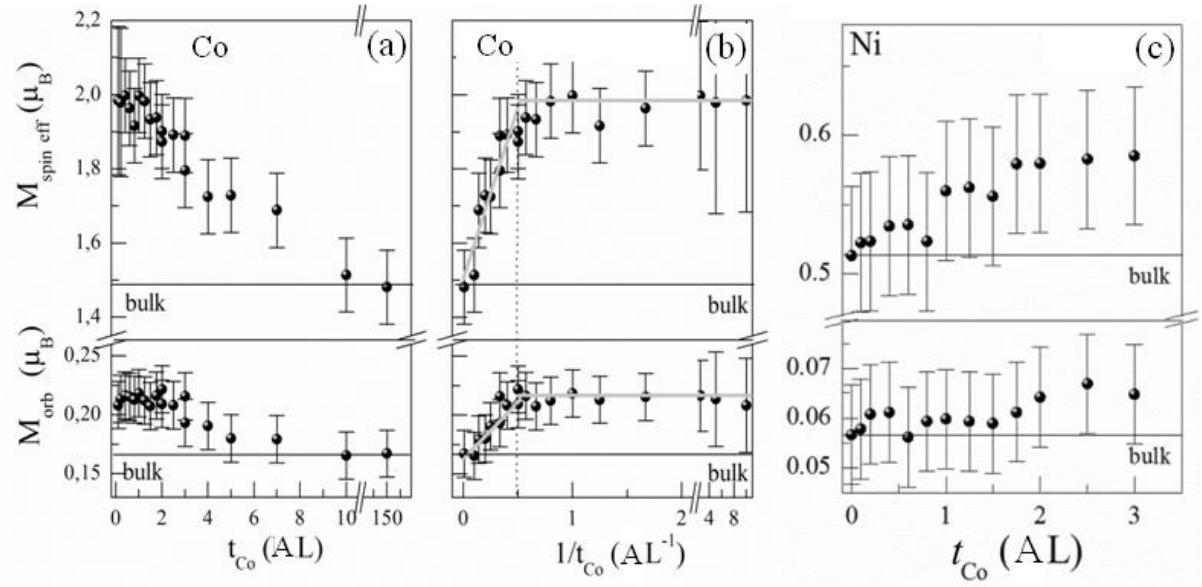

Fig. 11. Plot of the effective spin and orbital magnetic moments for Co vs the Co thickness *t*Co (left) and the inverse of *t*Co (right) for a series of SLs and for the wedges of Fig. 10. The two regimes described by gray lines are due to the existence of two different Co magnetic contributions, one at the interfaces with Ni and the other for Co surrounded by Co. The bulk values are obtained on a thick, hcp Co film grown by MBE.Plot of the effective spin and orbital magnetic moments for Ni in a series of Co/Ni SLs: (left) for a fixed Ni thickness equal to 3 ML and varying the Co thickness; (right) for a fixed Co thickness equal to 1 ML and varying the Ni thickness. The bulk values are obtained on a thick fcc Ni film grown by MBE.

At this stage, we know that both Co orbital moment and spin moment increase at the interface with Ni, while Ni properties do not change much. Nevertheless, on the one hand, magnetic anisotropy is related to the anisotropy of orbital moment more than the orbital moment amplitude itself. As a consequence further experiment needs to be performed to measure m_{orb} as a function of the direction regarding to the normal to the film. On the other hand, the increase of m_{spin} may originate from a magnetic dipolar term $\langle T \rangle$ that cannot be neglected as usual when considering chemical interfaces [28]. The above extracted value should be noted m^{eff}_{spin} instead of m_{spin} (done in Fig. 11). $\langle T \rangle$ depends on the anisotropy of

the electron spin-density distribution distorted by the crystal field [72] whereas, under sufficient external magnetic field, m_{spin} should be isotropic. Therefore studying m^{eff}_{spin} as a function of the direction regarding to the normal to the film would provide direct measurement of <*T*>.

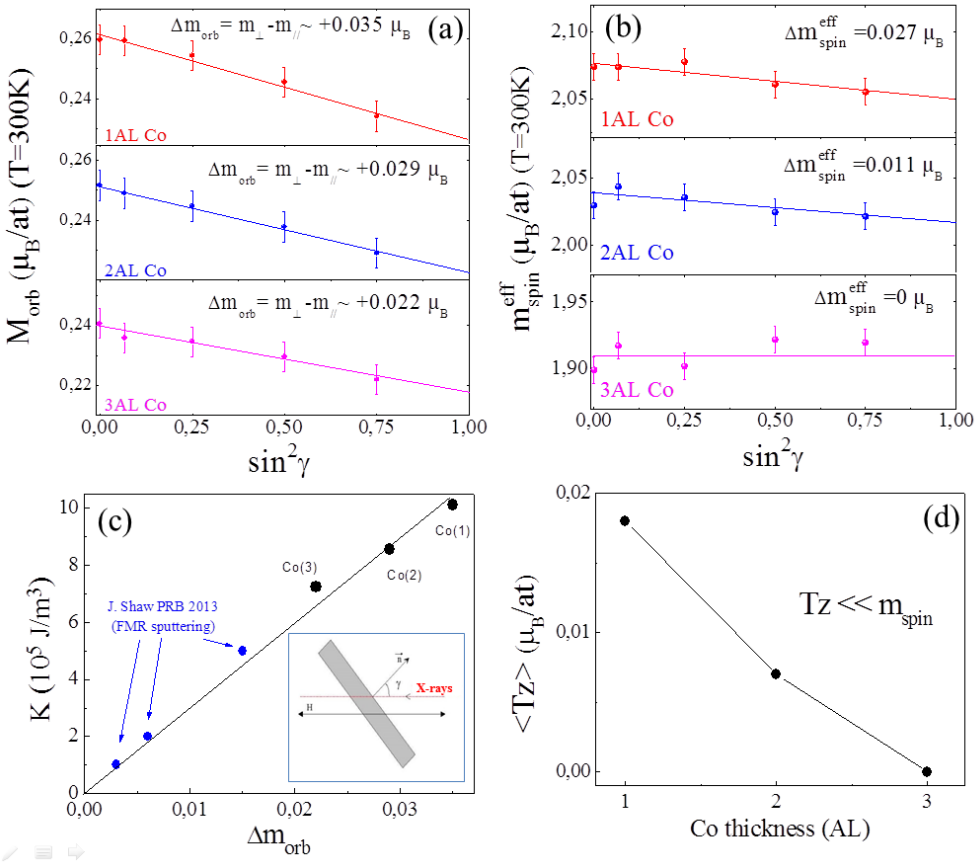

Fig. 12. Plot of the effective orbital (a) and spin moments for Co vs $\sin^2\gamma$, where γ is the angle between sample normal and X-ray propagation direction, for three sample with Co thickness of 1, 2 and 3 Atomic Layer. Solid line are guide for the eyes and allows extracting $\Delta m = m_{\perp} - m_{//}$ for both orbital and spin moments. (c) Anisotropy constant K as a function of the orbital moment anisotropy amplitude for our three Co/Ni samples and compared with results from the Ref. [70]. In inset a scheme of XMCD experiment geometry with rotation of X-ray propagation direction and 4 Tesla field (H) as compared to the normal to the Co/Ni film. (d) Projection of magnetic dipolar magnetic term <*T*> along the normal to the film, extracted from data in (b), as a function of Co thickness.

We recently performed a second run of experiments on DEIMOS at SOLEIL Synchrotron on similar samples as those measuredat ALS Berkeley. We are currently in the process of analyzing all the data but some tendency are already clear and summarize in the following here. During the second run, we measured XMCD measurements as a function the angle γ between the sample normal and the X-ray incidence direction as shown in inset Fig. 12(c). A set of three samples was investigated, namely V/Au(10AL)/Ni(3AL)/Co(xAL)/Ni(3AL)/Au(4AL) with x = 1, 2 and 3 atomic layer (AL). A magnetic field of 4 Tesla is applied in the direction of the X-ray propagation to insure that the sample magnetization stays parallel to this X-ray incidence direction. We have performed experiments at various temperatures from 20K to 300K but I will show here only 300K data. In Fig. 12(b) are shown the values of m^{eff}_{spin} as a function of $\sin^2\gamma$ for the three samples.

Again, we find that m^{eff}_{spin} values are much larger than bulk Co one and the new values are in good agreement with values extracted from ALS measurements. A linear variation is observed as expected from the literature [23,73]. A very complete explanation of m^{eff}_{spin} and m_{orb} dependence in γ can also be found in Ref. [74]. The relationship between m^{eff}_{spin} and γ is given by:

$$m_{spin}^{eff,\gamma} = (m_{spin} - 7Q_{\perp}^{\star}) + (21/2)Q_{\perp}^{\star}\sin^2\gamma$$

where the term $7Q^{*}\perp$ correspond to the value of dipolar magnetic term <T> that we try to calculate. From the variation of m^{eff}_{spin} as a function of $\sin^2$ γ, we can calculate $Q^{*}\perp$ and therefore $7Q^{*}\perp$. The values of <T> are reported in Fig. 12(d) for the three Co thicknesses. As expected, the <T> value decreases as the Co thickness increases and its maximum for 1 monolayer of Co is only one hundred times lower than the m^{eff}_{spin} value. As a consequence, one can conclude that the large value of m^{eff}_{spin} of Co in Co/Ni multilayer as compared with bulk Co does not originate from the magnetic dipolar term <*T*>. It must directly originate from the hybridization of the Co with Ni.

In Fig. 12(a), we plot orbital moment extracted from the XMCD signal at the Co edge as a function of $\sin^2$ γ. Again, as expected, we observe a linear behavior. The values are also similar to ALS ones. The difference between the orbitale moment perpendicular to the interface ($m^{\perp}_{orb}$) and along the interface ($m^{\backslash\backslash}_{orb}$) increases as the thickness of Co decreases. Such result is predicated by the theory discussed at the end of part I.2 and based on the energy splitting due to spin-orbit coupling. According to P.Bruno's work [23], the anisotropy K (the magnetic anisotropy energy density) must be directly related to the difference of orbital moment ($m^{\perp}_{orb}$ -$m^{\backslash\backslash}_{orb}$) as :

$$K = \frac{\alpha\varepsilon}{4\mu_B}\,(m_{orb}^{\perp} - m_{orb}^{\backslash\backslash})$$

where ε is spin-orbit constant (an energy parameter that express the strength of the spin-orbit coupling) and α a correcting term that is usually between 0 and 0.2 depending on the publication you read. I will not discuss here the pre-factor term since we are still investigating it. Nevertheless what is clear from Fig. 12(c) is that the magnetic anisotropy constant (K) extracted (including Kv and Ks but no shape anisotropy) of Au/Ni(3)/$[Co(x)/Ni(3)]_{10}$/Au samples are close to be proportional to our experimental $m^{\perp}_{orb}$ -$m^{\backslash\backslash}_{orb}$. Even more impressive is that data obtained on sputtered $Co_{90}Fe_{10}$/Ni multilayers from a recent paper [70] aligned very well with our own data.

We tried the past five years to theoretically reproduce our experimental data on Co/Ni interface physics by collaborating with Lionel Calmels from CEMES Toulouse (who does ab-initio calculations). Unfortunately so far we could not reproduce the large spin moment of Co neither find the splitted states that generate the perpendicular anisotropy yet. Finally, regarding the anisotropy, in Fig. 12(c), I only consider the Co orbital moment asymmetry. But we also observed a slight asymetry in the Ni orbital moment that needs to be included in the magnetic anisotropy calculation. This is work in progress.

II.1.5. Spin-polarization measured by spin-resolved photo-emission spectroscopy

Since all our experimental data tend to demonstrate that the hybridization between Co and Ni is main phenomenon which explains the magnetic properties of Co/Ni, we should observe similar impact on the electronic band structure. In order to investigate the spin-resolved electronic structure of [Co/Ni] superlattices, spin-resolved photoemission was performed on the CASSIOPEE beamline at SOLEIL synchrotron (see [75] for more details about the beamline features and Fig. 50 for the set up scheme). Co/Ni multilayers were epitaxialy grown in a molecular beam epitaxy (MBE) chamber connected to the beamline so that surface pollution is forbidden. The films were deposited on single-crystalline sapphire substrates with V/Au buffer according to Fig. 4 to 6. A first serie of $[Ni(3)/Co(x)]_3$ multilayers were tested with x ranging from 1 to 3 monolayers (ML). Thick (111) Co and (111) Ni films were also grown as bulk reference. All Co/Ni films have been magnetized with a 6kOe field applied perpendicularly to the films before PES experiments. Spin-resolved photoemission experiments have been initially conducted with a Mott detector facing the sample surface and with a detector aperture fixed to +/- 8° so only electrons around the normal of the surface are detected. The photon energy was kept 30 eV. Unfortunately, in this geometry, only half of the Brillouin zone is investigated. Nevertheless by rotating the sample by 8 degree, it is possible to access to more space of the Brillouin zone (still need to be precisely quantified). We measured the photoemission spectra (PES) at room temperature. Finally, CASSIOPEE beamline's Mott detector allows measuring the electron spin-polarization along the direction perpendicular to the film and along one direction parallel to the film plane, so that we could check that the samples were perpendicularly magnetized.

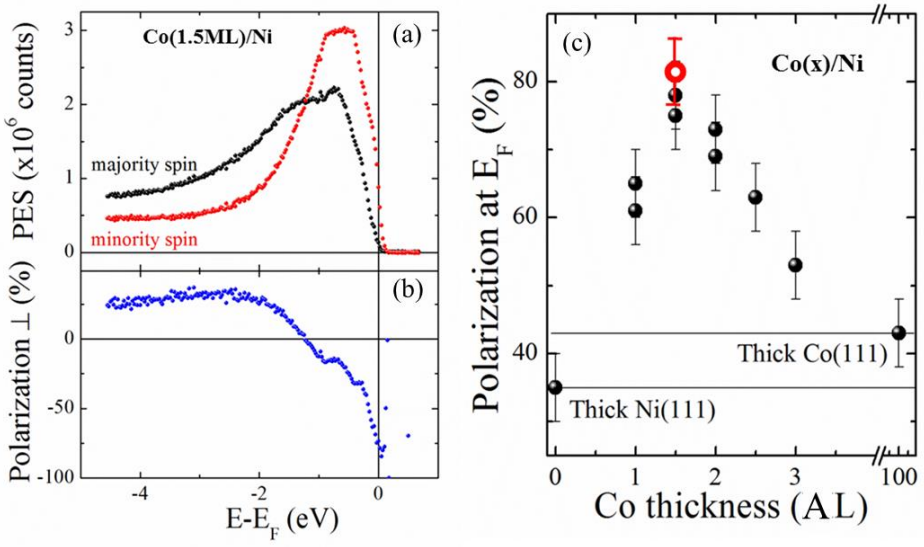

Fig. 13. Photo-emission spectrum (PES) for both minority and majority spin (a) and corresponding spin polarization (b) as a function of electron energy, measured on $[Co(2AL)/Ni(3AL)]_2/Co(1.5AL)$ stack. Here the top layer is the Co 1.5 atomic layer (AL) thick layer. (c) Spin-polarization of $[Ni(3AL)/Co(xAL)]_3$ with x ranging from 0 to 100 monolayers (AL). Here the top layer is a Co x atomic layer (AL) thick layer.

Fig. 2 shows a typical measurement of photoemission spectra measured for $[Ni(3AL)/Co(2AL)]_2/Co(1.5AL)$. Figure 2a shows the majority and minority spins density for spins aligned perpendicular to the film surface. Strong differences appear between the two

curves, especially close to the Fermi level (E_F) where the majority spins density is almost zero. As a consequence, the spin-polarization defined as the difference between the majority and minority spin density shows a large peak at E_F. The amplitude of this peak is here 80 % (Fig. 2(b)). On the contrary, no difference is observed between the majority and minority spin density for the component of spin laying in the film plane (not-shown here). The absence of spin asymmetry along the in-plane direction, verified for all tested Co/Ni multilayers except bulk Co and Ni, confirms that the film is perpendicularly magnetized for all texted x except 100 AL. Fig. 2(c) presents the evolution of the Ni/Co(x) spin-polarization as a function of x value. With nul x, we obtained a spin-polarization of less than 40% which is coherent with bulk Ni spin-polarization [76,77]. As x increases, spin-polarization increases and even above the bulk Co value, reaching an 80% peak around 1.5 AL. Then as x increases from 1.5 AL, spin-polarization decreases until reaching the bulk Co value around 45% [77-79]. Since the SR-PES technic is sensitive only to about 2 to 3 AL at most due to the limited escape length of the electrons (exponential decay with depth), we mostly probe here the last Co layer and a part of Ni layer underneath (at least up to 2 AL of Co). The slight sensitivity to Ni may explain why we do not have the spin-polarization maximum at 1.5 AL insteadof 1 AL where the electronic exchange between Co and Ni must be the largest.

Our SR-PES results tend to confirm that the electronic structure is changing when a Co atom is next to a Ni atom. I have to mention that a large spin-polarization in Ni/Co(x) has been predicted in Ref. [80]. Nevertheless similar large spin-polarizations are reported in this Reference for Co thickness equals to 1 AL and 5 AL. It is puzzeling. More DFT work is required to simulate Co/Ni electronic band structure. One can also notice that a spin-polarization value up to 80% has been extracted in Co/Ni nanowires from spin transfer torque experiments [81]. Nevertheless this value of spin-polarization cannot be directly compared to our SR-PES results, since it depends also on the carrier speed for instance. Finally, although we cannot fully explain the physics behind this result yet, it is promising in terms of spin-polarized electronic transport (especially for tunnel junctions).

II.2. Co/Ni-based spintronic devices

Because of the good control and understanding we have about Co/Ni multilayers, and because of the easy tuning of their magnetic (and maybe spin-polarization) features, this system is a nice playground to study the interaction between conduction electrons and magnetism down to the nanometer scale. In this part, I describe our work on Co/Ni-based nanopilars which we used to study spin transfer torque switching and our work on Co/Ni-based micro and nano-wires which we used to stdy spin transfer torque domain wall motion.

II.2.1. Introduction to spin transfer torque in perpendicular anisotropy devices

Spin-transfer torque (STT) has been predicted in 1998 and experimentally demonstrated two years later [82]. It allows to control magnetization direction by spin-polarized injection under zero external field [83,84] and is thought to be used as writing mechanism for the highly pursued Magnetic random Access Memory (for recent review on MRAM see for instance Refs. [85,86]). The first system used to study STT is the metallic spin-valve whose free layer is thin (of the order of 5 nm or less). As described in the introduction, such a system knows two states of resistance : a low resistance state when the hard and soft magnetic moment are parallel (P) and a high resistant state in the anti-parallel (AP) configuration. It has been originally explained in Refs [87,88] and has been called giant magnetoresistance (GMR) effect. GMR value (usually in %) is defined as the resistance in AP state minus the resistance of the P state divided by the resistance of the P state. The current can flow from the hard layer towards the soft layer or vice-versa. In the first case, the electrons spin-polarized as they cross the hard layer, usually parallel to the hard layer magnetization. The metallic inter-layer is thinner than the spin-diffusion length characterizing the length over which the electronic current depolarizes. As a consequence, spin-polarized current is consecutively injected into the soft layer. If the spins direction (i.e. the hard layer magnetization) and the soft layer magnetization are not perfectly aligned, the spins reorientate through the free layer. The lost transverse component of the spin is transmitted to the free layer magnetization that rotates itself to conserve the total kinetic moment. Therefore the spin transfer acts as a torque on the soft layer magnetization. When the current density is strong enough (typically of the order of 10^{10}-10^{11}A/m^2), STT can reverse the magnetization to achieve a parallel configuration of the hard and soft layer magnetizations. Note that such a high current density is only achieved for nanometer scale device [82]. Starting from a parallel configuration, the soft layer magnetization can be switched to reach anti-parallel state if the current flows from the soft towards the hard layer. Here the electrons of opposite polarization as compare to the magnetizations are reflected towards the soft layer and can force the soft magnetization to reverse due to STT.

The dynamics of the magnetization M or of the total moment m under an effective field (that includes anisotropy, demagnetization field and external field if any) is well described by the Landau-Lifshitz-Gilbert equation :

$$\frac{dm}{dt} = -\gamma m \times H_{eff} + \alpha\left(m \times \left(m \times H_{eff}\right)\right) + \beta I(m \times m \times p)$$

which considers in addition to the torque due to the effective field [Landau1935], a second torque which is due to an energy loss term, so called phenomenological damping term, that tends to align the moment along the effective field. When considering STT, a third term has to be taken into account as proposed in Refs. [89,90]. The influence of these three terms is shown in Fig. 14(a) in the case where the STT term opposes to the damping term.

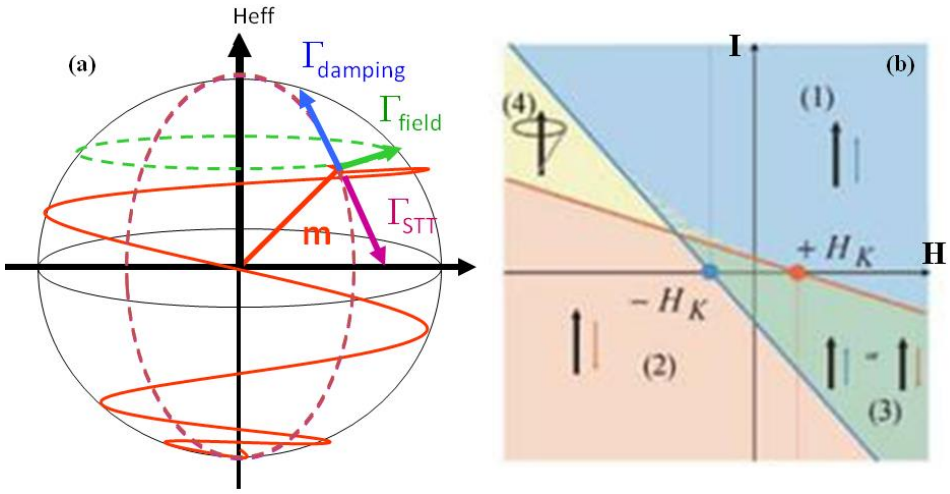

Fig.14 (a) Scheme of the torque describes by the LLG equation including the damping torque, field torque and Spin tranfer torque (STT). The red path show the magnetic moment (m) trajectory when the STT term overpass the damping term. Thus the magnetic moment switches. (b) « Current vs Field » phase diagram calculated as explained in the text. Black, resp. ligth colored, arrows represent magnetization direction for the fixed, resp. free, layer magnetization. In the blue region (1), both magnetizations are parallel. This the P state. In the pink region, free layer magnetized anti-parallel to the fixed layer one. It is called AP region. The green region correspond to a zone of bistability where P and AP can exist. The yellow region is a region where the free layer precesses.

In 2006, it has been demonstrated that samples exhibiting perpendicular magnetic anisotropy (PMA) requires by nature lower current density to achieve STT switching in spin-valve [53,91]. To convince ourselves, let's plot the "current versus field" diagram as described in Ref. [53] and in more details in Ref. [92]. This diagram allows the determine, as a function of both external magnetic field and spin-polarized current amplitudes, the stable state of the free layer magnetization of a spin-valve device where both free and fixed layer have PMA (Fig.14(b)). The fixed layer magnetization is assumed as insensitive to the field and current (and points up in the diagram). A macrospin model is considered with uniaxial symmetry where the contributions of the effective magnetic field, the magnetization, the polarizer layer, and current are along the same axis. Based on these assumptions, considering the STT torque as a torque created by an effective field added to the external field, anisotropy field and eventually dipolar field, one can analytically calculate the two boundaries between stable and unstable P state (i.e. parallel alignment of free and fixed magnetizations) on the

hand and between stable and unstable AP state (i.e. anti-parallel alignment of free and fixed magnetizations) :

$$I_P(H) = -\frac{2e}{\hbar}\frac{\alpha M_S V}{g(0)P}\left(H + H_K^{eff}\right)$$

$$I_{AP}(H) = -\frac{2e}{\hbar}\frac{\alpha M_S V}{g(\pi)P}\left(H - H_K^{eff}\right)$$

where M_S and V are the saturation magnetization and volume, α is Gilbert's damping constant, and P is the spin polarization of the current. The factor $g(\theta)$ depends on the relative angle θ of the reference- and free-layer magnetization vectors [93]. Since the spin-transfer torque is more efficient in the antiparallel configuration than in the parallel one the slopes of the two borders which depend on the $g(0)$ and $g(\pi)$ functions are different. So they cross and divide the (H, I) plane into four regions. In three of them the magnetization has access to at least one stable magnetic configuration: P, AP, or both. In the fourth region there are no stable and static magnetic states as shown in Fig.14(b). Therefore, the magnetization has to be in a dynamic state.

The effective field acting on the free layer ($H_K^{eff} = H_K - 4\pi M_S + H_{dip}$) contains contributions from the uniaxial PMA field H_k, the dipolar field from the reference layer H_{dip}, and the demagnetization factor $-4\pi M_S$ arising from the thin film geometry. This last term is the key parameter for comparing PMA and in-plane systems. First the magnetic response for PMA stack is more strongly determined by the intrinsic properties of the materials rather than being dominated by the shape of the device so Ms can be tune more easily and distribution of switching behavior is reduced [53,92]. More importantly, the demagnetization term favors in-plane direction of the magnetization so that it helps reversal in case of PMA whereas in the case of in-plane magnetized system, it opposes to reversal. Interestingly the thermal stability of the free element is determined by the height of the energy barrier $U_K = [M_S V(H_K - 4\pi M_S)]$ between the two stable magnetization configurations (up or down for a single layer). Thus the critical current is directly proportional to the energy barrier in the absence of external field, i.e. $H_{dip} + H = 0$ [53,84,91]. As a consequence, since to maintain good thermal stability one cannot decrease too much, decreasing I_{c0} requires to decrease the $\alpha Ms/P$ term.

From both the requirements on PMA and the "αMs/p" term, we can conclude that Co/Ni multilayers hold all the requested features to well behave as a STT memory bit cell. Indeed, as we show in Part I.1, Co/Ni interface produces PMA. Anisotropy value is as large as few MJ/m^3 and so insure good thermal stability for the bit at rest. Changing the thickness of Co allows an easy tuning of PMA amplitude. Magnetization of Co/Ni MLs is moderate, of the order of 700 kA/m. Gilbert damping has been found to be quite insensitive to the composition and down to 0.01 [36]. Finally, high spin polarization has been deduced from our SR-PES experiments presented in Part I.1.5 and confirmed in recent STT experiments [81]. In the following we will provide experimental evidence of magnetization switching induced by STT

in Co/Ni-based spin-valves. We will show that the phase diagram based on simple macrospin model mostly reproduce the experimental data. Nevertheless, we also show that it fails to describe regular device with diameter larger than 50 nm either because of anisotropy distributions, intrinsic dipolar effect and incoherent reversal.

II.2.2.Co/Ni-based metallic spin-valve and spin transfer experiments

Epitaxial Au/Ni/$[Co/Ni]_x$/Au(y)/[Co/Ni]z with various number of repeats x and z, as well as Au spacer thickness y, were grown by MBE at Nancy. Note that we were constrained to use Au as a spacer layer because of the limited amount of materials in our MBE chamber. From TEM images, we found that both Au and [Co/Ni] relaxed into their own lattice parameter. From magnetometry measurement, we have shown that both bottom and top Co/Ni electrodes have PMA. By tuning the thickness of Co (0.5nm) for the top free layer and Co(0.2) for the bottom hard layer, we could achieve different coercivity for these two layers and therefore achieve the necessary anti-parallel state for a certain field as presented in Fig. 15(a). Nevertheless to insure magnetic decoupling between the two layers, one has to increase the thickness of Au spacer up to at least 4 to 5 nm. For instance, in Fig. 15(a), the hysteresis loop of two spin-valve are presented. The two only differ by their Au thickness : the red curve correspond to y = 4nm whereas the black one corresponds to y = 5nm. Here interlayer coupling has two possible origins. The first is the dipolar interaction which acts in extended film only when domains exist (whereas it has a constant effect in nanostructures). The second coupling is RKKY coupling that originate from electronic quantum wells inside the spacer layer and which is oscillatory, i.e. ferro- or anti-ferromagnetic depending on the spacer thickness [94-96]. Orange-peel type coupling should not exist because of MBE growth and small lattice mismatch, providing limited interface roughness. We did not observe any anti-ferromagnetic coupling up to 6 nm. Similar results have been reported in Ref. [97]. As I could not observe the same effect in sputtered film, I strongly believe that the coupling originates from electronic structure features more than dipolar interaction. Whatever the origin of this coupling is, it has a strong impact on the potential use for device; indeed for too thin spacer electrodes are coupled so that one cannot stabilize anti-parallel state, whereas for thick Au layer, the full film current in-plane (CIP) GMR is small, usually lower than 1% at room temperature. Lithographic process to form nano-pilars devices has been tempted twice on these MBE films in collaboration with Y. Suzuki's group at Osaka University but very low current-perpendicular-to-plane (CPP) GMR (about 0.01%) and no STT were observed.

I have been more successful with magnetron sputtering Co/Ni-based spin-valves and Cu spacer. Fig. 15(b) show GMR measurements performed at 300K on full film for Cu thickness from 2 nm to 6nm with the current flowing in the film plane. No coupling is observed and the AP state can be stabilized for a significant range of field. The stack used was Ta/Pt/ $[Co(0.2)/Pt(0.9)]_5$/ $[Co(0.2)/Ni(0.7)]_2$/Co(0.2)/ Cu(x) /$[Co(0.2)/Ni(0.7)]_4$/Co(0.2)/Pt/Au with thicknesses in nm. CIP GMR amplitude doubles from 2.5 to 5 % as the spacer thickness is reduced from 6 to 2 nm. For the CPP nano-pilar, we choose Cu(3nm) spacer. All lithography steps were performed by Jordan Katine at HGST. The magnetoresistance of a 50 nm circular nanopilar versus field loop is shown in Fig. 15(c). CPP GMR is about 1.5%.

When performing a reversal cycle only for the free layer, so-called minor loop (red curve in Fig. 15(c)), the hysteresis loop is not center on zero but shifted by 1kOe. This shift originates from the dipolar field induced by the bottom hard layer. It corresponds to the H_{dip} discussed in the analytical calculations.

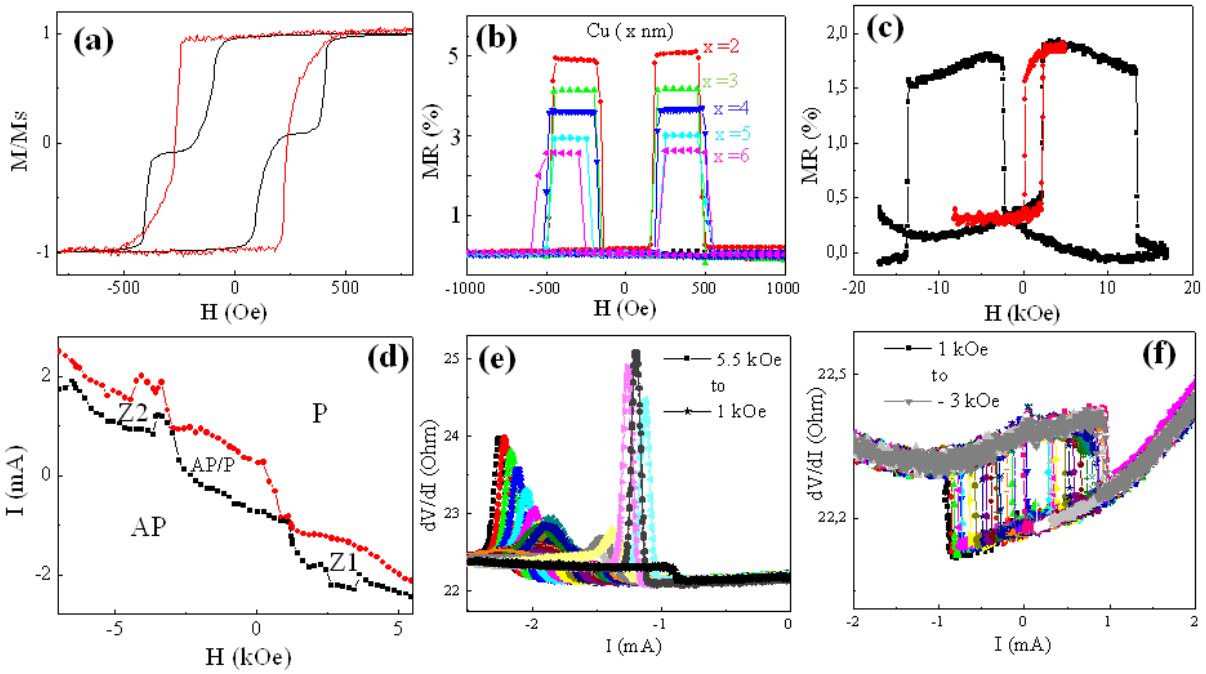

Fig. 15. (a) Room temperature normalized magnetization versus magnetic field for an MBE-grown epitaxial $[Co/Ni]_x/Co/Au(y)/Co/[Co/Ni]_z$ with y = 4 nm (red curve) and 5nm (black curve). (b) Room temperature CIP Magnetoresistance as a function fielda Ta/Pt/ $[Co(0.2)/Pt(0.9)]_5$/ $[Co(0.2)/Ni(0.7)]_2/Co(0.2)$/ Cu(x) $/[Co(0.2)/Ni(0.7)]_4/Co(0.2)/Pt/Au$ spin-valve. The red curve is a minor loop. (c) Current/Field phase diagram for a 50 nm wide nano-pilar made of the latest spin-valve. The black, resp. red, curve correspond to the stability of boundary of the AP, resp. P, state. Z1 and Z2 correspond to range of free layer dynamics (coherent or incoherent precession regime). (e) and (f) are differential resistance versus injected current amplitude used to plot the phase diagram in (c), more precisely Z1 zone and AP/P zone respectively.

Using the 50 nm wide spin-valve nanopilar, it is easy to get high current density of the order of 10^{10}A/m^2 as requested to observe STT effect. The most common experiment for characterizing the dynamical magnetic states consists in recording the differential resistance dV/dI, i.e., detecting the ac voltage response to a small alternating current (ac) with a frequency (e.g. 1 kHz) much lower than that of the spin precession [53,82,98]. The differential resistance can be written as dV/dI = R_{dc} + I dR/dI. The first term is the DC resistance which can help probe magnetization switching through GMR. The second term probes all reversible processes leading to a change of resistance as a function of current. This second term usually gives rise to peaks in the dV/dI signal that provides an easy and low cost way to characterize the STT-induced steady precessions. In measuring the resistance as a function of field and injected DC current, one can define which of the P and AP state is stable as well as if none of them is stable. Therefore one can construct the phase diagram introduced in Fig 15(b). Fig. 15(f) shows hysteresis while changing the current under various applied field. As the field is 1kOe or -3kOe, almost no hysteresis is observed (extreme black and gray

curves). On the contrary for an intermediate field (e.g. blue, yellow or pink curves), a hysteresis opens when both AP and P state can exist. The current value of the two hysteresis branches of each hysteresis are used as frontier points of the bistable AP/P state in Fig. 15(d). Fig.15(e) shows a reversible peaks in between the P (low resistance) and AP (high resistance) stable state. The width in current of theses peaks define the Z1 zone in Fig. 15(d). In this region, the STT balances the damping torque and field. As a consequence it gives rise to steady magnetization precession and spin wave excitation. Going beyond the measurement of the differential resistance d*V*/d*I* requires to use a spectrum analyzer in order to detect the variation of resistance in the Gigahertz frequency range [99]. Note that similar results have been obtained on 100 nm and 200 nm circular nano-pilars as well as $100*200nm^2$ and $100*300nm^2$ elliptical nanopilars.

When comparing the theoretical (Fig. 14(b)) and experimental (Fig. 15(d)) phase diagram, one can notice that three regions (region 1, 2 and 4 in Fig.14(b)) are in good agreement. However, the region 3 is not infinite in positive field as expected from the calculation and the region Z2 does not exist theoretically. In [92], it is shown that if the uniaxial symmetry assumed by the analytical macrospin model is broken such a region appears. Possible origins of the symmetry break are misalignment of the applied field, anisotropy axis, or incoherent reversal of the magnetization. To get more information experimentally on this discrepancy, one would either study the beginning of dynamical Z2 regime or the AP/P regime end. As I was not familiar with high frequency experiments and more involved in synchrotron imaging techniques as well as magnetic features distribution, it was “easier” for me to focus on imaging magnetization switching process in the AP/P region. “Easier” is not really adapted here since it tooks three years and many attempts to obtained the following results from the first meeting until getting the right scanning transmission X-ray microscopy images.

To get a more complete understanding of STT-switching in a nano-pillar, two extreme time scales need to be considered: a long time scale dominated by thermal activation [100,101] and a short time scale dominated by angular momentum conservation [100,102]. Most of the first studies on spin-transfer in PMA-based devices had been devoted to a description of quasi-static phenomena on longer time scales [53,103]. Only very recent experiments have used time resolved transport measurement on PMA devices with current pulses as short as 300 ps [100,102]. In order to image the magnetization reversal process, the scanning transmission x-ray microscope (STXM) available on beamline 11.0.2 at the Advanced Light Source (ALS) was used in collaboration with T. Tyliszczak, David P. Bernstein, Björn Bräuer and Y. Acremann. Images of the spatially resolved magnetic contrast with a time resolution of 70 ps were obtained as described in Refs. [104-107]. In our experiment, the incident beam was parallel to the surface normal (as show in Fig. 16) and focused by a zone plate with a 25 nm resolution. The photon energy is tuned to the characteristic Ni L3 resonance edge. The experiment is repeated for both left- and right-circular polarizations to provide a magnetic contrast through the XMCD effect. STXM experiments required to use sample on membranes transparent to the X-ray. Therefore I grew the ML films by sputtering on a Si substrate covered with a 300 nm thick Si_3N_4. The ML film

was then patterned by J. Katine using electron beam lithography and ion etching to form 100×300 nm^2 nanopillars with an ellipsoidal shape. We did not succeed to image smaller nanopilars. A last chemical etching step was performed on the sample backside to open a 200×200 nm^2 window in the Si wafer so that the spin-torque devices sit in the center of the Si_3N_4 membrane window. A critical feature of the experimental setup is the ability to synchronize the current pulses to the bunch structure of the ALS ring within a precision of 70 ps, yielding the time resolution of our experiment [104,105]. As presented in Fig. 16, the current pulse sequence was applied as follow: 4 ns positive or "set" pulse/4 ns no current/ 4 ns negative or "reset" pulse/ 4 ns no current. Voltages of ±748mV were applied during the set and reset pulses, respectively, corresponding to a current density of about 5×10^7 $A.cm^{-2}$. The rise time of the current pulses was 100 ps. By varying the delay between the x-ray probe and the current pulses, we were able to measure the time evolution of the magnetization.

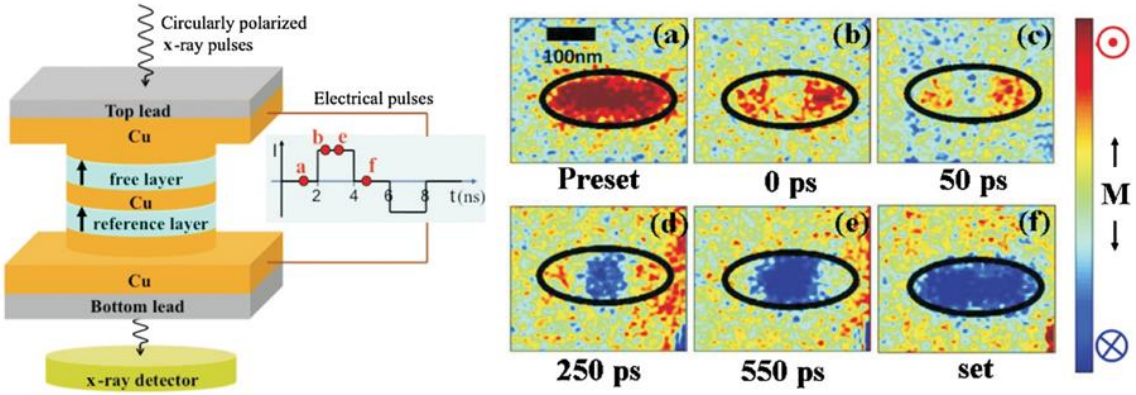

Fig. 16. On the left, schematic of the Scanning Transmission X-ray microscopy (STXM) experiment performed on a [Co/Ni]-based nanopillar spin valve. The pulse sequence (current versus time) is shown on the right. Letters (a), (b), (d) and (f) represent, respectively, the experimental STXM images of the magnetic contrast in 100 × 300 nm^2 ellipsoidal PMA nanopillar spin-valve. Image (a) is the initial state and (f) the final state. The color scale corresponds to the perpendicular component of the free layer magnetization, from parallel (red) to anti-parallel (blue) with respect to the reference layer.

Fig.16 shows a typical switching event as electrons travelled from the free layer to the reference layer. The imaged STT process therefore corresponds to the free layer magnetization switching from a parallel to an anti-parallel alignment with respect to the reference layer magnetization. The experiment was carried out at room temperature and in absence of magnetic field. The "preset" image in Fig. 16(a) shows the free layer magnetization state before a current pulse is injected into the structure. Images shown in Fig. 16 are obtained by accumulating data while repeating the method described above. It is important to note that, since our experiment uses STXM in a pump-probe mode, the images show the perpendicular component of the Ni sublattice magnetization averaged over a large number of pulse sequences. As a consequence of the averaging, this method does not allow us to identify stochastic processes. Fig. 16(b) shows that the sample undergoes a so-called

"incubation" time during which the pillar is subjected to a spin polarized current but the free layer has not started to reverse its magnetic orientation [108,109]. After this incubation time a central region of the pillar starts reversing. This region of nucleation appears more clearly after 50 ps in Fig. 16(c). Times quoted in Fig. (16) are given with respect to the first observed domain nucleation because of a possible offset in the absolute time. In other words, the precision on the pulse onset time does not allow us to quantify the 1.3 ns incubation time with a better precision than 300 ps. The relative times, however, are accurate within the quoted time resolution. In Fig. 16(d) and Fig. X(e) the reversed domain grows by domain wall motion towards the edges. In Fig. 16(e), at 550 ps, the sample magnetization has not fully switched yet. An image taken in between the set pulse and the reset pulse confirms the total saturation of the sample (Fig. 16(f)).

We performed at Nancy micromagnetic calculations of the Landau Lifshitz Gilbert (LLG) equation using the Scheinfein code [110] where the injected current pulse was taken into account in the Slonczewski spin-torque term [89]. The calculations performed considered a 100×300 nm^2 ellipsoidal element mimicking the same stack as described above where the reference layer is divided into 3750 cells and the soft layer into 1875 cells. Temperature was taken into account within an initial 5 degree tilt of the free layer magnetization. Current duration and amplitude were 4 ns and 15 mA, respectively. The electrons were injected from the free to the hard layer starting with a parallel initial configuration. The micromagnetic simulations shown in Fig. 17(a)–17(g) and the experimental STXM results are in good qualitative agreement. The simulated incubation time and switching time are 1.3 and 1.2 ns, respectively. The size of the nucleated domain is smaller than 50×50 nm^2, and the domain-wall width is on the order of 20 nm. The simulated domain walls are Bloch-like walls, but this information is not experimentally confirmed because the STXM spatial resolution is about 25 nm. Rough calculations based on successive experimental images in Fig. 17(c)-17(e), as well as simulated results, lead to a domain-wall propagation speed on the order of 100m⁄s. The position of the magnetization nucleation inside the free layer must result from the addition of the dipolar field originating from the reference layer on the free layer and the free-layer internal demagnetization field. Indeed, starting from a parallel (P) configuration of the layer magnetizations, both these dipolar and demagnetization fields favor a magnetization reversal at the ellipse center. On the contrary, here, starting from the antiparallel (AP) state, the nucleation occurs at the edge of the ellipse but close to the middle of the length as favored by the competition between dipolar field and free layer demagnetization field.

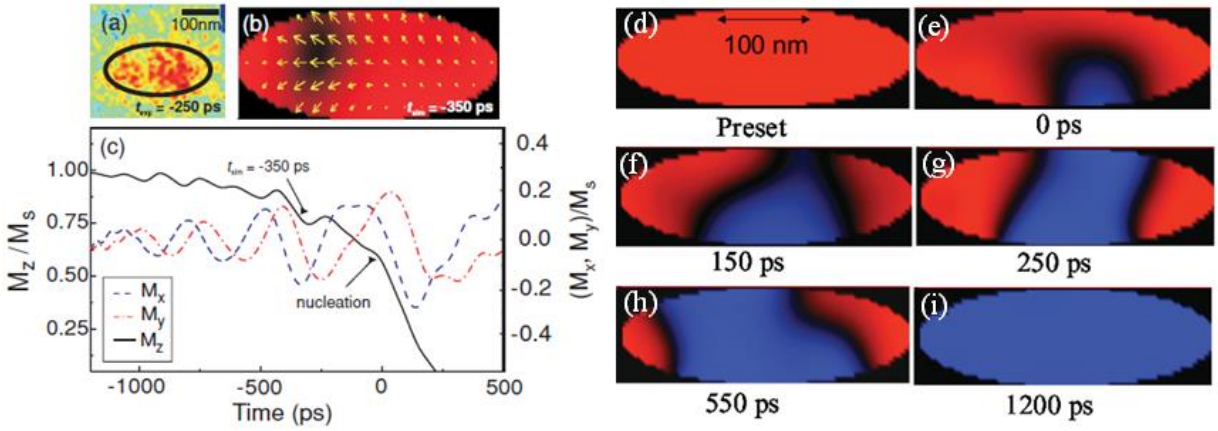

FIG. 17. (a) Experimental image of the magnetization along the PMA axis in the free layer at −250 ps where the color scale ranges from parallel (red) to AP (blue) and the negative sign indicates that the image was taken prior to nucleation. (b) The simulated magnetization in the free layer at −350 ps where the length of the yellow arrows corresponds to the amplitude of the in-plane magnetic component. (c) Simulated component of the magnetization along the PMA direction (*Mz*, left vertical axis) as well as the two in-plane components (*Mx* and *My* , right vertical axis). (d)–(i) correspond to a series of micromagnetic simulations showing the free-layer configuration at different times during the STT-induced switching in a 100 × 300 nm^2 PMA nanopillar as described in the text. The color scale is the same as in Fig.16 and corresponds to the perpendicular component of the free-layer magnetization, from parallel (red) to anti-parallel (blue) with respect to the reference layer. Times are given with respect to domain nucleation.

Finally, information on the free layer magnetic behaviour during the incubation time can be extracted from comparison between STXM data and simulation. Simulations in Fig. 17(c) show the out-of-plane (Mz) and in-plane (Mx, My) components of the free layer magnetization during the incubation time. The pre-nucleation dynamics features are a small amplitude oscillatory behaviour of Mz correlated to dephased Mx and My component oscillations. Mx and My oscillation amplitude increases continuously until domain nucleation is reached. Such evolution is typical of a current-induced magnetization precession that leads to switching over a certain magnetization tilt angle. The precessional modes may be uniform [111] or non-uniform [109]. Fig. 17(a) corresponds to a STXM image taken at -250 ps where the minus sign indicates that the image was taken prior to the nucleation. The component of magnetization along the PMA axis is undoubtedly non-uniform over the pillar area when compared with the preset image (see Fig. 16(a)). This experimental result is well described within the simulations. A symptomatic case of the non-uniformity during the incubation time dynamics is shown in Fig. 17(b). Although all the simulated spins precess as the current is turned on, a localized area of larger amplitude precession is observed that is continuously displaced during the incubation time and ultimately results in nucleation within that region. The initial precessionnal behavior, e.g. the incubation time, is observed for various type of excitation apart from STT and has a strong impact even for nano-objects much smaller than 100*300nm^2 [112,113].

The present data set offers direct proof of incoherency in the short time regime STT. It provides explanation for the discrepancies between macrospin model and very recent time

resolved macroscopic transport measurements performed on similar PMA devices [92,100-102]. All recent works on MRAM cells show that the latest have to be shrinked down to 20 nm to really behave as a macrospin [114].

II.2.3. Co/Ni-based magnetic tunnel junctions

Since 2006, PMA spin-valves are a nice playground to study STT features. Nevertheless, for many years already, magnetic tunnel junctions (MTJs) having PMA electrodes have attracted even more interest since they are being implemented as active cell in MRAM in the view of replacing flash memory, DRAM or SRAM. For instance, Toshiba has announced in june 2014 that its PMA STT-MRAM cache for microprocessor reduces power consumption of regular CPU cache by about 60% and improves access speed. In Toshiba's cache, the read, resp. writing, time is 4.1 ns, resp. 2.1 ns, very close to that of SRAM. As discussed in the introduction, MTJs have similar structure as spin-valves but the metallic spacer is replaced by an insulator. The tunnel magnetoresistance (TMR), which quantify the difference of resistance between the P and AP state, is defined in terms of resistance R or conductance G in P and AP configuration as:

$$\mathrm{TMR} = \frac{\mathrm{R_{AP}} - \mathrm{R_P}}{\mathrm{R_P}} = \frac{\mathrm{G_P} - \mathrm{G_{AP}}}{\mathrm{G_{AP}}}$$

where R_{AP} (G_{AP}) and R_P (G_P) are the resistance (conductivity) of the parallel state and anti-parallel alignment of electrodes moments respectively.

One of the most heavily pursued system is CoFeB/MgO/CoFeB stack where CoFeB/MgO and MgO/CoFeB provide perpendicular interface anisotropy and large tunnel magnetoresistance (TMR, i.e. difference between anti-parallel state resistance minus parallel state resistance normalized to the parallel state resistance) [115,116]. Buffer and capping layer generally provide additional interface PMA [117,118]. One limitation of this stack comes from thermal stability as the thickness of CoFeB electrodes has to be thin. Rare-earth/transition metal ferrimagnet alloys [119], [$Fe_{1-x}Co_x$ /Pt] MLs [120,121] and $L1^0$ (Fe,Co)Pt alloys [122] have also been tested as electrodes since they have large PMA. However they hold large damping and low spin polarization [123]. Mixing high stability of MLs with the efficiency of CoFeB/MgO/CoFeB trilayer has become one choice of interest for many companies like IBM [124,125]. I will come back to this system in my on-going works chapter.

As demonstrated in Part II.2.1, Co/Ni MLs provides good efficiency for spin transfer writing as well as good data thermal stability. However, no TMR or STT torque experiments have been reported yet for magnetic tunnel junction (MTJ) based on PMA Co/Ni electrodes. Difficulties to grow bcc MgO (100) barrier on top of fcc Co/Ni (111) stack as well as Co/Ni on MgO barrier is the limiting factor [126]. Only You et al. recently succeeded to grow MgO-based magnetic tunnel junction with two PMA Co/Ni electrodes but only magnetometry

measurements were shown [127]. We have tried to grow MgO on epiaxial (111) Co/Ni MLs and Co/Ni on epiaxial MgO (100) by MBE but we did not succeed to get any good tunnel barrier properties or good PMA for the top electrodes. So we decided to use sputtering growth method with amorphous Al_2O_3 tunnel barrier. This work has been performed during Iaryna Lytvynenko's phD at Nancy. Samples were prepared at CNRS-Thales lab by Cyrile Deranlot on silicon substrate by a magnetron sputtering with a base pressure of 5.10^{-8} mbarr. The Si wafer is capped with a 400 nm thick thermal SiO_2. The deposition was performed at room temperature with no annealing. Co/Ni and Co/Pt MLs, as well as the Ta and Pt layers, were grown by dc-magnetron sputtering. Two MTJs were deposited. Both have the same bottom electrode Ta(5)/Pt(10)/Co(0.6)/ [Ni(0.6/Co(0.3)]*3. The Al_2O_3 (2.5nm) barrier is obtained through the deposition of 1.5nm Al layer within a $Ar+O_2$ plasma. Then the first MTJ has [Co(0.2)/Ni(0.6]*3/Pt(2)/[Co(0.6)/Pt(1)]*3 as top electrode while the second MTJ top electrode consists in Co(15) single layer. UV lithography was used to pattern MTJ devices with junction size from 10*10 μm^2 up to 50×50 μm^2 having 1 $G\Omega.\mu m^2$ RA product.

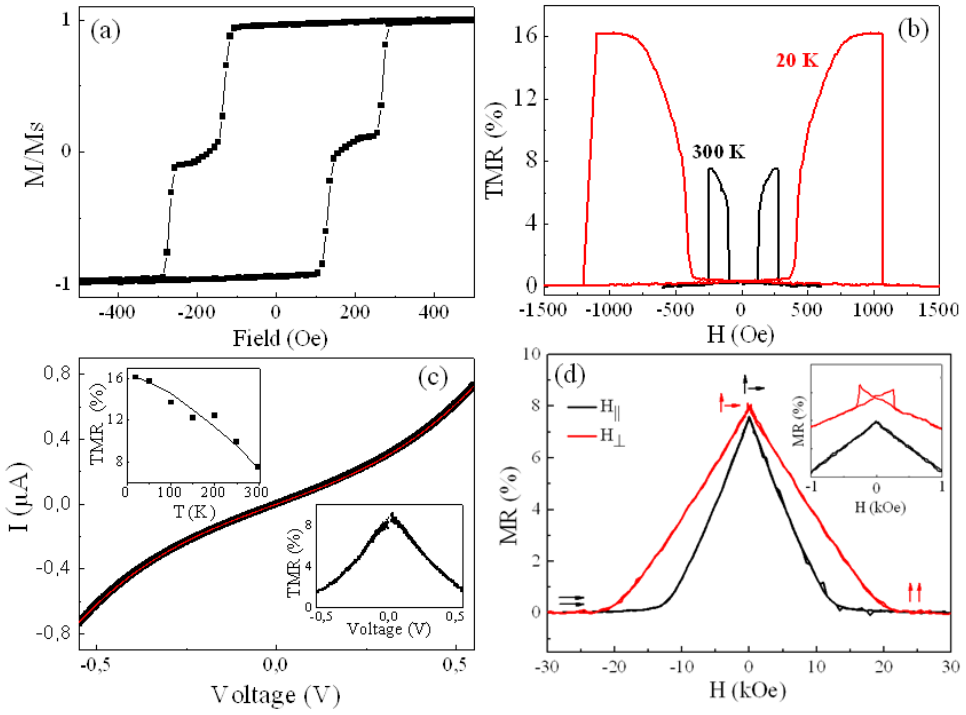

Fig.18. (a) Room temperature normalized magnetization vs field measurements of Co(0.6)/[Ni(0.6/Co(0.3)]*3 /AlOx(2.5)/ [Co(0.2)/Ni(0.6]*3/ Pt(2)/[Co(0.6)/Pt(1)]*3 MTJ under out-of-plane applied magnetic field. (b) MR vs out-of-plane field for sample A with both PMA hard [Co/Ni] and soft [Co/Ni][Co/Pt] electrodes measured under 50 mV bias voltage, at the 300 K (black line) and 20 K (red line). (c) Experimental current vs bias voltage (black points) for the same MTJ at 300K is compared with Brinkman fit (red line). Inset 1: Experimental TMR as function of the bias voltage (black points) compared with theoretical (solid line) as explained in the text. Inset 2: TMR versus bias voltage measured at 300K. (d) MR of Pt/Co(0.6)/[Ni(0.6)/Co(0.3)]*3/ AlOx(2.5)/Co(15) MTJ measured applying the magnetic field in-plane (black line) and out-of-plane (red line) under 50mV bias voltage at room temperature. Inset corresponds to a zoom around zero field and highlights the reversal of PMA Co/Ni bottom electrode magnetization at -270 Oe.

Fig. 18(a) shows normalized magnetization curve measured for the PMA/Al_2O_3/PMA sample. As the field is applied perpendicularly to the layers, we observe loop with remanent full magnetization and two successive jumps in negative field (at -130 Oe and -270 Oe respectively) when starting from positive saturation. The first magnetization jump has larger

amplitude than the second one. It indicates that, here, the top [Co(0.2)/Ni(0.6]*3/Pt(2)/[Co(0.6)/Pt(1)]*3, that has the largest total moment, is softer than the bottom Pt(10)/Co(0.6)/ [Ni(0.6/Co(0.3)]*3. This result is counter-intuitive since earlier we used Co/Pt ML to harden the Co/Ni. However the well established layer by layer growth of the bottom Co/Ni ML on smooth and (111) texture Pt buffer provide much larger PMA (here effective anisotropy field is about 12 kOe) than the island-like growth process of top ML on Al2O3 oxide barrier [128]. Magneto-resistance measurements performed on patterned sample A are shown in Fig.18. We successfully measure significant TMR in MTJ with two Co/Ni PMA electrodes. Overall MTJs TMR value as high as 8 % at 300 K and 16 % at 20 K are measured for 50 mV bias voltage. Such value is much smaller than the best reported TMRs (about 80%) for CoFeB/Al_2O_3-based MTJ [129]. Nevertheless it is of the same order of magnitude as the previously reported Al_2O_3-based MTJs with PMA electrodes [120,121]. As shown in inset of Fig. 18(c), Temperature dependence of TMR fits well with the $(1-\alpha T^{3/2})$ dependence usually reported and linked to spin-polarization decrease and increase of the inelastic processes as the temperature increases [132]. One can use Brinkman model that describes the bias-voltage dependence of tunnel current to get a better description of the barrier features [120,130]. Room temperature I(V) curve measured in parallel state is presented in Fig.18(c) and compared with a Brinkman fit using a 2.5nm barrier width. Good match is obtained when considering a 1.18 eV zero bias barrier height and no barrier asymmetry. The barrier height value confirms the average quality of our Al_2O_3 layer. Nevertheless, values up to 3 eV can be achieved so that much larger TMR can be expected if we further improve our Al_2O_3 barrier [131]. Interestingly, no barrier asymmetry is needed in the Brinkman fit. It indicates that the bottom and top interface are similar. The same conclusion can be drawn from the voltage dependence of TMR (inset of Fig. 18(c). The decrease of TMR with increasing bias voltage, mostly due to inelastic scattering by magnons excitations and electronic density of state shape [132], is symmetric. Lack of asymmetry implies that roughness at the bottom and top barrier interface are similar and that DOS of both PMA electrodes are not too different either. One could have expected a difference between top and bottom layer since their Hk are different and strongly depend on the layering quality. The layering quality can also be correlated to the TMR value that is much lower than expected form the SRPES results in Part I.1.5. With 80% spin-polarization, one would expect 300% TMR from simple Jullière's model [133]. Most probably the layering close to the barrier is not as good as in MBE-grown MLs and the interface with Al_2O_3 needs to be improved.

Finally, Fig. 18(d) shows magnetoresistance measurements performed on the second MTJ which differs from the first one by its in-plane magnetized thick Co top electrode. Interest has grown the past years for this crossed geometry because of its possible use in sensors [134], OST-MRAM [135] and RF oscillators [136,137]. Here, when the external magnetic field is large enough both electrode magnetizations are aligned along the field (applied either in-plane or out-of-plane). At zero field, the Co/Ni ML is perpendicular whereas Co magnetization lays in plane. Hysteresis occurs for the out-of-plane field case as the bottom Co/Ni ML magnetization reverses. In the in-plane case, no hysteresis is observed for the Co layer. Note that the in-plane curve gives access to the Co/Ni ML effective

anisotropy field, about 12 kOe [138]. The difference of resistance between the saturated state and the remanent state is about 8 % at 300K. This value is actually half of the TMR which refers to the difference of resistance between the parallel and anti-parallel state. The difference of TMR between the two samples may originate from a lower polarization of the Co/Ni top PMA electrode due to mixing at Co/Ni interfaces or from a difference in barrier tunnel quality.

Overall the difficulties for growing Co/Ni-based MTJ as well as the low TMR achievable with Al_2O_3 tunnel barrier does not make this system suitable for implementation in MRAM type devices. As of now, it cannot compete with CoFeB/MgO based MTJ. It may be of interest for more specific use for RF oscillator or sensors where more than one tunnel barrier is requested. To our knowledge, no nano-pilar and no spin-transfer experiments have been reported yet on Co/Ni-based MTJ, but some MTJ based on CoFeB/MgO/CoFeB use Co/Ni to induce PMA electrodes [139,140].

II.2.4. Domain wall motion in Co/Ni micro and nanowires

Study of domain wall nucleation and propagation in full film

STT can be used to control the magnetic moment of a nano-pilar devices down to the macrospin limit. It can also affect nanosystems where magnetic domain wall (DW) motion plays a large role. In the 300*100nm^2 pillars discussed in part I.2.1, the current is flowing perpendicular to the plane and has no specific influence on pushing the DW [103]. However if the pillars have in-plane magnetized or if the current is flowing in the plane of the layer, then the spin-polarized current can depin and move DW [141,142]. Besides the fundamental interest of studying STT effects on domain wall, the control of DW in nanowires by STT is being considered to develop new data storage electronic devices with high data areal density and low power consumption. The concept of race track memory will be later detailed in part III.2.1. Materials with PMA are interesting candidates to study STT-induced DW motion since they can produce narrow DW and less complex DW magnetic configurations as compared with in-plane magnetized systems [142]. Various materials have been investigated. STT induced remanent motion in GaMnAs with a density of current lower than 10^8 A/m² [143,144] but GaMnAs is ferromagnetic only at low temperature. Sputtered Pt/Co [145], Co/Ni [146,147],or amorphous CoFeB [148] hold interesting properties such as high PMA and low coercive field, but still require high current density (i.e. around 10^{11} to 10^{12} A/m²), to move domain walls.

At Institut Jean Lamour in Nancy, we thought PMA single crystal (111) Co/Ni could be a model system to study the physics of STT because of its low damping, tunable high spin-polarization, anisotropy and magnetization. Work started during M. Gottwald phD in 2009 and continued with S. Le Gall post-doc until 2014. A lot of effort has been put by the team, especially Francois Montaigne, to develop lithographic process for electrically connected micro- and nano-wires as well as methodology for DW motion imaging (in-field Kerr

microscopy, MFM). Note that in parallel, we have also focused on TbCo alloys but we did not obtain any proof of STT induced DW motion in this system. A first type of sample, epitaxial V(5nm)/Au(1nm)/Ni(0.2nm)/ $[Co(0.5nm)/Ni(0.6nm)]_{\times 3}$/Au(1.2nm) stack, was deposited on Sapphire substrate by MBE under ultra-high vacuum. The same material (Au) used for the capping and seed layer on the stack prevent undesired effect as spin-orbits torque observed in ferromagnetic nanowire with strong structural inversion asymmetry [149,150]. Room temperature hysteresis loop for the full film is shown in Fig. 19(a). Static coercivity is 225 Oe. We have mostly studied nucleation and propagation in full film as well as in microwires under STT by in-field Kerr microscopy at Nancy and at IEF Orsay (in collaboration with Nicolas Vernier). All measurements have been done at room temperature.

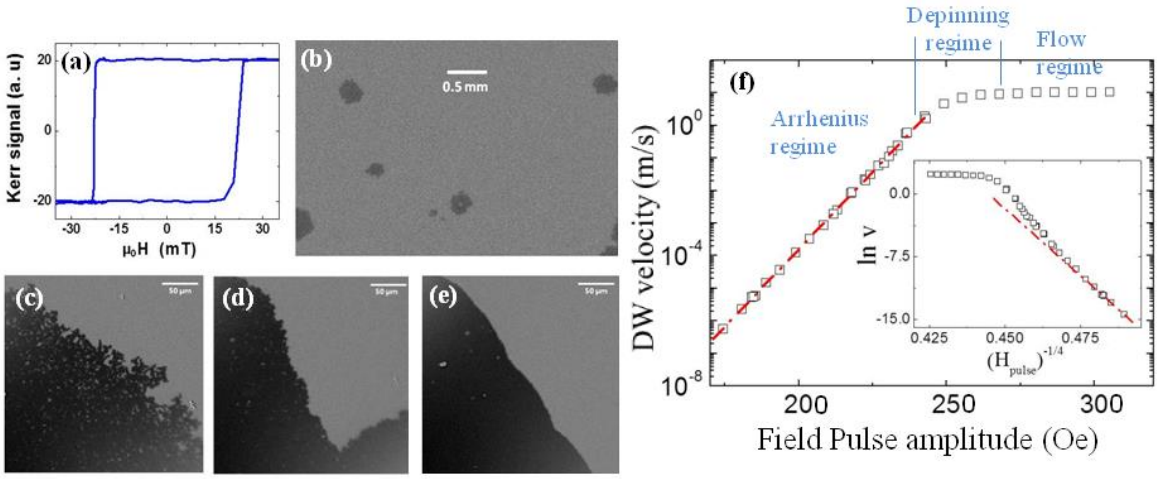

Fig. 19. (a) Magneto-optical Kerr magnetometry loop performed by Kerr microscope on epitaxial Co/Ni ML over 2.6×4 mm² area. (b) 2.6×4 mm² Kerr microscopy images measured at remanence after a 5 µs field pulse of 211 Oe. The black contrast means reversed magnetization as compared to the background grey region still saturated in negative field. (c) to (e) 275×275 µm² Kerr microscopy images after DW propagation under µs-pulsed magnetic fields with amplitude of 237 Oe, 256 Oe and 293 Oe respectively. (f) DW Velocity in semi-logarithmic scale as a function of 5 µs pulsed magnetic fieldamplitude. The red dash line is a linear fit at low field. Inset shows logarithm of DW velocity as a function of $(H_{pulse})^{-1/4}$. The red dash lines are linear fits at low field.

To quantify the nucleation process, one 5µs field pulse of 211 Oe amplitude is applied that generates only 7 nucleation spots over a 2.6×4 mm² area. Such a low density of nucleation sites is typical of epitaxial systems. Crystalline order is very good over large area and any local or extended disordered has a strong impact on magnetism. In PMA multilayers like Co/Ni, local anisotropy weakness usually comes from crystalline misorientation and interface intermixing (see part II.1). Note that the reversed region at the bottom-right corner on Fig. 19(b) is a part of domain coming from nucleation on the fullfilm border. From there additional µs field pulses were sent to investigate DW propagation process. The pictures in Fig. 19(c) to (e) show the magnetic configurations around DW after domain growth under µs-pulsed magnetic field with various amplitudes. For H_{pulse}=237 Oe, the domain has expanded through dendritic-growth [151,152]. Sputtered Co/Ni films [153,154] as well as eptixial FePt [155] show the same low field regime. During the dendritic-growth unreversed spots (not always but often hard switcher region as decribed in part II.1) are left behind the DW as it propagates [151,152]. The dendritic growth is still observed for pulses up to 256 Oe and

disappears above 268 Oe. As the domain growth transits from dendritic to flow regime, the number of residual unreversed sites decreases. Nevertheless some persists for fields up to 31mT (the maximum field we could investigate). Note that the size of the non-reversed domains in Fig. 19(c) to (e) is not relevant since we applied -170 Oe to highlight them. Without opposite field, the remaining domains are invisible to Kerr microscope. We can estimate that a circular domain stabilized by a dipolar field whose value at the center is $H_{dip}= t_{Co/Ni}M_S/r$ = 310 Oe (r is the radius of the spot and $t_{Co/Ni}$=3.5 nm the Co/Ni ML thickness) would be 260 nm diameter.

To further characterize the different regime of DW propagation, DW velocity was investigated. The velocity is measured by the DW displacement after application of a 5µs field pulse. The DW velocity as a function of H_{pulse} amplitude is shown on Fig. 19(f) for semi-logarithmic. Two main velocity regimes are observed. For fields lower than 240 Oe, DW velocity increases with field amplitude. For fields larger than 270 Oe, the velocity saturates around 10 m/s. In the low field regime, the linear evolution of DW velocity in semi-logarithmic scale over 7 decades of magnitude is consistent with a thermally activated process i.e Arrhenius-type law as $v(H)=v_0 \exp[2M_S V_a(H-H_{dep})/kT]$ where H_{dep} the depinning field equals 240 Oe [157]. This behavior is quite unique. Indeed, usually (e.g. in sputtered Co/Pt [158][159], CoFeB/MgO [160] and [Co/Ni]/[Co/Pt] [161]), the low field regime consists in a creep regime [162] where the velocity can be written as $v(H)=v_0 \exp[-E_B (H_{dep}/H)^{1/4}/kT]$. The plot of ln(v) as a function of $H^{-1/4}$ presented in inset of Fig. 19(f) show that our data deviates from the creep regime for field larger than 21 mT. Moreover, the experimental deviation tends overpass the linear fit which is opposite to what has been observed in previous studies [158,160,161]. The difference between creep regime and the so-called Arrhenius-type regime consists in the nature and number of the pinning defects. In the first case, wide distribution of defects [162] is considered whereas the second assumes that all defects are described by one unique energy barrier [157]. To our knowledge, only Au/Co/Au and FePt MBE-grown systems have been reported to present single type pinning potential similar to ours [157,163,164]. A regular single-type defect pattern is also consistent with dendritic domain with random-walk along of a defect network [165,166]. We have indentified two types of defect in our Co/Ni epitaxial multilayer films that could affect domain wall motion. The first one consists in the formation of twins domain in the V buffer layer presented in Fig.4 in part I.1.1. Twin domain boundary may affect Au and further form grain boundary defects in Co/Ni. The maximum period twin domains boundary is expected to be of the order of 100 nm. Some kind of extended misalignement zones have been highlighted by transmission electron microscopy. They may also originate from a second defect consisting in a fault of fcc stacking in the Co/Ni itself. Locally A-B-C pile can be mistakenly replaced by A-B-A pile for instance. We do not have the information about the average distance between grain boundaries due to this second type of defect.

For field larger than 240 Oe, DW velocity increase rate with increasing field is reduced. The DW motion enters in a viscous flow regime [158]. In the 1D interface model [Schryer1974], it was predicted a steady and then a precessional linear regime separated by the Walker field $H_w=\alpha.Ms.N_y/2$ [167] with Ms the magnetization at saturation and N_y the

demagnetizing factor across the wall. Due to the low damping constant α in our epitaxial Co/Ni epitaxial MLs (≈ 0.01), the theoretical H_w is estimated around 60 Oe, i.e. even lower than the studied field range. As a consequence H_w lies inside the thermally activated regime and hides the Walker breakdown as already observed in CoFeB/MgO [160]. Plotting DW velocity as a function of pulsed field (not shown here) allows to quantify H_{flow}=270 Oe which is the lower bound for the flow regime as well as the transition between dendritic growth and wall-motion. For $H > H_{flow}$, the velocity seems to reach a plateau at around 10 m/s (maybe indicative of a precessional regime) as reported in Refs. [154,160]. Between 240 Oe and 270 Oe, an intermediate regime exists, named depinning regime in Ref. [158]. Finally, one can notice the fact that MBE-grown Co/Ni multilayer does not show faster domain wall motion than Co/Ni sputtered films. It is not surprising since, in the flow regime, the DW propagation is less sensitive to pinning defects, and should behaves accordingly to 1D model.

STT-induced domain wall propagation in micro-wires

Based on this knowledge about the full film propagation regime, we micronic wires (2-10 µm width) were patterned in V(5nm)/Au(1nm)/Ni(0.2nm)/ $[Co(0.5nm)/Ni(0.6nm)]_{\times 3}$/Au(1.2nm) full film to study spin-tranfer induced domain wall motion. An optical view with electrical connection of typical 4 µm wire width is shown in Fig. 20(a). The magnetic 90 µm length wire consists of 2 hall crosses (not used for experiment here) extended by a triangular-shaped big pad where the DW nucleation is expected. Non-magnetic contacts are connected at each wire end for electrical injection/detection. The µs-pulsed excitation, field or current applied on the wire can be chosen according to the DW speed range. The field (H_{pulse}) or current (J_{pulse}) pulsed excitations applied by voltage pulse generator are synchronized as 5 µs for H_{pulse} and 3 µs for I_{pulse} with a delay of 2 µs (see oscilloscope signal in Fig.20(g)). Due to the high resistance of the vanadium layer, we consider the entire electrons flow to happen through a section of 2 µm × 6 nm. Example of DW displacement sequence is shown in Fig. 20(b) to (f) for $J_{pulse}=+38\times10^{10}$ A/m² and H_{pulse}=205 Oe. The DW nucleation takes place on the right big pad, and the DW was injected on the wire by the right side using low H_{pulse}. Fig. 20(b) shows the DW position at the entrance of the wire. Each subsequent frame pictures is the difference from the previous one and show the length of DW displacement after one single pulse. Average experimental results of DW velocity calculated in dividing the DW displacement by 5 µs (in order to compare with full film) for various large H_{pulse} and ± J_{pulse} range are summarized in Fig. 20(h).

The velocity plotted in for semi-logarithm and linear scale for zero current pulse (black asterisks) is similar as that obtained for the full film in Fig.20(f) except that the all curves seems to be shifted by 20 Oe towards lower field. Flow regime (i.e. velocity plateau) starts at H_{pulse} = 250 Oe instead of 270 Oe for the full film. Unfortunately the studied field range is restricted due to both wire length and time pulse limit. The shape of the curves in Fig. 20(h) indicates that DW motion here is mostly in the intermediate depinning regime which is not well described by any analytical expressions. As negative current (electrons flowing from the triangular pad in Fig. 20(b)) is injected in addition to the field, we notice that the velocity curve shifts downfield. The negative current facilitates DW displacement. On the other hand,

an applied positive current opposes to DW displacement (at least for low current as described later). We have not seen any impact of current pulses for current density lower than 8×10^{10} A/m².

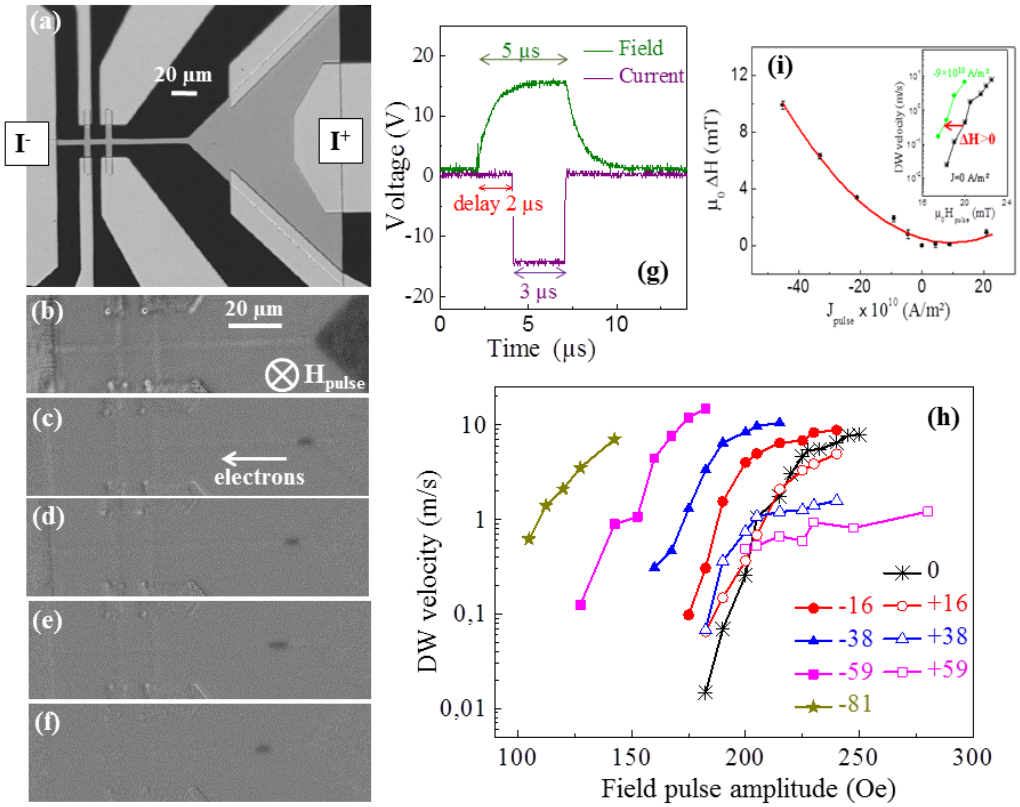

Fig.20. (a) Optical image of a typical 4 µm wire width studied here with electrical connections. (b) to (f) show example of DW displacement series on a 2 µm wire width using field and current µs-pulses (here 1 pulse/picture) for J_{pulse}=+38×10^10 A/m² and H_{pulse}=205 Oe. Here the black magnetic contrast corresponds to the DW displacement during 1 pulse. Each picture is taken at zero-field after the single pulse and is the difference from the previous one. (g) Pulsed signals synchronization for H field (green) and current (purple). (h) DW displacement as a function of H_{pulse} amplitude in semi-logarithmic scale for various J_{pulse} (in 10^{10} A/m²) sent in a 2 µm width wire. (i) Field shift (ΔH), as described in inset, as a function of J_{pulse} (in 10^{10} A/m²) in order to extract ε and δ parameters as explained in the text. The black symbols are experimental data, the red line is a polynomial fit.

In order to quantify the effect of current in the thermally activated regime, we introduce an effective field ΔH as defined in the inset of Fig. 20(i). The field shift ΔH will is counted positive for a shift to the left with respect to the zero-current velocity curve. In Fig. 20(i), we present the extracted ΔH values versus J_{pulse}. The experimental points can be fitted by a second-degree polynomial (red line): $\Delta H = +\varepsilon J_{pulse} + \eta J_{pulse}^2$ with $\varepsilon=-(6.3\pm0.9)\times10^{-15}$ T/A.m^{-2} and $\eta=(3.3\pm0.3)\times10^{-26}$ T/A².m^{-4}. It is equivalent to consider that the Arrhenius law can be rewritten as $v(H)=v_0\exp[2M_S V_a(H_{eff}-H_{dep})/k_B T]$, where $H_{eff} = H_{pulse} + \varepsilon J_{pulse} + \eta J_{pulse}^2$ is an effective out-of-plane field.

For the physical origin of the J dependence, we refer to Ref. [170], a theoretical analysis of the current-induced DW motion by magnetic field and including both non-adiabatic and

adiabatic components of STT. A non-adiabatic term proportional to the current (εJ) that acts as a magnetic field [168], and a quadratic adiabatic term (ηJ²) which introduces non-linearity to H, are added to the velocity expression in creep regime. This theory was successfully used to interpret the experimental observation of the DW motion in GaMnAs nanowires [159,169]. From the efficiency ε, we can deduce β, the so-called non-adiabaticity STT constant, since $|\varepsilon| = (\beta P\hbar)/(2eM_S\Delta)$ [168], where P is the spin polarization (measured at 0.77 in the flow regime, see below), and Δ=5.8 nm the DW thickness. We obtain β=(0.13±0.02), a value around 6 times bigger than reported on sputtered Co/Ni system in creep regime [147]. In sputtered Co/Ni systems, the contribution of both adiabatic and non-adiabatic terms is still debated: Burrowes *et al.* [147] found that the non-adiabatic torque dominates the DW creep motion and depinning, whereas Koyama *et al.* [146] found that it plays no significant role. If we base our analysis on the theoretical expression from [170], we find that both adiabatic and non-adiabatic components may play a significant role on DW propagation in the thermally regime in epitaxial [Co/Ni] samples. The sign of the quadratic term (ηJ²) can be positive or negative according to equation (1) of reference [169]. The J^2 dependence could also relate to Joule heating. We use the following estimation of the temperature rise ΔT coming from Joule heating by current pulse [171] : $\Delta T = RI^2 \times (\ln(16K/(dCw^2)) + \ln(\tau_{pulse}))/(2\pi lK)$, which depends on C, K and d, the specific heat, thermal conduction, and density of the substrate respectively, the resistivity R and dimensions (l, w) of the wire, and pulse duration τ_{pulse}. Taking d=4000 kg/m^3, K=40 W.m^{-1}.K^{-1}, C=700 J.kg^{-1}.K^{-1} for sapphire and R=1500 Ω, w=2 µm and l=165 µm for our Co/Ni layer, one calculates that an injected current between 20 and 45×10^{10} A/m² in our microwire gives rise to a slight temperature increase of about 4 – 20 K . In the thermally-activated DW motion regime, the Joule heating contributes to an increase of temperature by T+δJ² with δ a constant. This affects the slope of the v(J) curve because it decreases the potential energy barrier in the Arrhenius law. Therefore Joule heating does not cause the strong shift of the curves toward positive current that is observed.

As a conclusion for the part II, we have carefully characterized structural, magnetic and electronic features of Co/Ni ML system. We demonstrate that Co/Ni interface induces perpendicular anisotropy and that hybridization at the interface leads to a significant increase of the orbital moment, spin moment and spin-polarization at the Fermi level in the Co atoms while Ni properties do not change much. In a second part, we took advantage of the high PMA, low daming, high spin-polarization in spin-valve and magnetic tunnel junction devices. We used this model system to study the mechanism of magnetization reversal due to spin transfer torque effect in nano-pilar and micro-wire devices. We found that for nano-pilar larger than 50 nm diameter, STT induces a non-coherent reversal of the free layer magnetization. In extended film or micro-wires, magnetization reversal occurs by domain nucleation and DW propagation. Properties of DW propagation under external field are consistent with the expitaxial nature of the Co/Ni films. We confirmed that STT helps to propagate DW in a similar manner as an effective field would do.

Part III.

Multilayer-based bit pattern media and 3D Page memory

III. 1. Research on magnetic media for bit pattern media technology

III.1.1. Components of a hard disk drive

All hard disk drives (HDD) share a basic structure and contain the same main elements. In the following we will briefly describe the most important components of the hard disk drive and their interactions. A schematic of a magnetic recording system is shown in Fig.21.

One of the main components of an HDD is the disk, made form glass or Aluminum, which is coated on both sides by sputter deposition with a magnetic recording layer. This perpendicularly magnetized recording (PMR) layer is made up of nano-scale magnetic grains, and the signal-to-noise ratio (SNR) needed for high-density recording is determined by statistically averaging the contributions from a large number of such weakly interacting magnetic grains per bit. The granular structure limits the magnetic correlations and allows information to be written on a finer scale than is possible in a homogeneous magnetic film. As sketched in Fig.21a, the transitions generally follow the grain boundaries, and thus the storage density of the data is ultimately limited by the grain size. Scaling of magnetic media involves reducing the grain diameter and reducing the media's magnetic thickness $M_r t$ (where M_r is the remanent magnetization of the media and t is the media thickness). These films have evolved to the current media are based on CoPt or FePt alloys with so-called segregants, materials like B, Cr or oxides such as SiO_2 or TiO_2 that segregate at the grain boundaries, and help defining and controlling the exchange coupling between adjacent grains. Alloy developments, along with considerable improvements in underlayers, allowed the grain size and media thickness to scale appropriately to grain diameters on the order of 6 nm (Fig.21d). However, as already described in the general introduction, media scaling is limited by thermal instabilities when the grain volume V decreases to the point where the magnetic energy per particle $K_U V$ (where K_U is the magnetic anisotropy energy density) becomes comparable with thermal energies. The reversal of the magnetization of individual media grains due to thermal activation and the resulting loss of data is called the superparamagnetic effect. The minimum energy needed to maintain stability for 10 years is $K_U V = 60\ k_B T$, where k_B is the Boltzmann constant and T is absolute temperature. Reductions in V can be compensated by increasing K_U. However, increases in K_U are limited by available write fields needed to overcome the media's coercive field that is proportional to K_U/M_S. The combination of readability requirements, write-field limitations, and thermal activation of small particles is often referred to as the trilemma of magnetic recording.

In HDD products from 2014, the magnetic data are written in the medium in concentric tracks of about 80 nm width. Along these tracks, a succession of approximately 15nm long zones, having either a magnetization pointing up or down relative to disk plan, define the magnetic bits (Fig.21c). At these dimensions approximately $800 \cdot 10^9$ bits per square inch or 00 Gbit/in^2 can be written on the magnetic media surface. Note that each bit is not square but rectangular with a bit aspect ratio (BAR = width/length) of 6. The recording layer is generally covered with a 3-4 nm thick carbon-based overcoat layer that protects the magnetic grain from oxidation and mechanical damage, and a 1 nm thick lubrication layer made from long organic molecules that allows the write/read head to fly stably across the disk

surface (Fig.21). In a current HDD, typically between one to five disks are mounted on a rotating spindle that turns all the disks in unison. The spindle motor is mounted right below the spindle and spins the disks at a constant rotational speed ranging from 5000 to 15000 rotations per minute.

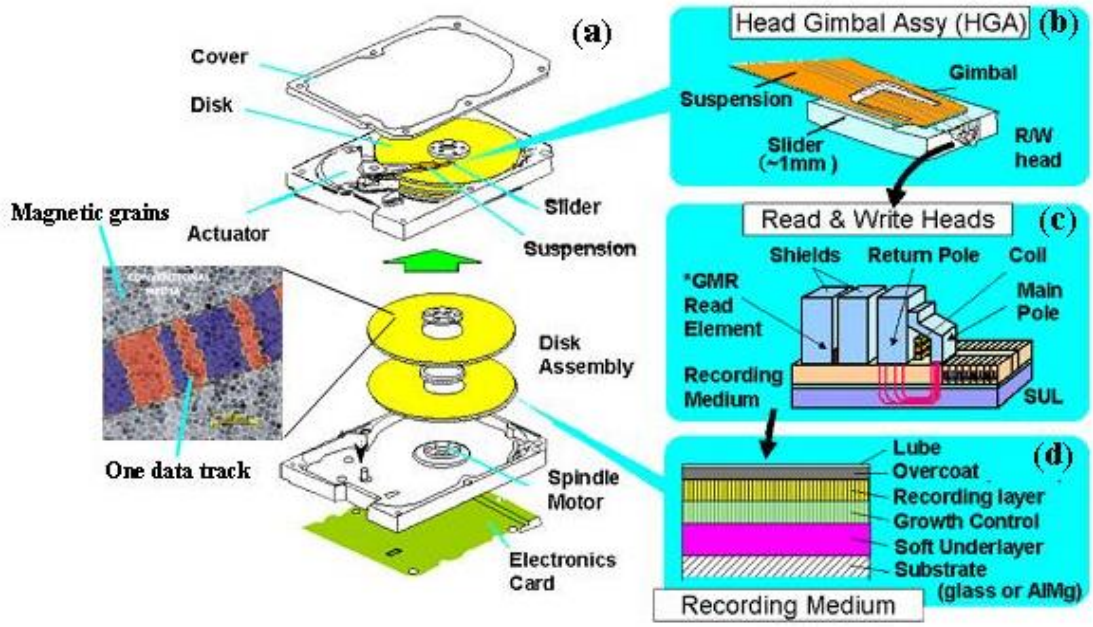

Fig. 21. The components of a hard disk drive. The basic design involves a rotating disk plus a rotary actuator that provides the access mechanism for the read/write heads (a). The heads are fabricated onto a ceramic slider that glides just a few nanometers above the surface of the spinning disk (b). A perpendicular recording configuration is illustrated (c) and recording medium constituents (d) are detailed [1].

The read/write head is the device that reads and writes data in the medium while the disk is rotating. This head contains various functional elements. The write element consists of a high-permeability magnetic pole with a few turns of a conducting coil wound around it. When an electrical current flows through the coil, magnetic flux flows through the writing pole, emanates from the pole and penetrates the magnetic medium (Fig. 21c), causing the bits to be magnetized up or down. In recent HDDs using media with a perpendicular orientation of the magnetization, a CoFe-based so-called “soft underlayer” (SUL) is introduced between the disk substrate and the magnetic medium (Fig. 21c and 1d). This SUL conducts the flux from the writing pole of the head and the medium to the return pole and helps increasing and localizing the effective write field of the recording head. Binary data are encoded via the direction (up or down) of the bit magnetization, in coincidence with a clock, which is synchronized with the disk. The second magnetic element of the recording head, the so-called read head or sensor, is used to sense the magnetic flux emanating from the recorded bits in the magnetized medium during the read back process. The read element is protected from any spurious magnetic fields by two large soft-magnetic shields (Fig.21c). Then, sophisticated signal processing electronics are used to convert the waveforms of the signal measured by the read head back into digital data.

Since the magnetic field coming from the bits decreases rapidly with distance from the magnetic medium, the space between the head and medium must be reduced as much as possible. The separation between the recording head and the media surface is less than 5 nm. When in motion this spacing is maintained by an aerodynamic air-bearing surface patterned lithographically onto the bottom of the slider carrying the magnetic head elements (Fig. 21b), and even though the head-disk separation is less than the typical mean free path of an air molecule, the head is said to fly or glide over the disk (As a scale comparison, with the same spacing constraint, a 70 meter long Boeing 747 Jumbo Jet would have to fly 1.5 mm from the ground). If the head hits the disk's surface or any defects like dust at the disk surface, the aerodynamic stability of the head-disk interface can be disturbed and the head can crash into the disk surface and damage it, which may in turn result in data loss and an inoperable device. This necessitates the hard drive assembly to be done in a clean room in which the concentration of dust in the air is strongly reduced. Many HDDs have multiple disks and heads, but typically all heads are attached to a common head actuator so that they all move in unison. However, only one of the heads is active at a time, i.e. reading or writing data. The actuator controls the movement of the head arm, also called head gimbal assembly. The guidance system that keeps the head on a track of data is called a servo. Outside of the head disk assembly is the electronic card that controls the movements of the internal parts and controls the movement of data into and out of the drive (Fig.21).

III.1.2. Introduction to Bit Pattern Media (BPM) recording

When I arrived in january 2007 at Hitachi GST San Jose research center, the various solutions to recording trilemma were heavily debated (see Fig. 22). On the one hand, the approach called patterned media proposes to lithographically define magnetic islands, each one corresponding to one bit, whose volume can be increased as compared with the current grain size that rules the thermal stability. Signal to noise ratio would then be maintained through reduction in grain size distribution and position jitter. On the other hand, the approach called heat-assisted recording or thermally assisted recording (HAMR) consists in increasing the magnetic anisotropy of the media and overcome the resulting limitation in writeabilty by using some sort of assist mechanism to (temporarily) lower the required switching field of the media during the writing process. Today, it seems that, PMR recording will last until 1.5 Tb/in^2. Then HAMR will step in with 10 Tb/in^2 target or, in parallel, pattern media technology would be merged with TAR to further improve areal density. As of 2007, bit pattern media was still supposed to be launched before HAMR and my work has been mostly devoted to understand and develop the magnetic features of bit pattern media. Interestingly most of bit pattern media magnetic challenges are chaired by MRAM technologies, especially thermal stability and switching field distributions problems that I will describe in details later here.

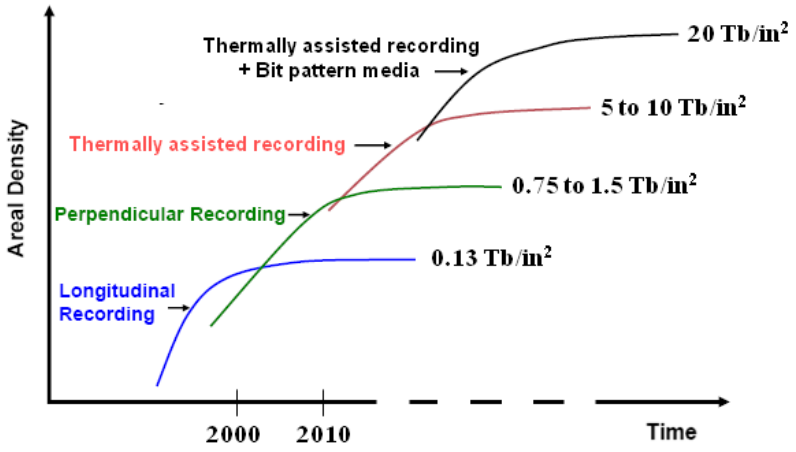

Fig. 22 One possible roadmap of the areal density of Hard disk drive products versus year. Thermal assisted recording (HAMR) and then Patterned media (BPM) must be introduced to solve the fundamental trilemma that forces trade-offs between 'writability', signal-to-noise, and thermal stability.

Bit patterned media (BPM) technology is expected to address the increasingly difficult challenges of reducing grain size in continuous media, by using lithographically patterned media where each magnetic island (or dot) corresponds to a single bit (Fig. 23 and 24). As an example, 1 Tb/in^2 recording in conventional PMR media would correspond to about 30 grains with a diameter of about 4 nm. In the case of a patterned recording medium, assuming a 50% lithography duty cycle magnetic dots or entities of 12.5 nm diameter would be required for storing the same amount of information. For the same thickness and anisotropy, the thermal stability, defined as K_uV, of a 12.5 nm diameter dot is up to 9 times higher than the stability of each 4 nm diameter grain. This offers a strong advantage to patterned media recording in terms of thermal stability as compared with current granular media. Besides, in order to increase areal density, track width has to be narrowed so that the read head and write head elements will have to be shrunk drastically as well to avoid writing or sensing more than one track at a time. This constitutes a real nanofabrication challenge, and faces also some limitations due to the according reduction in head-media spacing. The edge-noise errors and adjacent track over-write can be reduced by physically defining the track locations on the disk and thus no longer relying solely on the mechanical positioning capability of the HDD head. In bit pattern media tracks widths and locations are lithographically defined. Therefore the write and read elements can be made wider than the patterned track. The requirements on head tolerances may be eased, thus improving manufacturing yield.

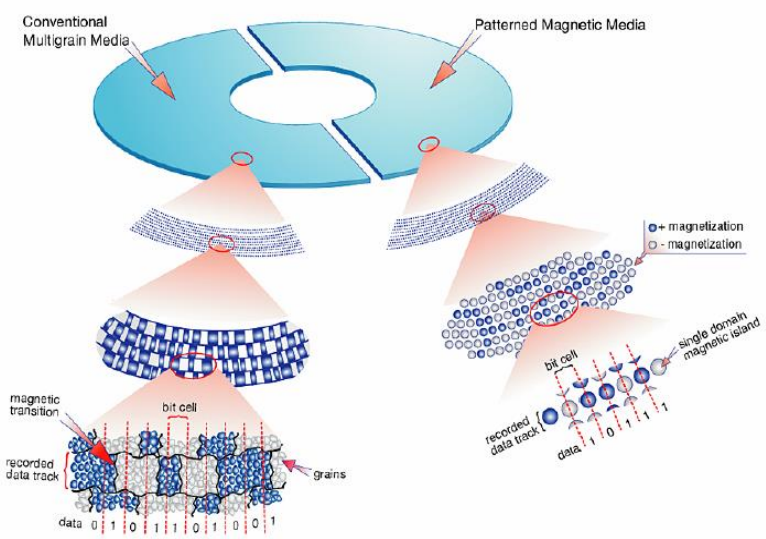

Fig. 23. Sketches and main features of current of continuous granular media and bit patterned media.

One of the most difficult challenges is to define a method of forming 10 to 16 nm diameter islands with extremely tight tolerances on the width, length, and positional fluctuation of dots. To achieve 1 Tb/in^2, one has to develop a lithography process to create billions of individual identical nano-islands that must be equally spaced within the circular symmetry of the rotating disk, while meeting an economically acceptable cost - the cost of manufacturing a current PMR disk (i.e. disk substrate and medium) is of the order of a few US dollars. Furthermore, according to the International Technology Roadmap for Semiconductors (ITRS), a DRAM gate length of 15 nm would not be reached until about 2020. Nevertheless, although these dimensional requirements for patterned media may seem daunting when compared with current state of the art silicon lithography, there are several important differences between the two. Patterned media is likely a one step mask process, while the fabrication of memory cells and logic gates requires many lithographic steps with precise mask alignments. Moreover the pattern does not even need to be well centered on the disk, as the disk will not be centered to better than approximately 10μm on the drive spindle.

There are many ways to obtain isolated magnetic nano-objects. For bit patterned media two classes of pattern transfer processes can be distinguished according to where in the process flow the lithography step occurrs. For the pre-patterning process, SUL and seed layers are first deposited on the substrate and patterned to create a surface of pillars and trenches, or with holes, over which the magnetic medium is sputter deposited (Fig.24a). In that case, the final magnetic bits stand either on the dots (Fig.24a) or in the holes [172,173]. On the other hand, in the processes referred to as post-patterning, SUL, seed layer and magnetic film are first deposited; then subtractive lithography steps are applied to create an array of magnetic dots (Fig.24b). The relative advantages and disadvantages of these two approaches are still under debate in view of their integration into real HDD recording. In the case of the pre-patterning processes, the main problem arises from the magnetic noise created by the magnetic materials deposited on both sidewall and trenches (Fig.24a). In the case of the post-pattern process, the magnetic material subtraction step may potentially damage the magnetic

layer in the bits. Although I worked on both methods, in the following, I will mostly focus on pre-pattern methods. In part III.1.5, I will described in more details three pre-patterning methods and show their influence on bit pattern media magnetic features.

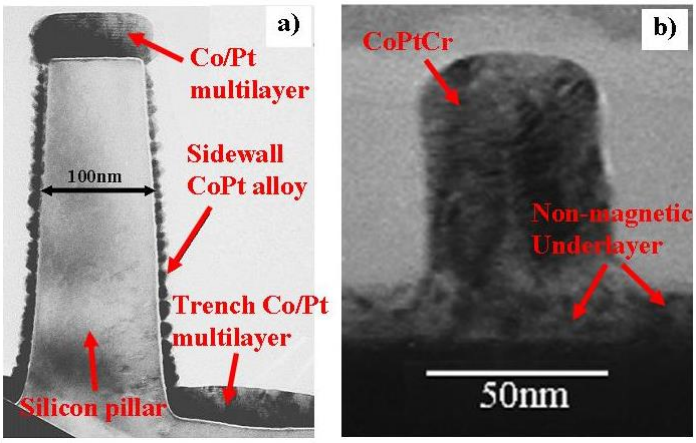

Fig. 24. a) Cross-sectional TEM view of a 200 nm height pre-patterned dot prepared by e-beam lithography followed by silicon RIE and covered by Co/Pt multilayer.[172] b) Cross-sectional TEM image of CoCrPt bit post-patterned media obtained by etching from a CoPtCr continuous film [173].

Finally, in addition to patterning issues, BPM technology needs to cope with many novel challenges not only in terms of patterning processes but also in terms of the recording physics. Detailed theoretical analyses have been performed in the last five years concerning the geometrical and magnetic tolerances of BPM at densities up to about 10 Tb/in^2 [174]. Head/media design depends on many parameters bit aspect ratio value, head size, write/read synchronization, field gradient, switching-field distribution and thermal stability for fixed values of the fabrication tolerances. In next two parts, I will only discuss the design and improvement the magnetic media design.

III.1.3. BPM magnetic media design and issues

As described in Ref. [175], the important magnetic features of the future bit pattern medium are : (1) the medium has a well defined uniaxial anisotropy axis, whose orientation is constant from one dot to another and perpendicular to the disk, (2) the saturation magnetization should be tuned to optimize write and readback processes; (3) the discrete island must always maintain a single domain remanent state, (4) the coercivity and hence anisotropy need to match the available write field while conserving a good thermal stability, (5) the switching field distribution (SFD) must be sufficiently narrow so that the write head field addresses only the island intended to be written.

Because of all their advantageous and tunable magnetic features detailed in Part I and II, I mostly work with Co/Pd, Co/Pt and Co/Ni multilayers as media for BPM. Typical Co/Pd BPM array are shown in Figs. 25(c) –25(e). Figure 25(c) is a [Co(2.8 Å) /Pd(9 Å)]*8 ML structure deposited onto prepatterned Si substrates with a 35 nm pitch (corresponding to 530 Gb/in^2). The bright field transmission electron microscopy (TEM) image shows trapezoidal-

shaped prepatterned Si pillars with the magnetic ML films deposited on top of the islands and in the trenches between the pillars [176]. Note that all TEM shown in this part have been performed by H. Yang, L. Vinh, X. Xu and D. Yaney at Hitachi GST. For well-defined multilayers the prepatterned pillars need to have flat tops, sharp corners, and steep sidewalls. Energy filtered TEM (EFTEM) images for a thicker ML structure are shown in Figs. 25(d) and 25(e) and demonstrate well-defined layering on top of the pillars. All ML structures presented in this part were deposited using a confocal sputter up geometry with the targets tilted and arranged in a circle around a center target (Pd) as illustrated in Fig. 25(b). We used a Ta/Pd seed layer to provide an outof-plane FCC [111] preferred grain crystal orientation with an x-ray rocking curve full width at half maximum of 8°.

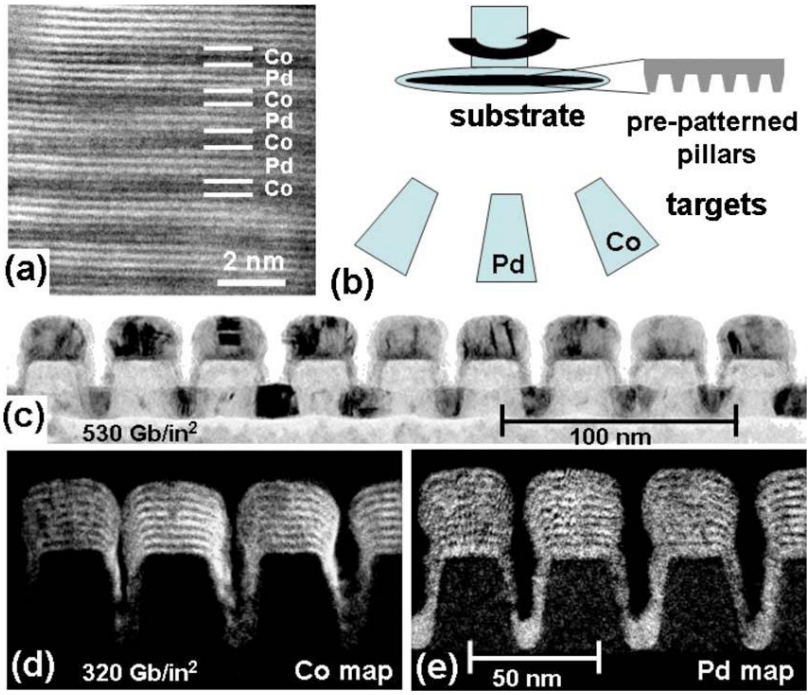

FIG. 25. BPM fabricated by ML deposition onto prepatterned Si substrates: (a) Aberration corrected, HAADF STEM image of a Co(4 Å) /Pd(8 Å) ML. (b) Illustration of the confocal sputter up geometry used for BPM fabrication. (c) Bright field TEM cross-sectional image of a row of islands with 35 nm pitch (530 Gb/ in^2) and a Ta(15 Å) /Pd(30 Å) / [Co(2.8 Å) /Pd(9 Å)]8 /Pd(11 Å) ML. (d) and (e) are cross-sectional EFTEM elemental maps of a row of islands with 45 nm pitch (320 Gb/ in^2). For the films in (d) and (e) the ML period was increased to [Co(17 Å) /Pd(17 Å)]*8 in order to spatially resolve the layering.

In Fig. 25(a) we present an aberration corrected, high angle annular dark field (HAADF) scanning transmission electron microscopy (STEM) image of a Co (4 Å) /Pd(8 Å) ML structure. These images show that the Co layers are two and the Pd layers three to four atomic rows thick (in agreement with the deposition parameters) with an interface roughness of one monolayer or below. The substrate, which rotates during deposition at 3 Hz, is at the focal point of the targets. With the Co target being tilted we obtain relatively more Co deposition onto the sidewalls than in the trenches, while for the center Pd target more material is deposited in the trenches and less on the sidewalls (Figs. 25(d) and 25(e)). After depositing the Pd cap layer we take the samples out of the vacuum process chamber, which leads to

oxidation of the Co-rich sidewalls, thus helping to magnetically decouple the ML islands from the Pd-rich trench material.

As shown in introduction (part I), Co/Pd, Co/Pt and Co/Ni multilayers are model system since they allow to tune high magnetic anisotropy nicely oriented perpendicularly to interfaces, as well as magnetization at saturation (Ms). Anisotropy field Hk and ML-averaged Ms versus individual Co layer thickness are summarized in Fig. 6(a) for [Co(t)/Pd(9)]*8 ML structures. We find the highest out-of-plane anisotropy (H_K=27 kOe, $H_{Keff} = H_K - 4\pi M_S$=21 kOe) for a Co thickness of 2.5–3 Å and a Pd thickness of 8–10 Å as expected from the discussion in chapter I about interface anisotropy. The maximum is obtained for a Co thickness higher than one atomic layer because of the roughness inherent to sputtering growth. Ms=500 emu/cm^3 (kA/m) at this Co thickness. As emphasized earlier, stability is the main advantage of bit patterned media compared with current continuous media technology. Considering [Co(2.8)/Pd(9)]*8 ML dots with $K_u = 5.10^6$ J/m^3 and a bit thickness of 10nm, and assuming that each bit behaves as a macro-spin, the thermal stability of each dot at 1 Tb/in^2 (defined earlier as K_u.V) would be much higher than 100 times the thermal energy at 350 K.

Depositing such high anisotropy MLs with Co(2.8 Å) on pre-patterned substrates we achieve Hc= 11 to 12 kOe, while for a continuous film we obtain Hc =500 Oe. This is shown in Fig.26(b) as measured by microfocused polar magneto optic Kerr effect (PMOKE) [177,178]. Most of the magnetic measurements presented here have been obtained with 633 nm wavelength laser and a focal spot size of 20 μm which allow to measure various areal density patterns on a single sample. The full film reversal is governed by nucleation and domain wall motion, while the isolated ML islands on the pillars reverse independently [177,179]. Nevertheless the reversal field for small islands is significantly less than the effective anisotropy field H_{Keff} =21 kOe so that incoherent magnetization must also occur within the dots. Upper value for magnetic exchange length is around 15 nm here so that uniform reversal cannot be expected for island width larger than 15nm, i.e. 1 Tb/in^2 BPM. Moreover demagnetization field, thermal activation and imperfections in the MLs all play to force non-uniform reversal and lower Hc [177,180-183]. In Fig. 26(c) we present the island coercivity Hc versus pattern period. We observe a slight, nearly linear increase in the coercivity as we move to higher areal densities. This is expected for incoherent reversal in a well behaving BPM system with little or no edge damage [177,181]. Besides, the loop from the patterned array in Fig.26(b) shows no trench reversal at low fields indicating that the amount of magnetic trench material is small (Fig. 26(d)). Full magnetization is preserved at remanence and the present Co/Pd BPM complies with the rule that each island must always maintain a single domain remanent state. Finally, it is to know that Ms of 500 emu/cm^3 has been calculated as a good magnetization for achieving 1Tb/in2 recording model, when incorporating all write and read requirements in recording models [174].

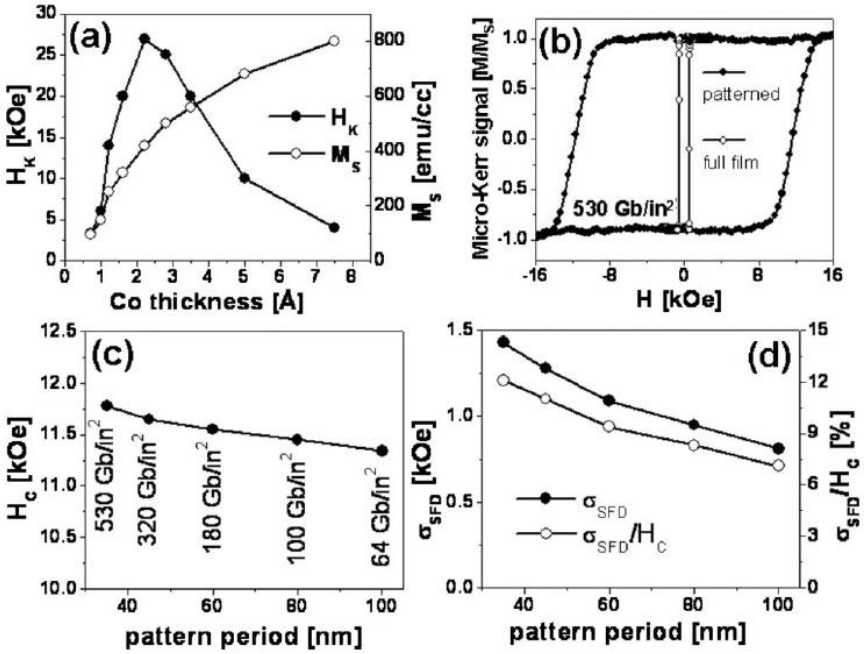

FIG. 26. BPM fabricated by ML deposition onto prepatterned substrates: (a) Anisotropy field HK and ML-averaged saturation magnetization MS vs individual Co layer thickness for [Co(t)/Pd(9 Å)]*8 MLs. (b) Microspot PMOKE hysteresis loop of the full film ML and from an array of islands at 530 Gb/ in2 areal density. (c) Coercivity (HC) vs pattern period for a [Co(2.8 Å) /Pd(9 Å)]*8 ML film. (d) Absolute SFD (σSFD) and normalized SFD (σSFD/HC) vs pattern period for the same ML film.

In Fig. 26(b), bit reversals occur over 3 kOe. In other word, there is about 3 kOe between the first and the last bit to reverse. This feature is called switching field distribution (SFD) and is a key issue for BPM implementation to a manufacturing level. The absolute SFD (σ_{SFD}) is quantified as the standard deviation σ of the Gaussian fitted to the derivative of the island reversal curve [176] or with an asymmetric error function, which is analytically defined as an inverse function $H(M) = H_C + \sqrt{2}\,\sigma\,\mathrm{erf}^{-1}(\,(M)/(1+\alpha\,M)\,)$ with H_C being the coercive field, σ the width of the SFD and α the asymmetry parameter [178]. The so-called relative SFD corresponds to σ_{SFD}/Hc. During the recording process such a distribution of switching field can result in non-writing errors in the case of higher reversal field dots or over-written neighboring bits with a lower reversal field. There are two main origins of switching field distribution (SFD). The first one, so-called dipolar field induced SFD, is inherent to the bit pattern medium and defines the minimum SFD that can be achieved. Indeed, in an array of single magnetic dots, the magnetic field generated by each individual dot affects the reversal of all the other dots. As a consequence, a magnetic bit with all its neighbors pointing in the down direction would have a different switching field than another bit with all his neighbors pointing in the up direction. In addition to the dipolar field induced SFD, the difficulties to control all the intrinsic and extrinsic parameters that influence the magnetization reversal mechanism lead to various origins of SFD as described in Fig.27. Intrinsic usually stands for the properties that are not induced by the patterning process. That includes anisotropy distribution or crystal boundaries which would be present in the full film (Fig.27). The extrinsic parameters, i.e. patterning induced, can be edge defects or interface mixing and strongly depend on the patterning method (pre- or post patterning).

Both absolute and relative SFDs increase with smaller pattern period (Fig. 26(d)). It is due to an increase of both the dipolar term and the intrinsic/extrinsic term. The dipolar contribution to the SFD can be quantified (and dissociated from the other origins) by measuring a series of minor reversal curves using the recently developed ΔH(M, ΔM)-method, in which the reversal of magnetic grains or in this case dots is analyzed while varying the magnetostatic environment [178,189,190]. This analysis performed on regular [Co(t)/Pd(9)]*8 ML shows that the dipolar broadening contributes only 22%, resp. 31%, to the observed SFD for a 100nm, resp. 45 nm period array. In parallel, to now understand the increase of the intrinsic/extrinsic SFD term with density increase, let's consider low anisotropy sites (instrinsic defects) randomly distributed over a surface including magnetic dots, and let's consider that nucleation field equals reversal field value. If one can fit four large dots in the area, there is a strong probability that at least one low anisotropy site belongs to each dots such that all dots switch under the same magnetic field and SFD is zero. As the dot diameter decreases, the probability of having one low anisotropy site per dot decreases, some dots starts switching at higher magnetic field, SFD becomes non null and tend to increase [177,182]. Stays one question to better understand and so improve BPM media to avoid SFD : what is the main cause of low anisotropy site ? As shown in Fig. 27 (right), many intrinsic and extrinsic reasons can be found. On Fig. 27(left), one can see that for very thick ML large grain boundary and c-axis distribution (due to Co/Pd layering tilt) appear. Using a combination of magnetic X-ray holography at BESSY synchrotron in Berlin (Germany) and high-resolution transmission electron microscopy at Hitachi GST we manage to reveal systematic correlations between the magnetic switching field and the internal nanoscale structure of individual dots in bit patterned media fabricated by Co/Pd-multilayer deposition onto pre-patterned substrates. We find that misaligned grains at the island periphery are a common feature independent of the island switching field, while irregular island shapes and misaligned grains specifically extending into the center of an island are systematically correlated with a reduced dot reversal field.

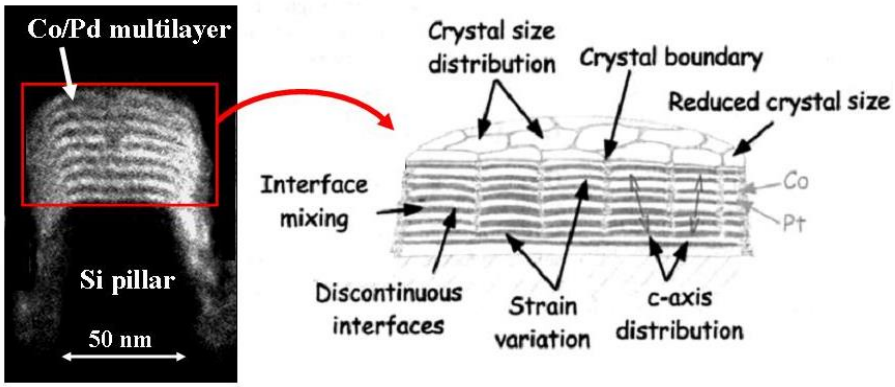

Fig. 27. Transmission electron microscopy image (left) and sketch (right) of a [Co(17 Å) /Pd(17 Å)]*8 multilayer-based deposited on top of a pre-patterned silicon substrate with 50 nm diameter dots. The ML thickness has been chosen large to highlight the grain-induced defects. Some of the possible switching field distribution origins are pointed out on the sketch.

The sample was prepared by sputter depositing Ta(15)/Pd(30)/[Co(5.5)/Pd(9)]24/Pd(11) Å) onto a pre-patterned, 150 nm thick Si_3N_4 membrane window (Fig. 8(a)). We increased the total number of repeats, compared with regular media (only 8 repeats) to fit the experimental pre-conditions in terms of available saturation field and necessary imaging contrast. The patterned areas are 6*6 μm^2 in size and consist of a periodic array of cuboidal pillars of size 80*80*40 nm^3 produced by e-beam lithography using polymethyl methacrylate resist and a CrMo (20 nm) alloy etch mask. The membrane window was generated by a potassium hydroxide silicon wet etch to remove the bulk of the silicon from underneath the membrane. The dot period is 120 nm, corresponding to an island area filling factor of 44% and a bit density of 41 Gbit/in^2. On the opposite side of the membrane, an FTH optical mask is produced into a 1 μm thick gold layer via focused ion beam (FIB) lithography. The mask contains an object aperture with a diameter of 1.5μm defining the field of view (FOV) and a 50 nm wide reference hole needed for the image reconstruction. More details about magnetic FTH imaging can be found in Ref. [191,192]. In addition, a small marker hole was drilled next to the FOV to attribute identical dots in the FTH and TEM images. The FTH experiments were performed at the undulator beamline UE52-SGM of the BESSY II synchrotron source. The energy of the circularly polarized photons was tuned to the Co L3 edge (778.1 eV) giving rise to a pronounced XMCD contrast in the images. In the purely magnetic contrast images (Fig.8(b) and 8(c)), the dots which have not switched appear on the uniform background of the already reversed continuous film in the trenches. Since the FTH method allows imaging the sample in an applied field, we were able to compare the island magnetization in applied field (up to 6kOe) and at remanence (not shown here). As can be expected, we never observed a re-reversal of an island when turning off the external field.

In total N = 112 dots are visible in the FTH FOV. They are labeled in a (12×12) elements matrix starting with 0 in the right bottom corner and ending with 143 in the left top corner (Fig. 1(e)). By counting the number of reversed islands (n) at a certain applied field (H) we gain a complete hysteresis loop for the dot ensemble in our FOV (Fig. 8(d)). The normalized magnetization (M) of the dot assembly is calculated as $2n/N - 1$. Altogether, we recorded 60 images at 22 different field values. Following [178], the results are fitted with an asymmetric error function. We obtain H_C = (4.02 ± 0.04) kOe, σ = (1.25 ± 0.03) kOe and α = 0.30 ± 0.03.

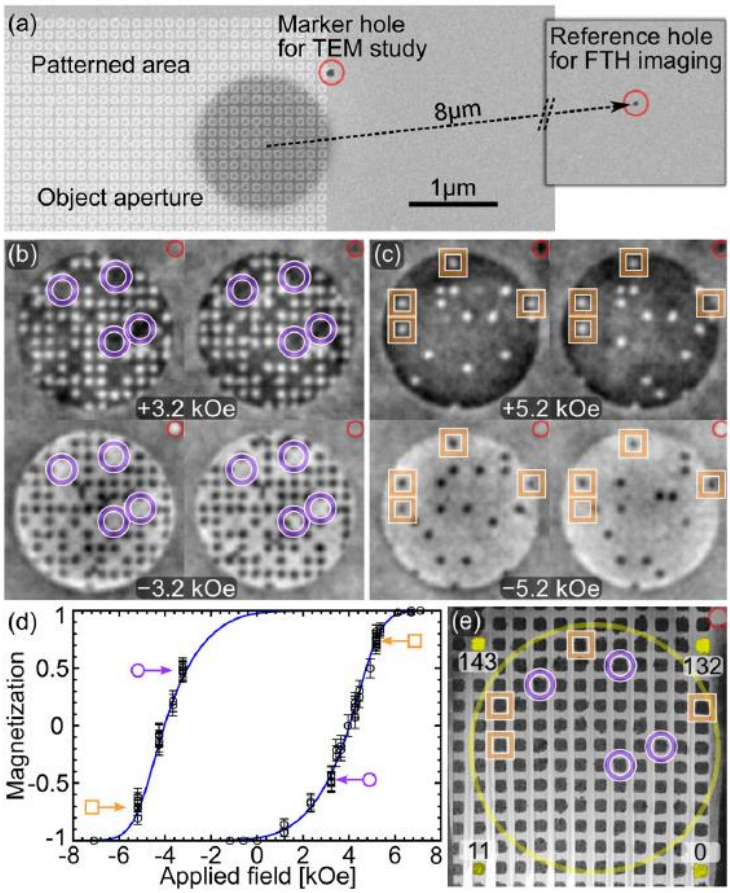

FIG. 28. (color online) (a) Scanning electron microscope image of the integrated sample design. (b, c) Examples of FTH magnetization state images at different applied fields. (d) Hysteresis loop for the dot ensemble in the FOV compiled out of 60 images. On the rising branch of the loop the islands switch from white to black, and vice versa. Images (b) are taken when the reversal is initiated and images (c) just before it is completed. The four easy (violet circles) and the four hard (orange squares) switchers that are selected for further TEM analysis are marked in the FTH images and in the TEM overview image (e) with the help of the marker hole (red). In (e) the yellow circle marks the holography FOV and the numbers illustrate the island labeling.

To check the switching repeatability, we recorded ten independent configurations at field values of H^{easy} = ±3.2 kOe and H^{hard} = ±5.2 kOe (Fig. 28(b) and 28(c)) (after each time saturating the sample), where 25% and 87% of the dots have switched, respectively. In Fig. 29(a) detailed statistics for every island are presented showing how frequent each island reversed its magnetization. The statistics reveal three different groups of islands : (i) islands that always did not switch, (ii) islands that occasionally switched, and (iii) islands that always switched. The apparent coexistence of deterministic and non-deterministic processes is explained in a statistical broadening of the dot's individual switching field from the intrinsic value due to thermal activation and due to the local demagnetizing field from the dot's environment, which varies with the actual magnetic configuration. When applying a certain external field, the field is either much lower than the individual switching field (island group (i)), much higher than the switching field (group (iii)) or lies within the statistical broadening of the switching field resulting in the random behavior of group (ii). We have selected four islands belonging to group (iii) at a field value, where the switching is initiated (H^{easy}) and four islands belonging to group (i) at the end of the reversal process (H^{hard}) for a detailed

TEM analysis in order to reveal the micro-structural peculiarities of the dots. We call those islands easy and hard switcher, respectively. The positions of the selected islands in the dot array are also marked in the FTH images and the TEM overview image (Fig. 28(b,c,e)).

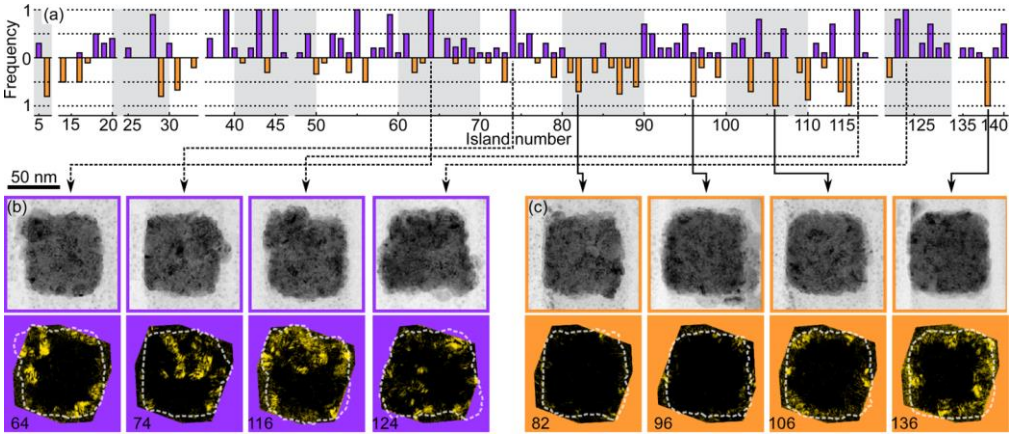

FIG. 29. (color online) (a) Detailed statistics of how often each island is among the first (violet, up) or last (orange, down) islands that switch. For the TEM analysis (b, c) only islands with high probability for being either easy (b) or hard switcher (c) were selected. In the top row of (b) and (c) we show bright-field TEM images and in the bottom row corresponding inverse FFTs generated using only lattice spacing information ranging from 0.185 to 0.200 nm.

A TEM sample was prepared from the array of nanodots (Fig. 28(e)) using a FIB milling technique, in which the space between the islands was initially filled by Si-oxide. The sample was thinned to electron transparency by milling from the substrate side of the islands, leaving only islands and filler material in the final thin section. High-resolution TEM images were acquired from the four selected easy (Fig. 29(b)) and four selected hard switching islands (Fig.29(c)). Only information related to the (200) lattice spacing was retained. Fig. 29(b) and 29(c) show regions (marked in yellow) with in-plane (200) lattice spacing, i.e. grains that are significantly misaligned from the fcc [111] out-of-plane crystal orientation. In agreement with Ref. [183], we identified (200) grains in every easy switcher. Indeed, as explained in chapter I, perpendicular magnetic anisotropy in Co/Pd does not only originate from Co/Pd interface. The crystalline structure of Co plays also a significant role. Whereas (111) textured Co provides perpendicular anisotropy, (200) textured Co lower perpendicular anisotropy. As a consequence a (200) orientated Co/Pt grain acts as a nucleation center for a mainly (111) orientated Co/Pt dot. (200) grains are large enough to reduce the average anisotropy of an island significantly. As shown in micromagnetic simulation in Fig. 30, introducing a 10 nm diameter zone 4.10^5 J/m^3 in a 50 nm diameter dot having 8.10^5 J/m^3 decreases reversal field by 4 kOe. As the defect diameter increases the overall switching field decreases even more (Fig. 30(b)).

In micromagnetic simulations from Ref. [182], the location of the defect seems not to matter (Fig. 30(c)). However, we also found hard switcher dots containing (200) grains (islands no. 106 and 136 in Fig. 29(c)). But in contrast to easy switchers, these grains are always located at the edges of the island. Obviously, the peripheral grains do not always act as trigger grains. The lower impact of edge (200) grains and the discrepancy with micromagnetic

simulation in Fig. 30(c) may have various origins. The first one is partial oxidation of the lateral grain as the pre-patterned side walls. Secondly the simulation considers [Co(0.3)/Pd(0.9)]*8 so that the demagnetization field that tends to reverse the magnetization in the center of the dot is much higher in the experiments which may compensate the edge (200) grain influence. A last explanation can be that a low anisotropy shell always exists at the edges which may be due to imperfections in the layering, surface anisotropy or oxidation, so that edge (200) grains have a insignificant impact as compared to (200) grain in the center of the dots.

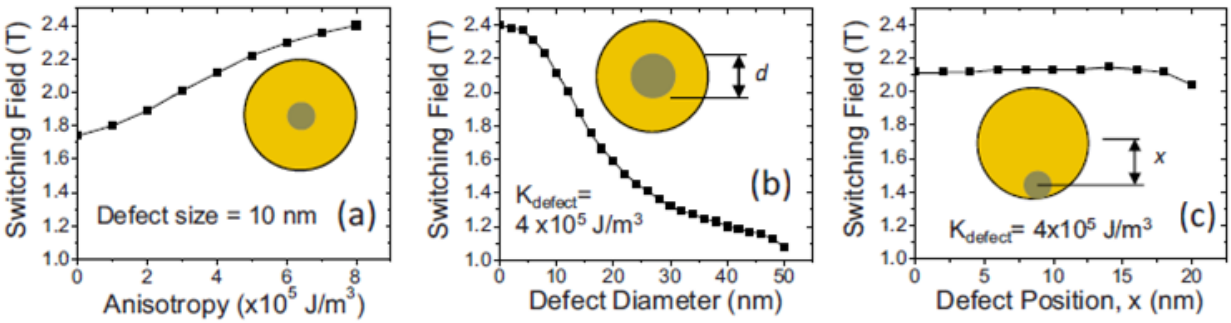

Fig. 30. Object-orientated micromagnetic framework (OOMMF) micromagnetic simulations of the switching field in a 50 nm structure that contains a defect with a reduced value of anisotropy as a function of the (a) defect anisotropy, (b) defect size, and (c) defect position [182].

We further confirmed the role of (200) grain as the main origin of SFD as compared with Co/Pd intermixing in using ion irradiation to tune switching field and SFD in $[Co(2.8Å)/Pd(9Å)]_8$-based BPM. Using carefull X-ray relectometry analysis and magnetometry, we found that light He^+ ion irradiation strongly decreases perpendicular magnetic anisotropy amplitude due to Co/Pd interface intermixing, while the granular structure, i.e. the crystalline anisotropy from (111) and (200) grain, remains unchanged. As a consequence the relative impact of misorientated grains on SFD is enhanced. Indeed in the BPM arrays, the interface anisotropy reduction leads to a decrease in Hc but also to a strong broadening of the relative switching field distribution. From these experiments, one has to conclude that the chemical interlayering (Co/Pd interface) provides the leading contribution to H_C, but only the second order term to the SFD, while the crystalline structure is the leading contribution to the SFD (misaligned grains) but second order to H_C and anisotropy.

Overall, Co/Pd ML as a magnetic media complies with most of the BPM magnetic features requirements defined in Ref. [174] in order to achieve 1 Tb/in^2. It has a well defined uniaxial anisotropy axis, whose orientation is constant from one dot to another and perpendicular to the substrate, the saturation magnetization can be tuned around 500 emu/cm^3 (kA/m). The coercivity can be tuned around 8 kOe while the anisotropy insure thermal stability over 100 k_BT at 350K. The magnetic recording trilemma is not an issue for this system. However, absolute (resp. relative) switching field distribution is higher than 1kOe for BPM with areal density higher than 300 Gb/in^2. This would be a show stopper on the way to implement BPM to an industrial level. I will show in the next part that exchange-spring

(ECC) media offers a solution to further improve thermal stability and writing features while strongly improve SDF below 500 Oe for 6kOe coercitive field.

Before going into exchange-spring, I would like to emphasis that I tried other types of media to avoid intrinsic growth defects like misorientated grains. The first idea was to use crystallines materials both for pre-pattern and post-pattern method. Especially I focused on Co_3Pt and Co/Ni systems. Co/Ni ML is too soft to maintain good thermal stability and coercive field around 8 kOe. Moreover we could have any proof of SFD improvement with improved crystallinity. Ta(5nm)/Ru(8)/Co3Pt(10)/(Ta(5) deposited flat surface Si substrate with post-deposition annealing treatment at 350°C allows to reach magnetocristalline anisotropy up to Ku = 1.48 .10^7 erg/cm^3 with Ms = 1050 emu/cm^3. Coercivity up around 10 kOe can be measured when the same stack is deposited onto 500 Gb/in^2 pre-pattern Si substrate. In Fig. 31, one can even see by atomic force microscopy (AFM) that the cristallinity is conserved on the dots, as the AFM image shows nice hexagonal island shape. However SFD is larger than 3 kOe (more than 30 %). This high value originates both from a large intrinsic SFD and a large dipolar coupling between the dots. Similar results have been obtained for post-patterning technique where the film quality has been previously checked by X-ray before patterning. In that case, edge defects due to patterning add to intrinsic SFD and dipolar SFD. Finally, at the opposite to crystalline systems, I have investigated TbCo amorphous alloys with post-patterning method. In this system amorphicity should provide excellent dot-to-dot magnetic homogeneity. No significant gain in intrinisic SFD has been observed yet that may be related to concentration variation from dot to dot when reach high areal density.

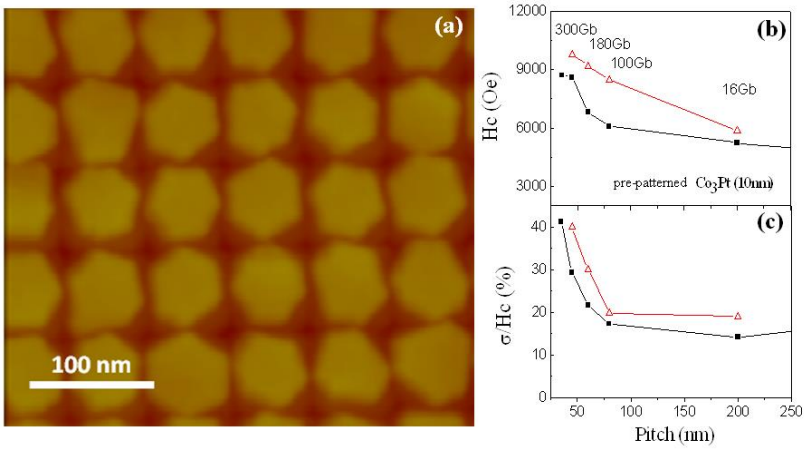

Fig. 31. AFM image (a), coercitivity (b) and relative SFD (c) of Ta(5nm)/Ru(8)/Co_3Pt(10)/(Ta(5) deposited on pre-pattern Si substrate. Co_3Pt alloy has been post-deposition annealed to 350°C in order to obtain good crystallization in a $L1_2$ phase with (0001) direction perpendicular to the pre-pattern substrate. (b) and (c) show data for two samples nominally identical. Differences in Hc must relates to crystallization quality.

III.1.4. Exchange-spring media to solve recording trilemma and SFD issues

While generally writeability and stability for conventional single material recording media are correlated through the magneto-crystalline anisotropy, it has been demonstrated in recent years that advanced multilayered media structures can be designed in such a way that an improved writeability to stability ratio can be achieved. Using such multilayered structures first allowed the extension of in PMR technology to beyond 800 Gbit/in^2, more than twice the areal density thought possible even just 5 years ago. In perpendicular recording the media technology used to achieve these areal densities is called exchange-coupled-continuous (ECC) media.

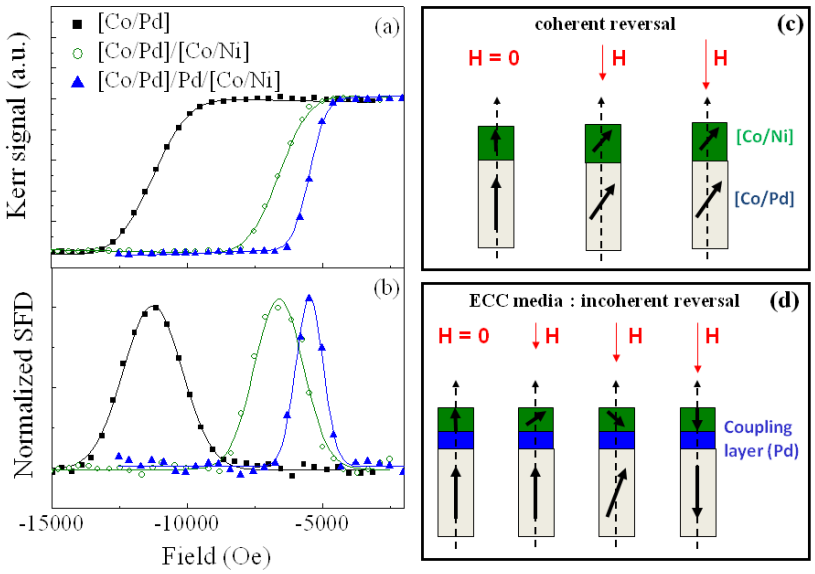

Fig. 32. PMOKE reversal curves (a) and their derivatives (b) for a 60 nm period island array. The lines in (a) and (b) are the corresponding field-integrated Gaussian and Gaussian fits used to extract H_C and σ_{SFD}. (c) and (d) are Scheme of reversal mechanism in strongly coupled [Co/Ni]/[Co/Pd] ML and slightly decoupled [Co/Ni]/Pd/[Co/Pd] ML respectively. The first one consists in a coherent reversal of both [Co/Ni] and [Co/Pd] moment at the same time whereas the second one starts with a rotation of [Co/Ni] magnetization that helps switching of [Co/Pd] magnetization at higher external field.

Within this new multilayer system, the usual granular magnetic media is coupled to an assist layer with a lower anisotropy that allows fundamental changes in the switching mechanism of the media magnetization. Indeed, in single granular media the magnetization switches via a so-called coherent reversal mechanism (also often referred to as Stoner-Wohlfarth switching), i.e., the magnetic moments inside one grain switch all at once and can be described by the response of a single spin, the so called macro-spin, to an external field. In contrast, in ECC media the reversal mechanism can best be described by a domain wall motion through the depth of the media stack: at first a domain wall, i.e., a continuous twist of the magnetization is forced into the depth of the assist layer, and is pinned at the interface between the assist layer and the granular media. At a certain field, the domain wall depins from the interface and propagates through the media layer, switching its magnetization in the process. For optimized composition of this bilayer system, the field at which the domain wall

propagates irreversibly into the media layer is lower than the switching field of the media layer by itself [184,185]. Therefore the addition of the assist layer allows reducing the required write field for a given media without affecting its thermal stability, or, conversely, for a given write field allows the use of higher K_U materials and a further reduction in grain size and resulting increase in areal density. I will demonstrate here that ECC media applied to BPM technology also help to drastically decrease SFD.

We used Ta/Pd/$[Co/Pd]_x$ /Pd(t) / [Co/Ni]y multilayers has a model system for ECC media adapted to BPM recording. From measurements on full film samples, we know that Ta/Pd/$[Co(2.8Å)/Pd(9Å)]_X$/Pd, with X ranging from 5 and 8, are hard MLs with a similar anisotropy field H_{keff} ~ 21 kOe and a similar magnetization density at saturation M_S = 500 emu/cm^3 (kA/m), whereas Ta/Pd/$[Co(1.5Å)/ Ni(7Å)]_Y$/Co(2.8Å)/Pd with Y ranging from 2 to 4 are soft MLs with $H_{k,eff}$ ~ 5 kOe and M_S = 700 emu/cm^3 (kA/m). In Fig. 32(a) we compare the PMOKE signal, and in Fig. 32(b), the curves derivative, measured on three different BPM samples. The first one, a Ta/Pd/$[Co(2.8Å)/Pd(9Å)]_8$/Pd ML acts as a reference sample. The two other samples are composed of Ta/Pd/$[Co(2.8Å)/Pd(9Å)]_5$ / Pd(t) / Co(1.3Å) / $[Co(1.5Å)/ Ni(7Å)]_3$ /Co(2.8Å)/ Pd, where the Pd(t) interlayer allows tuning the exchange coupling amplitude between the hard and soft MLs by varying its thickness t. The samples shown in Fig.32 have t = 0 Å and t = 10 Å. The areal density of these samples is 180 Gb/in^2, which corresponds to an island period of 60 nm. Note that the total thickness of magnetic materials is conserve from sample to sample. By adding [Co/Ni] to [Co/Pd] a large decrease of Hc is observed but no change in absolute SFD. It is coherent with a uniform reversal of the all stack at once since [Co/Ni] and [Co/Pd] are strongly coupled. The overall system has an average anisotropy field $Hk_{average} = 2(K_{[Co/Ni]}.t_{[Co/Ni]}+K_{[Co/Pd]}t_{[Co/Pd]}) / (Ms_{[Co/Ni]}.t_{[Co/Ni]}+Ms_{[Co/Pd]}t_{[Co/Pd]})$. One could also expect a gain in SFD if the SFD origin in Co/Ni and Co/Pd would be uncorrelated different; then $\sigma_{average}^2 = \sigma_{[Co/Ni]}^2 + \sigma_{[Co/Pd]}^2 + C.\ \sigma_{[Co/Ni]}.\ \sigma_{[Co/Ni]}$ where C is a SFD correlation factor. Unfortunately, here, there is no significant gain in SFD by adding soft [Co/Ni] ML to hard [Co/Pd] ML. On the other hand, adding a Pd interlayer in-between [Co/Ni] and [Co/Pd] further decreases Hc and more importantly decrease by half SFD as shown in Fig. 32 (b).

From the PMOKE curves, we obtain the coercive field H_C as the average reversal field of the island assembly and estimate the absolute SFD as the standard deviation σ_{SFD} of the reversal field distribution by fitting a Gaussian to the derivatives of the islands reversal curves (Fig. 32(b)). Corresponding values extended over a wider range of Pd interlayer thicknesses are summarized in Fig. 33(a) and 33(b). As expected from previous studies on continuous PMR media [186] and as calculated analytically [187], a non-monotonic evolution of H_C is observed as the interlayer thickness increases from 0 Å to 30 Å, i.e. as the exchange coupling between the hard and soft part diminishes. In absence of a Pd interlayer, the [Co/Ni] and [Co/Pd] moments are strongly coupled to each other and nearly coherent reversal occurs. As the Pd inter-layer thickness (t) increases we create a more decoupled structure and the soft moment can partially reverse under external field, thus inducing a torque onto the hard moment, which lowers the switching field value of the composite system (Fig. 32(d)). Weakening even more the interlayer coupling, by further increasing t,

enable the SL to reverse independently from the HL and the HL switching field increases back toward its intrinsic value. As a matter of fact, for Pd thicknesses higher than 20 Å, the PMOKE signal vs field contains two successive reversal steps corresponding to the separate reversal of the SL and HL magnetizations respectively. The typical behavior as shown in Fig. 32(a) for an island period of 60 nm was observed for a variety of densities down to 35 nm (i.e. 500 Gb/in^2). The H_C and SFD reduction obtained with the ECC structure is independent of areal density which is of primary important in view of implementing this technology at more than 1Tb/in^2. In addition we performed hard axis loop measurements on the corresponding full film structures in order to extract the anisotropy field, i.e. in first approximation the thermal stability, for various Pd interlayer thicknesses. Although the addition of $[Co/Ni]_3$ to $[Co/Pd]_5$ reduces its $H_{k,eff}$ from 21 kOe to 18 kOe mainly due to the change in M_S, varying the Pd interlayer thickness does not change the hard axis loop of the ECC structure further. Our results thus confirm that ECC media can be used to reduce the coercive field and the SFD of BPM while maintaining thermal stability.

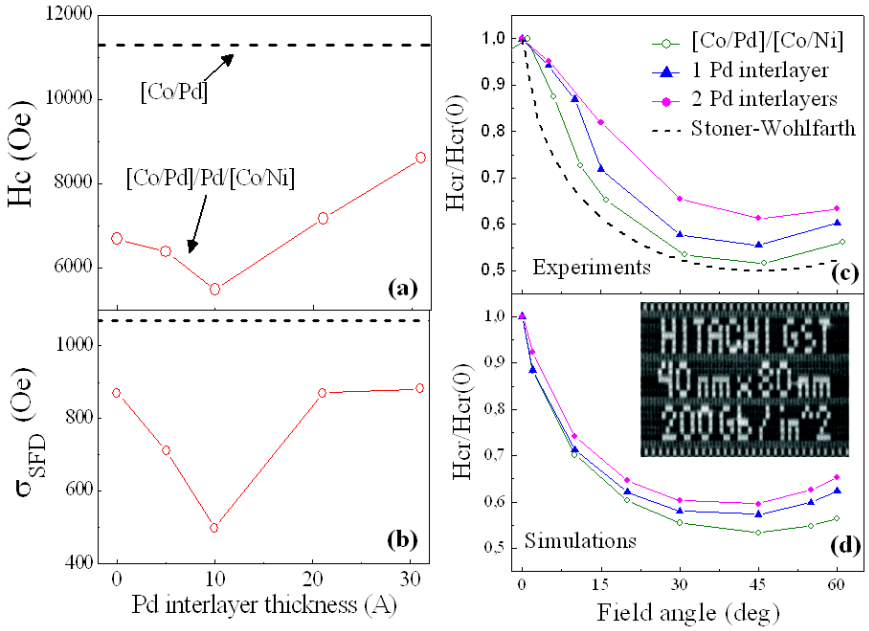

Fig. 33. Coercive field H_C (a) and SFD σ_{SFD} (b) extracted from PMOKE measurements performed on $[Co/Pd]_5/Pd(t)/[Co/Ni]_3Co$ as a function of Pd interlayer thickness t (a, b) for 180 Gb/in^2. The dashed lines in (a) and (b) indicate the value for a $[Co/Pd]_8$ reference sample. Measured (c) and simulated (d) relative remanent coercivity as a function of applied field angle for a 35 nm period (500 Gb/in^2) array composed of $[Co/Pd]_5/[Co/Ni]_3$, $[Co/Pd]_5/Pd(10Å)$ $/[Co/Ni]_3$, and $[Co/Pd]_3/Pd(10Å)/[Co/Pd]_2/Pd(10Å)/[Co/Ni]_3$. The dashed line in (c) is the Stoner-Wohlfarth curve. Inset in (d) shows magnetic read-back image showing patterns consisting of 2000 bits of $[Co/Pd]_6/Pd(5Å)$ $/[Co/Ni]_3$ written at 200 Gb/in^2 density. Black and white are up and down magnetized dots, i.e. 1 and 0 recorded data, respectively.

Let us now understand the origin of the gain in SFD for BPM ECC media. As calculated in [187,188], the magnitude of the coercivity reduction increases with an increasing difference between the hard layer anisotropy and the soft layer anisotropy, for a constant hard/soft exchange coupling. As a consequence, if we assume misorientated (200) grain in [Co/Pd] as the main cause of SFD, the dots with no (200) grain are characterized by a large

average [Co/Pd] anisotropy and ECC has strong impact whereas the dots with (200) grains have lower [Co/Pd] anisotropy and ECC is less efficient. This theoretical explanation can be directly observed in Fig. 32(b). Here, comparing the SFD of $[Co/Pd]_5/[Co/Ni]_3$ and $[Co/Pd]_5/Pd(10Å)[Co/Ni]_3$ samples one can see that H_C reduction for the hardest islands is about 1.8 kOe, while for the softest islands it is less than 500 Oe. This difference in ECC efficiency for hard and easy switchers makes ECC media a very powered tool to decrease SFD. Thanks to this large reduction of SFD as compared with regular single [Co/Pd] ML, M. Grobis could demonstrate with sub 10^{-4} two-dimensional Bit error rate recording at 200 Gb/ in^2 which was quite promising for future BPM technology (see inset in Fig. 33(d)). In order to reveal the enhancement of incoherency in the reversal process when adding Pd interlayers, we then investigated the angular dependence of the remanent coercivity. The relative remanent coercivity $H_{CR}/H_{CR}(0)$, where $H_{CR}(0)$ is the remanent coercivity at zero angle, measured for 35 nm island period is plotted as a function of the field angle in Fig. 33(c). Zero angle corresponds to a field applied perpendicular to the ML interfaces. The theoretical angular dependent coercivity of the different samples was simulated (see Fig. 33(d)) using a three-spin generalization of the macro-spin potential surface model developed by Bertram and Lengsfield [187]. We considered three coupled spins. Each $[Co/Pd]_3$, $[Co/Pd]_2$ and $[Co/Ni]_3$ ML corresponds to a single spin, characterized by its H_{k1} and M_S values. A variation of the exchange coupling constant in between the spins stands for the variation of Pd interlayer thickness. For instance, we consider $J = 1.5*10^{-11}$ J/m and $0.4*10^{-11}$ J/m for t_{Pd} = 0 Å and 10 Å respectively. In this simulation, the coercivity is determined by utilizing a second-order optimization procedure to locate the stable points on the potential energy surface as a function of the applied field. As presented in Fig. 33(d), the trends of the experimental data shown in Fig. 33(c) when adding Pd interlayers are reproduced by the calculation. In Fig. 33(c), the $H_{CR}/H_{CR}(0)$ variation of the $[Co/Pd]_5/[Co/Ni]_3$ sample is similar to the variation calculated for the Stoner-Wohlfarth type reversal [Stoner1948]. The relative remanent coercivity ratio has a minimum close to 0.5 when the field is applied at a 45º angle. The small discrepancy with the Stoner-Wohlfarth case may already result from a partial incoherency in the reversal process. As one Pd interlayers is inserted between $[Co/Pd]_5$ and $[Co/Ni]_3$, the minimum $H_{CR}/H_{CR}(0)$ value increases up to 0.56. To emphasize the gain obtained by tuning the vertical exchange coupling in ECC media, we fabricated a last sample, namely $[Co/Pd]_3/Pd(10Å)/[Co/Pd]_2/Pd(10Å)/[Co/Ni]_3$, where a second Pd interlayer was inserted inside the $[Co/Pd]_5$ HL. The second Pd interlayer allows further decreasing H_C as well as the SFD. With this last sample, 45° minimum in $H_{CR}/H_{CR}(0)$ rises up to 0.61. The same evolution has been obtained for the other densities and is well reproduced by the calculations (Fig.33(d)). Such gradual shallowing of the H_{CR} angular dependence has also been reported in PMR exchange-spring media and reveals a vertical incoherency in the reversal process [187]. The angular dependence of the switching field is nevertheless far from the Kondorsky-like behavior [193], since the magnetic layers in our ECC system are too thin and too hard to allow the nucleation of a vertical domain wall within the depth of the multilayer.

Finally, using ECC media which allows to maintain high thermal stability and to induce a large reduction of Hc and SFD as compared with regular single [Co/Pd] ML, M. Grobis could demonstrate with sub 10^{-4} two-dimensional Bit error rate recording at 200 Gb/

in^2 which was quite promising for future BPM technology (see inset in Fig. 33(d)). Today as heat-assisted recording is supposed to be associated with BPM, ECC model remains of high interest. It could still be based on soft/hard interface but it could also turn into anti-ferromagnetic/ferromagnet or strain-inducing layer (SIL)/ magnetic layer. In a recent patent, we propose to use for instance a shape memory alloy to induce, when heated, a strain onto a hard magnetic layer and affects its magnetization anisotropy through the magneto-elastic effect.

III.1.5. Searching for pre-patterning methods towards 1 Tb/in^2

As I mention in my introduction to BPM (part III.1.2), one of the most difficult challenges towards 1 to 10 Tb/in^2 BPM production is to define a method of forming 16 to 10 nm diameter islands with extremely tight tolerances on the width, length, and positional fluctuation of dots while meeting an economically acceptable cost (few dollars). Nanoimprint lithography appears most likely to meet the lithographic specifications for resolution, placement accuracy, and throughput. There are many imprint lithography techniques, all variations on a common theme, already widely developed for DVD or blue-ray disks [194-197]. The basic premise is that an expensive master mold, either rigid or flexible, would be replicated into subsequent daughter and granddaughter molds, which would imprint hundreds of disks per hour and eliminate the time penalty associated with complex e-beam based lithograpy. As shown in Fig. 34, granddaughter template or mold with a prefabricated topography is pressed into a displaceable material (i.e. resist) that is later use as a mask to pattern the disk using physical and/or chemical etching processes. In practice, a substantial amount of characterization is required to optimize conditions for pattern transference. The imprinted resist must adhere to the substrate and also completely wet the mold pattern, making the proper choices of low-viscosity resist and surface treatments of the mold essential for high reproduction fidelity. After the resist cures, it must then fully release from the mold or risk tearing of the pattern. Following its release, the imprinted resist pattern on a disk must have uniform thickness and be as thin as possible so that base layer topography variations will not be replicated into the etched disk. All these steps are very challenging when discussing areal density larger than 1 to 10 Tb/in^2 as compared with blue ray disks of only 12.5 Gbit/in^2. In the following part, I will focus on two original auto-assembly methods (e-beam directed assembly of block copolymer and anodic alumina templates nanobumps) for achieving the best master mold and how the pre-pattern substrate quality affects magnetic properties of the final BPM media.

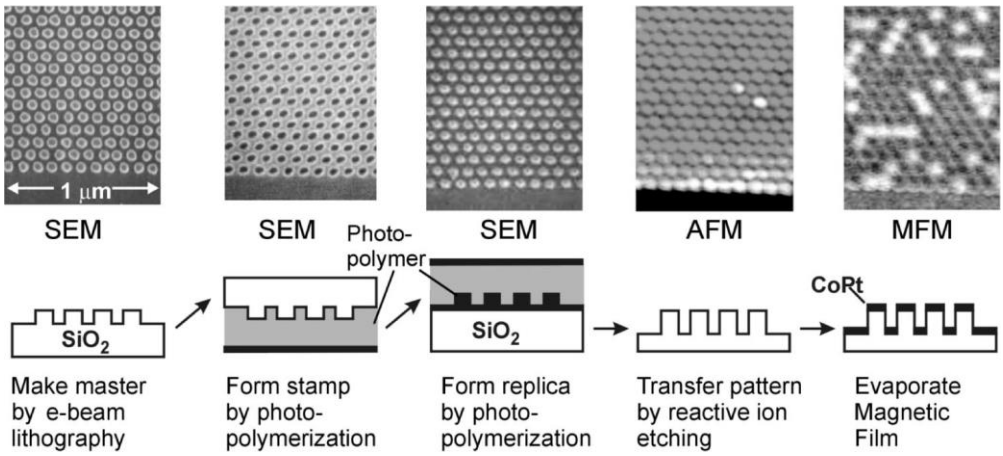

Figure 34 - Steps in the fabrication of patterned magnetic media. The final panel displays a magnetic force microscope image, showing quantized up and down magnetization of isolated domains. Taken from Ref. [197].

Directed block copolymer self-assembly

It is important to note that ultimately nanoimprint lithography is a copy process, and so the ultimate resolution is only as good as the imprint mask used. The use of diblock copolymers has been explored in conjunction with NIL for the purpose of improving the fabrication of BPM. As opposed to the more traditional "top-down" fabrication approaches discuss in this section, diblock copolymers represent a "bottom-up" approach, using the uniform nano- and supermolecular structures that result from organized macromolecule packing, the so-called "self-assembly" process. Block copolymers tend to self-assemble into a variety of well-ordered nanostructures with almost continuously tunable resolution from several to hundreds of nanometers because of the chemical immiscibility of the covalently linked segmental chains [198-200]. Through various templating processes with these block copolymer microdomain masks, high-resolution functional nanostructures can be generated, such as spheres, cylinders, and lamella.

The molecular packing, and thus thermodynamically stable microdomain patterns, of block copolymers in the bulk state are governed by the positive mixing enthalpy and low mixing entropy of component segments. Because of the covalent bonding between the segments, the system can not macroscopically phase separate, and so it minimizes the interfacial energy by adopting well-defined microdomain patterns with constant interfacial curvature and stretched interfacial chain configurations [198,199]. However, intrinsic obstacles remain for large-scale nanofabrication with block copolymer patterns: (1) the inherent small domain size or, in other words, short-range lateral order; and (2) unfavorable domain orientation. Fortunately, it has been shown that both substrate topography and chemical modification of the substrate surface can generate periodic thickness or surface/interface energy profiles which guide the overlaying block copolymer nanopattern into long range order. So mixing e-beam lithography and block copolymer will most probably be used to the master BPM template. Even more interestingly, it has also been shown that pattern density multiplication is possible, enhancing patterning resolution while reducing e-beam lithography exposure time [201]. Fig. 35(a) shows the e-beam directed block

copolymer template after selective removal of the PMMA cylinder cores (500 Gb/in^2, average diameter d=22.9nm and normalized standard deviation σ_d=2.6%). A Cr lift-off followed by CF_4 reactive ion etching is used to generate Si-pillars 20-30nm tall with nearly vertical walls and flat tops as shown in Fig. 35(b) (d=24.1nm, σ_d=3.3%). A Ta(15Å)/Pd(30Å)[Co(2.8Å)/Pd(9Å)]$_8$Pd(11Å) ML film is sputter deposited onto the Si pillar substrates. Corresponding Scanning Electron Microscopy (SEM) and Transmission Electron Microscopy (TEM) images are shown in Fig.35(c) and 35(d) respectively (d=29.2nm, σ_d=2.8%). The magnetic islands have a larger filling factor with a more spherical overgrown shape resulting from the film growth conditions as seen in cross-sectional SEM (Fig.35(c)) and TEM images (Fig.35(d)).

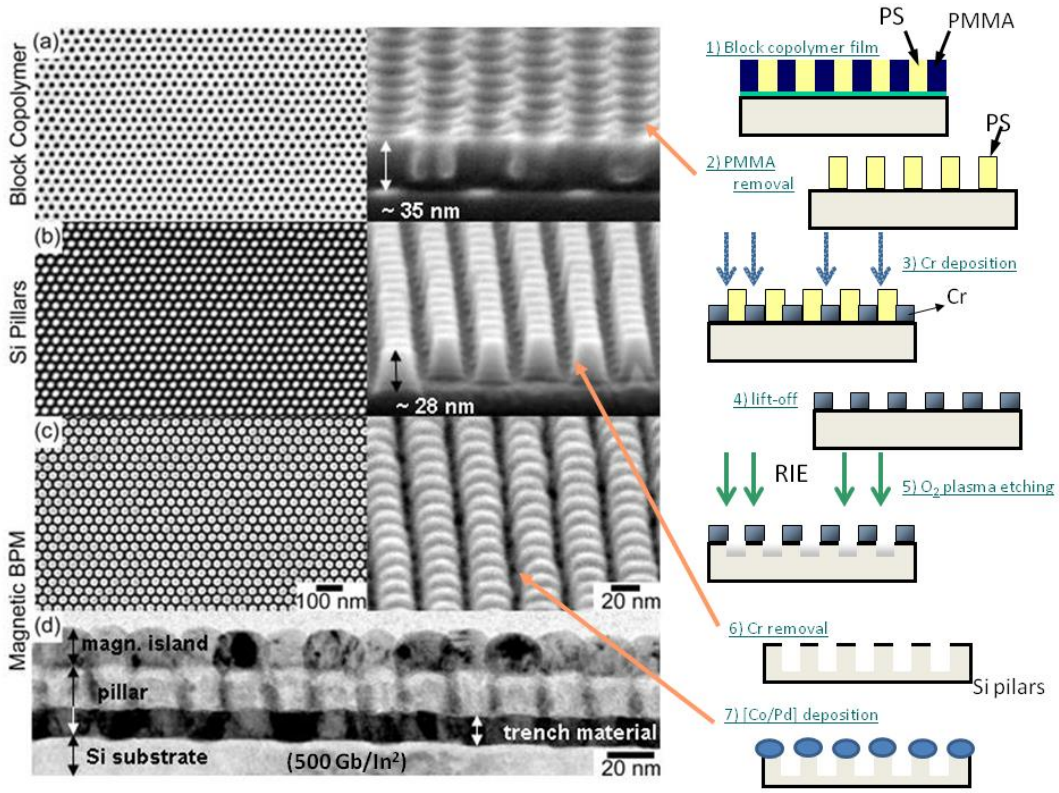

FIG.35: 500 Gbit/in^2 (L_o = 38 nm) BPM array fabricated by [Co/Pd] ML deposition onto pre-patterned Si-pillar substrates fabricated via e-beam directed assembly of block copolymer films. SEM micrographs (and in the right corresponding procedure sheme) of (a) the block copolymer film after selective removal of the PMMA cylinder cores, (b) Si-pillars after Cr lift-off using the template in (a) and subsequent reactive ion etching and (c) magnetic BPM after depositing a Co/Pd ML thin film onto the pre-patterned pillar structures (left: top view, right: section view at 85^o angle). (d) Bright field TEM cross-sectional image through two consecutive rows of bits (into the image plane) that are 180^o phase shifted with respect to each other.

Let us now compare the difference in magnetic features for BPM based on pre-pattern Si substrate obtained by (i) e-beam directed assembly of block copolymer films, (ii) undirected block copolymer self-assembly, and (iii) pure e-beam lithography : (i) The block copolymer templates were made from polystyrene-block-poly(methyl methacrylate) (PS-*b*-PMMA) thin films forming cylindrical PMMA domains oriented perpendicular to the substrate in a PS matrix (Fig. 35a). Polymers with two different molecular weights (both with ~70% PS

content) were used to generate patterns at two different densities. PS-b-PMMA (Polymer Source) with total molecular weights M_n of 65 kg/mol and 39 kg/mol were used to create patterns with a center-to-center pitch of L_o=38nm (500 Gb/in^2). Directed assembly of highly uniform magnetic dots (d=29.2nm, σ_d=2.8%) was achieved by treating the substrates with a polystyrene brush and then using e-beam lithography to generate a sparse chemical contrast pattern (density multiplication factor of four) as described elsewhere [201]. (ii) Undirected, randomly oriented patterns with L_o=38nm were obtained from block copolymer films applied to substrates with neutral random PS-r-PMMA copolymer brushes [202], which induces perpendicular alignment of the PMMA cylinders, but does not otherwise dictate the orientation of the hexagonally packed polymer lattice within the film. As shown in Fig. 36(b) and (c) samples with two different size distributions have been produced with respectively "d=25.1nm, σ_d= 9.0%" and "d=21.6nm, 19.0%". The difference between the two samples originate from the block copolymer annealing temperature that is higher (220°C instead of 190°C) for low distribution sample (Fig. 36(b)). The Cr lift-off process is extremely sensitive to the defect density and domain boundaries resulting in a lower yield of pillar density and a corresponding lower filling factor on the less ordered samples (Fig. 36(c)). (iii) templates made by e-beam lithography alone, defined circular dots on a square lattice with a center-to-center pitch of 35 nm and σ_d = 10.5%.

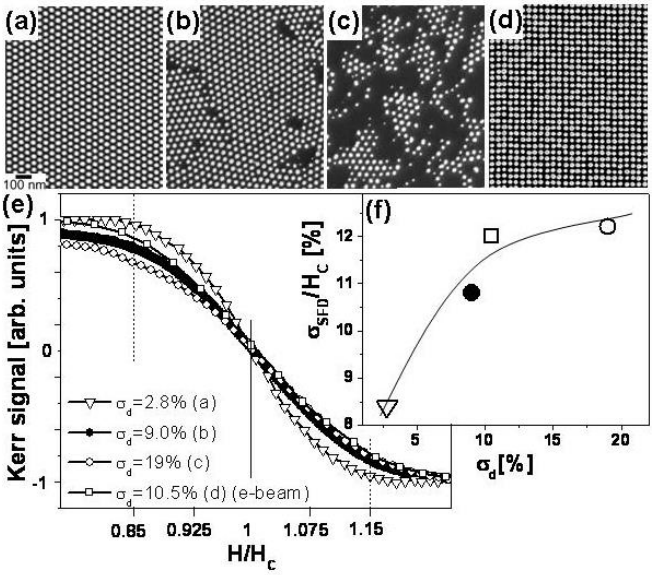

Fig.36. SEM images of BPM at 0.5 Tb/in^2 with various size distributions fabricated by (a) directed block copolymer assembly, σ_d=2.8%; (b-c) undirected block copolymer assembly, σ_d=9.0 and 19% respectively, and (d) e-beam lithography alone, σ_d=10.5%. (e) PMOKE reversal curves of the same four patterns. (f) Normalized magnetic SFD vs. pillar size distribution σ_d for the 4 samples. The line is a guide to the eye.

We analyzed the magnetic properties of the four 500 Gb/in^2 BPM assembly by our usual micro-spot PMOKE. In Fig. 36(e), we superpose the reversal curve around normalized Hc (Hc is about 12±0.5 kOe for all arrays) and Fig.36(f) summarizes the normalized magnetic SFD as a function of magnetic σ_d. We find that samples made from undirected block copolymer self-assembly or e-beam patterning alone yield a broader magnetic SFD than those

made from e-beam directed block copolymer assembly. Moreover the reversal curves indicate that for the self assembled structures with multiple domains some small fraction of magnetic islands reverse already at significantly lower reversal fields than most of the other islands. We suspect that islands close to the defect lines are responsible for the low field switching tail in the island reversal curves of the self-assembled patterns since they reveal a large variation in diameter, shape and next nearest neighbor coordination number. To go further, one should perform imaging measurement and check magnetic features as a function of dots location, as we did earlier to reveal the role of (200 grains). As it will shown in the next part, the influence of auto-assembled array grain boundary stays of second order as compared to intrinsic SFD as long as dipolar field induced SFD is not the main cause of SFD. Nevertheless, in the view of BPM recording, dots position has anyway to be perfectly controlled and no grain boundary or mislocation is allowed for the read/write process to work. Finally, from the above study, we conclude that non-uniformities in bit size and placement as well as the introduction of defects in the dot lattice (for the case of undirected self assembly) lead to correspondingly broader magnetic SFDs. Moreover e-beam directed assembly of block copolymer films is so far the best method to obtain tight size distribution and high lattice order.

Nanobumps based on self-assembled anodic alumina oxide (AAO) templates

Pre-pattern silicon substrate is not the only pre-pattern substrate that can be used to form BPM template. Recently, a simple and inexpensive method of fabricating nanoscale magnetic patterns was developed by using self-assembly of colloidal nanospheres dispersed on regular substrate [203]. Self-assembled close-packed layer of polystyrene nanospheres of diameter in the range of 50 – 300 nm were used as curved substrate to deposit Co/Pt and Co/Pd multilayers and to create ordered arrays of single domain and magnetic exchange decoupled nanostructures [203,204]. However, several problems associated with the nanospheres approach were pointed out due to the presence of dislocations and domains, and also because the cleanness and hydrophilic properties of the substrate surface are critical in making well-ordered colloidal crystal films [205]. In addition, attractive forces between the spheres prevent the formation of a layer of spheres with good order when considering diameters below 50 nm so that only short-range order can be obtained, or their position need to be templated using lithography to impose long-range order [Kappenberger2009].

In 2012, Luc Piraux's team at in Louvain-la-Neuve (Belgium) together with our team in IJL Nancy have proposed a method for designing low-cost densely-packed magnetic nanobump assemblies on 2D curved substrates. This process involves the growth of magnetic nanocaps on the back of nanoporous anodic alumina templates (AAO). The voids of the nanoscale-channeled structure of AAO nanotemplates have been widely used in the past to form nanowires and multilayers in filling the pores by electrochemical deposition methods [206-208]. Electrodeposition is usually performed after the removal of the oxide barrier layer that closes the bottom ends of the pores. Therefore this barrier layer is typically considered undesirable. However, herein we emphasize that the surface of this layer possesses an ordered array of bumps that can also be used as a pre-patterned substrate to modulate the thickness of thin Co/Pt multilayers deposited on it, as sketched in Fig. 37(b). The AAO templates were

fabricated by an optimized anodization process (Fig. 37(a) in order to obtain highly ordered structures [209,210]. Templates with 105 nm average pore spacing consist of long channels (~50 μm) closed at the bottom end by a round-shaped Al_2O_3 barrier layer [Fig. 37(c)]. The barrier-layer surface is composed of a hexagonal close-packed lattice of nanobumps that possess the same spacing as the porous layer [Fig. 37(d)]. We used the method described in Ref. [211] to analyze the SEM images and characterize the degree of ordering in the barrier-layer surface. We calculate a mean inter-bump distance of 105 nm and a full width at half maximum (FWHM) of 15.5 nm. Height modulation profiles extracted from AFM images show a maximum bump to bump height variation of 5nm (only 1 nm maximum in region with no lattice defects) and an average bump height distribution of about 2nm over a few microns, but larger variations (up to 50 nm) can be observed from region to region for areas of tens of microns. This AAO template growth has been performed by Luc Piraux's team.

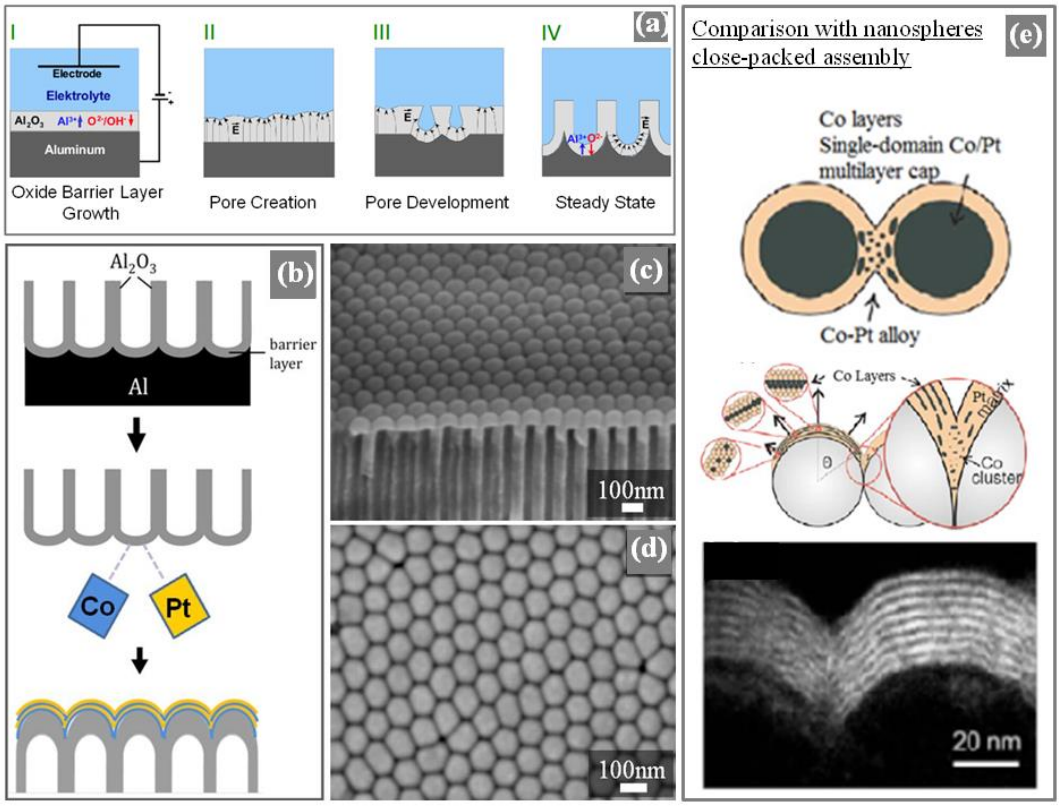

Fig. 37. Schematic representation of the 2D-ordered alumina oxide template by anodization of Aluminium substrate [211] (a) and then formation of BPM media by sputtering deposition on the AAO barrier-layer surface (b). SEM images of the tilted cross section of the AAO template (c) and its curved surface (d). Schemes of [Co/Pd] ML deposited on nanospheres close-packed assembly and explanation for the magnetic decoupling between magnetic nanocaps (e). SEM in (e) image confirms the intermixing of Co and Pt in between two naospheres [204].

Ta(5 nm)/Pt(5 nm)/[Co(0.4 nm)/Pt(0.7 nm)]$_4$/Pt(3.5 nm) was sputtered on top of the nanobump array and on a sister sample deposited on flat Si substrate (Fig. 37(b)). At 300K, magnetization at saturation measured on the sister sample is M_s = 760 emu/cm^3 (kA/m) and the effective anisotropy field extracted from the in-plane field loop equals H_k^{eff} = 4700 Oe. Hysteresis loop is squared and Hc = 120 Oe for this sample (Fig. 38(b)). Relative coercivity

Hc/Hc(0) follows a 1/cos(θ) if θ corresponds to the angle between the applied field and the perpendicular anisotropy direction (not shown here). Such a Kondorsky-like behavior is expected for strongly coupled films where magnetization reversal occurs by nucleation of reversed magnetic domain and then domain wall propagation until complete reversal. As AAO templates are fragile, it is difficult to measure them by regular magnetometry. We used Extraordinary Hall resistivity measurements with a standard four-probe method as a direct measurement of magnetization component perpendicular to film plane (Fig. 38(a)). At 300K, the loop obtained on the bumpy sample shows a fully saturated magnetization at remanence but the reversal branches are quite sheared (Fig. 38(a)). The evolution of the normalized coercivity as a function of magnetic field angle with respect to the surface normal is presented on Fig.38(b). Hc being considered as the switching field of the average dots, the field angle dependence is to be compared to the two extreme models that characterize a macrospin type reversal, namely the Stoner-Wohlfarth model, and a nucleation/ propagation type reversal, namely the Kondorsky model [193]**.** The experimental curve is shallower than Stoner-Wohlfarth model and is typical of a dot by dot reversal but with a nucleation/propagation process for each dot [212,213]. Changing the temperature from 300 K to 20 K does not drastically affect the hysteresis loop shape nor the field angle dependence of the coercivity (Fig. 38(a) and (b)). We also compared the magnetic features of 100 nm and 50 nm period nanobump arrays at 300 K. Their hysteresis loops, coercivity and angular dependence of coercivity are quite similar (Fig. 38(b)). The 50 nm period array has just a slightly sharper reversal curve and slightly larger end reversal tail in the hysteresis loop that may mark a slightly stronger exchange between bumps.

The difference between the bumpy sample and the flat sample reveals a change of magnetization reversal mechanism. In the flat film, nucleation of one or some reversed domains occurs at low anisotropy spots and magnetization reversal proceeds through propagation of the domain walls over the whole sample. In the bumpy sample, the reversal takes place dot by dot due to a partial exchange decoupling between the bumps as explained in [204]. Inter-bump exchange coupling must originate from the Co/Pt intermixing (leading to paramagnetic high Pt content CoPt alloy) between the bumps, as in the case of the very similar nanosphere system shown in Fig. 37(e) [204]. This new nanobump system is a quite complex system where the reversal mechanism depends on many parameters such as: regular anisotropy dispersion, the curvature of the bump [214], the strong dipolar interaction amplitude and gradient in each bump from the neighboring bumps, the inter-bump CoPt phase coupling (similarly to the ion milled edges in Ref. [181] or the irradiated region in [215]). Figure 38(c) shows the derivatives for the descending branches of loops showns in Fig. 38(a). For all temperatures, the derivative curve shows a double peak typical of a two step reversal. As confirmed by high-resolution under-field MFM measurements (not shown here), the double peak feature in the derivative reveals the competition between exchange coupling and strong dipolar interactions. Similar competition affects perpendicular anisotropy continuous films, like Co/Pt thin films. Tuning the dipolar field energy to a value of the same order as the exchange coupling energy leads to a double peak derivative whose first peak usually occurs before reaching zero field coming from the saturation field [216,217]. Note that the double peak derivative is observed for continuous films of Co(0.4nm)/Pt(0.7nm) multilayer (i.e. the

composition we are using here) having around 20 repeats [216] whereas our sample only holds 4 repeats. Therefore, in our sample the dipolar interactions are more effective, which implies a strong reduction of the inter-bump exchange coupling in our bump array. Moreover the inter-bump Co/Pt phase is a good pinning site for domain wall, if any. Recently, a shallow double peak shape of the hysteresis loop derivative, centered on the coercive field, has also been reported in a BPM with large inter-bit dipolar interactions and possibly under-etching, i.e. a non-zero inter-dot exchange coupling [218].

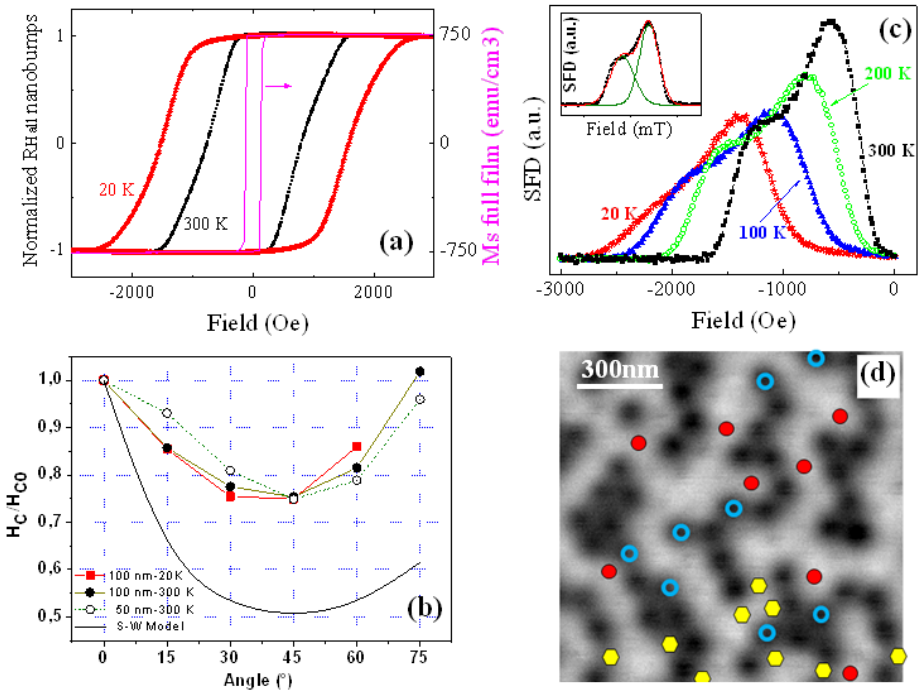

Fig. 38. Normalized Hall resistivity as a function of external magnetic field amplitude (a) and normalized coercivity as a function of the applied field angle (b), for Co/Pt ML on a bumpy surface with 100nm period measured at 20 (red curve) and 300 K (black curve). In (a), SQUID-VSM measurement for a sister flat sample at 300K (magenta curve) is shown. In (b), measure for a 50nm periode nanobump array (dotted line) at 300K is also shown and compared to the black continuous line that corresponds to Stoner-Wohlfarth model. (a) Derivative of Hall resistivity loops measured on a 100 nm period bump surface at 20, 100, 200 and 300 K. Inset of (c) shows the double peak Gaussian fitting of 300K data. (d) 1μm×1μm MFM images obtained close to half reversal after negative field saturation. Black and white color corresponds respectively to up and down magnetized dots. The solid red disks correspond to hard switchers, open blue disks to easy switchers and yellow hexagons to topological defects.

If the inter-bump exchange coupling is difficult to extract and quantify here, the strong influence of dipolar interactions acting as a long-range anti-ferromagnetic coupling, can be quantified through and analysis of switching field distribution. Indeed SFD is composed of a dipolar term and another term due to magnetic characteristic variations from dot-to-dot. And this second term can be extracted in using the ΔH(M, ΔM)-method [178,189,190]. Because of its double peak shape of the derivative, we chose to define SFD as the standard deviation sigma (σ) of a function equal to the sum of two Gaussians. At 300 K, SFD is about 370 Oe and increases up to 420 Oe at 20 K. The increase of SFD with temperature can originate both from the dot-to-dot variation of anisotropy based SFD or from the increase of dipolar field

induced SFD since Ms increases when the temperature decreases. The SFD value is high as compared with the coercivity value. The relative SFD, i.e., SFD/*Hc*, is about 46% at 300 K, which is much larger than usual values of approximately 10% found earlier here in regular Co/Pd-based BPM. We found by the ΔH(M, ΔM)-method that dot-to-dot variation leads to SFD equal to $\sigma_{internal}$ = 141 Oe. So the ΔH(M, ΔM)-method demonstrates that dot-to-dot variation counts for only about a third of the overall SFD (370 Oe) extracted from EHE loop derivative (Fig. 38(c)). The large dipolar effect deduced ($\sigma_{dipolar}$ = 229 Oe) has to be correlated with the high Ms of the experimental Co/Pt we used here. More generally the large filling factor of our nanobump array is a serious drawback for further implementation of AAO template as BPM pre-pattern master template.

Nevertheless, on a more fundamental level, the system is very interesting. High resolution MFM allowed imaging the magnetization reversal over hundreds of bumps, during sweeps of an external magnetic field of uniform value over the whole imaged area. Bump-by-bump individual magnetization switching is demonstrated. After the first switching events (whose reversal field amplitude is strongly reduced by the dipolar interaction), competition between exchange coupling and dipolar interaction is found to favor lines of switched bumps until 50% of the bumps have been switched. At this stage, a labyrinthine domain pattern (Fig.38(d)) is observed that has low field susceptibility, i.e. it is more stable than the previous and subsequent configuration. This loss of magnetic susceptibility at 50% reversal leads to the double peak feature of the macroscopic hysteresis loops. At this stage, the switching event location seems to be uncorrelated to the presence or the absence of switched neighbors. The easy and hard switchers indicated in Fig. 38(d) are found to be quite reproducible from field cycles to field cycles. In addition, AAO lattice stacking faults are found to form mostly boundaries between well-ordered bumps arrays. Lines of single defects seem not to drastically affect the magnetic features of the neighboring bumps, whereas larger defect density does (in good agreement with results obtained on e-beam directed assembly of block copolymer templates). All these results indicate that although the long-range dipolar fields affect the bump reversal, locally the interbump exchange coupling and the dipolar interaction more or less compensate each other. Therefore, besides a new support for BPM template, we think that the present our AAO-based system could be a model system to get a deeper understanding of the influence of the different thin film parameters (exchange coupling, dipolar interaction and more important intrinsic SFD or thermal fluctuations) on the reversal mechanisms in PMA films [216,219,220].

III. 2. Research on 3D page memory

III.2.1. Introduction to 3D memories

Advanced memory technologies of STT-MRAM and BPM, which we have discussed so far in Part II.2 and III.1, aim at pushing the data-storage density limitations due to thermally induced instabilities of nano-scale magnetic bits down to 10 Tb/in^2 and beyond. Undoubtedly these clever approaches will draw the road-map for magnetic storage in the next 10-20 years. However it naturally looks very attractive to explore the possibility of using the vertical dimension to boost the data storage capacities since a three dimensional memory solution may potentially be the ultimate universal storage device by providing orders of magnitude improvement in the storage-density as the planar confinement restriction is removed. The first version similar to the core magnetic memory [221] corresponds to an extension of magnetic random access memory at 3D [222,223]. No clear proof of the feasibity and advantage of such system has yet been shown. The added process complexity and space needed for 3D-RAM may indeed largely cancel out the benefits of moving into the third dimension. To avoid complex random access memory transistor architecture, Cowburn et al. have proposed in 2013 a novel concept to store and move binary information in three dimensions, based on the injection and motion of solitons in magnetic superlattices [224]. In superlattices formed by alternating magnetic/non-magnetic films, where neighbouring magnetic layers tend to be anti-parallel to each other due to RKKY antiferromagnetic interactions, a soliton is formed by magnetic layers pointing parallel to each other, which separate the two possible anti-phase domains. This localized frustration can be propagated along the system in a controlled manner, making possible its use as data carrier in a 3D magnetic shift register [225]. Although the idea looks promising, the read and write method require very good control of exchange coupling and switching field distribution in an extremely large 3D array of bit cells.

Magnetic race-track memory is also based on the physical motion of the magnetic information with vertical shift register but it is considered as much more promising because of its simplicity and its possible large gain in data density [226]. The operation of the magnetic race-track memory is summarized in Fig.39. Data is encoded as a magnetic domains pattern in a ferromagnetic nanowire. A series of spin-polarized current pulses can shift the whole pattern from one side of the track to the other lining up the region of the data pattern of interest with the reading element. The motion of the domain wall (i.e. of the domains marking the one or the zero information) will rely on STT as discussed in part II.2.3. A MTJ would sense the presence or absence of a domain wall through the tunneling magnetoresistance (TMR) effect. Data can be written to the track using the magnetic field from a write line or by any other mean like spin transfer torque. Ultimately building a large array of such race-tracks is necessary to maximize the data storage-density. Even though the vertical version of the race-track memory carries the additional benefit of using the third dimension, the fabrication of such a device is considerably more difficult compared to the horizontal version. The magnetic race-track memory can be potentially advantageous in several aspects. It does not suffer from any wear-out mechanisms due to cycling making it very reliable for long term operation. It is very efficient in terms of power consumption and the vertical race-track can boost the

information density as compare with the 2D version. However new advancements in nanofabrication techniques are needed to overcome the challenges in building such structures with a reasonable cost. So far no demonstrator of such technology has been developed yet.

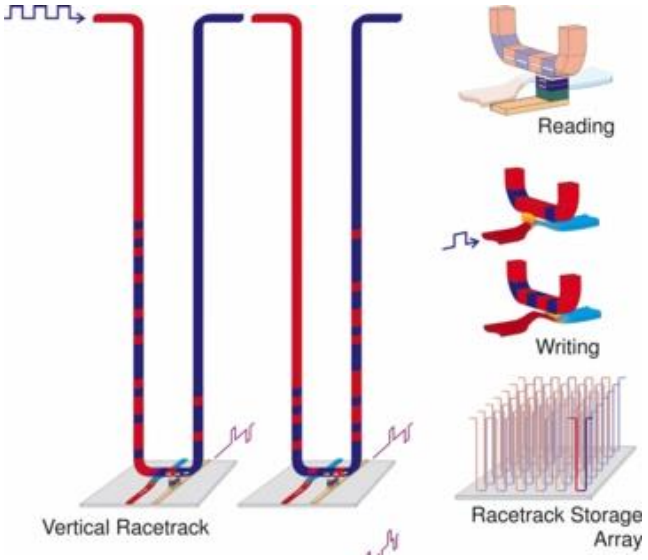

Fig. 39. The operation of the magnetic race track memory. (A) Vertical Race-Track configuration (B) Horizontal race-track configuration (C) Read-operation (D) Write-operation (E) Race-track storage array.[227]

In parallel, in 2008 an intermediate method to the above ones has been patented at Hitachi GST San Jose research center [228,229]. The concept is called magnetic page memory and relies on a 2D writing stage and then propagation of the information in the third dimension using dipolar duplication under thermal excitation. Lateral shift could also be implemented through in a more complex architecture. This concept has been a nice playground for me to get better understanding of thermal effect and dipolar interactions in magnetic stacks, as well as a subject of a successful collaboration with Ozhan Ozatay presently at Bogazici University in Istambul since 2009.

III.2.2. Page memory

The operation of the magnetic page memory device is summarized in Fig 40. A perpendicular anisotropy magnetic nanowire array with periodic domain nucleation sites in a cross-wire architecture (Fig.40(a)) is built on a single layer of read/write elements at the bottom of the stack (Fig.40(b)). After all the data have been recorded on the bottom magnetic layer in the form of the presence or absence of domains in the nanowire constrictions, the domain configuration is replicated to the next layer by instantaneously reducing the nucleation fields through local heating from electrical pulses. The increasing temperature in the nucleation sites of the second layer make its local magnetization susceptible to the stray fields coming from the recorded domains in the bottom magnetic layer. The third magnetic layer constrictions are also heated synchronously with the second magnetic layer so that the

stray field coming from the top layer is suppressed. After the electrical pulses are turned off, the second layer domain configuration ends up being a replica of the bottom magnetic layer. The shift of the information recorded on the second magnetic layer to the layer above it proceeds in a similar manner by sequential heating of the third and fourth magnetic layers and cooling in the presence of the stray fields available from the perpendicularly oriented domains, as shown in Fig.40(b).

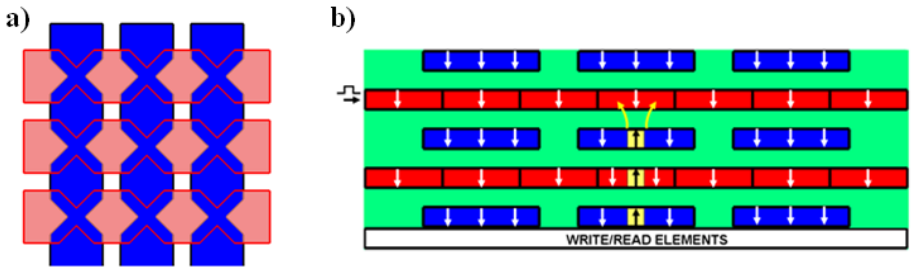

Fig. 40. (a) Top view schematics of the nanowire stack array displaying the vertical alignment of pinning sites acting as storage bits in the cross-wire architecture. Alternating layer of nanowires are colored blue and red. (b) Side view schematic drawing of the page memory device with a single layer of read/write elements, a stack of nanowire arrays with perpendicular magnetization separated by a SiN_x low thermal conductivity spacer (green region) where the straight arrows represent the local magnetization direction and the curved arrows represent the local stray field. A square electrical pulse is applied to the layer to be written to instantaneously lower its coercivity. A buffer stack on the right is a replica of the memory array that is used for temporary storage in the read process.

To reach a data point recorded on a given layer, a buffer stack is used to maintain the information stored beneath the layer of interest. For instance to read data from the second layer, the information on the first layer is read and transferred by the read/write elements to the first layer of a buffer stack. Then by applying electrical pulses in the same manner as above the first layer replicates the domain structure of the second layer making the data accessible to the read/write elements. Here the insulating spacer thickness must ensure both magnetic transparency and thermal isolation between layers to avoid disturbing the magnetization configuration of neighboring layers. The periodic constrictions where the domains nucleate act as pinning sites stabilizing the domains and also facilitate the localized heating process due to current pulses by enabling highly concentrated current densities for the vertical domain transfer process.

III.2.3. Magnetic media for dipolar fields and heat induced domain duplication

Page memory is based on the duplication of a magnetic data through the dipolar fields emitted by the magnetic bit to be copied. We first studied dipolar coupling interactions between superposed extended films having magnetic domain configuration.

Dipolar coupling and domain duplication

Page memory is based on the duplication of a magnetic data through the dipolar fields emitted by the magnetic bit to be copied. So one of our first work was to study dipolar coupling interactions between superposed extended films having magnetic domain configuration. Previous work had been performed both for in-plane and out-of-plane anisotropy films showing that the domain state of a "fixed" layer (also named hard layer) could influence the magnetization reversal in a "free" layer (also named soft layer) exchange decoupled from the first layer by a spacer layer [230,231]. The nomenclature refers of course to GMR spin valve systems that has been with multilevel magnetic recording one of the leading motivation for these pioneering works [203,232,233]. Here because of the final geometry of page memory, of the need for very small domain widths and of the need for high thermal stability at rest, we have focused on perpendicular anisotropy systems and especially magnetic Multilayer (ML) based on Co, Ni and Pt. For such a perpendicular anisotropy ML, in the assumption of a single domain wall (DW) in a infinite film of thickness *h*, an effective DW width δ, and a saturation magnetization *M*S, the dipolar stray field *Hz* perpendicular to the sample surface at a distance *z* over the surface is given by Ref. [234] :

$$H_z(x,z) = -4\,Ms\tan^{-1}\left(\frac{xh}{(z+\delta)(z+\delta+h)+x^2}\right)$$

Based on this expression, we can calculate the stray field coming from a 1D down magnetized domain of a width w as the stray field induced by two opposite DWs separated by w = 0.5, 1 and 2 μm respectively. We used typical values for magnetic [Co/Pt] ML like Ms = 550 emu/cm^3, h = 11nm, δ = 20nm, z = 14 nm (z being the distance between the fixed layer top surface and the middle of the free layer). In Fig. 41, one can see that the stray field created by the fixed layer tends to orientate the free layer magnetization parallel to the fixed layer magnetized from each parts of the two domain walls. The stray field is maximum around the domain walls and then slowly vanishes further away from the domain wall. Same stray field is generated at the edge of laterally finite film, like a nanostructure. We discussed it in part II.2.1. One can easily use this effect to induce data duplication from the fixed layer to the free layer. In figure 41(b), the magnetic stray field on top of the down domain is shown to increase as the distance between the two domain wall decreases, i.e. as the down domain width decreases, the magnetic stray field increases on top of the down domain. From a technology point of view, it makes a potential device based on scalable to low nanometer features and therefore adaptable to very large data areal density.

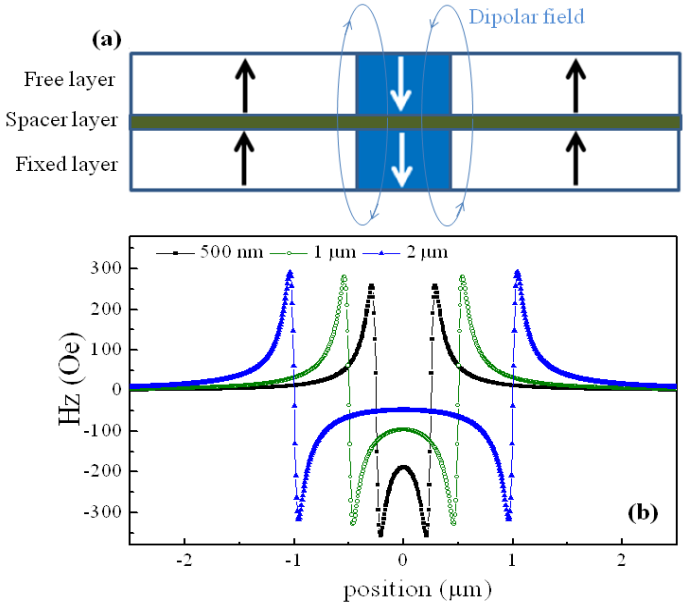

Fig. 41. (a) One-dimensional scheme of the magnetic domains state in Free layer/Spacer layer/Fixed layer around a 1 micron wide down domain in the Fixed domain. (b) One dimensional calculated stray fields Hz originating from a down magnetized domain in between 2 up magnetized domains in the fixed layer, having a width of 0.5, 1 and 2 µm respectively, at a high 11 nm from the top of the fixed layer.

Using DC magnetron sputtering, we deposited the layer sequence Pd(3nm) / $[Co_{30}Ni_{70}(0.2nm)$ / Pd(1.5nm)$]_{30}$ / Pd(10nm) / $[Co(0.3nm)/Pd(0.8nm)]_{20}$ / Pd(1.2nm) onto Si wafers as well as Si_3N_4 membranes for transmission soft X-ray imaging. Here Ni is introduced both to soften the bottom layer (which become the soft layer) as compared with the top [Co/Pd] ML (the hard layer). Figure 41(a) presents hysteresis loops measured at 300 K with the field perpendicular to the sample plane. The major loop reveals two distinct steps corresponding to the independent reversal of the soft and the hard layer. Starting from positive saturation the soft layer reverses at H^0_N= -350 Oe and stays anti-parallel to the [Co/Pd], until about H= -4 kOe, where the hard layer reversal occurs. A minor field cycle performed between +/-2 kOe shows no residual bias field and indicates that the Pd (10 nm) layer in between the two ferromagnetic multilayers prevents any direct exchange interaction. Sweeping the external perpendicular magnetic field from 8 kOe to -4.2 kOe, where the hard layer has reversed half of its magnetization, we create a domain state in the hard layer with about 50% up and 50% down domains.

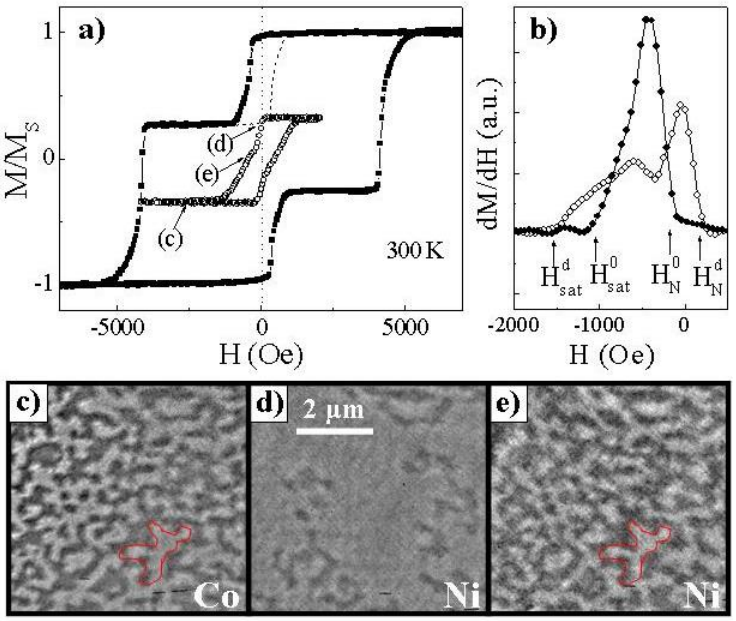

Fig. 42: a) Normalized hysteresis loops measured at 300 K. Square solid symbols show the major loop, while the dash line and the open circles correspond to minor loops with the hard layer in a uniform and a domain state, respectively. b) Derivative of the descending major and minor (solid and open symbols) hysteresis loop branch. c-e) MTXM images, each 6x6 µm^2 in size, showing the magnetic domain configuration as observed for the three states marked in a) at fields of –2, -0.1, and –0.3 kOe, respectively. Image c) was collected at the Co-L_3 edge (778 eV) with the soft layer saturated and thus shows the hard layer domain state only, while images d) and e) were obtained at the Ni-L_3 edge (854 eV), thus separating out the soft layer domains. The red shapes are just guides for the eye.

In most of the previous works on duplication in perpendicular anisotropy materials, two $[Co/Pt]_x$ multilayers of different reversal fields are separated by a thick Pt to avoid any direct exchange coupling [231,233,235]. Usual magnetization, MFM or Kerr microscopy measurements were performed to characterize the evolution of the hard/Pt/soft multilayer magnetic configuration during the field cycle. In other words, up to now, only measurements averaging over the complete ferromagnetic layer stack have been reported. Non-interactive and layer-by-layer specific studies are then needed to validate the previous results on domain duplication in perpendicular to the plane anisotropy system and prepare more complex experiments in temperature. To directly image with high spatial resolution these domains and the hard/soft layer dipolar interactions, we performed magnetic transmission soft X-ray microscopy (MTXM) using the full field soft X-ray microscope at beamline 6.1.2. at the Advanced Light Source (ALS) in Berkeley CA which provides a spatial resolution down to 25 nm provided by state-of-the-art Fresnel zone plate lenses used as X-ray optical elements [236,237]. X-ray magnetic circular dichroism (XMCD) provides element specific magnetic contrast, which for these studies enabled to separate layer resolved the magnetic domain configuration in both the hard and the soft layer by tuning the photon energy to the Co- and Ni-L_3 absorption edges, resp. MTXM images were recorded with magnetic fields up to 2kOe pointing perpendicular to the sample plane. After reversing half of the hard layer magnetization, we first confirm (Fig. 42(c)) the presence of a labyrinth pattern with 50% up and 50 % down domains in the hard layer with an average size similar to the natural size

measured at 300 K with MFM. Since the soft layer magnetization is saturated for Fig. 42(b), the domain state measured at the Co-L_3 edge at -2 kOe reflects the hard layer only. Subsequently we measure the reversal of the soft layer in a minor loop between +/–2 kOe (open circles in Fig. 42). Corresponding MXTM images measured at the Ni L_3 edge, to separate out the reversal of the soft layer only, are shown in Fig. 42(d) and 42(e). Starting from positive soft layer saturation, we lower the external field and observe domain nucleation in the soft layer (Fig.42(d)) around 0 Oe in good agreement with the VSM measurement (Fig. 42(a)). The nucleation field (H_N) and the saturation field (H_S) of the soft layer have significantly changed as compared to the previous minor loop measured for a uniform hard layer. It appears more clearly in the derivatives of the descending hysteresis branches in Fig. 42(b). H_N increases from H^0_N = -250 Oe to H^d_N = +130 Oe, while H_S decreases from H^0_S = -1.1 kOe to H^d_S = -1.55 kOe. Such changes in the soft layer hysteresis loop have already been reported on similar hard/soft systems and were associated with the influence of dipolar fields from the hard layer domains on the soft layer reversal [233]. At about –300 Oe we reach a 50% up and 50% down domain state (Fig. 42(e)) that appears to match very well with the state previously trapped in the hard layer (Fig. 42(c)). At this stage of the minor loop the domain state of the hard layer has completely been copied (replicated) into the soft layer. In Fig. 42(b), this replicated state reveals itself as a dip in the derivative. While the same replicated domain state was observed during several successive field loops, we found no evidence for an identical nucleation sequence.

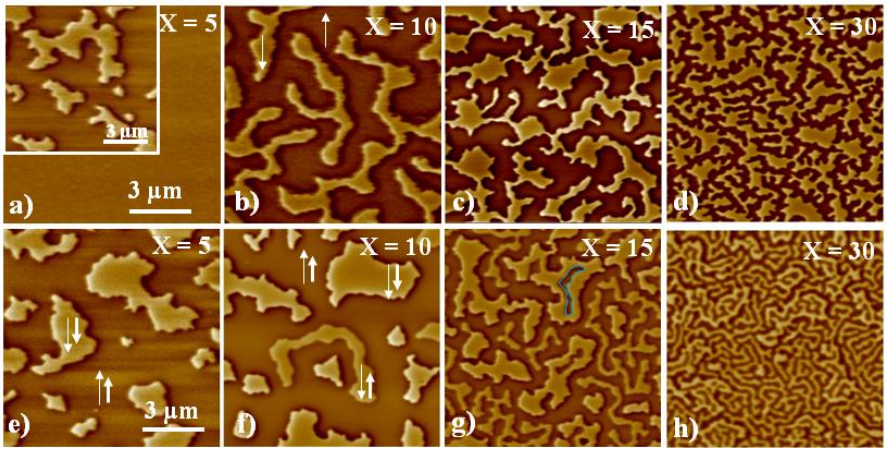

Fig. 43. 10*10 µm^2 MFM images of demagnetized $[Co/Pd]_X$ grown in a 3mTorr Ar pressure with X = 5 (a), 10 (b), 15 (c), 30 (d) and demagnetized soft/Pd/hard $[Co/Pd]_X$/Pd/$[Co/Pd]_{10}$ with X = 5 (e), 10 (f), 15 (g), 30 (h) respectively. Inset of (a) : MFM image of demagnetized $[Co/Pd]_{10}$ sample grown at 7 mTorr Ar pressure. The up and down arrows represent the up and down out-of-plane magnetization states respectively. The blue contour in (c) corresponds to the boundaries of a specific domain described in the text.

Exact duplication process strongly depends on the relative natural domain size of the soft and hard layer. Both natural domain needs to be of the same order to allow duplication. To highlight this dependence, we studied various $[Co(0.3nm)/Pd(0.8nm)]_X$/ Pd(10nm)/ $[Co(0.3nm)/Pd(0.8nm)]_{10}$ with x equal to 5, 10, 15, 30. The lower [Co/Pd]x has been deposited at 3 mTorr sputter pressure whereas the upper $[Co/Pd]_{10}$ is deposited at 7 mTorr sputter pressure. Fig. 43 presents first the MFM image of demagnetization magnetic

configuration of single $[Co/Pd]_X$ after AC demagnetization in a perpendicular field. We see that domains are hardly stabilized in the thinnest sample containing five repeats. Indeed, as observed in previous studies [216], for X = 5, the demagnetization field induces large micrometer size domains. As x increases, irregular two-dimensional domains form, whose mean domain width decreases to 900 nm, 700 nm and, 400 nm for X = 10, 15 and 30 respectively. The bright domains, resp. dark domains, correspond to a magnetization pointing towards the negative, resp. positive, field direction perpendicular to the sample plane (called in the following "down'', resp. "up"). The irregular pattern is typical of thin Co/Pd films after AC-demagnetization in an out-of plane field and the typical domain size originate from the competition between internal exchange coupling and demagnetization field as detailed in Ref. [216]. The inset of Fig. 43(a) shows a MFM image of the domain structure obtained after the same demagnetization procedure in the case of the high-Hc $[Co/Pd]_{10}$ multilayer. The mean domain size (about 1 μm) is similar to the one measured for the same number of repeats grown at 3 mTorr, but the dispersion in domain size and shape is much more pronounced. This difference is due to the increase of the multilayer interface roughness and crystallographic defects induced by the higher deposition pressure [220]. These defects usually lead as well to a higher coercivity and the magnetization reversal process of the high pressure film is then dominated by more frequent domain nucleation processes.

Fig. 43 presents a series of MFM images of the demagnetized state of the $[Co/Pd]_X/Pd/[Co/Pd]_{10}$ bilayer films with varying values of repeats X = 5, 10, 15 and 30. The samples have been demagnetized using the same procedure as that described for the single layer films. Using a Pd spacer thickness (10 nm), the MFM sensibility allows us to probe the stray field resulting from the top Hard layer (HCL) combined with that from the bottom soft layer (LCL). In Fig. 43(e), showing the X=5 case, the image displays mostly dark and bright domains. There is no domain with a distinguishable intermediate contrast in the image. The dark and bright contrast observed in Fig. 43(e) may respectively correspond to configurations where the "bottom soft - top hard" system is saturated "up-up" or "down-down", but it may also correspond to a zone of uniform LCL magnetization with up and down HCL domains. Unfortunately, it is not possible from the MFM image alone to conclude this. Nevertheless, when measuring the curve of first magnetization after demagnetization, a two step curve is measured and the saturation occurs at a 650 Oe field, i.e. 150 Oe higher than the saturation field of the soft layer when the hard layer magnetization is uniform. Similar MFM images and magnetization loops are observed for X up to 8. In Fig. 43(f), in $[Co/Pd]_{10}/Pd/[Co/Pd]_{10}$, a third type of domain appears on MFM images that is characterized by an intermediate darkness and the absence of a black inner contour. The black inner boundary is seen on most of the bright domains on Fig.43(e) and 43(b), and originates from the stray field profile whose intensity maximum is localized at the boundary between domains of opposite magnetization. The previous domain features, as well as its shape and size in comparison with Fig.43(b), indicates that this new "down" domain lays in the soft layer while the hard layer magnetization is kept in the opposite direction, i.e. "up". This new state is defined as "down-up" state. The fact that this new domain in Fig.43b spreads around the brighter domains is a confirmation that the "down-down" domains belong to both hard and soft layers. Indeed if there was no domains inside the soft layer, the most energetically stable position for the new

soft domain, would be on top of the hard domains. From X=8 to X=15, the density of soft layer domains increases since the mean domain size decreases (as explained above). For X equal to or higher than 15, as shown in Fig. 43(c), the demagnetized state contains four different contrast levels. In addition to the brightest "down-down" domains and the darkest "up-up" domains, intermediate contrast "down-up" domains spread like a de-wetting fluid inside the dark up-up domains, while avoiding the proximity of any "up-up"/"down-down" domain walls. Similarly "up-down" domains of dark contrast appear inside the brightest domains. At this stage intrinsic domain sizes in the HCL and LCL have become very different and thus are incompatible with each other. Underneath a "down" HCL domain, the LCL domains lay primarily where the dipolar field intensity is the strongest, i.e. close to the boundary of the HCL domains. But the self demagnetization field inside the LCL is strong enough to create an "up" domain in the center of the HCL domain (e.g. blue contour in Fig. 43(c)). This result reveals the competition between dipolar fields from the HCL domain and the self demagnetization field inside the LCL, whose relative influences vary as X increases.

Heat induced domain duplication

The goal of this step was to demonstrate the feasibility of temperature cycles-induced domain duplication. We used [CoNi/Pd]/Pd/[Co/Pd] where the Ni concentration in the soft [CoNi/Pd] was tuned to obtain a Curie temperature (T_C) close to 350 K. We checked by magnetometry that its magnetization and anisotropy decrease continuously from 5 K to 350 K and the system turns paramagnetic for higher temperatures [Weng1996]. We measured the temperature dependence of the magnetization at remanence as well as in an external field of 1 kOe and find slight differences between 310 and 350 K, indicating that the out-of-plane anisotropy competes with an in-plane shape anisotropy when approaching Tc. On the contrary, the hard [Co/Pd] system reveals a well-defined perpendicular-to-the-plane anisotropy and an almost constant magnetization within the considered temperature range from 5 K to 400 K.

First, to quantify the influence of temperature on domain duplication, we performed field-induced domain duplication at various temperatures. For instance at 150K, similar as for 300 K, the hard layer domain state is replicated in the soft layer during magnetization reversal. Nevertheless, analysis the derivatives of the hysteresis loop reveals that the amplitudes of H_N and H_{sat} variations (ΔH_N and ΔH_{sat}) due to the hard domain dipolar fields increase as the temperature is raised. The variation of ΔH_N from 100 K to 310K is two times larger than that of ΔH_{sat} over the same temperature range whereas the same variation was expected. We performed micromagnetic simulations to investigate the origin of the strong nucleation field reduction in the soft layer due to the domains in the hard layer. The hysteresis loop of the [CoNi/Pd] is calculated from the solution of the Landau-Lifshitz-Gilbert (LLG) equations with the [Co/Pd] magnetization held fixed to be in either the uniform state or the stripe domain configuration. In the simulations the domains in the hard layer are represented as 200 nm by 3000 nm parallel stripes of alternating magnetization perpendicular to the plane of the film. Thermal fluctuations are not considered explicitly in the LLG equations, but are

lumped into adjustments of the values for the magnetization M_s, the uniaxial anisotropy K_1, and the exchange A in the soft layer as a function of temperature. The modeling of the experimental nucleation fields proceeds in two steps. First, we aim to match the H^0_N (without stripe domains) by adjusting the [CoNi/Pd] parameters to obtain effective values for the anisotropy K_{eff} and the exchange A_{eff} as a function of temperature. Secondly, the calculations are repeated with K_{eff} and A_{eff} to obtain the nucleation field H^d_N when stripe domains are present in the hard layer to finally estimate the reduction in nucleation field $\Delta H_N = H^d_N - H^0_N$. We found that soft layer K_{eff} has to be significantly lowered (by 25-30%) compared to the experimental CoNi/Pd anisotropy measured from the hard axis loops. Such decrease is expected since nucleation in full film always occurs in lower anisotropy defective zone of the sample. This requires a scaling of the duplication fields by a factor of ~0.35 (e.g. by a commensurate adjustment of the hard layer magnetization). With these caveats in mind, leading to uncertainties of the simulated nucleation fields (estimated ±100 Oe), the calculated values qualitatively reproduce the trend of a reduction in nucleation field due to the stripe domains as well as the changes in the hysteresis loop shapes. Nevertheless, the thermal variations of ΔH_N cannot be quantitatively reproduced considering only soft layer parameters changes. We believe that thermal effects in the soft layer do not only lead to an effective reduction of the magnetization, exchange and anisotropy as a function of temperature but also initiate kinetics of magnetization hopping over local energy barriers.

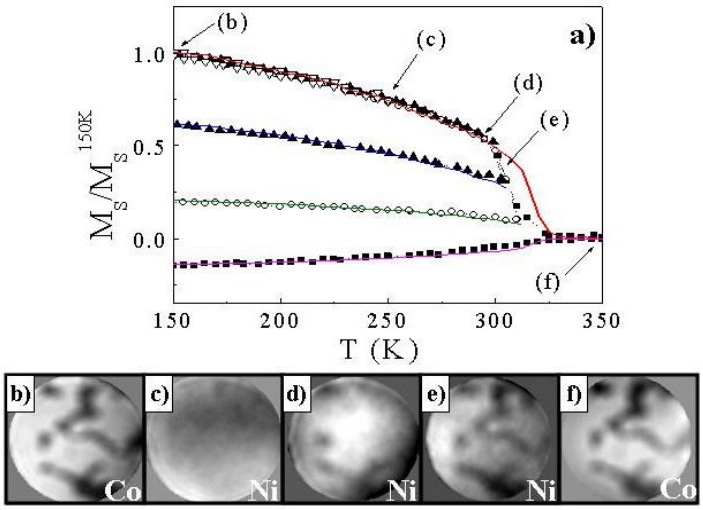

FIG. 44: a) Magnetization versus temperature cycles for remanence at 150 K after trapping a 50/50 domain state in the hard layer. The temperature was cycled from 150 K to T_{max}, where T_{max}=250 K (open triangles), 300 K (full triangles), 310 K (circles) and 350 K (squares). The red solid line is the remanent magnetization with no domains in the [Co/Pd] hard layer. The other solid lines correspond to simulations as described in the text. b) and f) 1.2 µm diameter FTH image of the magnetic domain configuration at the Co-L_3 edge for remanence at 150 K and 350K respectively. c) to e) Remanent magnetic domain configuration at the Ni-L_3 edge at 250 K, 290 K, 300 K.

Finally, to demonstrate duplication during temperétaure cycle, we measured by low-temperature VSM full film [CoNi/Pd]/Pd/[Co/Pd] magnetization at remanence as a function of temperature after introducing about half domains up and down in the hard layer at 150 K

(Fig. 44a). After saturating the soft layer at 3 kOe, the external field was released to remanence again. Subsequently starting at 150 K, the temperature was cycled at remanence between 150 K and four temperatures T_{max} (250 K, 300 K, 310 K and 360 K). After increasing the temperature beyond 290 K, we observe an irreversible reduction in magnetization when cooling back down to 150 K. To monitor spatially resolved changes in the magnetization, we performed FTH imaging during the temperature cycles. First, we verified that the hard multilayer domain state remains unaltered within the temperature range of 150 K to 390 K (Fig. 44b and 44f). Then we image the soft layer domain state at the Ni L_3 edge at 250 K, 300 K and 310 K (Fig. 44(c)-(e)). While at 250 K the soft layer remains uniformly saturated, at 290 K and 300 K, domains are progressively replicated (Fig. 44(d)-(e)). Since the FTH field of view is small, it is difficult to correlate the surface of the imaged domains and the macroscopic magnetization shown in Fig.44(a). To obtain a more statistical measure regarding domain replication rate as a function of temperature, we calculate the percentage of domains that we expect to reverse at a certain temperature. For this, we use the soft layer remanent magnetization change for a uniform hard layer state to fit the descending branch of the magnetic temperature cycle in Fig. 44. We were able to reproduce the magnetization variation as a function of temperature after T_{max} = 300 K, 310 K and 350 K, considering respectively 80 %, 61 % and 47 % of [CoNi/Pd] up domains. The good agreement between the fits and the experimental data confirms the formation of a stable soft layer domain state via dipolar duplication when the system is cooled back down to 150 K.

Method for improving thermal stability while maintaining low write heat requirement

In the previous section we used [CoNi/Pd] ML as recording layer to be imprinted by the dipolar field coming from another layer. This media has two disadvantages in the view of "page memory" implementation. First, the anisotropy at room temperature is weak and may not be sufficient to insure good data thermal stability for nanometric bit cell. Second each bit cell radiates a strong dipolar field at rest which can affect the writing process on neighboring bits. To maintain high thermal stability and insure low or no magnetization at rest, we looked for a materials that has similar properties as FeRh, i.e. a first order phase transition from an antiferromagnetic (AF) to a ferromagnetic (FM) phase in FeRh upon heating from room temperature to a transition temperature [238-240]. FeRh is not an option since it requires high deposition or post-annealing temperature to obtain the chemically ordered phase and limit the magnetic features distribution. Our basic idea was to use two layers with large perpendicular magnetic anisotropy and high Curie temperatures, T_C, separated by a layer providing antiferromagnetic coupling, and a layer with perpendicular anisotropy with a lower Curie temperature, $T_C^{interlayer}$ in the range of the desired AF-FM transition temperature, T_{AF-FM}. At room temperature this system behaves as two antiferromagnetically coupled layers with a low net perpendicular magnetic moment in remanence. As the temperature is raised to approach $T_C^{interlayer}$ the magnetization of the interlayer is gradually reduced to zero, and consequently the coupling strength provided by the combination of this low-T_C layer and the adjacent AF coupling layer is reduced. Eventually, the effective coupling between the two high-K_U, high-T_C layers becomes dominated by the external field (coming for instance from a bit laying

underneath in the memory), resulting in a parallel alignment of their moments at remanence and a net magnetic moment equal to the sum of the moments of the two high-T_C layers.

To prove the concept described above we deposited sequences two [Co/Pd] ML with large perpendicular magnetic anisotropy and high T_C separated by a Co/Ru (0.7nm) /Co structure providing antiferromagnetic coupling and a [CoNi/Pd] ML with perpendicular anisotropy and $T_C^{interlayer}$ in the range of the desired AF-FM transition temperature, T_{AF-FM}. The multilayer samples were deposited on glass substrates by magnetron sputtering. An Ar gas pressure of 1.4 mTorr was used for sputtering all layers except the topmost Co/Pd multilayer stack. This last multilayer was deposited at 5mTorr in order to achieve a somewhat larger coercivity compared to the previous layers. Typical film thicknesses and compositions of the constituting multilayers were [Co (0.5nm)/Pd (0.5nm)] for the first high-T_C multilayer, Co (0.5nm)/Ru (0.7nm)/Co (0.5nm) for the AF coupling layer, [$Co_{50}Ni_{50}$ (0.25nm)/Pd (1.2nm)] $T_C^{interlayer}$ of approximately 100 °C for the separation layer and [Co (0.35nm)/Pd (7.5nm)] for the second high-T_C multilayer. By proper choice of film thicknesses, compositions and multilayer repeats the net moment at room temperature can be adjusted to zero, as shown in Fig. 45 for a $[Co/Pd]_5/Co/Ru/Co/[CoNi/Pd]_3/[Co/Pd]_3$ sample. As the temperature of the sample is raised around $T_C^{interlayer}$, its magnetization is reduced to zero. Without the mediation of the CoNi/Pd multilayer the coupling strength provided by the Co/Ru/Co layers is greatly reduced and the external field orientates the Co/Pd moments parallel, resulting in a significant magnetization whose direction can be control by the direction of the external magnetic field. Consequently, as shown in Fig. 45(a), we succeeded to achieve a temperature dependence of the remanent magnetization similar to FeRh with, here, and AF to FM transition at 100°C.

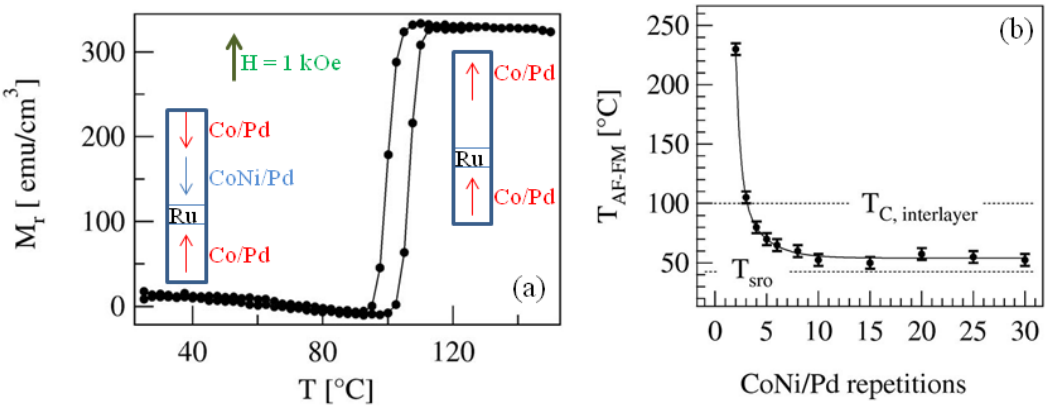

Fig. 45. (a) Remanent moment Mr of $[Co/Pd]_5/Co/Ru/Co/[CoNi/Pd]_3/[Co/Pd]_3$ as a function of temperature, measured after applying a field of 1 kG at each temperature. (b) AF-to-FM coupling transition temperature T_{AF-FM}, as a function of the number of repeats N in the CoNi/Pd multilayer in a series of $[Co/Pd]_5/Co/Ru/Co/[CoNi/Pd]_N/[Co/Pd]_3$.

Interestingly, while $T_C^{interlayer}$ of CoNi/Pd multilayers generally does not vary with the number of repeats, *N*, T_{AF-FM} of the complete structure increases significantly with decreasing number of CoNi/Pd repeats for a series of $[Co/Pd]_5/Co/Ru/Co/[CoNi/Pd]_N/[Co/Pd]_3$ samples (Fig. 45(b)). A decay length of the same order as the room temperature exchange length of the

CoNi/Pd equivalent to approximately 4 repetitions, i.e. about 6 nm, can be estimated from the data in Fig. 45(b). Moreover for N > 5, T_{AF-FM} converges to a value below $T_C^{interlayer}$. This temperature is slightly above the temperature of reorientation of out-of-plane to in-plane anisotropy (T_{sro}) for CoNi/Pd (see before). So T_{AF-FM} can be tuned to temperature lower than $T_C^{interlayer}$ which is favorable to further use in memory. Note finally that the same stack could also be used as media for bit pattern media if BPM technology is coupled to heat assisted recording as expected within 5 to 10 years.

III.2.4. Page memory demonstrator

We have recently achieved experimental proof of concept for page memory. The next set of measurements has been mostly performed by Ozhan Ozatay. As a first step, in order to easily demonstrate the successful write operation on a single magnetic wire conclusively, nanosecond electronic pulser set up was prepared on the metallic (grounded) sample stage of a AFM/MFM system. A magnetic microwires made of perpendicular anisotropy Ta (1.5)/Pd (3)/ [$Co_{55}Ni_{45}$ (0.22) / Pd (1.2)] x 22 repeats /Pd (2nm) multilayers was wire bonded onto a grounded chip carrier. Note that, here, the stack corresponds to the simplest CoNi/Pd stack with no anti-ferromagnetic coupling layer. Previously to the measurements, all wires were magnetized to saturation by applying a 2T perpendicular to plane magnetic field in an electromagnet. The magnetic wire was then placed under the microscope and electrically connected to a pulse generator and a sourcemeter via a bias tee. The wire resistance was monitored with the sourcemeter before and after the application of electrical pulses. The 2µm wide wire has about 50 Ω resistance. Any reflected pulse due to impedance mismatch was absorbed by the 50 Ω output impedance of the pulser. The stray field originating from the MFM tip is 500-700 Oe. The bulk nucleation field of CoNi/Pd film is ~3 kOe much higher than the stray fields available from MESP-HM magnetic tips. Therefore at room temperature the magnetic tip is not able to trigger magnetization reversal. However if an electrical pulse sufficiently high in amplitude (~3 10^7 A/cm^2) and width (~8ns) is applied to the nanowire, the local nucleation field can be reduced due to increasing temperature from current-induced resistive heating. Figure 46 shows the magnetic images of a 2 µm wide wire before writing and after the application of a series of 7.4 ns 3.2 V pulses in the presence of the stray field from the fixed MFM tip (stabilized at different position along the wire). This experiment provides a proof of local duplication of the magnetic data from the tip to the wire.

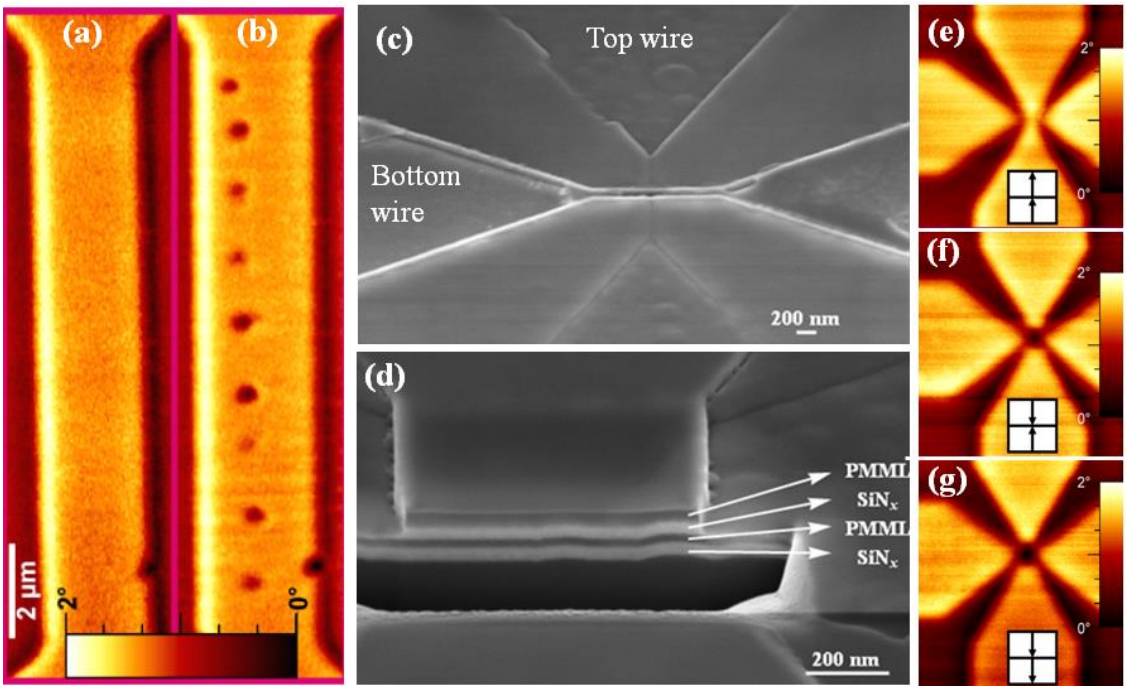

Fig. 46. Magnetic force microscopy (MFM) studies of writing onto [CoNi]/Pd microwires with a magnetic tip. (a) The MFM image of the remanent state after saturation with a 2T out of plane applied field. (b) The MFM image after writing a dot pattern with 7.4 ns 3.2V pulses (~ 3.10^7 A/cm^2)- 1nm tip height (c) The MFM image after writing HITACHI by controlling tip position with the same pulse parameters as in (b). SEM top view (c) and side view (d) two superposed 100nm wide constrictions separated by a 20 nm thick SiN_x spacer in a cross-wire configuration. (e) MFM images of the out-of-plane remanent state after saturation in a 2T (e), after the application of a "500mV, 10ns" pulse to the top constriction in the presence of a magnetic tip parked few nm above the surface (f), and after the application of a "500mV,10ns" pulse in the bottom constriction undergoing only the stray field from the top nanoconstriction respectively.

In a second step, a double constriction sample was designed (Fig. 46). The 100 nm wide constrictions acting as pinning sites and hot spot are aligned on top of each other. The two constrictions are rotated by 90° from each other as shown in the scanning electron microscope (SEM) image in Fig. 46(a). A focused ion beam (FIB) cut of the double-layer structure in Fig. 2(b) where SiN spacer layer is sandwiched in between perpendicular anisotropy magnetic CoNi/Pd multilayer nanowires. SiN isolates the individual layers electrically and thermally. MFM tip plays the role of the read/write element as described in Fig.46. It is placed a few nanometers above the surface of the top nanowire to induce magnetization reversal locally in the nanowire underneath (1^{st} writing step). By injecting current pulses only in the top wire, only this wire is made to be susceptible to the tip stray field. To transfer the top domain to the bottom nanowire the measurement setup is reconnected to the bottom nanowire and the perpendicularly oriented domain at the top nanowire is used as a source of the stray field. The magnetic tip is removed during this procedure. Analogous to the former case the bottom nanowire is heated with an electrical pulse and its magnetization is made susceptible to reversal due to the stray field coming from the top nanowire down magnetized domain. In Fig 46(e), (f) and (g) are shown the MFM image after each domain replication process respectively. The three images are plotted on the

same color scale. The relative contribution to the MFM signal from the bottom nanowire can visually amplified by multiplying each image by itself. Then one can be convinced that there is the black contrast is more important in Fig.46(g) than in Fig.46(f).

Fig. 46 demonstrates the process of vertical domain duplication in a real memory cell. We are currently working on the lateral displacement of the data by moving the domain from one constriction to another by spin transfer torque as discussed in II.2.3.

As a conclusion for the part III, we have presented two types of memory (bit pattern media and 3D Page Memory) based on magnetic multilayers. We have demonstrated that in sputtered Co/Pd multilayers nanodots assembly, switching field distribution (SFD) originates mostly from dot-to-dot dipolar interactions and misorientated grains with lower anisotropy. The latest is inherent to the sputtering growth so that we must propose a method to minimize its effect on SFD. Coupling a soft Co/Ni multilayer to hard Co/Pd multilayer allows to do it by changing the magnetization reversal mechanism from macrospin to incoherent exchange-spring like. We studied various patterning processes (pre-patterning, post-patterning, block c-polymer templates, nanoporous anodic alumina templates) to increase the bit density. Finally we proposed a new recording media concept that improves data areal density by using the third dimension perpendicular to the media. It uses data duplication by dipolar coupling and Joule heating to move the data in the third dimension. It uses spin transfer torque to move the data laterally. After a first fundamental study on dipolar replication, we realized a first demonstrator. A second demonstator is currently pursued through the great collaboration I have with the team of Ozhan Ozatay at Istambul (Bogazici University) and Giovanni Finocchio's team at Messina University.

Part IV.

Works in progress and manuscript conclusion

IV.1. Works in progress

IV.1.1. Magnetic bubbles

As already discussed in the previous chapter, the world will continue to create and consume of digital content such as movies, music, documents and other data, according to market researchers IDC. $8*10^9$Tbytes of new data are expected in 2015. In order to store and distribute this considerable amount of information, fast, high capacity, low form factor and low power non-volatile memories are are requested. They are a crucial enabler of tomorrow's Information Communication Technologies (ICT) and "storage and communication everywhere" society. Nano-devices based on magnetic materials and spin electronic are among the most pursued systems offering a solution to today's device limitations. When the dimensions of these magnetic materials are reduced to nanoscale, following the change in the critical balance of these energy terms, different micromagnetic configurations like vortex, anti-vortex or magnetic bubbles can be stable [241-243]. Magnetic vortex shown in Fig. 47(a) is maybe the most studied of theses configuration for in-plane magnetized systems. Both the detailed spin structure of this fundamental state and the spin dynamics under magnetic field have been extensively studied experimentally and theoretically [244]. Furthermore the recent demonstration of STT induced control of magnetic vortices has created technological opportunities for several types of nanoscale memories, oscillators, and radio frequency modulators and detectors [245-246].

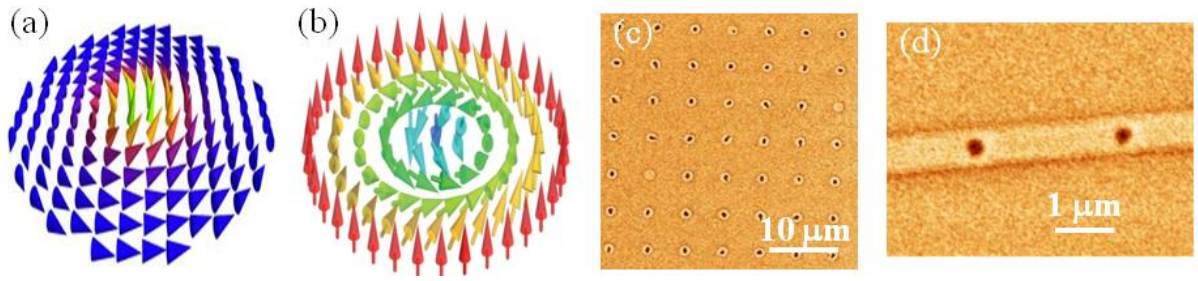

Fig. 47. Schematics of the magnetic moments in one (a) magnetic vortex and (b) magnetic soliton or bubble with perpendicular anisotropy, respectively. (c) Magnetic force microscopy image of an array of 1.25 mm circular dots. Each of them contains a single magnetic soliton (black spots). (d) Magnetic force microscopy image of a 800 nm width nanowire containing two magnetic solitons (black spots).

Magnetic bubble is the equivalent of vortex micromagnetic structure in PMA materials. Since 1970's it's known that magnetic bubbles (Fig.47(b)) can exist in PMA thin films at least in an external magnetic field or in some exotic ferromagnets in the absence of an external field but at low temperatures [247-249]. In 1996, bubble have been stabilized by the dipolar field in thin Co nanodots [243]. In 2007, similar results have been obtained in FePt disks [250]. More recently, Dzyaloshinskii-Moriya interaction in ultra-thin films with asymmetric interface is expected to help controlling the nature of the domain boundary of the bubble (i.e. either a Bloch type or Néel type magnetic domain wall) and stabilize bubble [251,252]. In Ref. [253] an analytical theory and numerical results are given for a localized oscillation mode (a droplet) which is viewed as a dissipative magnetic soliton and is related to

magnetic bubbles. The analysis performed in Refs.[253,254] clearly shows that PMA nanodots can be used to significantly widen the scope for dynamical experiments in ferromagnetic elements beyond the current work on vortex dynamics. In addition, recent theoretical predictions of very high propagation speed of solitons or bubbles in magnetic nanowires make them ideal candidates for spin torque driven magnetic memory [252,255]. These discoveries open a new route for theoretical and experimental works ranging from external magnetic field excitation to spin-transfer experiments, and from static to dynamical studies, with potential application in ultra-high density data storage, magnetic logic circuits, on-chip microwave oscillators, modulators and detectors.

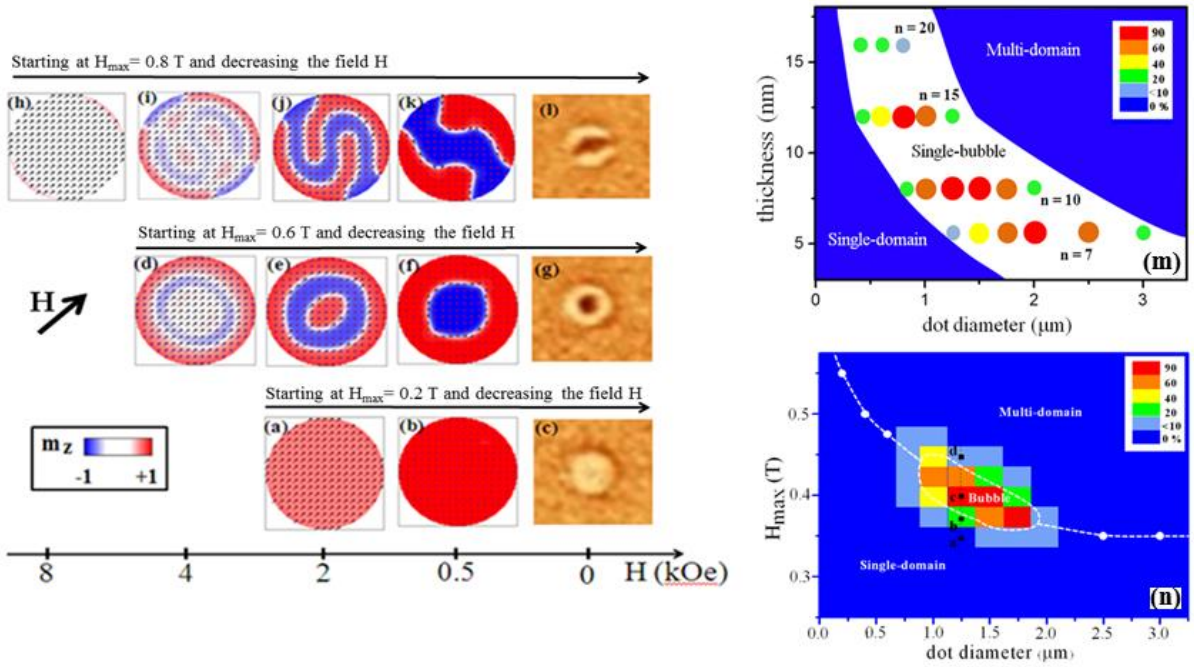

Figure 48. (a,b, d, f, e, h, i, j, k) Snapshots of the calculated magnetic configuration in a 0.8 μm diameter circular dot, having features of $[Co/Ni]_{15}$ sample, under in-plane applied field, starting from uniform out-of-plane state. The black arrow indicates the field *H* direction. The three rows correspond to the three different values of H_{max} leading respectively to (1) uniform magnetic state if H_{max} is low, (2) bubble nucleation for intermediate H_{max} value, and (3) multi-domain if H_{max} is strong enough to almost saturate the dot in-plane; (c,g,l) are MFM images, corresponding to calculated states. (m) and (n) correspond respectively to the experimental percentage of single bubble nucleation as a function of dot diameter and dot thickness, and as a function of the dots diameter and H_{max} after AC demagnetization. (n) has been measured on a$[Co/Ni]_{10}$ dot array. The color code quantifies the percentage of single bubbles.

Our first aim was to control the reproducible formation of single solitons (bubbles) in an array of Co/Ni dots. $[Co/Ni]_n$ PMA MLs films with the structure of Ta(5)/Pt(10)/$[Co(0.2)/Ni(0.6)]_{n=7,\ 10,\ or\ 15}$ /Pt(5) were deposited by Cyrile Deranlot à unité mixte CNRS-Thales (Saclay) on thermally oxidized Si wafers at room temperature by magnetron sputtering, where the numbers in parentheses are in nanometer. Anisotropy field H_k was tuned between 5 and 9 kOe. The $[Co/Ni]_n$ films were patterned into circular dots with the diameter from 0.2 to 4 μm by combining electron beam lithography (EBL) and ion beam etching (IBE) technique. The dots were adequately separated from each other so that magnetostatic interaction from other dots could be neglected in the analysis. Magnetic force

microscopy (MFM) was used to study the magnetic domain structures of the samples. We tested various method of bubble nucleation. We call success rate the number of bubble over the number of dot in a MFM image taken after the process. Out-of-plane applied field close to coercivity field or out-of-plane AC demagnetization were unsuccessful, so that the success rate was 0%. On the contrary, application of in-plane field with selected amplitude allows creating some bubbles (up to 50% of success rate). The best result was obtained for in-plane AC demagnetization with a success rate up to 90 % (Fig. 48(m) and 48(n)). The success rate drastically depends on the thickness and width of the magnetic dots since the bubble formation is mostly lead by the dipolar field energy (Fig. 48(n)). Nevertheless, it depends also strongly on the maximum in-plane field that starts the in-plane AC-demagnetization (Fig. 48(m)).

Micromagnetic calculations were performed to understand the mechanism leading to each of the three states of the phase diagrams in figure 48(m), depending on H_{max} amplitude of the AC demagnetizing process. We solved numerically the Landau-Lifshitz-Gilbert equation using three different micromagnetic codes based on finite difference, namely OOMMF [256], MUMAX3 [257], home-made solver[258]. Similar results have been obtained with the three solvers. We tested relaxation considering the equilibrium configuration achieved when the effective field energy and the magnetization are parallel for each computational cell (the algorithm stops for a residual down to 10^{-8}) as well as time evolution. For the effective field, we take into account the exchange, self-magnetostatic and out-of-plane uniaxial anisotropy fields. For the simulations in Fig. 48, we chose to simulate a 0.8µm diameter dot with n = 15 repeats (i.e. 12 nm) in order to limit computational time while maintaining discretization with1.5×1.5×12 nm^3 and 2×2×2 nm^3 cells. The simulation parameters are exchange A = 1x10^{-11} J/m, M_S = 550 kA/m and anisotropy constant K = 3.3x10^5 J/m^3. We computed the magnetic configuration while an in-plane magnetic field was set up to H_{max} and then decreased back to zero field. Three regimes could be observed depending on the value of H_{max}: (1) At H_{max} = 0.2 T, the dot magnetization is almost uniform and exhibits only a small tilt as compared with the perpendicular anisotropy axis (Fig. 48(a)). As the field decreases from H_{max} towards remanence, the magnetic state remains uniform and the magnetization goes back along the anisotropy axis (Fig. 48(b,c)). This process leading to the single-domain state is dominated by the exchange energy term. (2) For intermediate values of H_{max} around 0.4 T, the magnetic configuration exhibits a non-uniform spatial distribution of the *z*-component of the magnetization with both positive and negative region when applying H_{max} (Fig. 48(d)). Indeed H_{max} larger than a threshold value (the so-called nucleation field) changes the energy landscape in such a way that the energy barrier that separates the uniform state from the other minima is decreased and the magnetostatic energy balances the exchange energy. In other words, when the in-plane field amplitude is at intermediate values, the system reduces its dipolar field energy by forming a wavy magnetic configuration (Fig. 48(d)) with lateral variation of the *z*-component of the magnetization pointing successively in the up and down direction, instead of minimizing the exchange energy by maintaining all spins along a unique tilted direction as in Fig. 48(b). Then, when the external field is reduced back towards zero, the demagnetization field freezes the magnetic configuration in a bubble state whose shape and diameter depend on the interplay between

domain wall energy and dipolar energy. (3) For H_{max} higher than 0.5 T (the so-called saturation field) the bubble state is no longer stable under in-plane H_{max} field and the magnetic configuration tends to become uniform with all moments pointing mostly along the in-plane field direction (Fig. 48(h)). When the in-plane field is reduced, because of the symmetry of the magnetic configuration in Fig.48(i), the multi-domain state is then formed as a result of edge magnetic configuration (Fig. 48(l)). The micromagnetic simulations successfully reproduce our experimental data. Similar calculation results have been achieved for dots with diameter of 0.5 and 1 μm.

Finally, we tried to identify the reason why 100% success rate has never been reached during our experiments. Statistics on MFM images allowed us to conclude that strong edge defects (probably due to patterning) induce nucleation in the defective dots or favor propagation of the bubble domain wall up to the edge. Improving the patterning process and removing edge defects would most probably allow us to reach bubble formation success rate close to 100%. Currently, we focus on the further use of bubble in spin-valve nano-contacts, consisting of a Co/Ni ML soft thin ferromagnetic layer and a thick [Co/Ni][Co/Pt] hard layer. The cross section of the spinvalve is circular with a diameter of 250 nm (note that this width is lower than the one we used so far). The contact is circular as well, centrally positioned on the top of the free layer, with a diameter of 40 nm. The magnetic parameters used for the free layer are typical experimental values described in chapter II. These simulations have allowed us to get an idea of the dynamics of bubble magnetic configurations under different field and spin-polarized current excitation (through spin-tranfer torque effect). Under an external magnetic field applied in the film plane, we systematically computed the oscillation frequency as a function of the applied current density for various different values of in-plane field amplitude. The frequency (few Ghz) decreases with increasing current. With the chosen parameter, an in-plane external magnetic field of 50mT is sufficient to give rise to a measurable oscillation of the z-component of the magnetization below the contact area through the variation of the GMR signal achievable in this system. The external field also modifies the structure of the excited mode. Actually, together with a rotational motion similar to the one obtained at zero field, a phenomenon of expansion and contraction of the reversed domain area is present. Moreover, it is possible to notice that the bubble mode enlarges while the in-plane component of the magnetization aligns with the field direction and shrinks while it goes to the opposite direction. In addition, we found that for a fixed value of the current, the thicker the free layer is, the higher is the output frequency. This aspect can be qualitative explained by the reduction of the out-of-plane demagnetizing field at larger thickness. All these theoretical predictions have now to be confirmed experimentally. In order to do it, I spent Oct-Dec. 2014 in Pr. Andrew Kent's lab at New York university, whose team has capabilities of patterning complex nanostructures such as nanocontacts but we did not yet have any successful results. Ibrahim Cinar, phD student in Ozhan Ozatay's group, will stay at Nancy for one year, starting in Step. 2016, to help me on this project, as well as on bubble motion in microwires.

IV.1.2. New interface effects and novel electrodes for magnetic tunnel junctions

Half metallicity of Δ1 electrons in FeCo/MgO/FeCo MTJs

When I joined IJL Nancy in 2009, colleagues in "Nanomagnetism and spintronic" group have worked for more than ten years on single crystal bcc (100) Fe/MgO/Fe or similar MTJs [259-263]. MgO-based MTJ differs from Al2O3-based MTJ because of the single crystalline nature of the barrier and the electrodes. Four basic points have to be invoked to understand the electronic transport in MgO-based MTJs [262,264-266]: (i) The tunnelling current in the coherent regime (without electron scattering by defects or interfaces) is established keeping the spin and symmetry of the electronic states. The electrons are thus described by Bloch wave functions $\psi(r) = u_k(r)e^{ikr}$ where $u_k(r)$ gets the potential symmetry. (ii) For thick MgO barrier (1 to 3 nm), the current is roughly perpendicular to the interface that is along (001) direction (inclined trajectories are more attenuated) i.e. electrons have Δ propagation vector in the reciprocal lattice. In this geometry, the probability of finding the electron on the other side of the tunnel barrier exponentially decreases with the thickness d of the latter as $T \propto \exp - 2\kappa d$ where κ is the attenuation factor. (iii) There are four main types of Δ electrons which are classified as a function of their orbital symmetry Δ1, Δ2, Δ2' and Δ5 (Fig. 49(a,b)). They have a different κ value. The MgO barrier plays the role of symmetry filter and allows only Δ1 and Δ5 electrons to pass. The other channels of conduction are much more strongly attenuated by MgO (Fig. 49(c)). (iv) There is no density of state (DOS) for minority spin along (001) direction for Δ1 electrons. This properties is called half-metallicity and here it exists only for Δ1 electrons. As Δ1 are the less attenuated electrons, the resistance increases a lot in the case in the anti-parallel state of the electrodes magnetizations (Fig. 49(d,e)). So the difference between parallel state and anti-parallel state resistances is large, i.e. TMR is large.

Very high TMRs were calculated, around 1000% at 0K for Fe/MgO/Fe(001) [264,265]. Even larger TMR values are predicted using equimolar FeCo electrodes and pure Co electrodes since they do not hold Δ5 states at the Fermi level for majority spins (Fig. 49(f)) [267]. On the experimental point of view, very large TMR were indeed observed, but not as large as predicted. The best reported values were 480% at 20K in MBE grown Fe/MgO/Fe(001) [268,269], 530% in MBE grown $Fe_{0.75}Co_{0.25}$/MgO/ $Fe_{0.75}Co_{0.25}$(001) [270], and around 1100% in FeCoB/MgO/FeCoB at 5K [115]. Finally, if Lee et al. [271] observed CoFeB/MgO/CoFeB TMR increases as Co concentration increases from 0% to 25%, the TMR is also found to monotonically drop down for higher Co content until pure Co electrode. This result does not fit with theoretical predictions. The authors explained their result by the poor crystallization of the stack after annealing for high Co content. I'll briefly show here that the maximum of TMR for $Co_{25}Fe_{75}$ is actually linked to electronic structure more than structural effect.

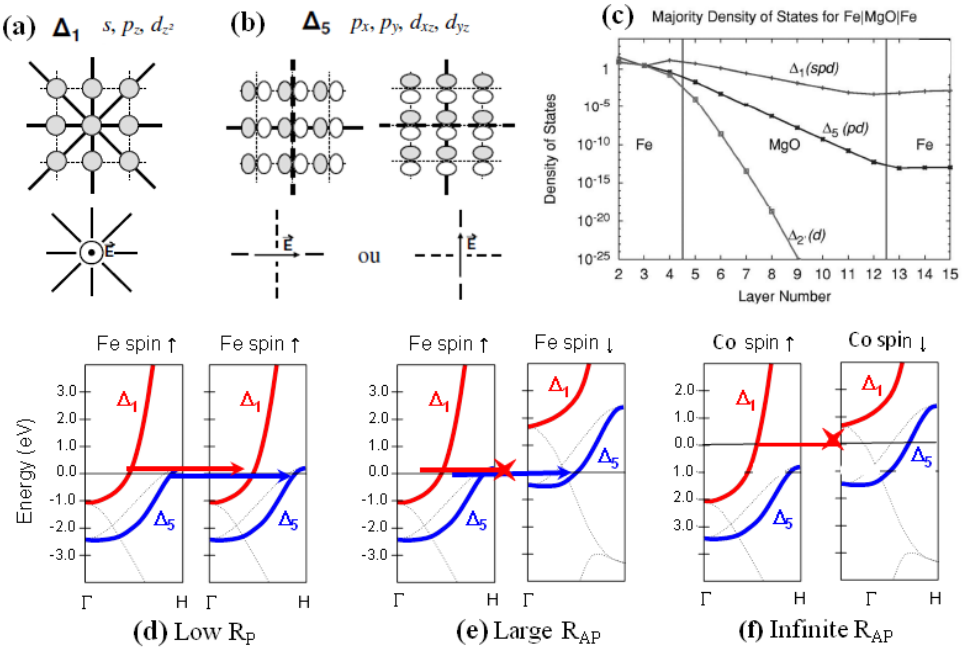

Fig.49. (a) Schemes of the so-called Δ1 and Δ5 orbital lobes with opposite sign (grey and white colors) as their symmetry planes (solid line) and anti-symmetry planes (dashed line). Underneath are represented the electric field that can excite transitions for these orbitals. (c) Calculated symmetry dependant majority DOS transmission for a (001)Fe/MgO(8 atomic layer)/Fe [264]. (d) Scheme of tunnel transport between two bcc Fe layer with parallel (d) and anti-parallel magnetizations (e) using the state present at the Fermi level in the band diagram in the Δ direction. (f) similar diagram for pure Co and show no state at the Fermi level. As a consequence infinite TMR was expected [267].

While being taught on MBE experiments by S. Andrieu for growing single crystal Co/Ni MLs, and while continuing in parallel F. Bonell phD work [272], we found that MBE grown (100) $Fe_{1-x}Co_x$/MgO/$Fe_{1-x}Co_x$ single crystal MTJs also show a maximum of TMR for $Co_{25}Fe_{75}$ while the MgO barrier is not affected by Co concentration (Fig.50). To understand this behavior, information on both spin and symmetry of tunneling electrons are needed. For that purpose, I benefited from the spin- resolved photo-emission spectroscopy (SRPES) developed by F. Bertran, P. Le Fèvre and A. Taleb-Ibrahimi on CASSIOPEE beamline [75] at SOLEIL synchrotron and the preliminary work of S. Andrieu and F. Bonell on pure Fe and FeV films. A detail description is to be found in F. Bonell phD thesis [272].

The SRPES geometry is shown in Fig.50. The small aperture (±1.8°) of the detector allows detecting electrons only with Δ symmetry. The spin information is obtained in SRPES using a Mott detector added to the energy detector. We used two light polarizations, either vertical (*s* polarization) or horizontal (*p* polarization). The final states reached by photoemission are far above the Fermi level (E_F) and have the Δ_1 symmetry of free electrons [273,274]. The dipolar selection rules indicate that only the initial states having the same symmetry as the electric field with respect to the [001] direction can be excited [272,275]. Thus, in *s* polarization, only $\Delta_5 \rightarrow \Delta_1$ transitions are explored, whereas both $\Delta_5 \rightarrow \Delta_1$ and $\Delta_1 \rightarrow \Delta_1$ transitions occur in *p* polarization. An experimental illustration of this orbital selectivity is given in Fig.50 on Fe(001) at a photon energy of 60 eV. The peaks observed in

PES spectra of (001) Fe film can be assigned unambiguously: when a transition is seen for both photon polarizations, the excited state's symmetry is Δ_5, and when it is only seen using p polarization, it is Δ_1. The observed s and p peaks in Fig.50 fit well with theoretical predictions of Fig. 50(d,e). Using both photon polarizations sequentially allows us to determine the symmetry of the detected peaks in the photoemission spectra. Such unique information is crucial in correctly understanding which states may participate in the spin-polarized electrical transport in MTJs.

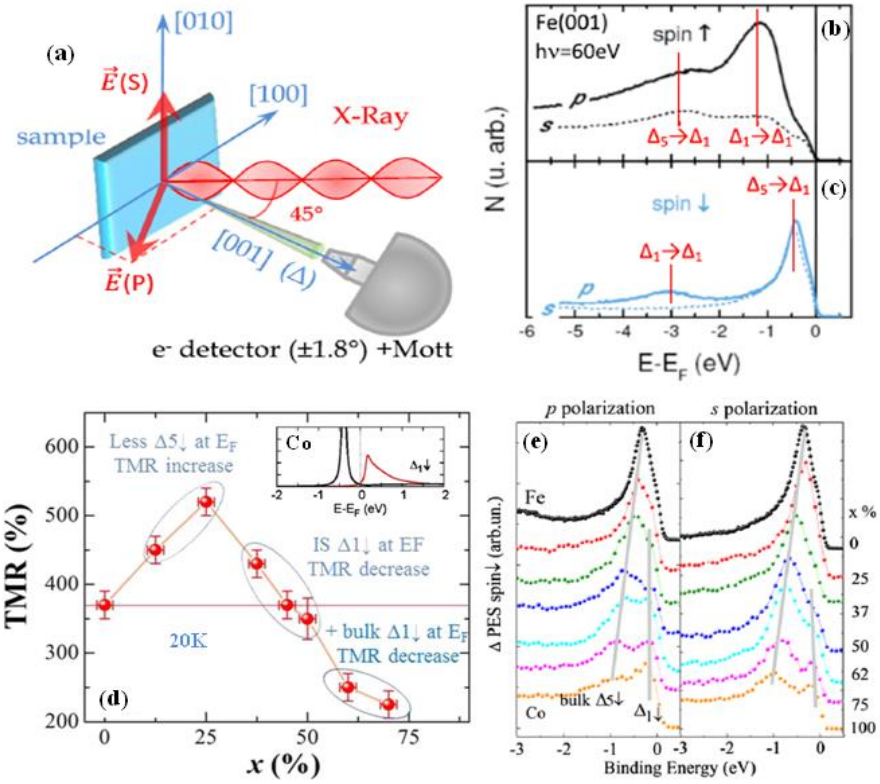

Fig. 50. (a) Schemes of the SR-PES experiment and measurement on Fe(001) for majority spins (b) and minority spins (c) The incident photon field is in-sample-plane for s polarization and can be projected in sample in-plane and outof-plane components for p polarization. The small aperture of the detector allows detecting electrons only with Δ symmetry. (d) TMR variation at 20K with Co content for a series of $Fe_{1-x}Co_x$/MgO/$Fe_{1-x}Co_x$ (001) MTJs. The TMR increases at low Co content is consistent with calculation, whereas TMR decreases above 25% Co due to the interface State, plus the empty bulk Δ_1 minority band that crosses the Fermi level for Co content larger than 50%. In inset, Calculated bulk (red) and surface (black) Δ_1 DOS for pure Co. (e) and (f) show Spin-resolved PES spectra obtained at 60 eV photon energy, for p and s polarization respectively, on a series of $Fe_{1-x}Co_x$ (001) layers. The gray lines are guide to the eyes to visualize the energy displacement of the peaks.

Bcc $Fe_{1-x}Co_x$ alloys were grown on single crystal MgO covered with a Fe(10nm) buffer in a MBE chamber coupled to the SRPES chamber. One should note that to get large TMR the $Fe_{1-x}Co_x$ should be in the bcc structure. The crystalline structure of bulk $Fe_{1-x}Co_x$ layers is known to be bcc up to x around 70%, and hcp for higher Co content. However, it is possible to stabilize the bcc structure for the whole Co concentration range by growing very thin $Fe_{1-x}Co_x$ alloys on a bcc Fe(001) buffer layer, as verified with RHEED. The observed transitions on the SRPES spectra (Fig.50(e,f)) were thus identified with respect to their spin

and symmetry, based on density of states (DOS) calculated by L. Calmels from first principles for bulk BCC $Fe_{1-x}Co_x$ alloys as described in Ref. [276] and shown in Fig.50. Above 25% Co a new Δ_1 state is observed below E_F for minority spin channel and using angle-resolved PES this state was identified to be a surface state. We verified that this surface state still exist when growing MgO on top (becoming an interface sate). This interface state has been already predicted and discussed for Fe/MgO/Fe MTJs however for pure Fe, calculations show that it is empty [277,278]. Moreover, for concentration larger than 50% Co, Δ_1 minority bulk state reaches the Fermi level so that it adds to the conductivity in the anti-parallel state, thus further decreases TMR (see inset Fig. 50(d)). Finally, MTJ conductivity versus bias voltage curves have been used to confirm our SRPES findings.

Half metallicity in Heusler alloys

As minority spin density will always remain in MgO-based MTJs with Co_xFe_{1-x}(B) electrodes, one has to test other electrodes in order to reach higher TMR. Heusler coumpounds have been calculated to be half-metallic materials, i.e. there is no electron of any symmetry in the minority band at the Fermi level [279,280]. Recently, MR enhancements have indeed been observed by different research groups using materials with Heusler-like structure such as $Co_{2-x}Fe_{1+x}Ge$ in spin-valve [281] and Co_2MnSi in MTJs [282]. A second positive consequence in view of implementation to STT-MRAM is that the lack of minority spin state at E_F in such materials should lead to very low damping. Up to now, indirect method like transport measurements or FMR have lead to claim some Heusler alloys to be half-metallic [279,280]. Nevertheless, transport or FMR features cannot be simply linked to DOS since many other ingredient are involved in these processes.

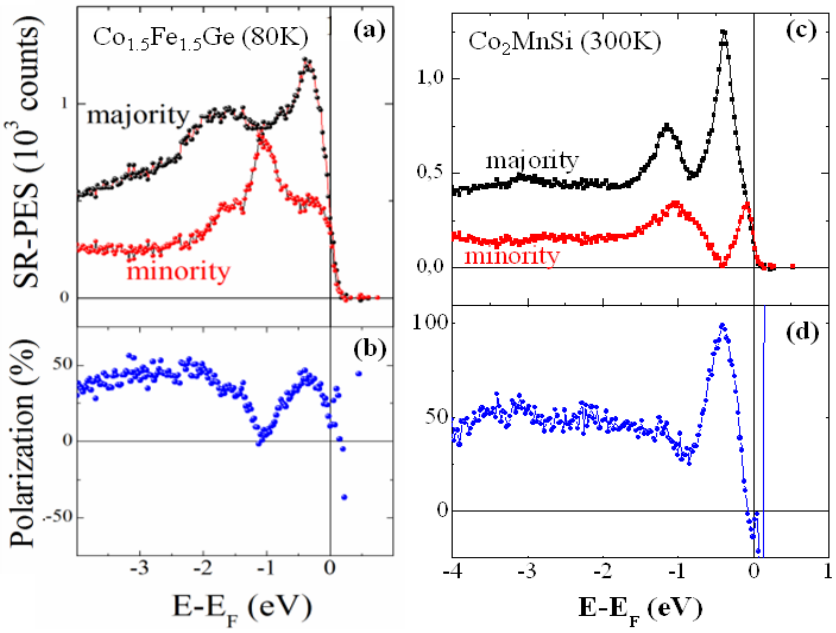

Fig. 51. SRPES (a) and spin-polarization (b) fully integrated in k measured at 80K on $Co_{1.5}Fe_{1.5}Ge$. No pseudo-gap is found. SRPES (c) and spin-polarization (d) fully integrated in k measured at 300K on Co_2MnSi. A pseudo-gap is observed at 0.5 eV below the Fermi level.

Our objective is to use SRPES fully integrated in k as a direct method to test the half-metallicity behaviour for both $Co_{2-x}Fe_{1+x}Ge$ and Co_2MnSi such materials. All ab-initio DOS calculations highlight the importance of chemical ordering [283][284]. In X_2YZ, while the chemical ordering between Y and Z seems not be crucial to conserve the pseudo-gap at the Fermi level, any substitution between X and Y or Z sites destroys it. For instance, calculations suggest that $Co_{1.5}Fe_{1.5}Ge$ is a good choice of alloy, because the reduced number of Co atoms decreases the probability of substitutional disorder between Co and Fe or Ge sites [283]. As of Co_2MnSi, the largest TMR have been observed so far with a small excess of Mn [282].

With the phD thesis of Amina Neggache (2011-2014), S. Andrieu and I have started to grow and study $Co_{1.5}Fe_{1.5}Ge(001)$ films and Co_2MnSi by MBE on MgO single crystal substrate. Regarding CFG, the proper Fm-3m crystalline structure with the expected lattice constant is obtained accompanied with chemical ordering. All structural and magnetic characterizations clearly indicate chemical ordering consistent with the full Heusler structure. In particular, low Gilbert damping coefficients (down to 0.007) are obtained. However, some chemical disorder involving Co atoms occupancy in Y sites instead of Fe cannot be ruled out here, which would lead in accordance to our theoretical investigations to a suppression or reduction of the pseudo gap at the Fermi level. The spin-polarization of $Co_{1.5}Fe_{1.5}Ge$ close to E_F is observed to be positive opposed to the negative spin-polarization of FeCo(001), but no pseudo-gap for minority spin at E_F is observed (Fig. 51(b)). Some minority spin DOS with Δ_1 symmetry was observed at E_F explaining the modest TMR values (lower than100%) observed in MgO-based MTJs using $Co_{1.5}Fe_{1.5}Ge$ electrodes. On the contrary, our very recent SRPES measurements on Co_2MnSi are very promising. Although the DOS and spin-polarization versus energy curves look similar to the ones of $Co_{1.5}Fe_{1.5}Ge$, Co_2MnSi shows 100% polarization at 0.3 eV below E_F (Fig. 51(d)) To our knowledge it is the first time that half-metallicity is observed experimentally for all the electrons of a compounds (indeed, e.g. Fe is also half-metallic when considering only Δ_1 electrons). We showed that a minority spin gap at *E*F can nevertheless be recovered either by tuning the concentration in Mn and Si or by covering the CMS surface by Mn, MnSi, or MgO. This spin-gap recovery at E_F results in extremely small damping coefficients, reaching values as low as 7×10^{-4}. Currently, magnetic tunnel junctions with CMS electrodes are tested and the next objective would be to achieve PMA Co_2MnSi to use it as electrode in PMA MgO-based MTJ or PMA spin-valve.

Electric field control of interface magnetic features

The interest about PMA CoFeB/MgO/CoFeB MTJ for STT-MRAM, started in 2010 [115,285,286], has increased even more recently when PMA has been shown to be tunable with MTJ bias voltage [116,287-289]. Theoretical studies have recently addressed this problem and explain the effect by electrons accumulation or depletion at the magnetic metal / dielectric interface that affects the interface PMA at CoFe/MgO interface [61,290,291]. Similar effect have been reported in other systems where “charge” and “discharge” of the ferromagnetic surface or interface can be controlled, proving that this effect can happen in a

large variety of magnetic systems [287,292]. Motivated by the lack of clean experimental data able to confirm theoretical calculations on the value and the electrical control of PMA at Fe/MgO interface, and based on the knowledge and experience about Fe/MgO/Fe epitaxial MTJ in Nancy, we have recently started an activity on this subject.

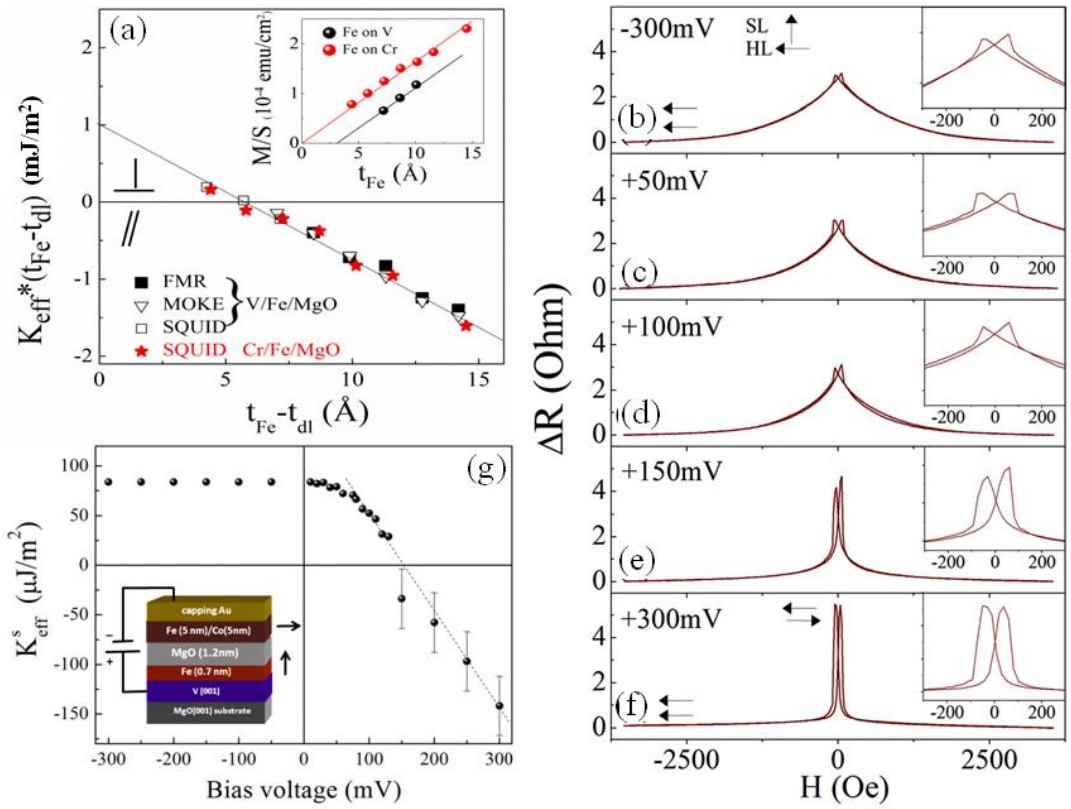

FIG. 52. (a) Effective anisotropy constant K_{eff} times t_{Fe}-t_{dl} as a function of t_{Fe}-t_{dl} deduced from SQUID-VSM, FMR and MOKE measurements at RT for both V/Fe/MgO and Cr/Fe/MgO systems. The line is a fit using eq.(2). In inset are plotted the areal magnetization versus Fe thickness, showing that t_{dl}=0 for Fe on Cr and t_{dl}=3Å for Fe on V. (b) ΔR vs in-plane field measured on Fe(0.7nm)/MgO(1.2nm)/Fe(5nm)/Co(5nm) MTJ at ΔV=-300(b), +50(c), +100(d), +150(e), and +300 mV(f). Zooms for low in-plane field range are shown in inset. The top and bottom arrows represent a schematic view of the magnetization orientation of the bottom and top layer respectively. (g) Effective anisotropy Ks times Fe soft layer thickness (t) as a function of the bias voltage applied to the MTJ. The dashed line is just a guide for the eye and has been used to determine the β parameter (see text).

Theoretical analyses highlight different possible mechanism that would lead to PMA at Fe/MgO interface. Particularly, Yang *et al.* attributed the PMA to a combination of two factors: overlap between O-pz and transition metal dz^2 orbitals, as well as degeneracy lift of out-of-plane 3d orbitals induced by spin-orbit coupling [61]. In addition He et al. demonstrated that the lattice mismatch between MgO and FeCo could also induce an additional PMA [293]. Predicted PMA amplitudes can reach 1.46 mJ/m^2 in Ref.[61] and 1.9 mJ/m^2 in Ref.[293] per Fe-MgO interface. Such values are more than 2 times larger the value obtained for other interface-induced PMA like in Co/Pd, Co/Pt, Fe/Ag, Fe/Au or Co/Ni as discussed here in part I [4]. Experimentally, the amplitude of PMA anisotropy found in the literature show a large spectrum of PMA amplitude and the largest values stay much below

the theoretical predictions. One could argue that CoFeB-MgO interfaces obtained by sputtering exhibit structural defects whereas perfect interfaces are generally assumed in calculations. However even in MBE-grown Au/Fe/MgO system, the Fe/MgO magnetic anisotropy is found to be much lower than the Au/Fe one, i.e. lower than 0.5 mJ/m^2 [288,289].

The samples were grown on single-crystal MgO (100) substrate using MBE with a base-pressure lower than 10^{-10} Torr. The V or Cr buffer layers were deposited at room temperature (RT) and then annealed at 600 °C. An Fe wedge was then grown on the V or Cr buffer layers and covered with a 6-ML (1.2nm) MgO(001) film. The typical stacking of a sample is thus V or Cr(10nm)/ Fe(t_{Fe}) /MgO(1.2nm) where the Fe thickness t_{Fe} is varied from 5 to 12 atomic layers every 1 atomic layer step. Fe was deposited at RT with no further annealing and capped with MgO also at RT. The epitaxial relationship, growth mode, number of deposited MLs and surface flatness were controlled in-situ using RHEED. The main difference between Cr/Fe/MgO and V/Fe/MgO originates from the "magnetic dead layer" that exists at V/Fe interface. The measured areal magnetic moment (i.e. M divided by sample area in erg/cm^2) vs thickness in inset of Fig. 52(a) shows that, if the M(t_{Fe}) slope in V/Fe/MgO is similar to the slope observed in Cr/Fe/MgO (corresponding to a magnetization of 1680 ± 50 kA/m which is close to the bulk Fe value), the linear fit crosses zero for 0.3 nm. The 2 effective dead atomic layer at V/Fe interface has been explained by roughness, charge transfer and anti-parallel polarization of the V [67,294,295]. An oxygen contamination of the starting V(001) surface should also contribute to these magnetic dead layers in Fe grown at RT [296].

The effective anisotropy constant K_{eff} was extracted from magnetometry measurements (i.e. area between the out-of-plane and in-plane loops in one of the hysteresis quadrants). The results are shown in Fig. 52 where we plot K_{eff} for the magnetic thickness (t_{Fe}–t_{dl}). We also measured the V/Fe/MgO wedge samples for t_{Fe} ranging from 7 to 12 atomic layers using MOKE and FMR. The FMR measurements were performed at UCSD San Diego. The values of effective anisotropies K_{eff} extracted from SQUID-VSM, FMR and MOKE experiments are plotted in Fig. 52(a) versus the active Fe thickness corrected from the dead layers at Fe/V interface. The unique linear variation for both Cr/Fe/MgO and V/Fe/MgO samples depend on the different anisotropy contributions as already described in part II.1:

$$K_{eff}(t_{Fe} - t_{dl}) = (K_V - 2\pi M_s^2)(t_{Fe} - t_{dl}) + K_s$$

where K_v is the magnetic volume anisotropy and K_s is the interfaces anisotropy acting in the Fe layer. The $-2\pi M_s^2$ term comes from the shape anisotropy for a thin film. The negative sign shows that this anisotropy term tends to align the magnetization in the film plane. The thickness t_{Fe}-t_{dl} is the effective thickness of the film where t_{dl}=2MLs for Fe on V and t_{dl}=0 for Fe on Cr.

From the slope of the experimental curve in Fig. 52(a), we can extract a value of the volume anisotropy K_v–$2\pi M_s^2$= -1.78*10^6 J/m^3. By taking into account M_s=1680±50 kA/m deduced from the inset of Fig.52, the calculated shape anisotropy term is $2\pi M_s^2$=1.8*10^6 J/m^3. Therefore we can conclude that K_V is small as compared with shape anisotropy. Indeed

volume anisotropy of cubic Fe is usually of the order of few 10^4 J/m^3 [Graham1958][57]and magneto-elastic contributions are expected to be small. It should be pointed out that a magneto-elastic contribution in K_v should also be taken into account in the case of strained epitaxial thin films. This contribution is very small in Cr/Fe/MgO since the Cr/Fe misfit is around 0.6%. But the misfit is much larger in V/Fe, around 5.6%. Consequently, if the Fe growth on V is pseudomorphic, the magnetoelastic anisotropy should be non-negligible. However, we have shown in a previous study [297] that the critical thickness for plastic relaxation during Fe growth on V at RT in our MBE system is lower than 1ML. This means that Fe layer relaxes to its stable bcc structure, leading to small magnetoelastic anisotropy. As a consequence the volume anisotropy originates mostly from the demagnetization term. On the other hand, the extracted Ks of 1 ±0.1 mJ/m^2 contains one contribution from the V/Fe or Cr/Fe interfaces and another one from the Fe/MgO. We have performed magnetometry measurement on our V/Fe/V and we extracted an interface anisotropy of 0 ± 0.1 mJ/m^2 in good agreement with previous experiments [298-300]. A value of K_s at Cr/Fe interface has been measured only once in Ref. [34] as +0.19 mJ/m^2 however, surprinsingly no out-of-plane magnetization has ever been reported even for very thin Cr/Fe/Cr films. As a consequence, we do think that Ks originat mostly from Fe/MgO interface. $Ks^{Fe/MgO}$ amplitude of 1 ±0.1 mJ/m^2 is about two times larger than Co/Ni(111) one. Nevertheless it is still slightly lower than the calculated in Ref. [61]. One possible explanation may be the level of oxidation of Fe in contact with MgO as pointed out in ref.[14]. Other defects like steps, kinks, vacancies present in real systems are difficult to take into account in calculations and may also decrease Fe/MgO interface anisotropy.

In a second V/Fe/MgO stack was used to study electric field effect on Fe/MgO interface anisotropy. MBE-grown V(10nm)/Fe(0.7nm)/MgO(1.2nm)/Fe(5nm)/Co(5nm) MTJ was prepared and UV-patterned. The bottom V/Fe(0.7nm) is the soft layer and has PMA. The Fe(5nm)/Co(5nm) bilayer forms the hard layer with in-plane anisotropy. In such MTJ, on the one hand, an electric field is naturally applied in the MgO barrier as a bias voltage is applied on the MTJ to measure its resistance and, on the other hand, any change of the magnetization direction may be detected using the large TMR of Fe/MgO/Fe(001). Resistance versus in-plane field measurements for several biases are shown in Fig. 52(b) to (f). When the bias is negative (negative charges added at the soft Fe/MgO interface), only shallow change in R(H) is observed, consistent with a coherent rotation of the soft layer from perpendicular to in-plane. On the contrary, for positive bias above 100mV (positive charges added at the soft Fe/MgO interface), the R(H) curves totally change and are consistent with in-plane magnetization for both electrodes. By performing resistance versus field measurement both for in-plane and out-of-plane field, the bottom Fe layer effective anisotropy is quantified as a function of bias voltage. The effective anisotropy energy per surface area K^S_{eff} is plotted as a function of the bias voltage in Fig.52(f). Two regimes are observed. From -300mV to +50mV, K^S_{eff} stays constant and positive (i.e. PMA), so the anisotropy is not affected by the voltage. Above +50mV, a linear variation is observed, and K_s switches from positive (out-of-plane anisotropy) to negative (in-plane anisotropy). Niranjan et al. [290] found such a linear variation using ab initio calculations and propose to quantify it by calculating the slope β_s defined as: $\Delta K_s = \beta_s . E$, with $E = \Delta V / t_{MgO}$ the electric field and t_{MgO} the MgO layer

thickness. The calculated slope is here equal to β_s = -1150±50 fJ.V^{-1}.m^{-1}. It would lead to is estimated around 0.01 electrons / atom at 300 mV which is five times larger than the previous reports on similar systems [289]. Unfortunately, such high values as compared with theoretical prediction and comparable experimental data, as well as the asymmetric effect with voltage also not predicted by theory show that the simple picture of electron accumulation/depletion at the Fe/MgO interface due the electric field is probably not sufficient to explain our results. One possible explanation is that the MgO barrier does not behave like an ideal dielectric layer, due to defects in the MgO barrier, like vacancies or dislocations. Thus these defects may trap charges, and electro-migration may occur to move these defects towards Fe/MgO interfaces as proposed in ref. [301]. The origin of the discrepancy may also come from the Fe/MgO interface. Bonell et al [302] recently observed that the Fe-O hybridization at the Fe/MgO interface is strongly affected by the electric field applied in the barrier.

Next step is to use either Cr/Fe/MgO/metal or V/Fe/MgO/metal by synchrotron techniques to investigate and further understand PMA origin as well as the changes induced by voltage. The approach will be similar to the XMCD experiments on Co/Ni(111) MLs presented in part I.1. These measurements will include XMCD measurement at the Fe edge as a function of Fe thickness to determine the elemental magnetization and to determine the spin and orbital moments of the Fe, and XMCD measurement at the Fe edge as a function of the Electric field to determine the evolution of the spin and orbital moments of the Fe. In the latest case, because of the applied voltage in our experiments, the electron yield detection scheme cannot be employed. We, therefore, will use the fluorescence yield. Similar experiment has been recently successfully performed as described in Ref. [302]. XAS will be taken at various positive and negative voltages and at zero bias.

In parallel, we would like to investigate on the voltage-induced control of Curie temperature (Tc). Such an effect has been reported in semi-conductors [303,304] but only in one metallic ferromagnetic system [305,306]. Chiba et al. have succeeded in changing by 10 K the Tc of a Co (0.4nm) ultra-thin layer [305,306]. Here the change in the number of electrons is presumed to play a central role in enhancing or reducing the overall magnetic coupling, leading to the modulation of the Tc. However, a change in magnetocrystalline anisotropy may also affect the Tc in a 2D ferromagnetic film [307]. We have just started working on FeV (1nm) alloys whose Tc can be tuned in changing the V concentration (see Tom Ferte's master thesis in 2014). Besides FeV alloys have also damping lower than 10^{-2} and can be used in a high TMR FeV/MgO/Fe/Co MTJ thanks to a very small tunable misfit between FeV and MgO [262]. So we will continue along this line to understand how the voltage can affect Tc in FeV alloy.

IV.1.3. Magnetic frustration in assembly of nano-dots

The ability to design "upon request" arbitrary network thanks to lithography and the possibility to determine completely the "spin" configuration with magnetic imaging offer a wide playground for statistical physics. While working on bit pattern media system with array of Co/Pt MLs PMA nanobumps in hexagonal lattice (see part III.1), we used AC out-of-plane field demagnetization to probe the interactions between bumps. Although some local inter-bump ferromagnetic exchange coupling was found, the main interaction is long range dipolar fields that tend to align neighboring bumps anti-parallel. However, in a triangular lattice, when considering the three first neighbours (Fig. 53(b)) one can notice a frustration since all three spins cannot be anti-parallel to their neighbours. Frustration of magnetic spins interacting through dipolar fields in triangular spin lattice has been heavily studied since the 50's [308,309] and remains a subject of current investigation due to the development of micro- and nano-patterning techniques[310-312].

In Fig. 53(c), we show MFM image at remanence after AC demagnetization under decreasing out-of-plane field. Unlike the labyrinth pattern at coercitive field observed during regular field loop, out-of-plane AC demagnetization leads to a mostly well-ordered succession of up and down magnetized stripes. Each stripe consists in a 1D chain of bumps. The width of both serpentine domains and stripes domains is mostly of the order of the array period. Kireev et al. have recently reported a work that is particularly well suited to help understanding the consequences of dipolar frustrations in our bump assembly [313]. They demonstrate that the ground state of an assembly of hexagonal array of perpendicularly magnetized Ising spins interacting only through the anti-ferromagnetic dipolar interactions consists in series of uniformly magnetized stripes of spins, each stripe being oppositely magnetized to its neighboring stripes. Indeed in this configuration, each dot has the maximum number of anti-parallely magnetized neighbors, i.e. four. We have reproduced their results taking into account 25 Ising spins (Fig. 53(c)). We have also calculated how the fundamental state evolves towards wider domains when considering non-null ferromagnetic coupling between closest neighbors.

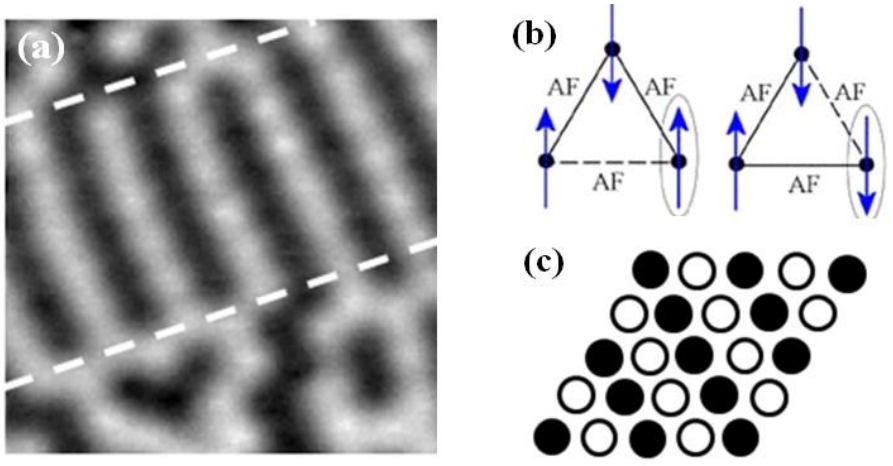

Fig. 53. 1µm×1µm MFM image measured at remanence after AC out-of-plane demagnetization of a 100 nm period array of Co/Pt MLs nanobumps (b) Scheme of dipolar frustrations in triangular (c) Ground states for 25 spins in dipolar interaction.

The well-ordered stripes configuration does not cover the whole MFM image of Fig. 53(a). Stripes have finite length as highlighted by the two dashed lines in Fig. 53(a). Higher energy configurations are observed in the case of structural defects. Intrinsic SFD can also affect the fundamental, although here it is a second order term. The short- and long-range influence of these structural defects have been studied and higher (but amongst the lowest) energy states have been investigated such as Y-shape domains and zigzag stripes spread perpendicularly to the stripes. This latest can be modeled by accounting for dipolarly coupled Ising spins is most probably stabilized by the non-null interbump ferromagnetic exchange-coupling.

Up to now only Ising spin systems have been studied. Multi axes Ising systems have first been realized as elongated nanomagnets with planar magnetization (on square [310] or Kagome [311] lattice) or dots with PMA [314]. However, beyond Ising spins, statistical physics and condensed matter physics have shown the interest of other spin models like *q*-state Potts models (*q* different possible spin orientation) or even XY model (isotropic in plane orientation). F. Montaigne and I have started in oct. 2013 to co-advise Damien Louis (as phD student) with the objective of fabricating and studying artificial lattices of “4-state spins" in dipolar interaction.

We studied the case of a so-called “dipolar Potts model” with 4 states and dipolarly coupled spins. We initially realized a theoretical study showing that on a square lattice, the fundamental state for the spin configuration changes with varying the angle between the spins. We found three mai regimes: anti-ferromagnetic configuration at low angle, loops at large angle, and ferromagnetic state at intermediate angle (around 22.5 degree). These states are shown in Fig. 54. The ferromagnetic state is particularly original for a 2D spins system with only dipolar coupling.

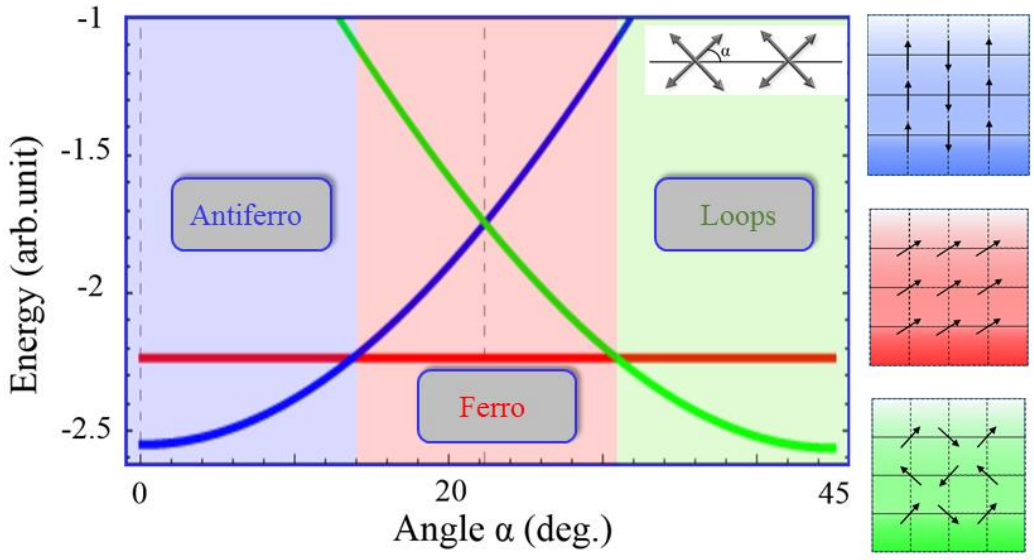

Fig. 54. Energy of three magnetic configurations (schemed on the rigth) according to the angle alpha defined as the angle between the anisotropy direction and one network axis.

In order to realize the Potts-like models, we need magnetic nanostructures with well defined magnetic configurations having 4 equivalent directions. We chose epitaxial Fe films for its cubic anisotropy and square dots to enhance the 4 anisotropy axis strength. Micromagnetic simulations have shown that a thickness below 2 nm of the Fe film is required so that the ground state of the "spin" is a monodomain state (and to avoid vortex state). The 2 nm thick epitaxial Fe films with a well defined cubic anisotropy (without uniaxial anisotropy) is grown by molecular beam epitaxy on MgO substrate and a 5 nm Vananium buffer. The nanostructures are then patterned by electron beam lithography and ion beam etching. Several capping layers have been successfully used (V, Au, MgO) and the capping layer (V) is selected in order to have zero interface anisotropy either at V/Fe or Fe/V interface. At room temperature the square dots have a single domain magnetic configuration which can take 4 equivalent directions, as desired for the Potts model dipole 4 states. Temperature raise up to 350 ° C (well below the Curie temperature) under zero field allows to thermally activate the reorientation of the spins so they are as close as possible to the ground state of the assembly spins. The magnetic configurations observed after annealing, using a magnetic force microscope, show the role of dipolar coupling when varying the dot-to-dot distance and the influence of the angle between the spin axis and the network when varying this angle. The different spin states theoretically predicted are observed and in particular the state of spins aligned "ferromagnetic".

Our thermal demagnetization is clearly not yet optimized and there is still a lot of effort to be provided to get closer to the fundamental state. Nevertheless we have demonstrated that it is here much better than any field demagnetization process. In the near future, we must image the dynamic of spin switching during the thermal process. We already plan to perform X-PEEM measurements at SOLEIL synchrotron to that purpose.

IV.2. Manuscript conclusion and perspectives

My research belongs to the field of nanomagnetism and spintronic. The work I performed during the last 8 years on magnetic multilayer with perpendicular anisotropy show how these two themes are closely linked and how they feed each other. Within the first one, I've been interested in the magnetic features induced interface between layers of different chemical nature (interface anisotropy, increased local magnetization, etc.), the influence of magnetic coupling (exchange coupling or dipolar coupling), as well as the competition between them. Besides I tried to follow the exponential flow of new spintronic effects. I mostly used model single crystal Perpendicular magnetic anisotropy multilayer systems whose properties were deeply characterized by many means, in order to properly study the spin-transfer torque effect. Overall, I have used complementary laboratory techniques (magnetization, susceptibility and magnetoresistance measurements, MOKE measurement and microscopy, MFM imaging, X-ray diffraction) or large facilities techniques (polarized neutron reflectometry, spectroscopy and microscopy based on X-ray magnetic dichroism) and micromagnetic calculations, to study the evolution of magnetic configurations of complex multilayer systems or assembled nano-objects based on extrinsic parameters such as an external magnetic field or temperature. I have learned that material science is the first step of very careful studies. I have therefore put quite a lot of effort in controlling the growth of various systems (alloys and multilayer) ferri-, ferromagnetic and non-magnetic films by molecular beam evaporation and magnetron sputtering. During a three-year stint in Silicon Valley (California, USA), I have gained a new vision of the research and development within the Hitachi GST group (hard disk drive company that now belongs to Western digital). It is clear to me that fundamental discoveries in the fields of nanomagnetism and spintronic will continue to be implemented in magnetic recording devices as well as communication devices. The three current projects I chose as perspectives (magnetic bubble, MgO-based systems and magnetic frustrations) are accordingly. Above all, the studies described in my manuscript brought me to work with many colleagues, supervised some young ones and learn a lot from young and less young ones. I have developed national and international collaborations, sometimes through a stint, in renowned institutes like the Laboratory of Fundamental Electronics d'Orsay (France), the CEMES at toulouse (France), the center of neutron NIST in Washington DC (USA), the SOLEIL synchrotron in Saclay (France), the Lawrence Berkeley national Laboratory (USA), the IFW Dresden (Germany), the Istambul Bebek University (Turkey), Messina University (Italy) or Hitachi GST in San Jose (USA). Finally, my position as head of the service center "MAGNETISME" of Institut Jean Lamour (since 2011) has lead me to open myself to new fields and new collaborations within the University of Lorraine and outside (especially trough the Great Region). Today I am coordinating two network of magnetometry plateform (in France and Europe respectively) which I hope will help me to get more involved with local SMEs or larger international companies, and to target long term and high impact stakes.

Bibliographical references

[1] R. Wood, J. Magn. Magn. Mater. 321, 555 (2009)
[2] L. Russell, R. Whalen, H. Leilich, IEEE Trans. Magn. 4, 134 (1968)
[3] D. Weller et al. Phys. Rev. Lett. 75, 3752 (1995)
[4] M.T. Johnson, P.J.H. Bloemen, F.J.A. den Broeder, J.J. de Vries, Rep. Prog. Phys. 59, 1409 (1996)
[5] F.J.A. den Broeder et al. J. Magn. Magn. Mater. 93, 562 (1991)
[6] C. Kittel. Physique de l'état solide : Cours et problèmes. Dunod, 8e édition Ed., 2006.
[7] G. Fernando. Metallic Multilayers and their Applications, Volume 4 : Theory, Experiments, and Applications related to Thin Metallic Multilayers. Elsevier Science, 1 Ed., 2008.
[8] H. Zabel and S. D. Bader. Magnetic heterostructures : advances and perspectives in spinstructures and spintransport. Springer, 2007.
[9] B. N. Engel, C. D. England, R. A. V. Leeuwen, M. H. Wiedmann, and C. M. Falco. Phys. Rev. Lett., 67, 1910 (1991)
[10] D. Weller, R F C. Farrow, R.F. Marks, G.R. Harp, H. Notarys, G. Gorman, *Proc. Materials Research Society Conf. (Materials Research Society 313),* 791 (1993)
[11] T. Burkert, L. Nordstrom, O. Eriksson, O. Heinonen, Phys. Rev. Lett. 93, 027203 (2004)
[12] G. Andersson, T. Burkert, P. Warnicke, M. Bjorck, B. Sanyal, C. Chacon, C. Zlotea, L. Nordstrom, P. Nordblad, O. Eriksson, Phys. Rev. Lett. 96, 037205 (2006)
[13] S. Hashimoto, Y. Ochiai, K. Aso, J. Appl. Phys. 66, 4909 (1989)
[14] Y.S. Kim and S.C. Shin, J. Appl. 76, 6087 (1994)
[15] K. Umeda, Y. Fujiwara, T. Matsumoto, K. Nagawa, A. Itoh, J. Magn. Magn. Mater. 156, 75 (1996)
[16] K. Nakamura, S. Tsunashima, M. Hasegawa , S. Uchiyama, J. Magn. Magn. Mater. 93 462 (1991)
[17] C. Chappert, P. Bruno, J. Appl. Phys. 64, 5736 (1988)
[18] S. Ouazi *et al.* Nat. Commun. 3, 1313 (2012)
[19] L. Néel, J. Phys. Radium 15, 225 (1954)
[20] G.H.O. Daalderop, P.J. Kelly, M.F.H Schuurmans, Phys. Rev. B (R) 42, 7270 (1990), G.H.O. Daalderop , P.J. Kelly P J and M.F.H Schuurmans, Phys. Rev. B 41, 11919 (1990), Phys. Rev. B 42, 7270 (1990); Phys. Rev. B 44 12 054 (1991)
[21] G.H.O. Daalderop, P.J. Kelly, M.F.H Schuurmans, Phys. Rev. B 50, 9989 (1994) and references therein
[22] R.H. Victora and J.M. MacLaren, J. Appl. Phys. 73, 6415 (1993); Phys. Rev. B 47, 11583 (1993)
[23] P. Bruno, Phys. Rev. B 39, 865 (1989)
[24] G. Van der Laan, J. Phys. Cond. Matter. 10, 3239 (1998)
[25] P. Bruno, J. Phys. F 18, 1291 (1988)
[26] D.-S. Wang, R. Wu, A.J. Freeman, Phys. Rev. B 48, 15886 (1993)
[27] D. Weller, Y. Wu, J. Stohr, M.C. Samant, B.D. Hermsmeier, C. Chappert, Phys. Rev. B 49, 12888 (1994)

[28] J. Stöhr, J. Magn. Magn. Mater. 200, 470 (1999)
[29]A. Winkelmann, M. Przybylski, F. Luo, Y. Shi, and
J. Barthel, Phys. Rev. Lett. 96, 257205 (2006)
[30] F. Yildiz, F. Luo, C. Tieg, R. M. Abrudan, X. L. Fu, A. Winkelmann, M. Przybylski, and J. Kirschner, Phys. Rev. Lett. 100, 037205 (2008)
[31] G. H. O. Daalderop, P. J. Kelly, and F. J. A. den Broeder, Phys. Rev. Lett. 68, 682 (1992).
[32] K. Kyuno, J. G. Ha, R. Yamamoto, and S. Asano, Jpn. J. Appl. Phys. 35, 2774 (1996).
[33] M. T. Johnson, J. J. de Vries, N. W. E. McGee, J. aan de Stegge, and F. J. A. den Broeder, Phys. Rev. Lett. 69, 3575 (1992).
[34] M. T. Johnson, F. J. A. den Broeder, J. J. de Vries, N. W. E. McGee, R. Jungblut, and J. aan de Stegge, J. Magn. Magn. Mater. 121, 494 (1993).
[35]Y. B. Zhang et al., IEEE Trans. Magn. 30, 6 (1994) and J. Appl. Phys. 75, 6495 (1994).
[36]J.-M. L. Beaujour, W. Chen, K. Krycka, C.-C. Kao, J. Z. Sun, and A. D. Kent, Eur. Phys. J. B 59, 475 (2007).
[37] F. J. A. den Broeder, E. Janssen,W. Hoving, andW. B. Zeper, IEEE Trans. Magn. 28, 2760 (1992).
[38] V. M. Naik, S. Hameed, R. Naik, L. Pust, L. E. Wenger, G. L. Dunifer, and G. W. Auner, J. Appl. Phys. 84, 3273 (1998).
[39] H. Kurt, M. Venkatesan, and J. M. D. Coey, J. Appl. Phys. 108, 073916 (2010)
[40] J. M. Gallego, D. Lederman, T. J. Moran, and Ivan K. Schuller, Appl. Phys. Lett. 64, 2590 (1994).
[41] C. Prados, D. Garcia, F. Lesmes, J. J. Freijo, and A. Hernando, Appl. Phys. Lett. 67, 718 (1995).
[42] D.-H. Han, Appl. Phys. Lett. 68, 2153 (1996).
[43] D. H. Han, IEEE Trans. Magn. 32, 4585 (1996).
[44] R. J. Pollard, S. E. McCartney, and R. Atkinson, J. Magn. Magn. Mater. 176, 134 (1997).
[45] R. J. Pollard, S. E. McCartney, and R. Atkinson, IEEE Trans. Magn. 34, 879 (1998).
[46] F. Lesmes, A. Salcedo, J. J. Freijo, D. Garcia, A. Hernando, and C. Prados, Appl. Phys. Lett. 69, 2596 (1996).
[47] J. M. Gallego, D. Lederman, S. Kim, and I. K. Schuller, Phys. Rev. Lett. 74, 4515 (1995).
[48] S. Kim, D. Lederman, J. M. Gallego, and I. K. Schuller, Phys. Rev. B 54, 5291 (1996).
[49] J. M. Gallego, S. Kim, D. Lederman, and I. K. Schuller, J. Magn. Magn. Mater. 156, 397 (1996).
[50] M. Weissmann, A. M. Llois, R. Ramirez, and M. Kiwi, Phys. Rev. B 54, 15335 (1996).
[51] B. Y. Yavorsky, I.Mertig, and V. N. Antonov, Phase Transitions 76, 481 (2003).
[52] L. Chico, M. P. Lopez-Sancho, and M. C. Munoz, Phys. Rev. B 65, 184429 (2002).
[53] S. Mangin, D. Ravelosona, J.A. Katine, M. J. Carey, B. D. Terris, and E.E. Fullerton, Nature Mater. 5, 210 (2006).
[54] B. Kierren, T. Gourieux, F. Bertran, and G. Krill, Appl. Surf. Sci. 68, 341 (1993)
[55] H.Homma, K.-Y. Yang, and I. K. Schuller, Phys. Rev. B, 36, 9435 (1987)
[Bauer1985] E. Bauer and Jan H. van der Merwe, Phys. Rev. B, 33, 36573671 (1985)

[56] S. Andrieu and P. Muller « Les surfaces solides : concepts et methodes » Crystal Tutorial Project, edition : EDP Science / CNRS edition, 2005.
[57]D. Sander, J. Phys. Condens. Matter 16, R603 (2004)
[58] S. Andrieu, F. Lahatra-Razafindramisa, E. Snoeck, H. Renevier, A. Barbara, J.M. Tonnerre, M. Brunel, M.Piecuch, Phys. Rev. B, 52, 9938 (1995)
[59] E.A.M. van Alphen, S.G.E te Velthuis, H.A.M. de Gronckel, K. Kopinga, W.J.M. de Jonge, Phys. Rev. B 49, 17336 (1994)
[60] S. T. Purcell, M. T. Johnson, N. W. E. McGee, W B. Zeper, and W. Hoving, J. Magn. Magn. Mater. 113, 257 (1992)
[61] H. X. Yang, M. Chshiev, B. Dieny, J. H. Lee, A. Manchon, and K. H. Shin, Phys. Rev. B 84, 054401 (2011).
[62] L. Gerhard, Thesis "Magnetoelectric coupling at metal surfaces" KIT scientific publishing (2012)
[63] G. Bochi, C. A. Ballentine, H. E. Inglefield, C. V. Thompson, and R. C. O'Handley, J. Appl. Phys. 79, 5845 (1996)
[63] B. T. Thole, P. Carra, F. Sette, and G. van der Laan, Phys. Rev. Lett. 68, 1943 (1992).
[64] P. Carra, B. T. Thole, M. Altarelli, and X. Wang, Phys. Rev. Lett. 70, 694 (1993).
[65] C. T. Chen, Y. U. Idzerda, H.-J. Lin, N. V. Smith, G. Meigs, E. Chaban, G. H.Ho, E. Pellegrin, and F. Sette, Phys. Rev. Lett., 75, 152 (1995)
[66] R. Nakajima, J. Stöhr, and Y. U. Idzerda, Phys. Rev. B 59, 6421 (1999).
[67] M. Sicot, S. Andrieu, P. Turban, Y. Fagot-Revurat, H. Cercellier, A. Tagliaferri, C. De Nadai, N. B. Brookes, F. Bertran, and F. Fortuna, Phys. Rev. B 68, 184406 (2003).
[68] J. Stöhr and H. C. Siegmann, *Magnetism: From Fundamental to Nanoscale Dynamics* (Springer Verlag, Berlin, 2006).
[69]A.J.P. Meyer and G. Asch, J. Appl. Phys. 32, 330S (1961)
[70] J.M. Shaw, H.T. Nembach, T.J. Silva, Phys. Rev. B 87, 054416 (2013)
[71] N. Nakajima et al. , Phys. Rev. Lett. 81, 5229 (1998)
[72]T. Oguchi and T. Shishidou, Phys. Rev. B 70, 024412 (2004).
[73] G. van der Laan, J. Phys. Cond. Mat. 10, 3239 (1998)
[74] These de W. GRANGE *Anisotropie magnétocristalline des films d'alliage CoxPt1-x étudiée par dichroïsme magnétique circulaire* 1999 université Louis Pasteur Strasbourg
[75] see for details http://www.synchrotron-soleil.fr/Recherche/LignesLumiere/CASSIOPEE
[76] T. Okuda et al., Phys. Rev. B 80, 180404 (2009)
[77]J. Sanchez et al., Phys. Rev. B 85, 205109 (2012)
[78] F.J. Himpsel et al., Phys. Rev. Lett. 44, 95 (1980)
[79] D.E. Eastman et al. Phys. Rev. Lett. 44, 95 (1980)
[80] F. Gimbert, L. Calmels, S. Andrieu, Phys. Rev. B 84, 094432 (2011)
[81] K. Ueda, T. Koyoma, R. Hiramatsu, D. Chiba, S. Fukami, H. Tanigawa, T. Suzuki, N. Ohshima, N. Ishiwata, Y. Nakatani, K. Kobayashi, T. Ono, Appl. Phys. Lett. 100, 202407 (2012)
[82] J. A. Katine, F. J. Albert, R. A. Buhrman, E. B. Myers, and D. C. Ralph, Phys. Rev. Lett. 84, 3149 (2000).
[83] D. C. Ralph and M. D. Stiles, J. Magn. Magn. Mater. 320(7), 1190 (2008).
[84] J.A. Katine et E.E. Fullerton, J. Magn. Magn. Mater. 320, 1217 (2008).
[85]A V Khvalkovskiy, D Apalkov, S Watts, R Chepulskii, R S Beach,
A Ong, X Tang, A Driskill-Smith, W H Butler, P B Visscher,
D Lottis, E Chen, V Nikitin and M Krounbi, J. Phys. D: Appl. Phys. 46 , 074001 (2013)

[86] T. Kawahara, K. Ito, R. Takemura, H. Ohno, J. Magn. Magn. Mater.52, 613 (2012)
[87] M.N. Baibich, J.M. Broto, A. Fert, F. Nguyen van Dau, F. Petroff, P. Eitenne, G. Creuzet, A. Friederich, and J. Chazelas, Phys. Rev. Lett. 61, 2472 (1988)
[88] P. Grünberg, R. Schreiber, Y. Pang, M.B. Brodsky, and H. Sowers, Phys. Rev. Lett. 57, 2442 (1986)
[89] J. C. Slonczewski, J. Magn. Magn. Mater. 159, L1 (1996)
[90] L. Berger, Phys. Rev. B 54, 9353 (1996)
[91] S. Mangin, Y. Henry, D. Ravelosona, J. A. Katine, and E.E. Fullerton, Appl. Phys. Lett. 94, 012502 (2009).
[92] S. Le Gall et al. Phys. Rev. B 86, 014419 (2012)
[93] M. D. Stiles and J. Miltat, in *Spin Dynamics in Confined Magnetic Structures III*, Springer Series Topics in Applied Physics, Vol. 101 (Springer-Verlag, Berlin, Heidelberg, 2006).
[94] P. Bruno J. Phys.: Condens. Matter 11, 9403 (1999)
[95] Chapter 2, in Ultrathin Magnetic Structures II, edited by B. Heinrich and J. A. C. Bland (Springer-Verlag, Berlin,1994)p.45.
[96] Y.Yafet,in Magnetic Multilayers, ed.L.H. Bennett and R.E.Watson (WorldScientific, Singapore1994) ,p.19
[97] S. M. Mohseni, R. K. Dumas, Y. Fang, J. W. Lau, S. R. Sani, J. Persson, and Johan Åkerman, Phys. Rev. B 84, 174432 (2011)
[98] M. Tsoi, A. G. M. Jansen, J. Bass, W. C. Chiang, M. Seck, V. Tsoi, and P. Wyder, Phys. Rev. Lett. 80, 4281 (1998).
[99] J. C. Sankey, P. M. Braganca, A. G. F. Garcia, I. N. Krivorotov, R. A. Buhrman, and D.C. Ralph, Phys. Rev. Lett. 96, 227601 (2006).
[100] D. Bedau, H. Liu, J. Z. Sun, J. A. Katine, E. E. Fullerton, S. Mangin, A. D. Kent, Appl. Phys. Lett. 97, 262502 (2010)
[101]J. Cucchiara, Y. Henry, D. Ravelosona, D. Lacour, Eric. E. Fullerton, J. A. Katine and S. Mangin,Appl Phys. Lett 94, 102503 (2009)
[102] D. Bedau, H. Liu, J-J Bouzaglou, A.D. Kent J.Z. Sun, J.A. Katine, Eric E Fullerton and S. Mangin, Appl. Phys. Lett 96,022514 (2010)
[103] D. Ravelosona, S. Mangin, Y. Lemaho, J. A. Katine, B. D. Terris, and E. E. Fullerton, Phys. Rev. Lett. 96, 186604 (2006)
[104] Y. Acremann, et. al Rev. of Sci. Instr. 78, 014702 (2007).
[105] J.P. Strachan, et. al Rev. of Sci. Instr. 78, 054703 (2007).
[106] Y. Acremann, J. P. Strachan, V. Chembrolu, S. D. Andrews, T. Tyliszczak, J. A. Katine, M. J. Carey, B. M. Clemens, H.C. Siegmann, and J. Stöhr, Phys. Rev. Lett. 96, 217202 (2006)
[107] J.P. Strachan, et. al. Phys. Rev. Lett., 100, 247201 (2008)
[108] T. Devolder, J. Hayakawa, K. Ito, H. Takahashi, S. Ikeda, P. Crozat, N. Zerounian, Joo-Von Kim, C. Chappert, and H. Ohno, Phys. Rev. Lett., 100, 057206 (2008)
[109] Y.-T. Cui, G. Finocchio, C. Wang, J. A. Katine, R. A. Buhrman, and D. C. Ralph, Phys. Rev. Lett. 104, 097201 (2010)
[110] LLG micromagnetic simulator developed by Prof. M. Scheinfein, http://llgmicro.home.mindspring.com
[111]J. Z. Sun Phys Rev B. 62, 570, (2000)
[112] S. Okamoto, N. Kikuchi, M. Furuta, O. Kitakami, T. Shimatsu, Phys. Rev. Lett. 109, 237209 (2012)
[113] R. Piquerel, O. Gaier, E. Bonet, C. Thirion, and W. Wernsdorfer,Phys. Rev. Lett. 112, 117203 (2014)

[114] M. Gajek, J. J. Nowak, J. Z. Sun, P. L. Trouilloud, E. J. O'Sullivan, D. W. Abraham, M. C. Gaidis, G. Hu, S. Brown, Y. Zhu, R. P. Robertazzi, W. J. Gallagher, and D. C. Worledge, Appl. Phys. Lett. 100, 132408 (2012)
[115] S. Ikeda,K. Miura, H. Yamamoto, K. Mizunuma, H. D. Gan, M. Endo, S. Kanai, J. Hayakawa, F. Matsukura and H. Ohno, Nature Mater. 9, 721 (2010)
[116] W.-G. Wang, M. Li, S. Hageman, C. L. Chien, Nature Mater.11, 64 (2012)
[117]V. Sokalski, M.T. Moneck, E. Yang, J.-G. Zhu, Appl. Phys. Lett. 101, 072411 (2012)
[118] D.-Y. Lee, T.H. Shim, and J.-G. Park, Appl. Phys. Lett. 102, 212409 (2013)
[119] L.-X. Ye, C.-M. Lee, Y.-J. Chang, T.-H. Wu, J. Appl. Phys. 103, 07F521 (2008)
[120] B. Carvello, C. Ducruet, B. Rodmacq, S. Auffret, E. Gautier, G. Gaudin, B. Dieny, Appl. 92, 102508 (2008)
[121] Yi. Wang, W. X. Wang, H. X. Wei, B. S. Zhang, W. S. Zhan, X. F. Han, J. Appl. Phys. 107, 09C711 (2010)
[122]M. Yoshikawa et al., IEEE Trans. Magn. 44, 2573 (2008)
[123] A. Rajanikanth, S. Kasai, N. Ohshima, and K. Ohno, appl. Phys. Lett. 97, 022505 (2010)
[124] K.Yakushiji, K. Noma, T. Saruya, H. Kubota, A.Fukushima, T. Nagahama, S.Yuasa and K. Ando, Appl. Phys. Express 3, 053003 (2010)
[125] D. C. Worledge, G. Hu, David W. Abraham, P. L. Trouilloud, S. Brown, Appl. Phys. Lett. 115, 172601 (2014)
[126] T. Moriyama, T. J. Gudmundsen, P. Y. Huang, L. Liu, D. A. Muller, D. C. Ralph, and R. A. Buhrman, Appl. Phys. Let. 97, 072513 (2010)
[127] L. You, R. C. Sousa, S. Bandiera, B. Rodmacq, and B. Dieny, Appl. Phys. Let. 100, 172411 (2012).
[128] C. Fowley, N. Decorde, K. Oguz, K. Rode, H. Kurt, and J. M. D. Coey, IEEE Trans. Magn. 46, 2116 (2010).
[129] H. X. Wei, Q. H. Qin, M. Ma, R. Sharif, and X. F. Han, J. Appl. Phys. 101, 09B501 (2007)
[130]W. F. Brinkman, R. C. Dynes, et J. M. Rowell, J. Appl. Phys. 41, 1915 (1970)
[131] S.-J. Ahn, T. Kato, H. Kubota, Y.Ando, T. Miyazaki, Appl. Phys. Lett. 86, 102506 (2005)
[132] E.Y. Tsymbal, O. N Mryasov, P.R. LeClair, Journal of Physics: Condensed Matter 15, R109 (2003) and References therein.
[133] M. Julliere, Phys. Lett. A 54, 225 (1975)
[134] C. Song, Y. Y. Wang, X. J. Li, G. Y. Wang and F. Pan, Appl. Phys. Lett. 101, 062404 (2012)
[135]H. Liu, D. Bedau, D. Backes, J. A. Katine, J. Langer, and A. D. Kent, Appl. Phys. Lett. 97, 242510 (2010)
[136] D. Houssameddine , U. Ebels , B. Delaët , B. Rodmacq , I. Firastrau , F. Ponthenier , M. Brunet , C. Thirion , J.-P. Michel , L. Prejbeanu-Buda , M.-C. Cyrille , O. Redon, B. Dieny, Nature Materials 6, 447 (2007)
[137] Z. Zeng, G. Finocchio, B. Zhang, P. K. Amiri, J.A. Katine, I.N. Krivorotov, Y. Huai, J. Langer, B. Azzerboni, K.L. Wang, H. Jiang, Scientific Reports, 3, 1426 (2013)
[138] A. Rajanikanth, T. Hauet, F. Montaigne, S. Mangin, S. Andrieu, Appl. Phys. Lett. 103, 062402 (2013)
[139] G. S. Kar, W. Kim, T. Tahmasebi, J. Swerts, S. Mertens, N. Heylen, T. Min, IEEE Int. Electron Devices Meeting 2014, 19.1.1 (2014)
[140] Y. Tomczak, J. Swerts, S. Mertens, T. Lin, S. Couet, E. Liu, K. Sankaran, G. Pourtois, W. Kim, L. Souriau, S. Van Elshocht, G. Kar, and A. Furnemont, Appl. Phys. Lett. 108, 042402 (2016)

[141] C.T. Boone, J.A. Katine, M. Carey, J.R. Childress, X. Cheng, I.N. Krivorotov, Phys. Rev. Lett. 104, 097203 (2010)
[142] G Malinowski, O Boulle, M Kläui . *J. Phys. D: Appl. Phys.* 44 384005 (2011)
[143]M. Yamanouchi, D. Chiba, F. Matsukura and H. Ohno, Nature (London) 428, 539 (2004)
[144] J-P. Adam, N. Vernier, J. Ferré, A. Thiaville, V. Jeudy, A. Lemaître, L. Thevenard, and G. Faini, Phys. Rev. B 80, 193204 (2004)
[145] T. A. Moore, I. M. Miron, G. Gaudin, G. Serret, S. Auffret, B. Rodmacq, A. Schuhl, S. Pizzini, J. Vogel, and M. Bonfim, Appl. Phys. Lett. 93, 262504 (2008).
[146]T. Koyama, D. Chiba, K. Ueda, K. Kondou, H. Tanigawa, S. Fukami, T. Suzuki, N. Ohshima, N. Ishiwata, Y. Nakatani, K. Kobayashi and T. Ono, Nature Mater. 10, 194 (2011)
[147] C. Burrowes, A. P. Mihai, D. Ravelosona, J.-V. Kim, C. Chappert, L. Vila, A. Marty, Y. Samson, F. Garcia-Sanchez, L. D. Buda-Prejbeanu, I. Tudosa, E. E. Fullerton and J.-P. Attané, Nature Phys. 6, 17 (2010)
[148]S. Fukami, T. Suzuki, Y. Nakatani, N. Ishiwata, M. Yamanouchi, S. Ikeda, N. Kasai, and H. Ohno, Appl. Phys. Lett. 98, 082504 (2011)
[149] K.-S.Ryu, S.-H. Yang, L. Thomas, S.S.P. Parkin, Nature Comm. 5, 3910 (2014)
[150] I.M. Miron, Miron, T. Moore, H. Szambolics, L.D. Buda-Prejbeanu, S. Auffret, B. Rodmacq, S. Pizzini, J. Vogel, M. Bonfim, A. Schuhl, G. Gaudin, Nat. Mater. 10, 419 (2011)
[151]S-B. Choe and S-C. Shin, Appl. Phys. Lett. 80, 1791 (2002)
[152] J.E. Davies, O. Hellwig, E.E. Fullerton, Greg Denbeaux, J. B. Kortright, and Kai Liu Phys. Rev. B 70, 224434 (2004)
[153] K.-J. Kim et al., APL 101, 022407 (2012)
[154] K. Yamada, J-P. Jamet, Y. Nakatani, A. Mougin, A. Thiaville, T. Ono, and J. Ferré, App. Phys. Express 4, 113001 (2011)
[155] J. P. Attan , M. Tissier, A. Marty, and L. Vila, Phys. Rev. B 82, 024408 (2010)
[157] A.Kirilyuk, J. Ferré, V. Grolier, J-P. Jamet, D. Renard, J. Magn. Magn. Mater. 171, 45 (1997)
[158] P. J. Metaxas, J. P. Jamet, A. Mougin, M. Cormier, J. Ferré, V. Baltz, B. Rodmacq, B. Dieny, and R. L. Stamps, Phys. Rev. Lett. 99, 217208 (2007)
[159] J-C. Lee, K-J. Kim, J. Ryu, K-W. Moon, S-J. Yun, G-H. Gim, K-S. Lee, K-H. Shin, H-W. Lee, and S-B Choe, Phys. Rev. Lett. 107, 067201 (2011)
[160] C. Burrowes, N. Vernier, J-P. Adam, L. Herrera Diez, K. Garcia, I. Barisic, G. Agnus, S. Eimer, J-V. Kim, T. Devolder, A. Lamperti, R. Mantovan, B. Ockert, E. E Fullerton, and D. Ravelosona, App. Phys. Lett. 103, 182401 (2013)
[161] C. Burrowes, D. Ravelosona, C. Chappert, S. Mangin, Eric E. Fullerton, J. A. Katine, and B. D. Terris, App. Phys. Lett. 93, 172513 (2008)
[162] P. Chauve, T. Giamarchi, and P. Le Doussal, Phys. Rev. B 62, 6241 (2000)
[163] J-P. Attané, D. Ravelosona, A. Marty, Y. Samson, and C. Chappert, Phys. Rev. Lett. 96, 1472041 (2006)
[164] F. Garcia-Sanchez, H. Szambolics, A. P. Mihai, L. Vila, A. Marty, J-P. Attané, J.-Ch. Toussaint, L. D. Buda-Prejbeanu, Phys. Rev. B 81, 134408 (2010)
[165] M. Plapp and A. Karma, Phys. Rev. Lett. 84, 1740 (2000)
[166] J-P. Attané, Y. Samson, A. Marty, J. C. Toussaint, G. Dubois, A. Mougin, and J-P. Jamet, Phys. Rev. Lett. 93, 257203 (2004)
[167] A. Mougin, M. Cormier, J-P. Adam, P. J. Metaxas and J. Ferré, Europhys. Lett. 78, 57007 (2007)
[168] O. Boulle *et al.*, Phys. Rev. Lett. 101, 216601 (2008)
[169] K-J. Kim, J-C. Lee, K-H. Shin, H-W. Lee and S-B. Choe, Curr. Appl. Phys. 13, 228-236 (2013)

[170] J. Ryu, S-B. Choe and H-W Lee, Phys. Rev. B 84, 075469 (2011)
[171]J. Curiale, A. Lemaître, G. Faini and V. Jeudy, Appl. Phys. Lett. 97, 243505 (2010)
[172] T. Koyama, K. Ueda, K.-J. Kim, Y. Yoshimura, D. Chiba, K. Yamada, J.-P. Jamet, A. Mougin, A. Thiaville, S. Mizukami, S. Fukami, N. Ishiwata, Y. Nakatani, H. Kohno, K. Kobayashi & T. Ono, Nature Nanotech. 7, 635 (2012)
[172] J. Moritz, phD thesis "Enregistrement ultra-haute densité sur réseau de plots magnétiques nanométriques à aimantation perpendiculaire au plan", Universite Joseph Fourier, Grenoble (2003)
[173] H. Oshima, H. Kikuchi, H. Nakao, K.-I. Itoh, T. Kamimura, T. Morikawa, K. Matsumoto, T. Umada, and H. Tamura. Appl. Phys. Lett. 91, 022508 (2007)
[175] B.D. Terris and T. Thomson, J. Phys. D: Appl. Phys. 38, R199 (2005)
[174] M. Schabes, J. Magn. Magn. Mater. 320, 2880 (2008)
[176] O. Hellwig, A. Moser, E. Dobisz, Z. Bandic, H. Yang, D. S. Kercher, J. D. Risner-Jamtgaard, D. Yaney, and E. E. Fullerton, Appl. Phys. Lett. 93, 192501 (2008)
[177]T. Thomson, G. Hu, and B. D. Terris, Phys. Rev. Lett. 96, 257204 (2006).
[178] O. Hellwig et al., Appl. Phys. Lett. 90, 162516 (2007), J. Magn. Magn. Mater. 319, 13 (2007)
[179] J. Moritz, B. Dieny, J. P. Nozieres, S. Landis, A. Lebib, and Y. Chen, J. Appl. Phys. 91, 7314 (2002)
[180]M.P. Sharrock and J.T. McKinney, IEEE Trans. Magn 17, 3020 (1981)
[181]J.M. Shaw, S.E. Russek, T. Thomson, M.J. Donahue, B.D. Terris, O. Hellwig, E. Dobisz, M.L. Schneider, Phys. Rev. B 78, 024414 (2008)
[182] J.M. Shaw, M. Olsen, J.W. Lau, M.L. Schneider, T.J. Silva, O. Hellwig, E. Dobisz, and B.D. Terris, Phys. Rev. B 82, 144437 (2010)
[183] J. W. Lau, R. D. McMichael, S. H. Chung, J. O. Rantschler, V. Parekh, and D. Litvinov, Appl. Phys. Lett. 92, 012506 (2008).
[184] D. Suess, T. Schrefl, S. Fahler et al., Appl. Phys. Lett. 87, 012504 (2005)
[185] R. Victora and X. Shen, IEEE Trans. Magn. 41, 2028-2033 (2005)
[186] A. Berger, N. Supper, Y. Ikeda, B. Lengsfield, A. Moser, E.E. Fullerton, Appl. Phys. Lett. 93, 122502 (2008)
[187] H.N. Bertram and B. Lengsfield, IEEE Trans. Magn. 43, 2145 (2007), T. Thomson et al., J. Appl. Phys. 103, 07F548 (2008)
[188] D. Suess, J. Lee, J. Fidler, T. Schrefl, J. Magn. Magn. Mater. 321, 545 (2009)
[189] A. Berger, Y. Xu, B. Lengsfield, Y. Ikeda, and E. E. Fullerton, IEEE Trans. Magn. 41, 3178 (2005)
[190] A. Berger, B. Lengsfield, and Y. Ikeda, J. Appl. Phys. 99, 08E705 (2006)
[191] S. Eisebitt, J. Lu¨ning, W. F. Schlotter, M. Lo¨rgen, O. Hellwig,W. Eberhardt, and J. G. Stohr, Nature 432, 885 (2004)
[192]S. Eisebitt, M. Lörgen, W. Eberhardt, J. Lüning, and J. Stöhr, Appl. Phys. A: Mater. Sci. Process. 80, 921 (2005)
[193] T. Thomson, B. Lengsfield, H. Do, B.D. Terris, J. Appl. Phys. 103, 07F548 (2008)
[194]M. Colburn, A. Grot, B.J. Choi, M. Amistoso, T. Bailey, S.V. Sreenivasan, J.G. Ekerdt, C.G. Willson, J. Vac. Sci. Technol. B 19, 2162 (2001).
[195]B. Heidari, T. Moller, R. Palm, E. Bolmsjo, and M. Beck, Proc. IEEE Int. Conf. Microprocess. Nanotechnol. Conf., Oct. 25–28, 2005, pp. 144–145.
[196]A. Bogdanov, T. Holmqvist, P. Jedrasik, B. Nilsson, Microelectron. Eng. 67–68, 381–389 (2003).
[197] G.M. McClelland, M.W. Hart, C.T. Rettner, M.E. Best, K.R. Carter, B.D. Terris, Appl. Phys. Lett. 81, 1483 (2002).

[198] I.W. Hamley, et al., *The Physics of Block Copolymers*, Oxford Science Publications, USA, (1998), 26
[199] L. Leibler, Macromolecules 13, 1602 (1980).
[200] F.S. Bates, and G.H. Fredrickson , Annu. Rev. Phys. Chem. 41, 525 (1990).
[201] R. Ruiz, K. M., F. A. Detcheverry, E. Dobisz, D. S. Kercher, T. R. Albrecht, J. J. de Pablo, and P. F. Nealey, Science 321, 936–939 (2008).
[202] P. Mansky, Y. Liu, E. Huang, T. P. Russell, C. J. Hawker, Science 275, 1458 (1997)
[203] M. Albrecht, G. Hu, I. L. Guhr, T. C. Ulbrich, J. Boneberg, P. Leiderer, and G. Schatz, Nature Mater. 4, 203 (2005)
[204] T. C. Ulbrich, C. Bran, D. Makarov, O. Hellwig, J. D. Risner-Jamtgaard, D. Yaney, H. Rohrmann, V. Neu and M. Albrecht, Phys. Rev. B81, 054421 (2010).
[205] L. Yan, K. Wang, J. Wu and L. Ye, Colloids and Surfaces A: Physicochem. Eng. Aspects 296, 123 (2007).
[206] C. R. Martin, Chem. Mater. 8, 1739 (1996).
[207] D. J. Sellmyer, M. Zheng and R. Skomski, J. Phys.: Condens. Matter. 13, R433 (2001).
[208]. Hernández-Vélez, Thin Solid Films 495, 51 (2006).
[209] H. Masuda and K. Fukuda, Science 268, 1466 (1995).
[210] O. Rabin, P. R. Hertz, Y. -M. Lin, A. I. Akinwande, S. B. Cronin, M. S. Dresselhaus, Adv. Funct. Mater. 13, 631 (2003).
[211] S. Matefi-Tempfli, M. Matefi-Tempfli and L. Piraux, Thin Solid Films 516, 3735 (2008)
[212] R. Dittrich, G. Hu, T. Schrefl, T. Thomson, D. Suess, B.D. Terris, J. Fidler, J. Appl. Phys. 97, 10J705 (2005)
[213] J. Lau, X. Liu, R.C. Boling, J.M. Shaw, Phys. Rev. B 84, 214427 (2011) and references therein.
[214] T.C. Ulbrich, D. Makarov, G. Hu, I.L. Guhr, D. Suess, T. Schrefl, and M. Albrecht, Phys. Rev. Lett. 96, 077202 (2006).
[215] T. Aign, P. Meyer, S; lemerle, J.P. Jamet, J. Ferré, V. Mathet, C. Chappert, J. Gierak, C. Vieu, F. Rousseaux, H. Launois, H. Bernas, Phys. Rev. Lett. 81, 5656 (1998)
[216] O. Hellwig, A. Berger, J.B. Kortright, E.E. Fullerton, J. Magn. Magn. Mater. 319 , 13 (2007) and references therein.
[217] A. Berger and H. Hopster, J. Appl. Phys. Lett. 79, 5619 (1996)
[218] N. Eibagi, J.J. Kan, F.E. Spada, E.E. Fullerton, IEEE Magnetic lett. 3, 4500204 (2012)
[219] M.S. Pierce, C.R. Buechler, L.B. Sorensen, S.D. Kevan , E.A. Jagla, J.M. Deutsch, T. Mai, O. Narayan, J.E. Davies, K. Liu, G.T. Zimanyi, H.G. Katzberger, O. Hellwig, E.E. Fullerton, and J.B. Kortright, Phys. Rev. B, 75, 144406 (2007).
[220] M.S. Pierce, J.E. Davies, J.J. Turner, J.E. Davies, K. Chesnel, E.E. Fullerton, R. Hailstone, S.D. Kevan, J.B. Kortright, K. Liu, J. Nam, L.B. Sorensen, B.R. York, and O. Hellwig. Phys. Rev. B 87, 184428 (2013).
[221] http://en.wikipedia.org/wiki/Magnetic-core_memory
[222] X. Dong, X. Wu, G. Sun, Y. Xie, Design Automation Conference, 45th ACM/IEEE, 554 (2008)
[223] A.M. Shukh (2009), US patent 20120155154 A1
[224] R. Lavrijsen, J.-H. Lee, A. Fernández-Pacheco, D.C.M.C. Petit, R. Mansell, R.P. Cowburn, Nature, 493, 647 (2013)
[225] A. Fernández-Pacheco, D. Petit, R. Mansell, R. Lavrijsen, J.H. Lee, R.P. Cowburn, Phys. Rev. B 86, 104422 (2012)
[226] Parkin SSP (2004-2007), US Patents 6,834,005; 6,898,132; 6,920,062; 7,031,178; and 7,236,386
[227] Parkin et al. Science 320, 190 (2008)

[228] Robert E. Fontana,A. Moser,H.J. Rosen,B.D. Terris,C.W. Tsang, US patent (2009) 7,606,065 B2
[229] O. Ozatay and B.D. Terris, US patent (2012) 8,164,940 B2
[230] L. Thomas et al. Phys. Rev. Lett. 84, 1816 (2000)
[231] S. Wiebel et al. , Appl. Phys. Lett. 86, 142502 (2005)
[232] S. Gider, B.-U. Runge, A.C. Marley and S.S.P. Parkin, Science 281, 797 (1998).
[233] B. Rodmacq, V. Baltz and B. Dieny, Phys. Rev. B 73, 92405 (2006).
[234] D. Rugar, H. J. Mamin, P. Guethner, S. E. Lambert, J. E. Stern, I. McFadyen, and T. Yogi. J. Appl. Phys. 68, 1169 (1990)
[235] V. Baltz et al. Phys. Rev. B 75, 14406 (2007)
[236] P. Fischer, Current Opinion in Solid State and Materials Science, 7, 173 (2003).
[237] W. Chao, B.H. Harteneck, J.A. Liddle, E.H. Anderson and D.T. Attwood, Nature (London) 435, 1210 (2005).
[238] M. Fallot, Annales de Physique (Paris) 10, 291 (1938); M. Fallot and R. Horcart, Revue Scientifique 77, 498 (1939).
[239] G. Shirane, C.W. Chen, P. A. Flinn, R. Nathans, J. Appl. Phys. 34, 1044 (1963); Physical Review 134, A1547 (1964).
[240] J. S. Kouvel, J. Appl. Phys. 37, 1257 (1966); J. S. Kouvel and C. C. Hartelius, J. Appl. Phys. 33 (3), 1343 (1962)
[241] K. S. Buchanan et al. Nature Phys. 1, 172-176 (2005)
[242] Chien, C. L., Zhu, F. Q. ve Zhu, J-G., Phys. Today, 60, 40-45, (2007)
[243] Hehn, M., Ounadjela, K., Bucher, J-P., Rousseaux, F., Decanini, D., Bartenlian, B., Chappert, C., Science, 272, 1782-1785, (1996)
[244] K. Y. Guslienko , J. Nanosci. Nanotechnol. 8, 2745-2760 (2008)
[245] V. S. Pribiag et al. Nature Phys. 3, 498-503 (2007)
[246] A. Dussaux et al. Nat. Commun., 1, #8, 1-6, (2010)
[247] Ivanov, B. A., Stephanovich, V. A. and Zhmudskii, A. A., J. Magn. Magn. Mater., 88, 116, (1990)
[248] Fukumura, T., Sugawara, H., Hasegawa, T., Tanaka, K., Sakaki, H., Kimura, T. and Tokura, Y., Science, 284, 1969-1971, (1999)
[249] Thiele, A. A., Phys. Rev. Lett., 30, 230-233, (1973)
[250] C. Moutafis et al., Phys. Rev. B 76, 104426 (2007)
[251] J.-P. Tetienne, T. Hingant, L. Rondin, S. Rohart, A. Thiaville, E. Jué, G. Gaudin, J.-F. Roch, V. Jacques, 115, 17D501 (2014)
[252] J. Sampaio et al., Nature Nanotech. 8, 839 (2013)
[253] M.A. Hoefer, el al, Phys. Rev. B 82, 054432 (2010)
[254] C. Moutafis et al., Phys. Rev. B 79, 224429 (2009)
[255] J Iwasaki et al. , Nature Nanotech. 8, 742 (2013)
[256] M.J. Donahue and D.G.Porter 1999 OOMMF User's Guide, Version 1.0, Interagency Report NISTIR 6376, Tech. Rep. (National Institute of Standards and Technology, Gaithersburg, MD)
[257] A.Vansteenkiste, J. Leliaert, M. Dvornik, M. Helsen, F. Garcia-Sanchez, B. Van Waeyenberge, AIP Advances 4, 107133 (2014)
[258] A. Giordano, G. Finocchio, L. Torres, M. Carpentieri and B. Azzerboni J. Appl. Phys. 111, 07D112 (2012)
[259] J. Faure-Vincent, C. Tiusan, C. Bellouard, E. Popova, M. Hehn, F. Montaigne, and A. Schuhl Phys. Rev. Lett. 89, 107206 (2002)
[260] C. Tiusan, J. Faure-Vincent, C. Bellouard, M. Hehn, E. Jouguelet, and A. Schuhl, Phys. Rev. Lett. 93, 106602 (2004)

[261] F. Greullet, C. Tiusan, F. Montaigne, M. Hehn, D. Halley, O. Bengone, M. Bowen, and W. Weber, Phys. Rev. Lett. 99, 187202 (2007)
[262] F. Bonell, S. Andrieu, A. M. Bataille, C. Tiusan, and G. Lengaigne, Phys. Rev. B 79, 224405 (2009)
[263] F. Bonell, S. Andrieu, C. Tiusan, F. Montaigne, E. Snoeck, B. Belhadji, L. Calmels, F. Bertran, P. Le Fèvre, A. Taleb-Ibrahimi, Phys. Rev. B 82, 092405 (2010)
[264] W.H. Butler, X.G. Zhang, T.C. Schulthess, J.M. MacLaren, Phys. Rev. B 63, 054416 (2001)
[265] J. Mathon and A. Umerski, Phys. Rev. B 63, 220403 (2001)
[266] Molecular Beam Epitaxy: From Quantum Wells to Quantum Dots. From Research to Mass Production Chapter 20: Epitaxial Magnetic Layers Grown by MBE : Model Systems to Study the Physics in Nanomagnetism and Spintronic K. Dumesnil & S. Andrieu, Ed. M. Henini, ELSEVIER (2012)
[267] X. G. Zhang and W. H. Butler, Phys. Rev. B 70, 172407 (2004)
[268] S. Yuasa, T. Nagahama, A. Fukushima, Y. Suzuki, K. Ando, Nat. Mater. 3, 868 (2004)
[269] S. Yuasa, A. Fukushima, H. Kubota, Y. Suzuki and K. Ando, Appl. Phys. Lett. 89, 042505 (2006)
[270] S. Yuasa, T. Katayama, T. Nagahama, A. Fukushima, H. Kubota, Y. Suzuki and K. Ando, Appl. Phys. Lett. 87, 222508 (2005)
[271] Y. M. Lee, J. Hayakawa, S. Ikeda, F. Matsukura, H. Ohno, Appl. Phys. Lett. 90, 212507 (2007)
[272] F. bonell, « Analyse du transport dans les jonctions tunnel magnétiques épitaxiées à barrière de MgO(001) par manipulation des interfaces, de la barrière et des électrodes » Thèse de doctorat de l'université Henri-Poincaré Nancy I (2009).
[273] P. D. Johnson, Rep. Progr. Phys. 60, 1217 (1997)
[274] L. N. Tong, F. Matthes, M. Muller, C. M. Schneider, C. G. Lee, Phys. Rev. B 77, 064421 (2008)
[275] C. Cohen-Tannoudji, B. Diu and F. Laloë, Mécanique quantique, Herman (1973)
[276] B. Belhadji and L. Calmels, Phys. Rev. B 83, 092401 (2011)
[277] J.A. Stroscio, D.T.Pierce, A. Davies, R.J. Celotta, M. Weinert, Phys. Rev. Lett. 75, 2960 (1995)
[278] M. M. J. Bischoff, T. K. Yamada, C. M. Fang,R. A. de Groot, and H. van Kempen, Phys. Rev. B 68, 045422 (2003)
[279] S. Trudel, O. Gaier, J.Hamrle, B. Hillebrands, J. Phys. D: Appl. Phys. 43, 193001 (2010) and references therein
[280] T. Graf, C. Felser, S. S. P. Parkin, Progress in Solid State Chemistry 39, 1 (2011) and references therein
[281] S. Maat, M. J. Carey, J. R. Childress, Appl. Phys. Lett. 93, 143505 (2008)
[282] H.-X. Liu et al, App. Phys. Lett., 101, 132418 (2012)
[280] T. Graf, C. Felser, S. S. P. Parkin, Progress in Solid State Chemistry 39, 1 (2011) and references therein
[283] H. Lee & al, Appl. Phys. Lett. 95, 082502 (2009)
[284] S. Picozzi and A. Continenza, A. J. Freeman, Phys. Rev. B 69, 094423 (2004)
[285] J. H. Jung, S. H. Lim, S. R. Lee, Appl. Phys. Lett. 96, 042503 (2010)
[286] Q.L. Ma, S. Lihama, T. Kubota, X.M. Zhang, S. Mizukami, Y. Ando, T. Miyazaki, Appl. Phys. Lett. 101, 122414 (2012)
[287] M. Weisheit, S. Fähler, A. Marty, Y. Souche, C. Poinsignon, D. Givord: Science 315 (2007) 349
[288] Y. Shiota, T. Maruyama, T. Nozaki, T. Shinjo, M. Shiraishi, Y. Suzuki, Appl. Phys. Express 2, 063001 (2009)

[289] T. Maruyama, Y. Shiota, T. Nozaki, K. Ohta, N. Toda, M. Mizuguchi, A.A. Tulapurka, T. Shinjo, M. Shiraishi, S. Mizukami, Y. Ando, Y. Suzuki, Nat. Mater. 4, 158 (2009)
[290] M.K. Niranjan, C.-G. Duan, S.S. Jaswal and E.Y. Tsymbal, Appl. Phys. Lett. 96, 222504 (2010)
[291] K. Nakamura, R. Shimabukuro, Y. Fujiwara, T. Akiyama, T. Ito, A.J. Freeman, Phys. Rev. Lett. 102, 187201 (2009)
[292] A. Sonntag, J. Hermenau, A. Schlenhoff, J. Friedlein, S. Krause, and R. Wiesendanger, Phys. Rev. Lett. 112, 017204 (2014)
[293] K.H. He, S.J. Chen, J.Appl.Phys. 111, 07C109 (2012)
[294] C.-H. Lambert, A. Rajanikanth, T. Hauet, S. Mangin, E.E. Fullerton,and, S. Andrieu, Appl. Phys. Lett. 102, 122410 (2013)
[295] J. Izquierdo, R. Robles, A. Vega, M. Talanana, and C. Demangeat, Phys. Rev. B 64, 060404(R) (2001)
[296] F. Dulot, P. Turban, B. Kierren, J. Eugène, M. Alnot, S. Andrieu, Surf. Sci. 473, 172 (2001)
[297] P. Turban, L. Hennet, S. Andrieu, Surf. Sci. 446, 241 (2000)
[298] A. N. Anisimov, M. Farle, P. Poulopoulos, W. Platow, K. Baberschke, P. Isberg, R. Wäppling, A. M. N. Niklasson, O. Eriksson, Phys. Rev. Lett. 82, 2390 (1999)
[299] H. Fritzche, T. Nawrath, H. Maletta, H. Lauter, Physica B 241, 707 (1998)
[300] A. Broddefalka P. Nordblada, P. Blomqvist, P. Isberg, R. W.appling, O. Le Bacq, O. Eriksson, J. Magn. Magn. Mater. 241, 260 (2002)
[301] U. Bauer, M. Przybylski, J. Kirschner, G.S. Beach, *NanoLett*. 12, 1437 (2012)
[302] F. Bonell, Y. T. Takahashi, D. D. Lam, S. Yoshida, Y. Shiota, S. Miwa, T. Nakamura,3 and Y. Suzuki, *Appl. Phys. Lett.* 102, 152401 (2013)
[303] H. Ohno, D. Chiba, F. Matsukura, T. Omiya, E. Abe, T. Dietl, Y . Ohno, K. Ohtani, *Nature* 408, 944 (2000)
[304] D. Chiba, M. Yamanouchi, F. Matsukura, H. Ohno, *Science* 301, 943 (2003)
[305] D. Chiba, S. Fukami, K. Shimamura, N. Ishiwata, K. Kobayashi, T. Ono, Nature Materials, 10,853 (2011)
[306] K. Shimamura, D. Chiba, S. Ono, S. Fukami, N. Ishiwata, M. Kawaguchi,K. Kobayashi, T. Ono, Appl. Phys. Lett. 100, 122402 (2012)
[307] P. Bruno, Phys .Rev. B 43, 6015 (1991)
[308] G.H. Wannier, Phys. Rev. 79, 357 (1950); Phys. Rev. B 7, 5017 (1973);
[309] R. M. F. Houtappel, Physica (Amsterdam)16, 391 (1950); 16, 425 (1950).
[310] R. F. Wang et al., Nature 439, 04447 (2006)
[311] N. Rougemaille, Phys. Rev. Lett 106, 057209 (2011)
[312] E. Mengotti, L. J. Heyderman, A. Bisig, A. Fraile Rodríguez, L. Le Guyader, F. Nolting, and H. B. Braun, J. Appl. Phys. 105, 113113 (2009)
[313] V. E. Kireev, R. S. Khymyn, B. A. Ivanov, C. E. Zaspel, arXiv:1201.1747v1 (2012)
[314] S. Zhang et al., Phys. Rev. Lett. 109, 087201 (2012)

Annexe A

Curiculum Vitae et autres activités

A.I. CV

HAUET THOMAS

Date de naissance : 22/11/1980
Statut familial : marié, 1 enfant

Institut Jean Lamour (Dép. P2M)
Nancy Université - Faculté des Sciences
Bd des aiguillettes B.P. 239
54506 Vandœuvre-lès-Nancy (France)
Tél : 06.83.05.48.22
Fax : 03.83.68.48.01
E-mail : **thomas.hauet@univ-lorraine.fr**

FORMATION

2003-06	Doctorat de Physique et Chimie de la Matière et des Matériaux, Université Henri Poincaré Nancy 1
2002-03	DEA de physique et chimie de la matière et des matériaux (2^{nd}/12), Université Henri Poincaré Nancy 1
2000-02	Licence+Maîtrise de sciences physiques, Université Henri Poincaré Nancy 1
1998-2000	DEUG (1et 2) Sciences de la matière, Université Henri Poincaré Nancy 1

EXPERIENCES PROFESSIONNELLES

- UNIVERSITE DE LORRAINE (FRANCE), INSTITUT JEAN LAMOUR (EQUIPE 101)
  - **Maitre de conférences :**
    Enseignements : Faculté des sciences, ESTIIN, Ecole des Mines de Nancy, Sciences Po Nancy.
    Recherche : croissance MBE, magnétisme de nano-objet 3D, système à anisotropie perpendiculaire pour mémoires magnétiques et spintronique.
    (sept. 2009-…)

- HITACHI GST, SAN JOSE RESEARCH CENTER (U.S.A.)
  - **Chercheur permanent :** "Renversement d'aimantation dans des nanostructures à anisotropie perpendiculaire et applications aux nouveaux media discrets (BPM)". (jul.2008- sept. 2009)

- HITACHI GST, SAN JOSE RESEARCH CENTER (U.S.A.)
  - **Post-doctorat :** "Effets de couplage dipolaire et effets de transfert de spin dans des multicouches à anisotropie perpendiculaire pour mémoires magnétiques "; Allocataire d'une Bourse Lavoisier générale. (Janv. 2007 – jul. 2008)

- UNIVERSITE DE NANCY (FRANCE), LABORATOIRE DE PHYSIQUE DES MATERIAUX (UMR 7556)
  - **Doctorat de Physique et Chimie de la Matière et des Matériaux :** "Décalage d'échange et magnétorésistances dans des bicouches à base de ferrimagnétiques amorphes couplés par échange" (bourse MENRT, directeurs : Alain SCHUHL, S. MANGIN (2003-2006))

- UNIVERSITE DE YORK (ANGLETERRE), "DEPARTMENT OF PHYSICS"
  - **Stage volontaire :** Installation d'un VSM (encadrant: Kevin O'GRADY, août 2003)

A.II. Activités d'enseignement et de vulgarisation

A.II.1. Enseignements

Depuis ma prise de fonction en tant que maitre de conférences de l'Université de Lorraine en septembre 2009, j'ai eu la chance de travailler dans diverses composantes de l'université : Faculté des sciences et technologie (FST, Vandoeuvre-les-Nancy), Ecoles des Mines de Nancy, ESSTIN. Etant rattaché au départelment de physique et mécanique de la FST, j'ai réalisé des Travaux dirigés, travaux pratiques et cours magistraux dans le domaine des sciences physiques comme décrits ci-dessous :

Electromagnétisme : TD L2 (20h/an, 2009-2011, 2013-2014)
TD L1 (40h/an, 2010-2016) ;
CM/TD L1 Math (60h/an, 2011-2012),
Colles L1 (2010-2014)
Soutien (10h, 2013-2014)

En L1, ce cours donne d'abord des bases mathématiques (types de repères, intégration, gradient, fonction de Taylor) aux étudiants puis introduit les notions de champ et potentiel électrostatique et les methodes pour les calculer dans le cas de système simple (objet unique ou condensateur). Ensuite la notion de courant électrique est approfondie et mène au champ magnétostatique dont on présente également les méthodes de calcul. En L2, les équations de Maxwell sont utilisées (utilisant les outils mathématique de divergence et rotationnel). On définit et utilise les notions d'induction magnétique, d'énergie électromagnétique et de phénomènes dépendant du temps (régime transitoires). Cela nous permet d'aboutir aux ondes électromagnétiques. En L1, des devoirs maisons, colles et heures de soutien sont utilisés pour motiver les étudiants à travailler une matière assez abstraite pour eux.

Mécanique des fluides : TD L2 (20h/an, 2009-2011)

Ces TDs étaient couplés à ceux d'Electromagnétisme pour faciliter la compréhension des champs de vecteurs. Ils introduisent les concepts de statique et cinétique des fluides, les différents types de fluide, équation d'Euler et relations de Bernoulli.

Mécanique quantique : TD ESSTIN 3ème année (24h/an, 2009-2012)
TD Ecole des Mines 1ère année (30h/an, 2003-2005, 2009-2016)
TD L2 (20h/an, 2009-2010) ; CM/ TD L2 (20h/an, 2010-2013)

Ces différents TD et cours sont tous dédiés à la mécanique ondulatoire et l'introduction aux nouveaux concepts de la mécanique quantique, en opposition à la mécanique Newtonienne. On y discute la dualité onde-corpuscule (fentes d'Young), la fonction d'onde, les opérateurs, l'équation de Schrödinger, l'effet tunnel, les puits de potentiels, les liaisons chimiques. A l'école des Mines, ce cours permet aussi une introduction rapide à la relativité. Un effort particulier est apporté pour mettre en lumière les impacts technologiques de la mécanique quantique sur notre quotidien via les exemples d'application des TDs (laser, semi-conducteurs, STM, RMN, XPS) et la présentation par les étudiants de poster (présenté en binome, 10min+5min de question, sur des sujets comme la radiographie X, le Laser, la diode électroluminescente, les têtes de lecture de disques durs, le GPS). EN L2, j'ai réalisé un set de transparents powerpoint mis à disposition des élèves.

Physique Statistique: TD Ecole des Mines 1ère année (30h/an, 2012-2014)

Dans le même esprit que les TDs de mécanique quantique, le but est de transmettre aux étudiants des notions très fondamentales à travers un rapport au monde quotidien et de montrer la diversité des applications de ces notions (posters : la buée, les quasi-cristaux, la supraconductivité, les nanocristaux

fluorescents, la cosmologie, le graphène). Un autre objectif ici est de mettre en avant la mise en équation de problématique et la comparaison des conclusions théoriques avec l'expérience afin d'analyser les limites des hypothèses sur lequels sont basées les modèles théoriques choisis. Comme pour les TDs de méca Q, les TD se font par groupes de 4 étudiants pour favoriser l'entre-aide et les discussions scientifiques entre étudiants. Les notions introduites sont les ensembles micro-canonique, canonique et grand canonique qui sont utilisés pour traiter la statistique des gaz parfaits classiques et quantiques (fermions, bosons). Des concepts importants de la physique sont en particulier introduits comme la densité d'état, l'entropie, l'origine microscopique de la diffusion de matière et d'énergie.

Mesure Physique : Electrocinétique TP L2 (24h/an, 2009-2012)
Electrocinétique TP L1 (30h/an, 2012-2013)
Physique générale TP L2 (24h/an, 2013-2014)

Ces modules réalisés à la FST pour des étudiants de 1ere et 2eme année des Physique-Chimie ont pour buts de familiariser les étudiants avec les méthodes et les bons usages expérimentaux. La lecture d'une notice, la rédaction d'un compte-rendu de TP, les calculs d'incertitudes, comparaison expérience-théorie. La partie électrocinétique de ces TP est dédiée à la mise en pratique des notions acquises durant les cours d'Electromagnétisme (condensateurs, résistance, inductance). Le montage de circuit électrique et l'utilisation d'oscilloscopes y sont appris à des étudiants qui désormais n'ont que très peu de contact avec l'électricité au collège ou lycée. Les TPs de 1ère année traitent des éléments électriques en régime continu, l'oscilloscope et le régime variable, les réseaux en régime alternatif permanent – RLC série, les filtres, les régimes transitoires. Les TPs de 2ème année traitent des filtres passifs, de l'amplificateur opérationnel, des diodes électroluminescentes. La partie TP de physique générale L2 permet aux étudiants de mettre le doigt sur des notions assez abstraites introduites par ailleurs en 2ème année comme les chams électriques, l'effet photo-electrique, l'optique géométrique, la quantification des énergies dans la matière et les photons, la chaleur, les tensions de surfaces.

Optique : TP ESSTIN 3ème année (24-48h/an, 2013-2016)

Ces TP sont destinés à des étudiants futurs ingénieurs et se focalisent sur les phénomènes d'intérférences, de diffraction, de polarisation de la lumière ainsi que sur sa nature électromagnétique (émission d'information via un module acousto-optique, laser). L'outil informatique est très présent et permet d'enregistrer d'images, de faire des mesures précises de longueur ou encore de faire de la spectroscopie. Des appareils comme les interféromètres de Michelson et de Fabry-Perot forcent les étudiants à prendre le temps de bien optimiser leur mesure pour obtenir de grandes précisions sur les paramètres quantifiés grâce à l'expérience. Les TP concernant le laser et la cellule acousto-optique ouvre sur des applications industrielles de l'optique. Les étudiants doivent avoir préparé la partie théorique avant le TP et rendent un compte rendu guidé par des questions assez précises.

Semestre Rebond : CM/TD (20h/an 2014-2016) + resp. physique (3 intervenants)

Ce dispositif propose une aide pour les étudiants en situation d'échec à la fin du semestre 1 et qui se destinent à des métiers en lien avec les sciences dures. Le public visé correspond donc principalement aux étudiants inscrits à la FST / PACES / IUT / BTS / école d'ingénieurs qui veulent ou doivent changer de cursus à la fin du premier semestre de L1. Il s'agit d'aider les étudiants à :

- faire le point sur leur orientation et leur projet professionnel,
- sortir d'une situation d'échec, i.e. regagner en confiance et motivation.
- se remettre à niveau dans les disciplines scientifiques pour se réorienter (à priori principalement en Licence, IUT, BTS ou école d'ingénieur) ou redoubler dans de meilleures conditions qu'en poursuivant dans un S2 qui ne les préparera pas à mieux réussir l'an prochain (leurs lacunes du S1 seront toujours les mêmes).

En 2014-2015 et 2015-2016, environ 30 étudiants se sont inscrits et ont reçu un enseignement scientifique général en math, physique, chimie, biologie, français, anglais. En tant qu'animateur des

60h de physique, j'ai travaillé avec mes collègues à définir un contenu basé sur les livres d'enseignement de 1ère et terminale, incluant principalement la mécanique, l'optique, l'électromagnétisme, et les rappels de mathématiques pour la physique.

A.II.2. Vulgarisation scientifique

- Participation régulière aux visites de laboratoire (élèves du secondaire, étudiants école des Mines, étudiants université, étudiants ESSTIN, grand public)

- Participation régulière aux journées portes ouvertes de l'université et à la fête de la science (e.g. conférences sur les Nanos du quotidien).

- Visites collégiens (1 semaine) : **Loic Jenin** (2011)

- Gestion du cours de **Scientific Humanities, Sciences Po Nancy** 1ère année (CM 24h/an, langue anglaise, 2011, 2012, 2013). Ce cours a pour objectif de présenter les challenges liés aux sciences et en particuliers aux nanotechnologies (au sens le plus large du terme) à des étudiants d'une filière non-scientifique mais pouvant être amenés à discuter et peut être même rendre des décisions sur le sujet dans le futur. Je réalise six séances assez générales seul et joue le rôle d'animateur pour les 6 autres sessions durant lesquels des intervenants spécialistes invités font une présentation d'1h30. La note finale correspond à la moyenne d'une dissertation maison et une dissertation finale concernant des questions sur « Sciences et Société ». Les 12 séances de cours sont les suivantes :

Session 1. What is a "scientific stake"?
Session 2. Communication in sciences. Discussion about "ethics".
Session 3. Political treatment and organization of sciences in France and in Europe
Session 4. Scientific/technologic monitoring and economic intelligence applied to micro- and nanotechnologies (with Philippe Lambert, Institut Jean Lamour and Sahbi Sidhom, Loria)
Session 5. Introduction to nanosciences and nanotechnologies
Session 6. Micro & nano : a pharmacological point of view (with Olivier Joubert, pharmacy faculty)
Session 7. Biotechnologies and GMO (with Jean-Yves Le Déaut, député, vice président de l'OPECST)
Session 8. Nanoelectronics
Session 9. Virtual reality and augmented reality (with Pierre-Frederic Villard, INRIA)
Session 10. Web: Computing systems securities against threats (with Jean-Yves Marion, Loria)
Session 11. Energy : from to nucleus to nuclear energy (with Alexandre Bataille, CEA)
Sesssion 12. Debate on nanotechnologies: can we do better than the recent french one ?

A.II. 3. Administration et tâches collectives

- **Membre élu au conseil de secteur (ex-UFR)** « Physique, Chimie, Géologie et Mécanique » de l'Université de Lorraine (2010-2014)

- **Responsable du Centre de Compétence Magnétisme de l'Institut Jean Lamour**, incluant la responsabilité d'1 AI, et du fonctionnement et de la promotion de 8 appareils de magnétométrie (2011-…)

- **Membre élu au sénat académique de l'Université de Lorraine** (2012-…)

- **Membre élu titulaire au CNU 28ème section** (2015-…)

A.III. Activités de valorisation et de transfert

Ayant travaillé comme post-doc puis comme chercheur permanent au sein du centre de recherche d'Hitachi GST à San Jose (Californie, USA), une des trois grandes sociétés mondiales de disque dur (aujourd'hui en cours de rachat par western digital), j'ai été amené à collaborer étroitement avec des chercheurs R&D plus en aval dans la chaine de création de nouveaux produits. Par ailleurs, j'ai pu enregistrer trois brevets découlant de mes recherches :

- "System, method and apparatus for strain-assisted magnetic recording for controlling switching field and tightening switching field distribution in bit patterned media" Olav Hellwig, Lidu Huang, Thomas Hauet (**US patent 2010/0259846**) (2010)

- "System, method and apparatus for multiple anisotropy layered magnetic structures for controlling reversal mechanism and tightening switching field distribution in bit patterned media" Manfred Schabes, Olav Hellwig and Thomas Hauet (**US patent 2010/0247969**) (2010)

- "Patterned perpendicular magnetic recording medium with data islands having a flux channelling layer below the recording layer" Olav Hellwig, Kentaro Takano and Thomas Hauet (**US patent 2011/0085264**) (2011)

A Nancy, une de mes activités de cherche concerne toujours les mémoires magnétiques. Récemment, j'ai pu déposer un nouveau brevet qui concerne une méthode pour permettre l'authentification d'une information numérique, e.g. lors de transactions bancaires numériques, lors d'authentification biométrique, ou tout type de contrôle d'accès sécurisés. Ce brevet est en cours de publication.

- "Apparatus, system, and method for data pattern comparison" Thomas Hauet, Michel Hehn, Daniel Lacour, Francois Montaigne (**brevet francais, numéro de dépôt 1450427**)

Par ailleurs dans le cadre du centre commun de MAGNETISME que je présente ci-dessous, je propose un travail de service, de R&D et de conseil aux entreprises, avec l'aide du Centre de Valorisation-Innovation-Transfert de l'IJL. Ce travail s'est traduit par exemple depuis 2011 par l'ANR COMSIQUE dans laquelle je soutien, avec mon collègue Stéphane Mangin, l'effort R&D de la société NIPSON Technology de Belfort. Cette société d'environ 50 employés est leader mondial dans la conception de presses numériques magnétiques. NIPSON Technology possède principalement une excellente connaissance phénoménologique des processus magnétiques d'écriture sur le tambour et d'attraction des particules d'encre qui permet des améliorations incrémentales. Cependant seule une compréhension plus fondamentale des processus à l'échelle du micron, voire du nanomètre, permettra des changements disruptifs des méthodes d'impression. Lors d'un premier travail soutenu par une ANR MPPP entre 2012 et 2015, nous avons travaillé au remplacement la couche media magnétique épaisse de CoNiP utilisée comme média d'écriture sur le tambour de l'imprimante et jusqu'à présent déposée par voie chimique, par des couches de CoNiX (ou X = Cr, Pt, N) plus fines déposées par pulvérisation cathodique, meilleure au niveau environnemental. Après 3 ans d'étude, NIPSON a pu réaliser des tests d'écriture en condition de fonctionnement réel avec un tambour couvert de CoNiCr. Le résultat est très positif puisque l'écriture a fonctionné et que la quélité de résolution est proche de celle obtenue avec le média déposé par voie chimique. Depuis, nous nous attachons à mieux comprendre les processus d'écriture et d'effacement des imprimantes. Cela

nécessite la modélisation des champs magnétiques créés par les têtes d'écriture et d'effacement ainsi que de lamagnétométrie et de la microscopie magnétique afin de comprendre les configurations magnétiques résultantes du média. Afin de préreniser cette collaboration un projet de laboratoire commun (projet Labcom) entre l'IJL et NIPSON a été déposé sans succès en 2015, et est redéposé en 2016.

Enfin, je collabore depuis fin 2015 avec la société CRYOSCAN, spin-off de l'université de Lorraine. Dans le cadre d'une thèse CIFRE. Cette collaboration est née dans le contexte du projet TUBE de l'Institut Jean Lamour, qui consiste en la mise en place d'un système ultravide de 70 mètres de long permettant l'interconnexion d'enceintes spécifiques de dépôts de films minces (pour l'électronique, l'énergie, le magnétisme, etc.) et de caractérisation physique (microscopie, spectroscopie). Parmi les appareils attachés au TUBE, j'ai été chargé du développement d'un système, à ce jour unique au monde, de magnétométrie sous-ultravide permettant divers types de mesure magnétique dans une large gamme de température. La société CRYOSCAN a remporté l'appel d'offre pour la construction de cet appareil et souhaite en faire un des produits phare de son catalogue. L'appareil offre un atout majeur dans la compétition mondiale actuelle pour le développement de nouveaux micro- et nano-systèmes pour l'enregistrement magnétique, les capteurs et la communication. Anton Kyianytsia en thèse CIFRE permet d'assurer une relation forte entre CRYOSCAN et l'IJL afin d'optimiser au mieux l'appareil (pour les marchés futurs de CRYOSCAN et pour les besoins scientifiques de l'IJL). Le doctorant, par son travail de recherche, démontrera durant sa thèse les capacités uniques de cet instrument et devra avoir un impact sur la communauté du nanomagnétisme et de la spintronique.

A.IV. Activités d'administration de la recherche

A.IV. 1. Gestion du centre commun MAGNETISME de l'institut Jean Lamour

Depuis 2011, je suis responsable du centre commun (CC) MAGNETISME de l'Institut Jean Lamour. Celui-ci s'appuie sur les compétences techniques d'un assistant ingénieur (Stéphane Suire, opérant en parallèle le liquéfacteur d'Helium auquel tous les cryostats du CC sont connectés) et regroupe des appareils permettant d'effectuer diverses mesures physiques en fonction de la température (2K-1000K) et d'un champ magnétique (0 à 9 Tesla). Il s'agit ici d'effectuer des mesures d'aimantation, de susceptibilité magnétique, mais aussi de caractériser les propriétés de transport électrique des matériaux (résistance, magnétorésistance, effet Hall) et les propriétés thermiques (chaleur spécifique, constante thermoélectrique) comme décrit dans la Table 1. En plus de ces six appareils, le CC s'est récemment doté d'un nouveau cryostat PPMS et d'un magnétomètre Kerr (avec possibilité de mesures en géométrie longitudinale et polaire). Le CC fournit un service de mesure dans le cas de besoins ponctuels d'un utilisateur ou une formation puis mise a disposition des appareils pour des utilisations plus récurrentes. Il fournit également du conseil quant aux méthodes de caractérisation les plus adaptées aux questions scientifiques des utilisateurs et de l'aide dans le traitement des résultats expérimentaux. Enfin Stéphane Suire réalise des travaux de développements techniques spécifiques aux besoins des utilisateurs pour des outils innovants intégrables aux appareils du CC (conception/design, suivi de fabrication).

	MOKE	SQUID magnetometer		Tunable Cryostats			Vibrating sample magnetometer	
Tools	Home-made	MPMS	SQUID-VSM	3 PPMS			VSM Lake Shore	VSM DMS
Magnetic fields	ElectroM	Supraconducting magnet					Electromagnet	
	0.4T	7 T		7 T	9 T	9T	2 T	2.5 T
Temperature	RT	2- 400K	2 – 1000 K	2 – 350 K			300 K	77 -300 K
Type of measure	Rotation Kerr	M (10^{-8} emu)	M + χ (10^{-8} emu)	M + χ	M + χ + C+ R	M + χ	M (10^{-6}emu)	
Avantages	High speed		High speed	Resistance, Hall effect, Calorimetry, VSM, etc.			Rotating field	Automatic Rotating field

Table A.1. Descriptif des appareils du CC MAGNETISME

A travers la gestion du CC et les besoins de chercheurs soit interne à l'IJL ou à l'Université de Lorraine soit extérieurs académiques (Université d'Orsay, de Sumy State, de Saarbruck, d'Alger, etc.) ou industriels (NIPSON, Institut de Soudure, BLS Magnet, etc.), je découvre de nouvelles thématiques scientifiques : supraconductivité, nanoparticules multiferroiques, média pour l'impression magnétique, ferro-fluides, nanomatériaux pour le vivant, etc.

Depuis 2012, nous travaillons en collaboration avec les laboratoires de Saarbrucken et Kaiserslautern afin de valoriser le magnétisme dans la « Greater Region ». Aujourd'hui nous travaillons au fonctionnement d'un centre commun transnational dont le but est de faire le pont entre la recherche fondamentale et les activités R&D d'entreprise de la « Greater région », notamment dans le cadre de l'Université de la Grande Region et de l'INTERREG VA. Il y a une très bonne complémentarité entre les outils présents dans les trois centres : Nancy (mesures statiques), Saarbruck (imagerie), Kaiserlautern (mesures dynamiques). Nous offrons un service à l'aide de ces appareils et du conseil aux entreprises. Le 1er octobre 2015, j'ai co-organisé un workshop à Nancy avec l'ensemble des acteurs du magnétisme de Nancy, Sarrebruck, Kaiserslautern, Luxembourg et Liège afin d'étendre le centre commun. Je co-organise également actuellement un workshop concernant les nanoparticules magnétiques et leurs applications qui est prévu le 20 et 21 octobre 2016 à Nancy.

Enfin depuis 2015, je mène une action de réseautage afin de fédérer les plateformes de magnétométrie, pour l'instant francophones. Le « réseau de magnétométrie » rassemble à ce jour 25 plateformes en France et en Belgique. Son objectif premier est de faire collaborer les plateformes afin d'optimiser les pratiques de chaque centre, augmenter le savoir et savoir-faire de chaque centre, assurer une veille technologique efficace, coordonner les nouveaux développements techniques, et surtout de permettre la résolution de problèmes techniques par le partage d'expérience et de pièces. Le réseau peut également jouer le rôle de porte d'entrée pour des besoins en magnétométrie, qu'ils proviennent d'institutions académiques, de sociétés privées ou du grand public. Enfin, des actions collaboratives de publication de documents techniques, d'organisation de workshops, de

formation (initiale ou pour des travailleurs) aux méthodes de mesures et traitement des données, et de vulgarisation vers le grand publique sont menées afin de pérenniser les savoirs et savoirs-faire dans le domaine de la magnétométrie. Avec mon collègue Philippe Lambert, nous avons développé un premier site collaboratif CORE CNRS qui permet de partager des documents et surtout d'échanger sur nos problèmes techniques via un forum (avec un certain succès puisqu'il est utilisé en moyenne 1 fois par semaine). Nous venons de mettre en place un second site web (http://magnetometry.cnrs.fr/) qui aura les mêmes fonctionnalités mais sera plus ouvert vers les non-membres.

A.IV. 2. Liste des stage de masters et post-doc encadrés et thèses co-dirigées

Encadrement étudiants licence et master

-Stage Master 1 : **Saadia El Mandour** et **Mamhiana Rajaonarison** (2 mois, 2006)
Etude des effets de magnétorésistance dans des barreaux submicroniques obtenues à partir de matériaux ferrimagnétiques (Coencadrement avec S. Mangin)

-Stage Master 1 : **Priscilla Gris** et **Pierre Jean Girardot** (2 mois, 2006)
Sujet: Etude des configurations magnétiques dans les systèmes à aimantation perpendiculaire couplés par échange : [Co/Pd]/TbFe (Coencadrement avec S. Mangin)

-Stage Master 2 : **Olivier Rigaut** (6 mois, 2010) propriétés magnétiques et magnétotransport de clusters de CoFeB (co-encadrement avec F. Montaigne)

-Stage L3 césure recherche : **Alex Didillon** (5 mois, 2011) Mesure de nanopilier pour l'étude du phénomène de transfert de spin

-Stage Master 2 : **Thibault Boulec** (6 mois, 2011) Etude du renversement d'aimantation de plots nanométriques à base de TbCo (co-encadrement avec S. Mangin et T. Thomson de Manchester University)

-Stage Master 2 : **Amal Sediri** (6 mois, 2012) Assemblée de nanocaps Co/Pt à aimantation perpendiculaire

-Stage étudiant en thèse étranger : **Serhii Vorobiov** de Sumy university, Ukraine (4 mois, 2012) VSM characterization of Gd/Co multilayers and GdCo alloys.

- Stage labo L3 (30h, 2013) **Rouane Redha**, magnetic tunnel junction

-Stage Master 1: **Tom Ferte** et **Vincent Joly** (2 mois, 2013), Electric field control of Curie temperature in Fe1-xVx. (co-encadrement avec S. Andrieu)

- Stage étudiant en thèse étranger : **Serhii Vorobiov** de Sumy university, Ukraine (4 mois, 2013) VSM characterization of Gd/Co multilayers and GdCo alloys.

- Stage Master 2 (école Ingé. ESSTIN) : **Weiling Li** (6 mois, 2013), spin transfer induced domain wall motion (co-encadrement avec S. Le Gall)

- Stage Master 2: **Tom Ferte** (5 mois, 2014), Electric field control of Curie temperature in Fe1-xVx. (co-encadrement avec S. Andrieu)

-Stage tutoré Master 1 : **Julien Claudot** (60h, 2014), Simulation réseaux de plots magnétiques

-Stage IUT informatique : **Guillaume Migeon** (3 mois, 2014), Création d'un site de réservation et base de donnée du CC Magnétisme (co-encadrement avec C. Senet)

- Stage Master 2 (Ecole des Mines) : **Pierre vallobra** (6 mois, 2015), « Elaboration, analyse et simulation de couches magnétiques à anisotropie perpendiculaires » (co-encadrement avec Ch-H Lambert, S. Mangin)

- Stage Master 1 : **Jordan Ledig** et **Amani Ben-Hnia** (2 mois, 2016), effets thermiques sur l'aimantation d'assemblées de plots ferromagnétiques

- Stage Master 2 (école des.Mines de Nancy) : **A. Dekens**,(6 mois, 2016), étude des processus d'écriture et de désaimantation dans l'impression magnétique

Co-direction de thèse :

- **Iaryna Lytvynenko** (2012-2016, thèse Ukrainienne) : Control of perpendicular magnetic anisotropy in tunnel junctions (directeur de thèse Vitaliy V. Bibyk). Travail effectué en partie à Sumy university (Ukraine) et IJL (séjour total en France de 11 mois). **Thèse soutenue le 3 juin 2016 à SUMY**.

- **Damien Louis** (sept. 2013- …, Thèse MNRT) : Frustrations dipolaires magnétiques (directeur de Thèse F. Montaigne). **Date de soutenance prévue octobre 2016**

- **Anton Kyianytsia** (oct. 2015-…, Thèse CIFRE IJL-CRYOSCAN) : Thermal features of magnetic systems studied by In-situ Kerr magnetometry (directeur de Thèse B. Kierren)

Encadrement de post-doc :

- **Ammanabrolu Rajanikanth** (Indien, 2 ans, 2011-2012), ANR ELECMADE : voltage-induced magnetic anisotropy change (co-encadrement avec S. Andrieu)

- **Tao Liu** (Chinois, 2 ans, 2013-2014), ANR COSMIQUE : designing new media and recording methods for magnetic printers / magnetic bubbles

- **Crosby-Soon Chang** (Australien, 2015-…), Univ. Grande Région/Région Lorraine : R&D by magnetometry measurements

A.V. Rayonnement scientifique

- **Prix Suzanne Zivi 2015**

- **Allocataire d'une bourse Lavoisier Générale 2007**

- **Comité de programme grands instruments** : Chaque centre grand-instrument, i.e. mettant à disposition de la communauté scientifique sur projet des appareils de pointe très couteux, demande à des chercheurs extérieurs d'expertiser les demandes (proposals) d'expériences. J'ai réalisé ce travail pour deux centres de neutrons, l'un à Washington (NIST ncnr, 2007-2013) et l'autre à Orsay (CEA LLB, 2010-2014).

- **Membre de l'observatoire des micro- et nano-technologies (OMNT)** : veille scientifique et technique dans le groupe Nanoélectronique et spintronique (2014-2016)

- **Comité de sélection MCF :** Toulouse (poste MCF0378, section 28, juin 2011)

- **Project Reviewer** : J'ai réalisé divers expertises de projet pour UEFISCDI ("ANR" Roumaine, 2010), SNSF ("ANR" Suisse, 2011-2014), FWO ("ANR" Flamande, 2015)

- **Expertise/Contrôle « Crédit Impôt Recherche »** : Depuis 2011, je me suis engagé auprès du ministère de l'enseignement supérieur et de la recherche pour expertiser en amont l'éligibilité d'entreprise au CIR (34 expertises) et pour contrôler à posteriori la validité des dépenses de R&D des entreprises (2 contrôles).

- **Publications reviews**: Ces dernières années j'ai réalisé des rapports d'expertise pour divers journaux internationaux comme Phys. Rev. Lett, Phys. Rev. B, Appl. Phys. Lett., J. Appl. Phys., IEEE trans. Magn., Cond. Mater., J. Magn. Magn. Mater.

- **Conférences et séminaires internationaux :** depuis 2006, 20 oraux (5 invités) et plus de 45 oraux (dont 12 invités) présentés par un co-auteur, 17 séminaires invités.

- **Mobilité nationale et internationale :**

Séjours de recherche longs dans des instituts étrangers
Hitachi GST San Jose (USA, 2 ans et 8 mois, 2007-2009)
New York University (USA, 3 mois, 2014)

Séjours de recherche courts dans des instituts étrangers
York University (UK, 2 mois, 2003, montage d'un VSM), IEF Orsay (France, 1 mois, 2008, préparation concours CNRS), Dresden Rosendorf (Allemagne, 1 semaine, 2011, Kerr microscopy), Bebek Univ.Istambul (Turquie, 1 semaine, 2011, transport experiments), Chemnitz (Allemagne, 1 semaine, 2012, MFM)

Semaines d'expériences synchrotron et neutrons
NIST ncnr (Washington, USA, 7 semaines), BESSY (Berlin, Allemagne, 4 semaines), ALS (Berkeley, USA, 3 semaines), SSRL (Stanford, USA, 1 semaine), SLS (Villigen, Suisse, 1 semaine), SOLEIL (Paris, France, 7 semaines), ESRF (Grenoble, France, 1 semaine)

- **Développement de collaborations internationales pérennes :**

SUMY STATE UNIVERSITE (UKRAINE)

Dans le cadre du CC MAGNETISME, une collaboration a été développée depuis 2012 avec l'Université de SUMY en Ukraine. En effet l'université de SUMY ne possède pas les appareils de magnétométrie nécessaire à l'étude des composés magnétiques qu'ils font cloitrent. Par conséquent des étudiants et chercheurs viennent quelques mois par an afin d'utiliser les appareils du CC MAGNETISME. Je me suis également rendu en Ukraine en 2012 afin de visiter l'université et comprendre leur problématique. Le doyen de la faculté des sciences de SUMY est lui venu en juin 2013.Cette collaboration est majoritairement financée par l'Ukraine. Les résultats de cette collaboration sont : 4 publications (1 JAP, 2 JMMM, 1 Vacuum), 1 thèse co-dirigée (Iaryna Lytvynenko (2012-2016), 4 étudiants et chercheurs (Serhii Vorobiov Iaryna Lytvynenko, Olga Shutylieva, Iryna Cheshko) formés aux outils de magnétometrie de pointe, 2 chercheurs francais dans l'advisory board du journal « Nano- and Electronic Pysics » édité par l'université de SUMY.

BOGAZICI UNIVERSITY (TURKEY), MESSINA UNIVERSITY (ITALY)

Depuis mon arrivée à Nancy en 2009, je continue à collaborer avec un ancien collaborateur d'Hitachi GST, Ohan Ozatay, désormais associate Prof. a Istambul. Nous travaillons sur des nouvelles mémoires magnétiques type disque durs (media nanostructures « bit pattern media ») et tout solide (mémoire magnétique 3D « page memory »). Nous profitons en particulier des énormes

investissements actuels de ce pays en faveur de la recherche dans les nanotechnologies (e.g. création de salle blanche semi-industrielle notamment à Ankara). Tous deux chercheurs-experimentateurs, nous collaborons avec Giovanni Finocchio (associate prof. de l'Université de Messina en Italie) qui est spécialiste des simulations magnétiques. Cette collaboration se réalise sur trois projets différents liés au magnétisme et à l'électronique de spin : "3D Page memory" (Application pour l'enregistrement magnétique), "Magnetic bubble stability and dynamics" (étude fondamentale) et "Simulation of thermal excitations in ferromagnetic materials" (étude fondamentale). Le financement de cette collaboration provident de diverses sources francaise, Italienne et Turqu : "International Mobility" and "Invited Prof." programs of UL (2011, 2014, 2015), CNRS/TUBITAK "PEPS "program (2015), CNR Italy/TUBITAK Bilateral agreement (B52I14002910005), MIUR-PRIN 2010–11 Project 2010ECA8P3 'DyNanoMag'. Cette collaboration a donné lieu à divers séjours de recherche : Thomas Hauet à Istanbul (sept. 2011), Ozhan Ozatay à Nancy (june 2014), G. Finocchio à Nancy (april 2015), à Istambul (Sept. 2011, march 2014), V. Karakas (turkish student) à Messina (2014**).** Les résultats de cette collaboration sont : 6 séminaires donnés à Nancy/Istanbul/Messina, 5 publications (2 APL, 1 PRB, 2 JAP), 1 chapitre de livre, 6 présentations dans des conférences internationales.

- **Participation à l'organisation de conférences :**

IWST 2006, Nancy (co-organisateur)
Workshop Quantum Design/Lot-Oriel 2014, Nancy (local organizer)
M-SNOW 2014, Nancy (local co-organizer)
JMC/CDM 2014, Paris (co-organisateur du mini-colloque « Nanomagnetism : Magnetization dynamics and spintronics »)
IEEE Advances in Magnetics Conference 2016, Bormio (International steering committee)
Colloque Louis Néel 2016, Saint Dié des Vosges (co-organizer)
WorkShop IWST+ Smart Sensor 2016, Nancy (co-organizer)

+ 7 international conference session Chairs : MMM Tampa 2007, JEMS Dublin 2008, Intermag-MMM Washington DC 2010, Intermag Vancouver 2012, MMM-Intermag Chicago 2013, Zakopane 2013, Intermag Dresden 2014

- **Implication dans des projets nationaux et internationaux :**

Porteur : **Bourse Lavoisier générale** : allocataire (2007)
Programme "Initiative Post-doc" du MESR (2007-2008)
Projet UL pour « dimension internationale » Turquie (2011)**, Ukraine** (2012)
Aide Région Lorraine-UL « Soutien à la recherche » (canons UHV, 80keuros, 2013)
PICS CNRS-Tubitak (2015)
PEPS UL-CNRS (2015) : GREEN-IJL (30 keuros)
Projet Européen EIT Raw Materials (2017-2020, 200 keuros)

Partenaire : **ANR Blanche** : ELECMADE (A Marty, 2010-2013)
ANR MPPP : COSMIQUE (E. Aubry, 2012-2015)
ANR Jeune Chercheur : ELECTRA (A. Bataille, 2011-2014)
ANR SIC : ULTRAMOX (T. Pezeril, 2014-2017)
INTERREG IVA Grande Région : GrosseRegionMagneticNetwork (2012-2015)

A.VI. Liste de publications et communications

Depuis 2005 : 69 publis ou actes (h-index 17 google-scholar), **2** chapitres**, 4** brevets**, 21** oraux (dont 6 invités)**, 18** séminaires invités**,** plus de **65** oraux (dont 18 invités) présentés par un co-auteur

A.VI.1. Publications dans journaux avec comité de lecture :

59 publications (dont 3 Phys. Rev. Lett., 28 Appl. Phys. Lett., 15 Phys. Rev. B, 4 J. Appl. Phys.)

59. "Influence of the Cr and Ni concentration in CoCr and CoNi alloys on the structural and magnetic properties" E. Aubry, T. Liu, A. Billard, A. Dekens, F. Perry, S. Mangin, T. Hauet, **J. Magn. Magn. Mater. 422**, 391 (2016)

58. "Torque magnetometry of perpendicular anisotropy exchange-spring heterostructures" P. Vallobra, T. Hauet, F. Montaigne, E.G Shipton, E.E. Fullerton, S. Mangin, accepted to **J. Appl. Phys.** (2016)

57. "Transport and magnetic measurements on Bi2Sr2CaCu2O8 nanowire networks prepared via electrospinning", M.R. Koblischka, X.L. Zeng, T. Karwoth, T. Hauet, U. Hartmann, **IEEE Trans. Appl. Superconductivity** 26, 1800605 (2016)

56. "Mechanism of single bubble formation in patterned dot array under in-plane magnetic field" T. Liu, V. Puliafito, F. Montaigne, S. Petit, C. Deranlot, S. Andrieu, O. Ozatay, G. Finocchio and T. Hauet, **J. Phys. D: Appl. Phys.** (2016) *editor pick JPhys+*

55. "Magnetic properties of electrospun non-woven superconducting fabrics", M. R. Koblischka, X. L. Zeng, T. Karwoth, T. Hauet, and U. Hartmann, **AIP Advances 6**, 035115 (2016)

54. "Direct evidence for minority spin gap in the Co2MnSi Heusler alloy" S. Andrieu, A. Neggache, T. Hauet, T. Devolder, A. Hallal, M. Chshiev, A. Bataille, P. Le Fèvre, F. Bertran, **Phys. Rev. B 93**, 094417 (2016)

53. "Enhanced magnetization at the Cr/MgO(001) interface" M.-A. Leroy, A. M. Bataille, Q. Wang, M. R. Fitzsimmons, F. Bertran, P. Le Fèvre, A. Taleb-Ibrahimi, A. Vlad, A. Coati, Y. Garreau, T. Hauet, C. Gatel, F. Ott and S. Andrieu, **Appl. Phys. Lett. 107**, 251602 (2015)

52. "Long range phase coherence in double barrier magnetic tunnel junctions with large thick metallic quantum well" B. S. Tao, H. X. Yang, Y. L. Zuo, X. Devaux, G. Lengaigne, M. Hehn, D. Lacour, S.Andrieu, M. Chshiev, T. Hauet, F. Montaigne, S. Mangin, X. F. Han, Y. Lu, **Phys. Rev. Lett. 115**, 157204 (2015)

51. "Time scales of bias voltage effects in Fe/MgO-based magnetic tunnel junctions with voltage-dependent perpendicular anisotropy" Ia.M. Lytvynenko, T. Hauet, F. Montaigne, V.V. Bibyk, S. Andrieu, **J. Magn. Magn. Mater. 396,** 333 (2015)

50. "Generation and manipulation of domain walls using a thermal gradient in a ferrimagnetic TbCo wire" R. Tolley, T. Liu, Y. Xu, S. Le Gall, M. Gottwald, T. Hauet, M. Hehn, F. Montaigne, E. E. Fullerton, and S. Mangin, **Appl. Phys. Lett. 106**, 242403 (2015)

49. "The effect of annealing on magnetic properties of Co/Gd multilayers", S. Vorobiov; I. M Lytvynenko; T. Hauet, M. Hehn, D. Derecha, A. M. Chornous, **Vacuum 120**, 9 (2015)

48. "Needle-type GMR sensor to estimate the magnetic properties of diluted ferrofluid for biomedicine application" H. Shirzadfar, R. Haraszczuk, M. Nadi, D. Kourtiche, S. Yamada, T. Hauet, **Innovation and Research in BioMedical Engineering 36**, 178 (2015)

47. "Thermally activated domain wall motion in [Co/Ni](111) superlattices with perpendicular magnetic anisotropy" S. Le Gall, N. Vernier, F. Montaigne, M. Gottwald, D. Lacour, M. Hehn, D. Ravelosona, S. Mangin, S. Andrieu, T. Hauet, **Appl. Phys. Lett. 106**, 062406 (2015)

46. "Extraordinary Hall effect based magnetic logic applications" T. Liu, D. Lacour, F. Montaigne, S. Le Gall, M. Hehn, and T. Hauet, **Appl. Phys. Lett. 106**, 052406 (2015)

45. "Magnetic tunnel junctions using Co/Ni multilayer electrodes with perpendicular magnetic anisotropy" Ia. Lytvynenko, C. Deranlot, S. Andrieu, T. Hauet, **J. Appl. Phys. 117**, 053906 (2015)

44. "Spectroscopic and transport studies of CoxFe1-x/MgO(001) based magnetic tunnel junctions" S. Andrieu, L. Calmels, T. Hauet, F. Bonell,P. Le Fèvre, F. Bertran, **Phys. Rev. B 90**, 214406 (2014)

43. "Influence of stray fields on the switching-field distribution for bit-patterned media based on pre-patterned substrates", B. Pfau, C. M. Günther, E. Guehrs, T. Hauet, T. Hennen,S. Eisebitt, and O. Hellwig, **Appl. Phys. Lett. 105**, 132407 (2014)

42. "Interfaces anisotropy in single crystal V/Fe/V trilayer" D. Louis, I. Lytvynenko, T. Hauet, D. Lacour, M. Hehn, S. Andrieu, and F. Montaigne, **J. Magn. Magn. Mater. 372**, 233 (2014)

41. "MgO-based magnetic tunnel junction using $(CoFe)_3Ge$ electrodes" A. Neggache, T. Hauet, F. Bertran, P. Le Fevre, S. Petit-Watelot, T. Devolder, P. Ohresser, P. Boulet, C. Mewes, S. Maat, J. Childress, and S. Andrieu, **Appl. Phys. Lett. 104**, 252412 (2014)

40. "Tunnel-mediated coupling between antiferromagnetic thin films", M.-A. Leroy, A.M. Bataille, B. Dkhil, F. Porcher, A. Barbier, V.L.R. Jacques, Y. Lu, C. Bellouard, T. Hauet, S. Ravy,J.Herrero-Martin, C. Gatel, S. Andrieu, A. Gukasov, and C. Tiusan, **Phys. Rev. B 90**, 035432 (2014)

39. "Reversal mechanism, switching field distribution, and dipolar frustrations in Co/Pt bit pattern media based on auto-assembled anodic alumina hexagonal nanobump arrays" T. Hauet, L. Piraux, S. K. Srivastava, V.A. Antohe, D. Lacour, M. Hehn, F. Montaigne, J. Schwenk, M.A. Marioni, H.J. Hug, O. Hovorka, A. Berger, S. Mangin, F. Abreu Araujo, **Phys. Rev. B** 89, 174421 (2014)

38. "Influence of magnetic domain size on dipolar interactions and hysteresis field asymmetry in layered high/low coercivity perpendicular anisotropy systems" T. Hauet and O. Hellwig, **J. Appl. Phys.** 115, 123911 (2014)

37. "Measurement of magnetization using domain compressibility in CoFeB films with perpendicular anisotropy" N. Vernier, J.-P. Adam, S. Eimer, G. Agnus, T. Devolder, T. Hauet, B. Ockert, and D. Ravelosona, **Appl. Phys. Lett 104** , 122404 (2014)

36. "Microstructural, electrical and magnetic properties of $Fe_{35}Co_{65}$ thin films grown by thermal evaporation from mechanical alloying powder", N. Redjdal, H. Salah, T. Hauet, H. Menari, S.M. Chérif, N. Gabouze, **Thin Solid Film** 552, 164 (2014)

35. "Compositional dependence of the magnetic properties of epitaxial FeV/MgO thin films" T. Devolder, M. Manfrini, T. Hauet, and S. Andrieu, **Appl. Phys. Lett. 103**, 242410 (2013)

34. "Nanoscale spintronic oscillators based on the excitation of confined soliton modes" G. Finocchio, V. Puliafito, S. Komineas, L. Torres, O. Ozatay, T. Hauet, B. Azzerboni, **J. Appl. Phys. 114**, 163908 (2013)

33. "Interface magnetic anisotropy modified by electric field in epitaxial Fe/MgO(001)/Fe magnetic tunnel junction" A. Rajanikanth, T. Hauet, F. Montaigne, S. Mangin, S. Andrieu, **Appl. Phys. Lett. 103**, 062402 (2013)

32. "Quantifying perpendicular magnetic anisotropy at Fe/MgO interface", C.-H. Lambert, A. Rajanikanth, T. Hauet, S. Mangin, E.E. Fullerton and S. Andrieu, **Appl. Phys. Lett. 102**,

122410 (2013)

31. "Magnetic Switching Driven by Nanosecond scale Heat and Magnetic Field Pulses: An Application of Macrospin Landau-Lifshitz-Bloch Model", U. Kilic, G. Finocchio, T. Hauet, S. H. Florez, G. Aktas and O. Ozatay, **Appl. Phys. Lett. 101**, 252407 (2012)

30. "Periodic array of magnetic nanostructures by depositing Co/Pt multilayers on the barrier layer of ordered anodic alumina templates", L. Piraux, V.A. Antohe, F. Abreu Araujo, S.K. Srivastava, M. Hehn, D. Lacour, S. Mangin, T. Hauet, **Appl. Phys. Lett. 101**, 013110 (2012)

29. "Co/Ni(111) superlattices studied by microscopy, X-ray absorption and *ab-initio* calculations" M. Gottwald, S. Andrieu, F. Gimbert, E. Shipton, L. Calmels, C. Magen, E. Snoeck, M. Liberati, T. Hauet, E. Arenholz, S. Mangin, E. Fullerton, **Phys. Rev. B 86**, 014425 (2012)

28. "Spin-Polarized Electron Tunneling in bcc FeCo/MgO/FeCo Magnetic Tunnel Junctions" F. Bonell, T. Hauet, S. Andrieu, F. Bertran, P. Le Fevre, L. Calmels, A. Tejeda, F. Montaigne,B. Warot-Fonrose, B. Belhadji, A. Nicolaou, and A. Taleb-Ibrahimi, **Phys. Rev. Lett. 108**, 176602 (2012)

27. "Asymmetric magnetization reversal in dipolarly coupled spin valve structures with perpendicular magnetic anisotropy" M. Gottwald, M. Hehn, D. Lacour, T. Hauet, F. Montaigne, S. Mangin, P. Fischer, M.-Y. Im, A. Berger, **Phys. Rev. B 85**, 064403 (2012)

26. "Origin of magnetic switching field distribution in bit patterned media based on pre-patterned substrates" B. Pfau, C. M. Gunther, E. Guehrs, T. Hauet, H. Yang, L. Vinh, X. Xu,, D. Yaney, R. Rick, S. Eisebitt, and O. Hellwig, **Appl. Phys. Lett. 99**, 062502 (2011)

25. "Non- uniform switching of the perpendicular magnetization in a spin-torque-driven magnetic nanopillar" D.P. Bernstein, B. Brauer, R. Kukreja, J. Stohr, T. Hauet, J. Cucchiara, S Mangin, J.A. Katine, T. Tyliszczak, K.W. Chou, Y. Acremann, **Phys. Rev. B (R) 83**, 180410 (2011)

24. "Influence of ion irradiation on switching field and switching field distribution in arrays of Co/Pd-based bit pattern media" T. Hauet, O. Hellwig, S.-H. Park, C. Beigne, E. Dobisz, B.D. Terris, and D. Ravelosona, **Appl. Phys. Lett. 98**, 172506 (2011)

23. "High-Density Bit Patterned Media: Magnetic Design and Recording Performance" M.K. Grobis, O. Hellwig, T. Hauet, E. Dobisz, T.R. Albrecht, **I.E.E.E. Trans Magn. 47**, 6 (2011)

22. "Magnetic susceptibility measurements as a probe of spin transfer driven magnetization dynamics, Weiwei Lin, J. Cucchiara, C. Berthelot, T. Hauet, Y. Henry, J. A. Katine, Eric E. Fullerton, and S. Mangin, **Appl. Phys. Lett. 96**, 252503 (2010)

21. "Bit patterned media based on block copolymer directed assembly with narrow magnetic switching field distribution" O. Hellwig, J. K. Bosworth, E. Dobisz, D. Kercher T. Hauet, G. Zeltzer, J. D. Risner-Jamtgaard, D. Yaney, and R. Ruiz, **Appl. Phys. Lett. 96**, 052511 (2010)

20. "Measurements of the write error rate in bit patterned magnetic recording at 100–320 Gb/ in2" M. Grobis, E. Dobisz, O. Hellwig, M. E. Schabes, G. Zeltzer, T. Hauet, and T. R. Albrecht, **Appl. Phys. Lett. 96**, 052509 (2010)

19. "Role of reversal incoherency in reducing switching field and switching field distribution of exchange coupled composite bit pattern media" T. Hauet, E. Dobisz, S. Florez, J. Park, B. Lengsfield, B.D. Terris and O. Hellwig, **Appl. Phys. Lett. 95**, 262504 (2009)

18. "Angle dependence of the interface magnetic configuration in a model antiferromagnetically coupled ferrimagnetic/ferrimagnetic bilayer GdFe/TbFe", S. Mangin, L. Thomas, F. Montaigne, W. Lin, T. Hauet, Y. Henry, **Phys. Rev. B 80**, 224424 (2009)

17. "Coercivity Tuning in Co/Pd Multilayer Based Bit Patterned Media" O. Hellwig, T. Hauet, T. Thomson, E. Dobisz, J. D. Risner-Jamtgaard, D. Yaney, B. D. Terris, E. E. Fullerton, **Appl. Phys. Lett. 95**, 232505 (2009)

16. "Revealing the reversible rotation of magnetization in exchange-coupled composite media switching" T. Hauet, S. Florez, D. Margulies, Y. Ikeda, B. Lengsfield, N. Supper, K. Takano, O. Hellwig, and B.D. Terris, **Appl. Phys. Lett. 95**, 222507 (2009)

15. "Probing activation energy barrier distribution for reversal of strongly exchange coupled magnetic multilayer thin films" O. Ozatay, T. Hauet, S. H. Florez, J. A. Katine, A. Moser, J.–U. Thiele, L. Folks and B. D. Terris, **Appl. Phys. Lett**. **95**, 172502 (2009)

14. "Suppression of the perpendicular anisotropy at the CoO Néel temperature in exchange-biased CoO/[Co/Pt] multilayers" E. Shipton, K. Chan, T. Hauet, O.Hellwig and E. E. Fullerton, **Appl. Phys. Lett. 95**, 132509 (2009)

13. "Magnetoresistances in an amorphous exchange-coupled bilayer" T. Hauet, F. Montaigne, M. Hehn, Y. Henry, S. Mangin, **Phys. Rev. B 79**, 224435 (2009)

12. "Influence of an interface domain wall on spin-valve giant magnetoresistance" T. Hauet, F. Montaigne, M. Hehn, Y. Henry, S. Mangin, **Appl. Phys. Lett. 93**, 222503 (2008)

11. "Mechanism of chirality reversal for planar interface domain walls in exchange coupled hard/soft magnetic bilayers" J. McCord, Y. Henry, T. Hauet, F. Montaigne, E.E. Fullerton and S. Mangin, **Phys. Rev. B 78**, 094417 (2008)

10. "Field driven ferromagnetic phase nucleation and propagation in antiferromagnetically coupled multilayer films with perpendicular anisotropy" T. Hauet, C. Günther, O. Hovorka, A. Berger, M.-Y. Im, P. Fischer, T. Eimüller and O. Hellwig, **Appl. Phys. Lett. 93**, 042505 (2008)

9. "Dipolar field screening in perpendicular systems [Pt /Co]x/TbFe and [Pt /Co]x/Pt/TbFe " S. Mangin, T. Hauet, P. Fischer, D.H. Kim, J. Kortright, K. Chesnel, E. Arenholz and E.E. Fullerton, **Phys. Rev. B 78**, 024424 (2008)

8. "Design of Co/Pd multilayer system with antiferromagnetic-to-ferromagnetic phase transition" J.-U. Thiele, T. Hauet and O. Hellwig, **Appl. Phys. Lett. 92**, 242502 (2008)

7. "Interfacial magnetic domain wall formation in perpendicular-anisotropy exchange-spring films" S. Watson, T. Hauet, J.A. Borchers, S. Mangin, E.E. Fullerton, **Appl. Phys. Lett. 92**, 202507 (2008)

6. "Direct observation of field and temperature induced domain replication in dipolar coupled perpendicular anisotropy films" T. Hauet, C. Günther, B. Pfau, M. Schabes, J.-U. Thiele, R.L. Rick, P. Fischer, S. Eisebitt and O. Hellwig, **Phys. Rev. B 77**, 184421 (2008)

5. "Exchange bias training effect in GdFe/TbFe : Micromagnetic mechanism" T. Hauet, S. Mangin, J. McCord, F. Montaigne and E.E. Fullerton, **Phys. Rev. B 76**, 144423 (2007)

4. "Tuning exchange-bias properties by thermal effects in hard/soft bilayer" T. Hauet, S. Mangin, J.A. Borchers, F. Montaigne and Y. Henry, **Appl. Phys. Lett. 91**, 022505 (2007)

3. "Positive exchange-bias induced by interface domain wall quenching in GdFe/TbFe films" Y. Henry, S. Mangin, T. Hauet, and F. Montaigne, **Phys. Rev. B 73**, 134420 (2006)

2. "Influence of lateral domains and interface domain walls on exchange bias phenomena in TbFe/GdFe bilayers" S. Mangin, T. Hauet, Y. Henry, F. Montaigne, and E. E. Fullerton, **Phys. Rev. B 74**, 024414 (2006)

1. "Training effect in exchange bias system : role of interfacial domain wall" T. Hauet, J.A. Borchers, Ph. Mangin, Y. Henry, and S. Mangin, **Phys. Rev. Lett. 96**, 067207 (2006)

A.VI.2. Actes de conférence et autres publications

10. "High Magnetic Field Generated by Bulk MgB2 Prepared by Spark Plasma Sintering" K. Berger, M. Koblischka, B. Douine, J. Noudem, P. Bernstein, T. Hauet, J. Leveque, **I.E.E.E. Trans. Applied Superconductivity**, 26, 6801005 (2016)

9. "Microstructural and magnetic analysis of a superconducting foam and comparison with IG-processed bulk samples" A Koblischka-Veneva, M.R. Koblischka1, N. Ide, K Inoue, M. Muralidhar, T. Hauet, and M. Murakami, **J. of Physics: Conf. Series** 695, 012002 (2016)

8. "Development of MgB_2-based bulk supermagnets" M. R. Koblischka, A. Wiederhold, M. Muralidhar, K. Inoue, T. Hauet, B. Douine, K. Berger, M. Murakami and U. Hartmann, **I.E.E.E. Trans. Magn.** 50, 0018-9464 (2014)

7. "Micromagnetic analysis of dynamical bubble-like solitons based on the time domain evolution of the topological density", V. Puliafito, S. Komineas, L. Torres, O. Ozatay, T. Hauet, B. Azzerboni, G. Finocchio, **J. Appl. Phys. 115**, 17D139 (2014)

6. "Magnetotransport in MgO-based magnetic tunnel junction grown by MBE", S. Andrieu, F. Bonell, T. Hauet, F. Montaigne, L. Calmels, E. Snoeck, P. Lefevre and F. Bertran, **J. Appl. Phys. 115**, 172610 (2014) **(Invited)**

5. "Spin-Polarized Electron Tunneling in bcc FeCo/MgO/FeCo Magnetic Tunnel Junctions" F. Bonell, T. Hauet, S. Andrieu, F. Bertran, P. Le Fevre, L. Calmels, A. Tejeda, F. Montaigne,B. Warot-Fonrose, B. Belhadji, A. Nicolaou, and A. Taleb-Ibrahimi, **Soleil synchrotron research Highlights** 16 (2012)

4. "Magnetic behavior of Co/Pt and TbCo nanocaps assembly for bit pattern media" A. Sediri, L. Piraux, V. A. Antohe, F. Abreu Araujo, M. Hehn, D. Lacour, S. Mangin, T. Hauet, **Proceedings of the international conference nanomaterials** : applications and properties, 1, 04MFPN11 (2012)

3. "First Neutron Observation of an Interfacial Domain Wall in Perpendicular Magnetic-Media Prototypes" S. Watson, J.A. Borchers, T. Hauet, S. Mangin, F. Montaigne and E.E. Fullerton, **NIST ncnr research Highlights 2007**, 20 (2007)

2. "Field-Dependent Magnetic Domain Walls in Exchange-Biased GdFe/TbFe Bilayers" T. Hauet, S. Mangin, J. Borchers and Ph. Mangin, **NIST ncnr research Highlights 2005**, 30 (2005)

1. "Nanostructured magnetostrictive material induced by heavy ion irradiation" J. Juraszek, J. Teillet, A. Grenier, N. Tiercelin, T. Hauet, S. Mangin, **Proceedings 28th International Conference on the Applications of the Mössbauer Effect**, ICAME (2005)

A.VI.3. Ouvrages scientifiques

3. Chapter "Electric and Magnetic Characterization of Bulk Ag-added MgB2" A. Wiederhold, M. Koblischka, K. Inoue, M. Muralidhar, K. Berger, B. Douine, T. Hauet, M. Murakami, U. Hartmann, **Superconductivity: Applications Today and Tomorrow, Nova Science Publishers**, Editor Muralidhar Miryala (Shibaura Institute of Technology, Toyosu, Koto-ku, Tokyo, Japan).Chapter 12, pp. 269-277 (2015)

2. Chapter "Spin-based data storage", O. Ozatay, T. Hauet, P. Braganca, P.G. Mather, J.-U. Thiele, chapter **"Comprehensive Nanoscience and nanotechnology" Elsevier B.V.** (2010)

1. Chapter "Spin-based data storage", O. Ozatay, T. Hauet, P. Braganca, P.G. Mather, J.-U. Thiele, p236, chapter 7, **"Handbook of nanoscale optics and electronics" Elsevier B.V.** (2009)

A.VI.4. Brevets

1. "System, method and apparatus for strain-assisted magnetic recording for controlling switching field and tightening switching field distribution in bit patterned media" Olav Hellwig, Lidu Huang, Thomas Hauet (**US patent 2010/0259846**) (2010)

2. "System, method and apparatus for multiple anisotropy layered magnetic structures for controlling reversal mechanism and tightening switching field distribution in bit patterned media" Manfred Schabes, Olav Hellwig and Thomas Hauet (**US patent 2010/0247969**) (2010)

3. "Patterned perpendicular magnetic recording medium with data islands having a flux channelling layer below the recording layer" Olav Hellwig, Kentaro Takano and Thomas Hauet (**US patent 2011/0085264**) (2011)

4. "Circuit de vérification d'informations binaires telles qu'une clé de sécurité pour un dispositif électronique" Thomas Hauet, Daniel Lacour, Francois Montaigne, Michel Hehn (**FR3016735A1**) (2014)

5. "Circuit de vérification d'informations binaires telles qu'une clé de sécurité pour un dispositif électronique" Thomas Hauet, Daniel Lacour, Francois Montaigne, Michel Hehn (**WO2015107104A1**) (2015)

A.VI.5. Séminaires invités (18)

Versailles Univ. (2006), Lyon Univ. (2006), Spintec Grenoble (2007), IEF Orsay (2008), Eindhoven univ. (Pays-Bas, 2008), Julich Forschungzentrum (Allemagne,2009), Dresden Rosendorf (Allemagne, 2011), Chemnitz Univ. (Allemagne, 2011), Leuven (Belgique, 2011), Bebek Univ.Istambul (Turquie, 2011), Chemnitz Univ. (Allemagne, 2012), Sumy State Univ. (Ukraine, 2012), Saarrbruck (Allemagne, 2014), ENS Cachan (2014), IBM Yorktown (USA, 2014), New York University (USA,2014), Lyon Univ. (2014), Kaiserlautern (2015)

A.VI.6. Oraux présentés dans des conférences internationales

21. **Invité :** Energy Materials and Nanotechnology (Hong Kong) 2015 : "Reproducible formation and features of single bubble state in array of Co/Ni dots" T. Hauet

20. EMRS (Lille) 2015 : "Mechanism of single bubble formation in patterned dot array under in-plane magnetic field" T. Liu, V. Puliafito, C. Deranlot, F. Montaigne, S. Petit, S. Andrieu, O. Ozatay, G. Finocchio, T. Hauet

19. MSNOWS-UNIGR (Nancy) 2014 : "Demonstration of high spin-polarization in perpendicular anisotropy [Co/Ni] multilayers" T. Hauet, M. Gottwald, A. Neggache, A. Rajanikanth, F. Montaigne, S. Mangin, F. Bertran, P. Le Fèvre, A. Taleb, F. Gimbert, L. Calmels, S . Andrieu

18. Intermag (Dresden, Allemagne) 2014 : "Demonstration of high spin-polarization in perpendicular anisotropy [Co/Ni] multilayers" T. Hauet, M. Gottwald, A. Neggache, A. Rajanikanth, F. Montaigne, S. Mangin, F. Bertran, P. Le Fèvre, A. Taleb, F. Gimbert, L. Calmels, S . Andrieu

17. **Invité :** XLVIII Zakopane School of Physics (Zakopane, Pologne) 2013 : "New Schemes for bit pattern media" T. Hauet

16. Joint MMM-Intermag (Chicago, USA) 2013 : "Testing the half-metallic magnetic behavior of Co1.5Fe1.5Ge(001) by spin-resolved photoemission." A. Neggache, T. Hauet, F. Bertran, F. Porcher, A. Bataille, P. Boulet, P. Lefevre, A. Taleb, S. Maat, J.R. Childress and S. Andrieu

15. Joint MMM-Intermag (Chicago, USA) 2013 : "Strong electric field effect on Fe/V(001) epitaxial film with perpendicular anisotropy." A.R. Rajanikanth, T. Hauet, G. Lengaigne, F. Montaigne, S. Mangin and S. Andrieu

14. **Invité** : Nanomaterials : Applications and Properties (Crimea, Ukraine) 2012,"Magnetic behavior of Co/Pt and TbCo nanocaps assembly for bit pattern media" A. Sediri, L. Piraux, V. A. Antohe, F. Abreu Araujo, M. Hehn, D. Lacour, S. Mangin, T. Hauet

13. Intermag (Vancouver, Canada) 2012 "Contribution of Spin *and* Symmetry Resolved Photoemission on Transport in Magnetic Tunnel Junctions" F. bonell, T. Hauet, F. Bertran, L. Calmels, P. Le Fevre, F. Montaigne, G. Langaine, A. Taleb, S. Andrieu

12. ITFPC-MIATEC (Nancy, France) 2011, "Spin and symmetry resolved photoemission applied on magnetic tunnel junctions" *F*. Bonell, T. Hauet, F. Bertran, P. Le Fèvre, A. Taleb, S. Andrieu

11. **Invité** : MML conference (Berkeley, US) 2010, "Reducing switching field and switching field distribution in magnetic memories", T. Hauet

10. Intermag-MMM conference (Washington DC, US) 2010, "Role of reversal incoherency in reducing switching field and switching field distribution of exchange coupled composite bit pattern media", T. Hauet. Dobisz, S. Florez, J. Park, B. Lengsfield, B.D. Terris and O. Hellwig

9. Innovations in Thin Film Processing and Characterisation (Nancy, France) 2009, "Reducing switching field and switching field distribution of bit pattern media" T. Hauet, E. Dobisz, S. Florez, T. Thomson, J. Park, B. Lengsfield, J. D. Risner-Jamtgaard, D. Yaney, E.E. Fullerton, B.D. Terris and O. Hellwig

8. **Invité.** APS March meeting (Pittsburgh, US) 2009, "Measuring interfacial magnetic configurations with Polarized Neutron Reflectometry" T. Hauet

7. **Invité.** JEMS conference (Dublin, Ireland) 2008, "Micromagnetic mechanism of Exchange Bias and EB training effect in an anti-ferromagnetically coupled hard/soft bilayer" T. Hauet

6. Intermag conference (Madrid, Spain) 2008, "Field driven ferromagnetic phase evolution in AF-coupled perpendicular anisotropy films" T. Hauet, C. Günther, O. Hovorka, A. Berger, M.-Y. Im, P. Fischer, T. Eimüller and O. Hellwig

5. 52 th MMM conference (Tampa FL, USA) 2007, "Direct observation of field and temperature induced domain replication in dipolar coupled perpendicular anisotropy films", T. Hauet, C. Günther, B. Pfau, S. Eisebitt, M-Y Im, P. Fischer, K. Chen , R.L. Rick, W. F. Schlotter, J. Stöhr, J.-U. Thiele, B. Terris and O. Hellwig

4. 10th Joint MMM/ Intermag conference (Baltimore MD, USA) 2007, "Role of interface domain wall on magnetoresistance in bilayers and spin-valve structures", T. Hauet, S. Mangin, M. Hehn, F. Montaigne, Y. Henry and E.E. Fullerton

3. 10th Joint MMM/ Intermag conference (Baltimore MD, USA) 2007, "Influence of the cooling field and temperature on exchange bias effects in GdFe/TbFe bilayer", T. Hauet, S. Mangin, J.A. Borchers, F. Montaigne and E.E. Fullerton (Finalist for Best Student award)

2. Workshop Interreg III C "Material sciences" (Luxembourg, Luxembourg) 2006, "Training effect in exchange coupled GdFe/TbFe", T. Hauet, J. Borchers, S. Mangin, Y. Henry, F. Montaigne

1. 50th Magnetism and Magnetic Materials conference MMM (San Jose CA, USA) 2005, "Training effect in exchange coupled GdFe/TbFe: role of Interface domain wall evidence by Polarized neutron reflectometry ", T. Hauet, J. Borchers, Ph. Mangin, Y. Henry, S. Mangin

+ > 18 oraux invités et > 50 oraux présentés par un co-auteur

+ International conference session Chair : MMM Tampa 2007, JEMS Dublin 2008, Intermag-MMM Washington DC 2010, Intermag Vancouver 2012, MMM-Intermag Chicago 2013, Zakopane 2013, Intermag Dresden 2014, JEMS2016

A.VI.7. Oraux dans des conférences nationales françaises

1. Colloque Louis Neel (La Grande Motte, France) 2008, "Field and temperature induced domain replication in dipolar coupled perpendicular anisotropy films" T. Hauet, C. Günther, B. Pfau, P. Fischer, R.L. Rick, O. Hovorka, A. Berger, J.-U. Thiele, S. Eisebitt and O. Hellwig

A.VI.8. Présentations de posters dans des conférences nationales et internationales

8. Intermag (Dresden, Allemagne) 2014 : "Domain wall motion induced by spin transfer torque in MBE-grown Co/Ni based multilayer" S. Le Gall, T. Hauet, F. Montaigne, M. Gottwald, D. Lacour, M. Hehn, J. Mc Cord, N. Vernier, D. Ravelosona, S. Mangin, S. Andrieu

7. Joint MMM-Intermag (Chicago, USA) 2013 : Strong spin polarization of Co/Ni(111) epitaxial layers with perpendicular anisotropy. T. Hauet, A. Neggache, A.R. Rajanikanth, F. Montaigne, F. Bertran, P. Lefevre, A. Taleb, S. Mangin and S. Andrieu

6. Colloque Louis Néel (Brest, France) 2011, « Contribution of Spin *and* Symmetry Resolved Photoemission on Transport in Magnetic Tunnel Junctions" F. bonell, T. Hauet, F. Bertran, L. Calmels, P. Le Fevre, F. Montaigne, G. Langaine, A. Taleb, S. Andrieu

5. Colloque Louis Néel (Dourdan, France) 2005, "Influence of lateral domains and interfacial domain wall formation on exchange bias phenomena in TbFe/GdFe », T. Hauet, S. Mangin, Y. Henry, F. Montaigne and E. Fullerton (prix poster)

4. Colloque Louis Néel (Autran, France) 2004, "Magnetoresistances study in a domain wall model system" T. Hauet , S. Mangin, Y. Henry, F. Montaigne

3. Colloque JMC9 (Nancy, France) 2004, "Magnetoresistances study in a domain wall model system" T. Hauet, S. Mangin, Y. Henry, F. Montaigne

2. Colloque JMC9 (Nancy, France) 2004, "exchange-bias négatif et positif dans des bicouches ferrimagnétique/ferrimagnétique", S. Mangin, Y. Henry, F. Montaigne, T. Hauet

1. Colloque IWEBMN'04 (Anglet, France) 2004, "Exchange-bias négatif et positif dans des bicouches ferrimagnétique/ferrimagnétique", S. Mangin, Y. Henry, F. Montaigne, T. Hauet

Annexe B

Résumé du document en langue Francaise

Mon travail de recherche s'insère dans le domaine du nanomagnétisme et de l'électronique de spin. Deux axes principaux rassemblent les diverses études que j'ai menées ces dernières années. Le premier traite de l'influence sur le magnétisme d'interfaces entre films minces de nature chimique différente (anisotropie d'interface, augmentation ou diminution locale d'aimantation, etc.), l'influence des couplages magnétiques (couplage d'échange ou couplage dipolaire), ainsi que les compétitions pouvant exister entre eux. L'utilisation de diverses techniques complémentaires de laboratoire (mesures d'aimantation, de susceptibilité, de magnétorésistance, d'imagerie MFM) ou de grands instruments (réflectométrie de neutrons polarisés, techniques de microscopie et spectroscopie basées sur le dichroïsme magnétique des rayons X) et de calculs micromagnétiques, a permis d'étudier l'évolution des configurations magnétiques de systèmes multicouches complexes ou d'assemblés de nano-objets en fonction de paramètres extrinsèques tels qu'un champ magnétique externe ou la température. Durant ces travaux, je me suis également formé aux méthodes de croissance par évaporation par jet moléculaire et pulvérisation cathodique et de maitriser la croissance de films (alliages ou multicouches) ferri- ou ferromagnétiques à anisotropie planaire ou perpendiculaire au plan des couches. La compréhension des configurations magnétiques de ces systèmes a souvent nécessité de corrélé les propriétés de structure cristallographiques et les mesures magnétiques. De nombreuses études de développement de matériaux innovants ou optimisés ont donc été réalisées. Durant un séjour de trois ans dans la Silicon Valley (Californie, USA), j'ai pu acquérir une vision nouvelle du travail de recherche et développement au sein du groupe Hitachi GST (une des 3 compagnies majeures produisant des disques durs dans le monde). Dès lors mes études, même les plus fondamentales, sur le contrôle de l'aimantation à l'échelle micrométrique et nanométrique se sont toujours inscrites dans la recherche plus appliquée de nouvelles méthodes d'enregistrement magnétique (disques durs et tout solide). La seconde thématique à laquelle je me suis intéressé concerne les propriétés de transport dépendant du spin, i.e. les interactions entre le spin des électrons de conduction et l'aimantation) dans différentes multicouches magnétiques telles que des jonctions tunnel magnétiques, des vannes de spins ou des jonctions à paroi de domaines. Ces systèmes électroniques permettent soit de lire une information (capteurs, tête de lecture, mémoire tout solide, clé magnétique), soit d'enregistrer une information par un contrôle de l'aimantation (mémoire magnétique à accès aléatoire pressentis pour remplacer les mémoires flash et DRAM). Je me suis ainsi familiarisé avec les techniques de mesures de magnéto-transport électriques DC et AC dont j'ai pu coupler les résultats soit avec des mesures de photo-émission résolu en spin soit avec des techniques de microscopies magnétiques. Une de mes principales activités à Nancy a consisté en la croissance et la caractérisation de jonctions tunnel magnétiques épitaxiées dans lesquelles la barrière tunnel dont on cherche à optimiser électrodes magnétiques afin d'obtenir la plus grande polarisation en spin, un amortissement faible et une anisotropie perpendiculaire. En parallèle, je me suis intéressé au renversement d'aimantation ou au déplacement de paroi magnétique par courant polarisé dans des systèmes multicouches à aimantation perpendiculaire. Dans ce dernier cas, ce sont les électrons polarisés qui affectent l'aimantation de couches traversées. L'ensemble de ces études cité ci-avant m'a permis de développer des collaborations nationales et internationales. Enfin, ma fonction de responsable du centre commun MAGNETISME de l'Institut Jean Lamour (depuis 2011) m'amène à m'ouvrir à de nouvelles thématiques et à de nouvelles collaborations au sein de l'Université de Lorraine et en dehors.

B.1. Anisotropie, moment et polarisation induits à l'interface Co/Ni et Co/Pd

Pour des raisons de stabilité thermique et de géométrie d'écriture/lecture, des films minces ou nano-objets ayant une anisotropie magnétique perpendiculaire au media sont recherché pour les nouveaux systèmes d'enregistrement magnétique (disques durs ou tout solide). Une partie de mon activité a consisté à étudier dans le détail l'anisotropie magnétique perpendiculaire induite par les hybridations électroniques aux interfaces Co/Ni et Co/Pd principalement. Dans ces multicouches, chaque couche de Co ou de Ni a une épaisseur typique de 1 à 10 plans atomiques, i.e. 0.2nm à 2nm. L'influence des contraintes et de l'anisotropie magnétocristalline a aussi été quantifiée. Des mesures XMCD nous ont permis de mesurer l'anisotropie de moment orbital et de moment de spin, que nous avons pu comparer aux calculs théoriques. Par ailleurs les mesures XMCD et de photo-emission résolue en spin ont aussi révélées une forte augmentation du moment de spin du Co et de la polarisation en spin au niveau de Fermi à l'interface Co/Ni (Fig. B1).

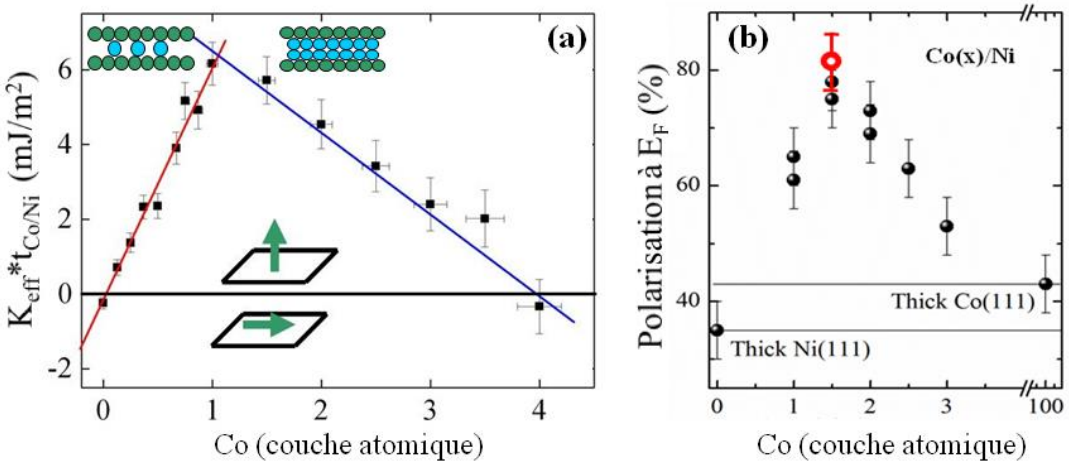

Fig.B1. (a) Produit de la densité volumique d'energie d'anisotropie (K_{eff}) fois l'épaisseur de l'échantillon multicouche [Co/Ni] ($t_{Co/Ni}$), et (b) polarisation en spin au niveau de Fermi, en fonction du nombre de plans d'atomes de Co dans une multicouche saphir/V/Au/[Ni(0.6nm)/Co(x)]$_n$ déposée par épitaxie par jet moléculaire.

J'ai par la suite utilisé les systèmes multicouches Co/Pd et Co/Ni ainsi que CoNi/Pd comme des systèmes modèle (on peut en effet optimiser leur anisotropie, leur aimantation ou encore leur température de Curie en changeant le poids relatif de chaque élément) pour divers études fondamentales (étude du transfert de spin et des couplages dipolaires) et appliquées (développement de mémoire « Bit pattern media » ou mémoire 3D)

Publication représentative : "Co/Ni(111) superlattices studied by microscopy, X-ray absorption and *ab-initio* calculations" M. Gottwald, S. Andrieu, F. Gimbert, E. Shipton, L. Calmels, C. Magen, E. Snoeck, M. Liberati, T. Hauet, E. Arenholz, S. Mangin, E. Fullerton, Phys. Rev. B 86, 014425 (2012)

B.2. Mémoire 3D : duplication de domaines dans des multicouches à anisotropie perpendiculaire

Les mémoires tout solide sont généralement formées d'un réseau 2D aux nœuds duquel reside un élément magnétique qui permet d'enregistrer l'information. Une des manières d'augmenter la densité d'information pouvant être enregistrée dans ces systèmes mémoires consiste à utiliser la troisième dimension de l'espace. Depuis 2008, j'ai travaillé à démontrer la faisabilité d'un réseau 3D dit « page memory » dans lequel les informations se déplacent dans la troisième dimension par duplication grâce au couplage dipolaire entre des nanostructures à anisotropie perpendiculaire, en particulier lors de cycles en température permettant de faciliter l'écriture. A travers cette étude appliquée, je me suis familiarisé avec la croissance par pulvérisation cathodique de multicouches ou d'alliages ferromagnétiques et ferrimagnétiques à base de métaux de transition (Co, Ni) et des métaux 5d (Pd, Pt).

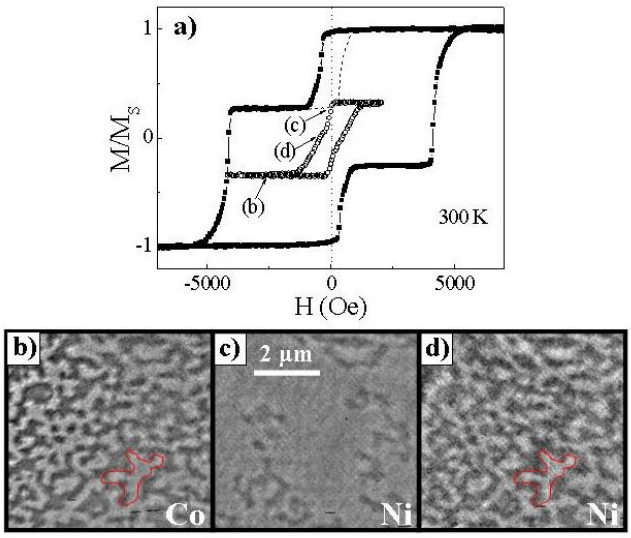

Fig.B2. a) Courbes d'hystérésis de $[CoNi/Pd]_{30}$/Pd/$[Co/Pd]_{20}$ mesurées a 300 K. Les ronds vides et pointillets correspondent respectivement au cycle de renversement de la couche douce $[CoNi/Pd]_{30}$ en présence ou non de domaines dans la couche dure. Les images de microscopie en transmission (c-d) représentent les domaines apparaissant dans la couche durs lorsque la couche dure contient les domaines représentés en (b).

Lors d'une première étude, les interactions dipolaires dans une multicouche doux/Pd/dur, $[CoNi/Pd]_{30}$/Pd/$[Co/Pd]_{20}$, ou une épaisse couche de Pd évite tout couplage d'échange direct entre les couches magnétiques, ont été révélées en combinant des mesures de magnétométrie et des techniques d'imagerie magnétique à haute résolution utilisant l'effet XMCD comme mécanisme de contraste (MTXM, holographie magnétique). Nous avons montré que les domaines se développant au sein de la couche magnétique douce lors de cycle de champ magnétique étaient identiques aux domaines artificiellement introduits au préalable dans la couche dure (Fig.B2). De plus, le choix de la composition de la couche douce telle que cette dernière possède une température de Curie très inferieure à celle de la couche dure, nous a permis de faire varier les paramètres intrinsèques de la couche douce et ainsi d'étudier leur compétition avec l'effet des interactions dipolaires. Des simulations micro-magnétiques basées sur l'équation Landau-Lifshitz-Gilbert et comparées aux résultats expérimentaux ont permis d'élucider le rôle de l'aimantation, l'anisotropie et l'échange de la couche douce dans le processus de duplication de domaines toutefois des effets d'activation thermique doivent être considérés afin de reproduire quantitativement nos expériences. En se

servant de la dépendance thermique du système $[CoNi/Pd]_{30}/Pd/[Co/Pd]_{20}$, nous avons démontré expérimentalement le concept de duplication de domaines activée thermiquement sous champ nul durant des cycles en température, nécessaire à l'implémentation de « page memory ». J'ai enfin travaillé sur un démonstrateur 3D connecté électriquement du système de « page memory ».

Des études complémentaires ont été réalisées pour tester l'influence des tailles de domaines intrinsèques dans les couches couplées par champ dipolaire. Nous avons démontré que la duplication de domaine n'est possible que pour des tailles intrinsèques similaires dans les couches dure et douce. Enfin d'autres travaux ont été menées dans lesquelles nous avons ajouté un nouveau degré de compétition en induisant un couplage antiferromagnetique à l'interface des deux couches magnétiques soit en remplaçant la couche épaisse de Pd par une couche de Ru permettant d'induire un couplage antiferromagnétique entre les couches magnétiques (dans des multicouches $[Co/Pd]_x$ /Ru/$[Co/Pd]_y$), soit par un couplage direct (dans des multicouches TbFeCo/$[Co/Pd]_x$). Il y a alors compétition entre les interactions dipolaires, assimilable localement à un couplage ferromagnétique, et le couplage antiferromagnétique. Ce conflit énergétique génère l'apparition de nouvelles phases magnétiques que j'ai étudiées par des techniques de magnétométrie et d'imageries magnétiques. En ce qui concerne plus directement « page memory », nous avons montré qu'un système [Co/Pd][CoNi/Pd]/Ru/[Co/Pd] d'aimantation rémanent nulle à température ambiante apporte l'avantage significatif de ne pas engendré de champ remanent sur les autres bits d'information tout en permettant une écriture de l'information grâce à une suppression du couplage anti-ferromagnétique lors de pulse de température.

Publication représentative: "Direct observation of field and temperature induced domain replication in dipolar coupled perpendicular anisotropy films" T. Hauet, C. Günther, B. Pfau, M. Schabes, J.-U. Thiele, R.L. Rick, P. Fischer, S. Eisebitt and O. Hellwig, Phys. Rev. B 77, 184421 (2008)

B.3. Média discret pour disques durs : étude des mécanismes de renversement d'aimantation dans des assemblées de nanostructures magnétiques

Le besoin permanent d'augmenter la densité d'information dans les disques durs a poussé le concept de media granulaire jusqu'à des tailles de grains d'environ 6nm, proche des limites de stabilité thermique de rétention d'information, de bruit de lecture et d'écriture. Dans ces anciens média granulaire un bit d'information consiste en une soixantaine de grains. Le nouveau concept de média nanostructuré répond à l'ensemble des problèmes des media granulaires en utilisant un réseau bien organisé de plots magnétiques d'environ 10 à 25 nm de large et espacés de quelques nanomètres (Fig.B3). Les plots ont un volume plus important que les grains ce qui assure une meilleur stabilité thermique. De plus, chaque plot contient un bit d'information d'où l'augmentation de la densité d'information stockable. Malgré tout, ce nouveau type de media nécessite une grande reproductibilité du comportement magnétique d'un plot à un autre. Dans les média nanostructurés à base de Co/Pd, j'ai pu démontrer que la première cause de distribution de champ de renversement est liée à la présence de zones cristallisées dans une direction (200), au lieu de (111). Ce type de défaut est difficile à supprimer, notamment du fait de la méthode de croissance (pulvérisation cathodique). Toutefois j'ai montré que l'addition d'une couche partiellement couplée de Co/Ni permet de fortement diminuer l'effet de ces défauts cristallins et de manière plus générale de tous types de défauts présents dans la couche de Co/Pt (Fig. B3). Ceci est du au renversement partielle

de la couche douce de Co/Ni qui aide au renversement de la couche dure de Co/Pt (Fig. B3). Ce mode de renversement favorise de plus la diminution du champ de renversement moyen, ce qui permet d'augmenter l'anisotropie de la couche dure donc sa stabilité thermique (Fig. B3). Ce nouveau type de media a permis d'aboutir à un processus d'écriture/lecture utilisant un média nanostructuré d'une densité (record pour 2009) de 320 Gb/in^2. La nouvelle limite à la réduction de la distribution de champ de renversement provient désormais du couplage dipolaire longue distance inhérent à une assemblée de plots aimantés. Cette distribution peut être minimisée en couplant légèrement les plots par échange direct mais cette méthode engendrera du bruit lors de la lecture de l'information.

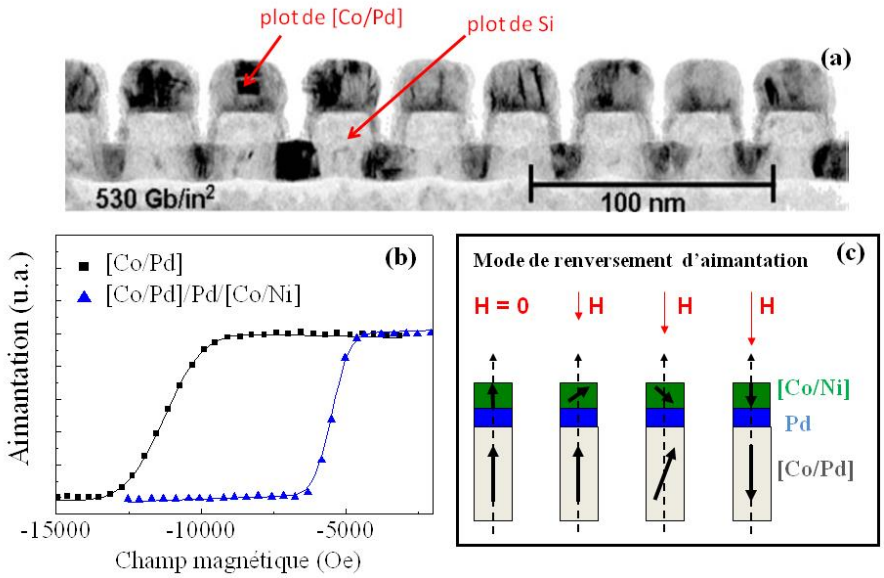

Fig. B3. Image de microscopie électronique en transmission en champ clair d'une assemblée de plots de [Co/Pd] déposés sur des substrats pré-gravés de Silicium, de période 35 nm (soit une densité de donnée magnétique de 530 Gb/ in^2). (b) Aimantation normalisée d'une assemblée de plot de [Co/Pd] (en noir) et [Co/Ni]/Pd/[Co/Pd] (en bleu) en fonction du champ magnétique extérieur. (c) Schéma du mode de renversement d'aimantation dans [Co/Ni]/Pd/[Co/Pd], à l'origine de la forte réduction du champ de renversement moyen et de la distribution de champ de renversement.

En parallèle, j'ai également travaillé à la réalisation de nouvelles méthodes de fabrication de substrats pré-gravés basées sur des systèmes nanométriques auto-assemblés (co-polymères et plus récemment à Nancy sur les membranes d'alumine anodisées) et j'ai effectué un travail de croissance de matériaux cristallins ou fortement texturés tels que des multicouches épitaxiées Co/Ni, des alliages Co_3Pt ou CoPt. Ces systèmes cristallins ont l'avantage d'une forte anisotropie (perpendiculaire au plan du film) nécessaire à la stabilité thermique de l'aimantation au sein de nano-plots de diamètre sub-20nm et, dans le cas d'une organisation cristalline parfaite, ne devraient pas présenter de distribution de champ de renversement. J'ai également testé les qualités d'un matériau amorphe à anisotropie perpendiculaire (TbCo) qui n'ayant pas d'ordre sur des distances de plus de 1nm, devraient également donner lieu à une faible distribution de champ de renversement. Cependant la qualité cristalline des matériaux épitaxiés déposés sur substrats pré-gravés de Si n'est pas suffisante, la gravure des couches parfaitement cristallisées pour faire des plots induit des défauts magnétiques importants, les alliages amorphes présentent des dispersions en concentration. Par conséquent, ces matériaux n'ont jamais montré d'aussi bonnes performances que les multicouches Co/Pd obtenues par pulvérisation cathodique.

Publications representatives :

"Role of reversal incoherency in reducing switching field and switching field distribution of exchange coupled composite bit pattern media" T. Hauet, E. Dobisz, S. Florez, J. Park, B. Lengsfield, B.D. Terris and O. Hellwig, Appl. Phys. Lett. 95, 262504 (2009)

"System, method and apparatus for multiple anisotropy layered magnetic structures for controlling reversal mechanism and tightening switching field distribution in bit patterned media" M. Schabes, O. Hellwig and T. Hauet (US patent 2010/0247969) (2010)

B.4. Jonctions tunnel magnétiques épitaxiées à barrière MgO

Nancy a une longue expérience dans la croissance par épitaxie par jet moléculaire sous ultra-vide de tricouche ferromagnetique/isolant/ferromagnétique épitaxié. Un tel système s'appelle une jonction tunnel car les électrons passent par effet tunnel à travers la couche isolante. Dans un tel système, la résistance dépend de l'orientation relative entre les aimantations des deux couches ferromagnétiques. Elle est minimum dans le cas parallèle et maximum dans le cas anti-parallèle. On appelle magnétoresistance TMR, la différence normalisée entre ces deux états. Parmi les systèmes épitaxiés, ceux à barrière de MgO sont intéressants d'une part car ils sont un système modèle riche pour tester les prédictions théoriques de transport tunnel dépendant du spin et d'autre part car ils sont fortement pressentis pour devenir la brique de base des mémoires magnétiques tout solide type MRAM.

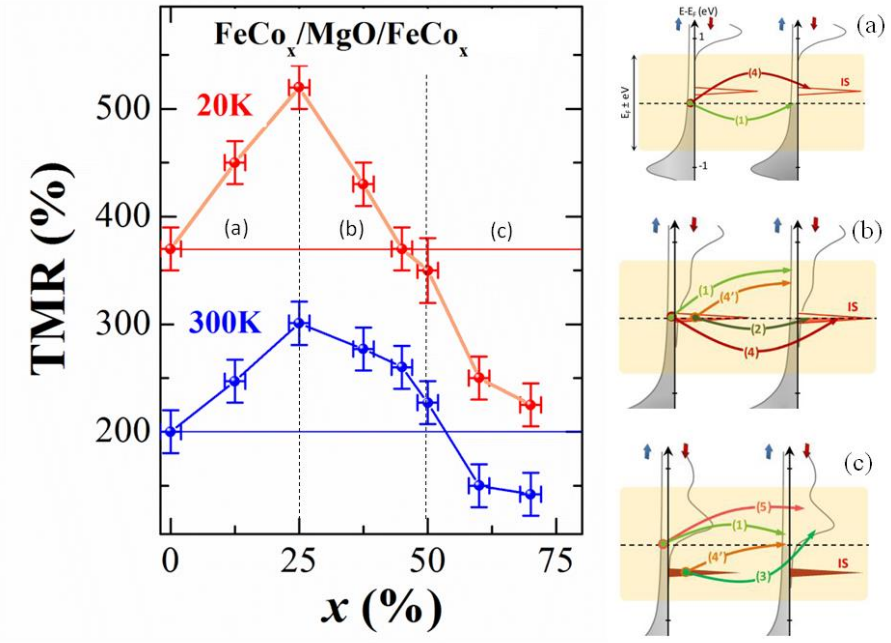

Fig. B4. A gauche, TMR mesurée à 20 K et 300 K sur une série d'échantillons jonction tunnel $Fe_{1-x}Co_x/MgO/Fe_{1-x}Co_x$ épitaxiée. A droite, schéma des canaux de conduction tunnel entre les états électroniques des deux électrodes ferromagnétiques pour des concentrations en Co inférieures à 25 % (a), comprises entre 25 et 50% (b), supérieures à 50% (c). L'état vide d'interface IS commence a participer à la conduction électrique lorsque la concentration en Co est supérieure à 25%.

Le système FeCoB/MgO/FeCoB est particulièrement investigué en raison de l'énorme TMR prédite par les calculs ab-initio pour l'alliage FeCo équimolaire et Co pur (jusqu'à 6000%). Cependant, les valeurs expérimentales ne dépassent pas 600% et le maximum de TMR est obtenu pour l'alliage $Fe_{75}Co_{25}$ à l'encontre des prédictions. En combinant des

expériences de photoémission résolue en spin et en symétrie (synchrotron SOLEIL) et les mesures de transport DC standard (magnétoresistance, conductivité en fonction de la différence de potentiel), le rôle dans la conduction tunnel du remplissage d'un état électronique d'interface (présent à l'interface FeCo/MgO) lorsque la concentration en Co augmente (i.e. lorsque le nombre total d'électrons de l'alliage augmente) a pu être mis en évidence et la décroissance de TMR après 25% de Co a ainsi pu être expliquée (Fig. B4). Le même système modèle $Fe_{1-x}Co_x/MgO/Fe_{1-x}Co_x$ m'a également servi à étudier l'anisotropie magnétique d'interface Fe/MgO, qui, de manière similaire à Co/Ni ou Co/Pd, favorise la direction de l'aimantation perpendiculaire au plan des couches. A l'aide de mesures de magnétométrie et résonance ferromagnétique (réalisée à CMRR San Diego), une valeur d'anisotropie d'interface de 1 ± 0.1 erg/cm^2 (mJ/m^2) a été obtenue, deux fois plus forte que celle obtenue pour l'interface Co/Ni par exemple. L'anisotropie d'interface Fe/MgO ici provient de l'hybridation entre les atomes de Fer et d'Oxygène et peut être modifiée à l'aide d'un champ électrique appliqué dans la barrière de MgO. Si nous travaillons toujours à comprendre la nature de l'effet du champ électrique, le système modèle épitaxié Fe/MgO/Fe nous a permis de montrer un effet géant de variation réversible d'anisotropie par effet de champ électrique dans une jonction tunnel. Ce phénomène nouveau (1ère observation en 2009 par un groupe Japonais) ouvre la voie à des gains significatifs en termes de consommation énergétique dans les mémoires MRAM en facilitant le processus d'écriture.

Publication représentative : "Spin-Polarized Electron Tunneling in bcc FeCo/MgO/FeCo Magnetic Tunnel Junctions" F. Bonell, T. Hauet, S. Andrieu, F. Bertran, P. Le Fevre, L. Calmels, A. Tejeda, F. Montaigne, B. Warot-Fonrose, B. Belhadji, A. Nicolaou, and A. Taleb-Ibrahimi, Phys. Rev. Lett. 108, 176602 (2012)

B.5. Effet de transfert de spin dans des multicouches à aimantation perpendiculaire

Si l'effet de champ électrique sera certainement une aide dans les prochaines générations de cellules mémoire MRAM, l'effet majoritaire qui permettra le contrôle de l'aimantation sera certainement l'effet de transfert de spin, i.e. le renversement d'aimantation par interaction avec un courant polarisé en spin. En 2006, il a été démontré que les systèmes à anisotropie perpendiculaire permettent de minimiser le courant critique, i.e. le courant nécessaire au renversement. Je me suis intéressé à deux systèmes : nanopiliers vanne de spin et fils microniques tous les deux à base de multicouche Co/Ni à anisotropie perpendiculaire.

Grâce à des mesures de résistance DC et AC couplées à des mesures de microscopie en transmission des rayons X (STXM à ALS Berkeley), réalisées sur des piliers de tailles latérales nanométriques (e.g. 50 à 100 nm de diamètres pour des piliers circulaires et 100*300 nm^2 pour les piliers ellipsoïdaux), j'ai en particulier étudié le mécanisme de retournement d'aimantation d'une couche magnétique douce de Co/Ni, au sein de vannes de spin type dur/Cu/doux [Co/Pd][Co/Ni]/Cu/[Co/Ni], sous l'effet d'un courant polarisé. J'ai mis en évidence un mécanisme de renversement sub-nanoseconde et non-uniforme spatialement dans le cas des piliers 100*300 nm^2. Ici le courant circule perpendiculairement au plan des couches (Fig. B5). Après précession de l'aimantation, une nucléation d'un domaine d'aimantation renversé est induite par le passage du courant polarisé. Celle-ci se fait au centre du pilier à cause du champ démagnétisant interne de la couche de Co/Ni (le champ dipolaire provenant de la couche dure favorise lui une nucléation au bord du pilier). Ensuite le domaine renversé

grossit et couvre la totalité du volume du pilier en moins d'une nanoseconde. La densité de courant nécessaire au renversement est de l'ordre de 10^7 A/cm^2 avec des pulses de 100 picoseconde. Ces images sont les premières images obtenues du renversement par courant de spin dans des empilements à aimantation perpendiculaire.

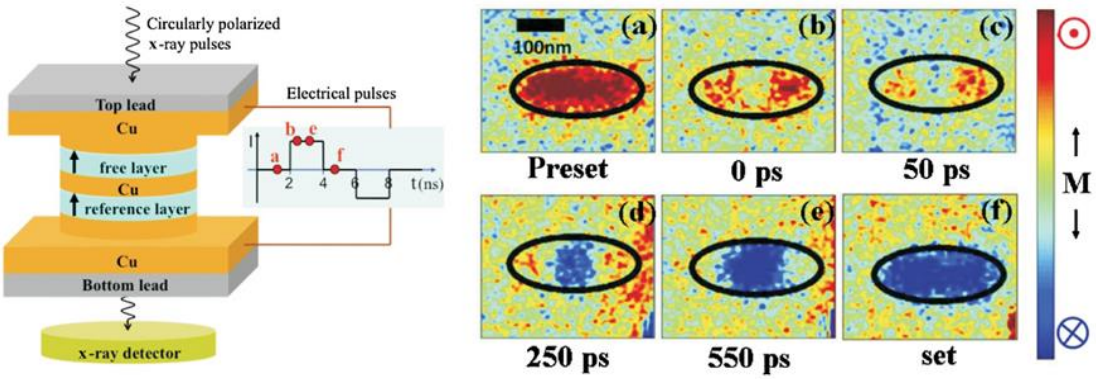

Fig. B5. A gauche, schéma de l'expérience de STXM effectuée sur un nanopilier dur/Cu/doux, [Co/Pd][Co/Ni]/Cu/ [Co/Ni]. La séquence d'impulsion de courant en fonction du temps est représentée. Les points rouges annotés informent sur les temps auxquels les images STXM (a) - (e) ont été enregistrées. Image (a) est l'état initial, et (f) est l'état final. L'échelle de couleur correspond à la composante perpendiculaire de l'aimantation de couche [Co/Ni], de parallèle (P) (rouge) à antiparallèle (AP) (bleu) par rapport à l'aimantation de la couche de référence [Co/Ni][Co/Pd].

En parallèle, je me suis intéressé à deux systèmes à base de Co/Ni. Le premier, des jonctions tunnel magnétiques, a fait en partie l'objet d'une thèse que j'ai co-encadré en collaboration avec Vitaliy Bibyk de l'université de Sumy en Ukraine. Durant ce travail nous avons réalisé les premières jonctions tunnel magnétiques avec des électrodes de Co/Ni à anisotropie perpendiculaire. Le second système, fils nano- et micrométriques, m'ont permis d'étudier le déplacement de paroi magnétique par transfert de spins. Sous l'effet d'un champ magnétique, l'aimantation d'une zone d'un film mince ou d'une nanostructure peut être amenée à se renverser comme dans le cas de la Fig. X. Est alors créée une zone d'aimantation opposée au reste de l'échantillon et entre les deux existe une paroi de domaine magnétique, i.e. une rotation monotone de l'aimantation similaire à la fig. X. Le déplacement de cette paroi peut se faire alors par application d'un champ magnétique d'amplitude supérieure ou par un courant d'électrons polarisés en spin. L'étude des vitesses de propagation de la paroi en fonction du champ magnétique extérieur par microscopies Kerr ont révélé que dans le film [Co/Ni] épitaxié les parois peuvent être piégées ou freinés par un type de défaut unique (certainement aux frontières entre des variants cristallins liés aux couches inférieures de V/Au qui sont utilisées pour obtenir une croissance cristalline de [Co/Ni]) répartis de façon homogène à l'échelle du micron. Ensuite, l'étude de la propagation de paroi dans des fils microniques permettant l'application de densités de courant d'électrons polarisés suffisantes pour l'influencer, a permis de mettre en évidence le rôle du courant comme un champ effectif supplémentaire poussant la paroi (transfert de spin non-adiabatique) ajouté à un effet de chauffage (effet Joule). Nous avons finalement obtenu une cartographie champ magnétique/ courant électrique donnant les zones où le transfert de spin, le champ d'Oersted, la température, le champ magnétique extérieur sont dominants respectivement.

Publication représentative : "Non- uniform switching of the perpendicular magnetization in a spin-torque-driven magnetic nanopillar" D.P. Bernstein, B. Brauer, R. Kukreja, J. Stohr, T. Hauet, J. Cucchiara, S Mangin, J.A. Katine, T. Tyliszczak, K.W. Chou, Y. Acremann, Phys. Rev. B (R) 83, 180410 (2011)

B.6. Travaux en cours

B.6.1. Bulles magnétiques

La possibilité de créer des objets de taille micro- et nanométrique (fils, plots, piliers contactés électriquement, nanoparticules 3D, etc.) a permis de mettre en lumière de nouvelles configurations de l'aimantation dont les propriétés sont originales (vitesse de déplacement, fréquence de précession, stabilité thermique, etc.) et qui ne peuvent s'observer que dans le cas ou la taille du système est finie dans la plage du micro- et nanomètre. Le vortex magnétique (Fig. B6), souvent généré dans les plots à base de matériaux à anisotropie magnétique planaire, est un exemple typique. Ces propriétés de stabilité et de réponse à une large variété excitations ont été étudiées de façon intensive ces vingt dernières années tant pour un objectif fondamental que pour leur possible utilisation dans des appareils haute fréquence. Récemment, le pendant du vortex pour des matériaux à anisotropie perpendiculaire est appelé bulle magnétique (Fig. B6). Cette bulle est formée d'une zone d'aimantation vers le bas entourée par une zone d'aimantation opposée. En fonction de la configuration magnétique de la paroi entre ces deux zones, les propriétés de stabilité et de réponse vont être différentes.

J'ai commencé depuis deux ans une collaboration avec O. Ozatay (Istambul, Turquie) et G. Finnochio (Messine, Italie) concernant l'étude de ce nouvel objet magnétique. Tout d'abord des simulations micromagnétiques ont été réalisées, principalement à Messine, afin de choisir les matériaux et les designs nécessaires à l'obtention de bulles stable. Les résultats théoriques nous orientent aussi sur les comportements sous champ magnétique et sous courant polarisé en spin. Nous avons choisis les multicouches Co/Ni, que j'ai étudié en détails, pour faire des plots à aimantation perpendiculaire de diamètre de 300nm à 2 micron. Nous avons ensuite démontré qu'un processus de désaimantation sous champ magnétique permet de générer de façon reproductible un grand nombre de bulles (Fig. B6). Le mécanisme de création de la bulle ainsi que les domaines de stabilité ont été compris et quantifiés en comparant calculs et résultats expérimentaux.

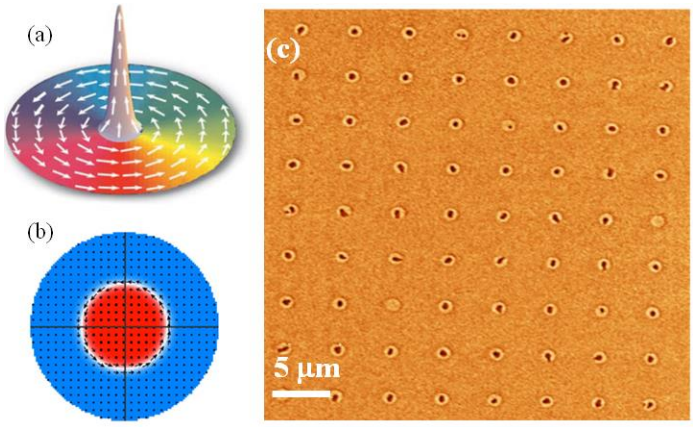

Fig. B6 : Représentation de la configuration magnétique au sein d'un vortex magnétique (a) et d'une bulle magnétique (b). (c) Image de microscopie à force magnétique, réalisée à Nancy, d'une assemblées de plots d'environ 1 micron de large au milieu desquels ont été nucléées des bulles magnétiques. Le procédé de désaimantation utilisé ici a mené à la création d'une bulle dans 80% des plots. Ce niveau de reproductibilité est important afin de mener à bien les futures études des réponses aux excitations de champ magnétique et de courant polarisé en spin.

La prochaine étape est de caractériser les modes de vibrations de ces bulles dans des assemblées de plots (par FMR) ou sur un plot unique à l'aide de mesure électrique. En parallèle, des études de microscopie seront menées pour comprendre l'enroulement des moments dans la paroi de la bulle. Des tests de déplacement d ebulles dans des fils micrométriques seront réalisés. Des grandes vitesses de déplacement ont été prédits dans la littérature. Enfin, nous voulons finalement démontrer la faisabilité d'un nano-oscillateur basé sur le contrôle de bulles magnétiques. Des études similaires vont être réalisées sur des nano-fils afin d'observer le déplacement des bulles magnétiques le long du fil sous impulsion de courant. Ibrahim Cinar en thèse à Bogazici University (Istambul) passera un an à Nancy à partir de sept. 2016 pour réaliser ces expériences.

Publication représentative : "Mechanism of single bubble formation in patterned dot array under in-plane magnetic field" T. Liu, V. Puliafito, F. Montaigne, S. Petit, C. Deranlot, S. Andrieu, O. Ozatay, G. Finocchio and T. Hauet, J. Phys. D: Appl. Phys. (2016) editor pick JPhys+

B.6.2. Matériaux demi-métalliques pour la spintronique

Dans la cadre du développement de l'électronique de spin, la polarisation en spin des électrodes magnétiques est un des paramètres cruciaux, par exemple pour obtenir une grande magnétorésistance (MR) ou un bon couple de transfert de spin. Nous l'avons déjà étudiée dans le cas des multicouches Co/Ni. Le graal est ici l'obtention de matériaux demi-métalliques magnétiques (HMM) présentant un pseudo-gap, et donc une polarisation de 100%, au niveau de Fermi (E_F). Dans ces matériaux, l'absence d'états de spin minoritaires à E_F doit également mener à un amortissement (Gilbert damping) très bas. Combiner haute polarisation et faible amortissement dans un dispositif mémoire est très utile, notamment dans le but de réduire la valeur de courant critique nécessaire à l'écriture dans des mémoires STT-RAM.

Parmi les matériaux ayant été théoriquement prédits HMM, les matériaux ayant une structure cristallographique Heusler sont les plus connus. En particulier deux matériaux ont retenu notre attention : (i) $Co_{1.5}Fe_{1.5}Ge$ (CFG) pour lequel une importante augmentation de la magnetoresistance géante dans les vannes de spin a été observée, et (ii) Co_2MnSi (CMS) pour lequel une très grande valeur de magnétorésistance tunnel a été observée dans des jonctions tunnels à base de MgO. Toutefois, à ce jour aucun HMM n'a été observé experimentalement. De plus la détermination des propriétés HMM a été réalisée en se basant sur des techniques indirectes telles que les mesures de transport. Or comprendre les propriétés de transport dans un dispositif en ne considérant que les densités d'états (DOS) à E_F est souvent une tâche compliquée car ce ne sont pas les seuls ingrédients impliqués dans le processus. Nous avons récemment commencé une étude CFG et CMS par photoémission résolue en spin (SRPES) en plus des mesures standard de caractérisation structurale, de résonance ferromagnétique, de magnétométrie et de mesure de transport électrique. Comme nous l'avons montré pour le système FeCo/MgO, SRPES est une méthode directe qui permet, outre la mesure de la DOS, la mesure de la symétrie des états électroniques nécessaire à la compréhension du transport dans les jonctions tunnel cristallisées.

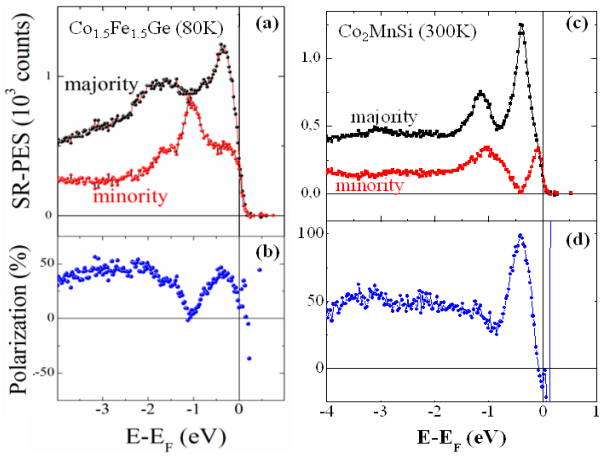

Fig. B7 : SRPES entièrement intégrés en k mesurés à 80 K et à la rémanence pour les alliages épitaxiés Heusler $Co_{1.5}Fe_{1.5}Ge$ et (c) Co_2MnSi. Une polarisation en spin de 100% a été observée pour la première fois.

Des films de CFG et de CMS ont été préparés par évaporation par jet moléculaire sous ultra-vide (UHV-MBE). L'ordre cristallographique et chimique de CFG a été étudié en détails par diffraction d'électron (RHEED) et diffraction de rayons X, ainsi que par diffraction de neutrons. D'après les calculs ab-initio, l'existence du pseudo-gap au niveau de Fermi est fortement dépendante de l'ordre chimique. Tandis que l'ordre chimique entre le Fe et le Ge n'affecte en rien le pseudo-gap, toute substitution entre les sites de Co et les sites du Fe ou du Ge amène à la destruction de ce dernier. Dans ces films bien caractérisés de CFG, nous n'avons pas observé de pseudo-gap par SRPES, en accord avec les valeurs faibles (<100%) de magnétorésistance tunnel (Fig. B7). En revanche, et bien que les DOS mesurées soient similaires à celles de CFG, les spectres de photoémission des films CMS, un pseudo-gap existe dans le DOS, environ 0.5eV en dessous du niveau de E_F générant une polarisation de 100% (Fig. B7). Dans le cadre de la thèse d'Amina Neggache, nous avons démontré qu'un état de surface de CMS était à l'origine de l'absence de gap au niveau de Fermi. Nous avons montré que cet état de surface pouvait être modifié en recouvrant CMS par du MgO ou du Mn, et donc il est possible de modifier la polarisation en spin par ce biais. Nous avons également montré qu'en modifiant les concentrations de CMS, il est possible de décaler le niveau de Fermi et donc d'augmenter la polarisation au niveau de Fermi. Des facteurs d'amortissement de Gilbert aussi bas que 7.10^{-4} ont été obtenus. Il reste quelques challenge pour cette théamtique. Notament réussir à imposer une anisotropie perpendiculaire sans diminuer la forte polarisation en spin.

Publication représentative : "Direct evidence for minority spin gap in the Co2MnSi Heusler alloy" S. Andrieu, A. Neggache, T. Hauet, T. Devolder, A. Hallal, M. Chshiev, A. Bataille, P. Le Fèvre, F. Bertran, Phys. Rev. B 93, 094417 (2016)

VII.3. Frustrations magnétiques

Au cours de mes études concernant les mémoires magnétiques nanostructurés, des effets de frustrations magnétiques sont apparues, notamment dans les réseaux hexagonaux. On peut considérer chaque plot comme un spin d'Ising orienté perpendiculairement au substrat, soit vers le haut, soit le bas. Dans les systèmes les plus simples, la seule intéractions entre les plots est l'interaction dipolaire qui tend à aligner les plots voisins anti-parallèles entre eux.

Dans un réseau hexagonal, les trois spins au coin du traingale de la maille de base du réseau ne peuvent pas être tous anti-parallèles à leur voisin. Deux de ces spins au moins sont parallèles. Par conséquent, le système est frustré. Nous avons étudié l'influence de cette frustration, calculé les états de minimum d'énergie pour ce système et pu les retrouver expérimentalement à l'aide de désaimantation sous champ magnétique.

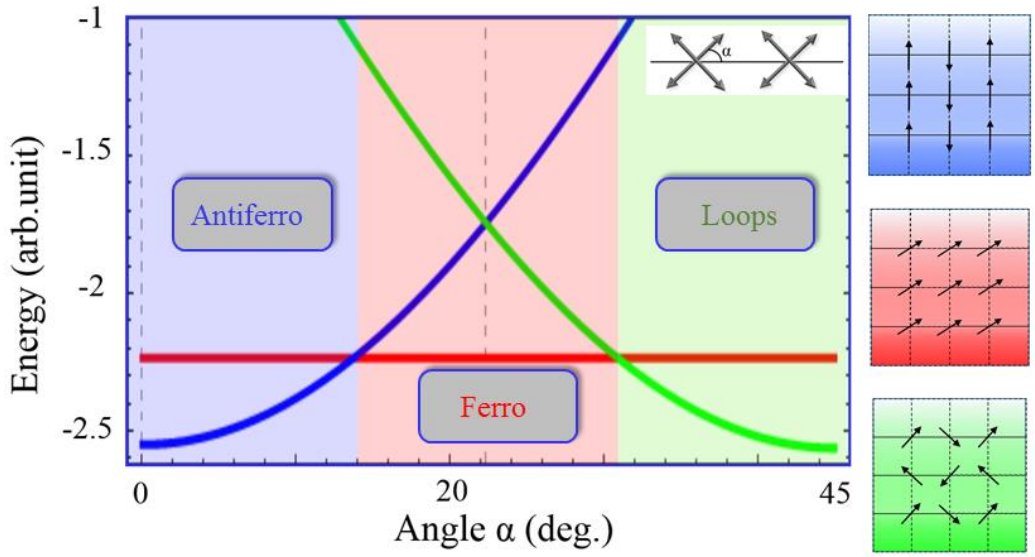

Fig. B8. Energie de trois configuration magnétique en fonction de l'angle alpha défini comme l'angle entre une direction d'anisotropie et un des axes du résau de spins.

Depuis quelques années, ces systèmes frustrés de spin d'Ising orientés dans le plan du substrat ou perpendiculaire sont beaucoup étudiés. En revanche, des systèmes avec deux directions de possible aimantation (i.e. 4 orientations possibles) n'ont pas encore été expérimentalement testés. Dans la thèse de Damien Louis que je co-encadre depuis oct. 2013, nous étudions, expérimentalement et théoriquement, les effets de frustration magnétique et la physique des monopoles dans des réseaux artificiels de nano-aimants à anisotropie planaire quadratique. Théoriquement, nous avons calculé que dans ce système, en fonction de l'angle relatif entre les axes d'anisotropie quadratique et les axe du réseau, l'état fondamental correspond à différentes configurations magnétiques (Fig. B8). En particulier, il apparait que pour une plage d'angle autour de 22°, un état ferromagnétique devient l'état de plus basse énergie. Ce résultat est très original car il n'est généralement prévu que, dans un système à deux dimensions, le champ dipolaire (seule intéraction existante ici) favorise un état ferromagnétique. En parallèle, nous avons développé des plots cubiques de V(20 nm)/Fe(2 nm)/V(5 nm)/Au(5 nm), dont les propriétés magnétiques ont été étudiées en détails. Ces nanostructures ont été définies par lithographie électronique et gravure ionique et observées en microscopie à force magnétique (MFM). Ce système nous a permis de démontrer experimentalement les résultats de nos calculs théoriques. Le rôle des effets de taille, de géométrie et des conditions de bords dans ces réseaux sur l'apparition de phases de spin ordonnées et désordonnées a été étudié. La procédure de désaimantation permettant d'accéder aux configurations de spin de plus basse énergie est critique dans ces études. Nous avons montré qu'une désaimantation thermique est plus performante qu'une désaimantation en champ pour atteindre des configurations de plus basse énergie.

Dans la suite de cette étude nous allons chercher à imager et à simuler en temps réel comment ces réseaux s'accommodent des effets de frustration pendant qu'ils sont désaimantés par excitation thermique. Des mesures X-PEEM dynamique au synchrotron SOLEIL devraient nous permettre de la faire.

Publications représentatives :

"Reversal mechanism, switching field distribution, and dipolar frustrations in Co/Pt bit pattern media based on auto-assembled anodic alumina hexagonal nanobump arrays" T. Hauet, L. Piraux, S. K. Srivastava, V.A. Antohe, D. Lacour, M. Hehn, F. Montaigne, J. Schwenk, M.A. Marioni, H.J. Hug, O. Hovorka, A. Berger, S. Mangin, F. Abreu Araujo, Phys. Rev. B 89, 174421 (2014)

'Towards a new artificial spin system: the dipolar 4-states Potts model" D. Louis, T. Hauet, D. Lacour, M. Hehn, F. Montaigne, to be published